

The Pennsylvania State University

The Graduate School

Department of Chemistry

Aluminum Cluster Anion Reactivity:
Applications in Energetic Materials and Catalysts

A Dissertation in

Chemistry

by

William Henry Hunter Woodward

© 2011 William H. H. Woodward

Submitted in Partial Fulfillment
of the Requirements
for the Degree of

Doctor of Philosophy

December 2011

The dissertation of William H. H. Woodward was reviewed and approved* by the following:

A. Welford Castleman, Jr.
Eberly Distinguished Chair in Science
Evan Pugh Professor of Chemistry and Physics
Dissertation Advisor
Chair of Committee

Nicholas Winograd
Evan Pugh Professor of Chemistry

John B. Asbury
Assistant Professor of Chemistry

Richard Yetter
Professor of Mechanical Engineering

Barbara J. Garrison
Head of the Department of Chemistry
Shapiro Professor of Chemistry

*Signatures are on file in the Graduate School

ABSTRACT

The research presented in this dissertation focuses on the size-selective properties of aluminum clusters and their applications in catalysis and energetic materials. As the size of metals approaches the molecular regime, their properties begin to differ from the bulk. In fact, individual clusters exhibit different properties as even a single atom is added or removed. Some of these clusters display characteristics similar to elements of the periodic table, giving rise to a “3-D periodic table.” Additionally, some clusters demonstrate characteristics that are unique from any element, which is desirable for use in a variety of applications including catalysis and energetic materials. It is the goal of this research to study these clusters in detail in order to one day construct a material which maintains these desirable properties. Specifically, the resistance of specific aluminum clusters to reaction with oxygen is explored, and it is discussed how this could lead to the use of aluminum cluster-based solids in combustible materials. Additionally, recent research has led to the discovery of a unique form of aluminum cluster reactivity wherein polar bonds are catalytically broken. It is discussed how this mechanism could be used to generate hydrogen from water/alcohol or cleave high-energy carbonyl bonds. The possibility of a “cluster-assembled material” would imply that material properties could be selectively tailored to fit the needs of the application, which would give rise to a whole new field of solid-state physical chemistry.

TABLE OF CONTENTS

List of Figures	vii
Acknowledgements	xiii
Chapter 1 Introduction.....	1
1. All-Metal Clusters: A Brief Pre-History.....	1
2. Size Dependant Characteristics of Clusters: The Jellium Model.....	6
3. Aluminum Clusters: Past Developments and Current Motivations	16
4. Clusters and Catalysis: Understanding Catalytic Mechanisms.....	23
5. Present Research	26
6. References	27
Chapter 2 Experimental Techniques and Applications	32
1. Overview of Instrumentation.....	32
2. Cluster Sources	34
a. Laser Vaporization Source.....	35
b. Magnetron Gas Aggregation Source	41
3. Multiple-Ion Laminar Flow Tube	45
a. The Importance of Laminar Flow	46
b. Kinetic Theory and Rate Constants	52
c. Conical Octopole Ion Guide	54
4. Differential Pumping	63
a. Ion Optics and Vacuum Pumps.....	64
5. Detection Methods.....	68
6. Deposition Methods and Considerations	69
a. Vacuum Suitcase.....	70
b. Cluster Deposition	76
c. Self-Assembled Monolayers.....	79
7. Scanning-Tunneling Microscopy/Spectroscopy	80
8. First-Principles Density Functional Theory.....	84
9. References	86
Chapter 3 Energetic Materials.....	95
1. Introduction	95
2. Experimental.....	97
3. Results and Discussion	98
4. Conclusions	108
5. References	108

Chapter 4 Catalysts	111
1. Introduction	111
2. Semi-Empirical Rules for Nucleophilic Attack	112
3. Extension of the Mechanism	117
a. Alcohols	118
b. Hydrogen Sulfide and Ammonia	121
4. Carbonyl Bond Cleavage	122
a. Formaldehyde	123
b. Acetone, Carbon Dioxide, and Carbon Monoxide	130
5. Conclusions	131
6. References	132
Chapter 5 Deposition	136
1. Introduction	136
2. Results and Discussion	139
3. Conclusions	142
4. References	143
Chapter 6 Final Considerations	147
1. Review of Current Aluminum Cluster Research	147
2. Future Research in Energetic Materials	148
3. Future Research in Catalysis and Surface Deposition	149
4. Closing Remarks	152
Appendix A Fine Experimental Details	154
1. Overview of Instrumentation	154
2. Cluster Sources	154
a. Laser Vaporization Source	154
b. Magnetron Gas Aggregation Source	156
3. Multiple-Ion Laminar Flow Tube	159
a. The Importance of Laminar Flow	159
b. Kinetic Theory and Rate Constants	160
c. Conical Octopole Ion Guide	163
4. Differential Pumping	163
a. Ion Optics and Vacuum Pumps	163
5. References	164

Appendix B Matrix-Isolation Cavity Ringdown Spectroscopy	166
1. Introduction	166
2. The Mathematics of Cavity Ringdown Spectroscopy	170
a. Ringdown Time for an Empty Cavity.....	170
b. Ringdown Time for a Non-Empty Cavity	173
c. Experimental Determination of Absorbance Spectra.....	175
d. Solving for the Absorption Cross Section	178
3. Experimental Concerns.....	179
a. The Cavity	180
b. The Matrix	182
c. The Substrate	184
4. Current and Future Experiments.....	188
5. Conclusions	190
6. References	191

LIST OF FIGURES

Figure 1.1. a) Example of a basic diatomic molecule, wherein the atomic orbitals form bonding and antibonding orbitals. b) Conceptual drawing of the growth of a metallic band, wherein the partially filled atomic orbitals create a partially filled band of nearly degenerate orbitals.	4
Figure 1.2. a) Mass spectrum of sodium clusters, $N < 100$. b) The calculated change in the electronic energy difference versus N . The labels of the peaks correspond to “magic” clusters (i.e. closed-shell jellium orbitals). Adapted from Reference 15.	6
Figure 1.3. Electronic jellium shells for sodium clusters of a) 8, b) 20, and c) 198 atoms. R is the calculated outer radius of the lowest energy shell and n/n_0 is the ratio of jellium electron density versus the average electron density of the bulk. Adapted from Reference 26.	11
Figure 1.4. a) Distortion parameter (used to determine spheroidal shape) of a cluster predicted by full and partial shell closings using the Clemenger-Nilsson model. b) Geometric representations of shell closings and c) theoretical structures for select sodium clusters are shown for reference. a), b) and c) are adapted from References 34, 30, and 41, respectively.	14
Figure 1.5. Select examples of predicted occupied and unoccupied molecular orbitals for Al_{13}^- (40 electrons) determined using density functional theory. Predicted jellium S, P, D, and F orbitals are labeled, which show remarkable resemblance to atomic s, p, d, and f orbitals, respectively. Adapted from Reference 43.	16
Figure 1.6. Artistic representation of the three dimensional periodic table with select examples. In reality, multiple clusters could be conceived which mimic the same element, giving rise to a truly three-dimensional aspect. Adapted from Reference 57.	18
Figure 1.7. Aluminum particle burning times over varying size. Adapted from Reference 67.	21
Figure 1.8. Example of an aluminum nanoparticle/ice-based rocket fuel. Photograph (Eric Barlow) adapted from Reference 70.	22
Figure 1.9. Examples of cyclical cluster-assembled materials consisting of Al_{13} superatoms and K_3O ligands, similar to a repeating or multidecker sandwich structure. Adapted from Reference 71.	23
Figure 1.10. Example drawing of a gas-phase zirconium-oxide cluster catalytic oxidation mechanism and its theoretical transfer to defect sites (step edges) on a surface. Adapted from Reference 78.	25

- Figure 2.1. Primary experimental apparatus. a) Aluminum clusters are created in a cluster source and b) carried into a laminar flow reaction vessel where they can be exposed to a reactant gas. c) The reactants and products are then focused via a conical octopole into d) the differential pumping region. e) The ions were transported around a bend via a quadrupole energy deflection filter to eliminate neutral species, and g) mass selected via a quadrupole mass spectrometer and channeltron electron multiplier. The entire system is controlled using a personal computer.....34
- Figure 2.2. Standard laser vaporization source. Focused laser light is used to ablate a target, which is typically a rotating/translating rod. Pulsed gas then carries the nascent clusters through the expansion nozzle into the vacuum instrument. Adapted from Reference 12.....36
- Figure 2.3. High-speed photographic images of a high-power laser pulse striking aluminum. Units of time are in ms, exposure time is 6 μ s. Adapted from Reference 22.....38
- Figure 2.4. a) Illustration of magnetron head depicting magnetic field lines and argon inlet. b) Illustration of custom magnetron gas aggregation source depicting adjustable iris and water cooling lines. Illustrations are not to scale. Clusters are condensed from the plasma formed by the magnetron head before escaping into the vacuum instrument. Linear translation allows the adjustment of the distance between the magnetron head and the iris, helium backing gas (inlet not shown) and argon pressures can be freely adjusted.....42
- Figure 2.5. Examples of two aluminum cluster anion distributions created a) with and b) without supersonic expansion. A strong step edge at the jellium shell closing Al_{13}^- can be observed in (a) due to the concomitant evaporation of clusters with expansion cooling. (a) Adopted from Reference 50.....50
- Figure 2.6. a) Illustration of field lines in a conical octopole predicted by Equation 2.20 ($V(r)$ and $V(z)$ are shown logarithmically and irrespective of each other for clarity). Red lines indicate physical poles, blue line indicates hypothetical ion trajectory (left to right). Note the wide exit angle. b) Three-dimensional depiction of the same field lines, for clarity. One can imagine the difficulty in rolling a marble through the slit at the end, and how large initial velocities would be required. c) Possible conical octopole ion trajectories in a vacuum environment: R) reflected, A) absorbed, and T) transmitted. (c) Adapted from Reference 67.....59
- Figure 2.7. Illustration of field lines in a conical octopole predicted by Equation 2.21, where a laminar flow backing gas is present ($V(r)$ and $V(z)$ are shown logarithmically and irrespective of each other for clarity). Note the funnel shape in the z -direction.....61

Figure 2.8. Diagram of the custom-built vacuum suitcase (to scale). a) The air-sensitive sample is prepared in a sample holder that is attached to the linear translator of the suitcase via a fixed screw thread. b) The suitcase is attached to the vacuum instrument via two gate valves, with a vent that enables both initial evacuation of the suitcase volume and, following deposition, venting of the small chamber between the instrument and the suitcase. c) Vacuum inside the chamber is maintained by a battery-powered ion pump (controller not shown). d) After sample preparation, the holder is linearly translated into the suitcase where the gate valve can be closed and e) the entire suitcase can be detached and transported. f) Once the suitcase is connected to the next vacuum apparatus, the sample can be securely removed by a wobble stick with modified jaws.....71

Figure 2.9. Diagram of sample transfer. a) The slot in the top jaw allows the claw to b) encompass the sample while allowing access to the tapped holes by the threaded coupling rod. c) Once the jaws are secured around the sample, the linear translator can be rotated to unscrew the thread from the sample. d) With the sample separated from the vacuum suitcase, it can be rotated and translated freely inside of the UHV chamber.....73

Figure 2.10. Theoretical deposition of Ag_7 cluster onto a $\text{Pd}(100)$ surface at 0 eV and 0 K. Filled circles represent Ag atoms and hollow circles represent Pd atoms. Arrows are used to identify when atoms undergo a site exchange. Adapted from Reference 85.....78

Figure 2.11. Example of liquid-phase self-assembled monolayer construction. Two-dimensional organization is promoted by the strong adsorption of the “headgroups” to the substrate. Adapted from Reference 111.....80

Figure 2.12. Illustration of constant-current STM imaging with a basic circuit diagram representation. As the tip is scanned across the conductive surface it is raised or lowered by a computer to maintain a constant current through the interface. This procedure can be used to rasterize across a 2-D surface, thus producing an image of the electronic density of the surface. Cartoon and graphs adapted from Reference 118. Circuit diagram adapted from Reference 119.82

Figure 2.13. a) Representative circuit diagram of a double barrier tunnel junction. b) Illustration of a cluster on a self-assembled monolayer. c) Actual scanning tunneling microscopy image of cluster. d) Scanning tunneling spectroscopy data for metallic cluster, where the double barrier tunnel junction can be seen. The current versus voltage graph (black) shows step-edges where additional electronic levels are tunneled to and from, and the derivative of this (indigo) produces a spectrum similar to that of absorption spectroscopy. Although not shown here, a current versus voltage graph of a single tunnel junction would imitate a sloped line as predicted by Ohm’s law. (a) is adapted from Reference 119; (b), (c), and (d) are adapted from Reference 120.83

Figure 3.1. Observed Al_n^- mass spectrum (black) before and (red) after introduction of a) 42.5 sccm $\text{O}_2(X^3\Sigma_g^-)$ and b) 42.5 sccm of a 12% $\text{O}_2(a^1\Delta_g)/\text{O}_2(X^3\Sigma_g^-)$ mixture. Intensities between (a) and (b) are arbitrary.....99

- Figure 3.2. Modeling results for rate constants of selected Al_n^- clusters with $\text{O}_2(\text{X}^3\Sigma_g^-)$. a) $n = 16$; b) $n = 13$; c) $n = 41$. The red line at a goodness-of-fit of 0.8 indicates the determined threshold above which the calculated abundances do not fit the experimental data within uncertainty. 103
- Figure 3.3. Observed and calculated branching ratios for (green) initial and final aluminum distributions with (black) $\text{O}_2(\text{X}^3\Sigma_g^-)$ and (red) $\text{O}_2(\text{a}^1\Delta_g)/\text{O}_2(\text{X}^3\Sigma_g^-)$. Observed values are represented by circles. Calculated values are represented by colored lines. 104
- Figure 3.4. Fitted rate constants for a) $\text{Al}_n^- + \text{O}_2(\text{X}^3\Sigma_g^-)$ and b) $\text{Al}_n^- + \text{O}_2(\text{a}^1\Delta_g)$. c) Relative rate constants for $\text{Al}_n^- + \text{O}_2(\text{a}^1\Delta_g)$ to $\text{Al}_n^- + \text{O}_2(\text{X}^3\Sigma_g^-)$ for each cluster size and d) for adjacent cluster sizes. 105
- Figure 4.1. Lowest fully unoccupied molecular orbitals for a) Al_{13}^- , b) Al_{23}^- , and c) Al_{20}^- . Metiu's semi-empirical rules for nucleophilic attack (Reference 21) suggest that those orbitals protruding into vacuum will be most susceptible to attack. 113
- Figure 4.2. Experimental mass spectra of aluminum cluster reactivity with water. a) Aluminum cluster distribution before introducing water; b) Aluminum cluster distribution after introducing a large amount of water; c) retuned aluminum cluster distribution before d) introducing a small amount of heavy water. e) Zoomed-in section of grayed box in (d) focusing on D_2 loss; D_2O and H_2O were used interchangeably with no discernible difference in reactivity. The specific mass spectra shown were acquired using D_2O for (c), (d), and (e), and H_2O for (a) and (b). The colored lines are to aid the reader in identifying aluminum cluster peaks, with Al_{12}^- , Al_{17}^- , Al_{20}^- , and Al_{23}^- represented by green, red, blue, and purple lines, respectively. Adapted from Reference 14. 114
- Figure 4.3. Graph comparing theoretically determined LUMO energies (blue) to experimentally observed aluminum cluster anion (Al_n^-) intensities after reaction with water (red) from $n = 11$ -25. Intensities between the two are normalized to Al_{13}^- to allow for comparison. The post-reaction intensities were acquired from the same data used in Figure 4.2.e. For even-numbered clusters the LUMO+1 was used, as is described in the main text. 115
- Figure 4.4. Reaction coordinate diagram for the reaction of Al_{17}^- with water. a) Water attacks the intact cluster, bonding to the LUMO. b) The resultant bond formation between the adjacent Al atom and the H atom requires sufficient energy to overcome a barrier. c) The LUMO of the final product is then susceptible to further nucleophilic attack, d) eventually leading to the liberation of a hydrogen molecule. Adapted from Reference 14. 116
- Figure 4.5. Full etching spectra with non-pure aluminum peaks $\text{Al}_n\text{ROH}_m^-$ labeled as (n,m). a) $\text{R} = \text{H}$; b) $\text{R} = \text{CH}_3$; c) $\text{R} = \text{C}(\text{CH}_3)_3$. The colored lines are to aid the reader in identifying aluminum cluster peaks, with Al_{11}^- , Al_{13}^- , and Al_{20}^- represented by red, green, and blue lines, respectively. 119

- Figure 4.6. Relative reactivities of a) water, b) methanol, and c) *t*-butanol with aluminum cluster anions (Al_n^-). Values determined by dividing final aluminum cluster intensities by initial intensities. Relative reactivity intensities are arbitrary. 120
- Figure 4.7. Etching spectra of Al_n^- cluster anions a) before and after reacting with b) H_2S and c) NH_3 . The colored lines are to aid the reader in identifying aluminum cluster peaks, with Al_{12}^- and Al_{20}^- represented by green and blue lines, respectively. 122
- Figure 4.8. Aluminum cluster anion distribution a) before and b) after reaction with formaldehyde. Aluminum clusters (Al_n^-) are labeled with blue numbers, formaldehyde additions [$\text{Al}_n(\text{OCH}_2)^-$] are labeled with red numbers, and oxygen losses [$\text{Al}_n(\text{CH}_2)^-$] are labeled with green numbers. Anomalies are labeled in black. Intensities are arbitrary. 125
- Figure 4.9. Theoretically determined reaction coordinate diagrams of $\text{Al}_n^- + \text{OCH}_2$ for a) $n = 9$, b) $n = 12$, and c) $n = 13$. For each initial structure, the HOMO and LUMO (LUMO+1) are shown in red and blue, respectively. The results reveal that Al_9^- and Al_{12}^- will react readily at the complementary active sites and subsequently lose an Al_2O , while Al_{13}^- does not have active sites and has both a barrier to carbonyl cleavage and Al_2O release is endothermic. This is in agreement with experimental observations. 127
- Figure 4.10. Theoretically determined reaction pathways for $\text{Al}_{11}^- + \text{OCH}_2$. The LUMO and LUMO+1 are shown in blue and aqua, respectively, while the HOMO and HOMO-1 are shown in red and orange, respectively. In the upper diagram, the oxygen attacks the LUMO and the carbon bonds to the HOMO, while in the lower pathway the O atom binds to a second site with significant LUMO density, and the C atom binds to the HOMO-1. In both cases, there is sufficient energy available for the reaction to proceed and an Al_2O is lost. 129
- Figure 4.11. Aluminum cluster anion distribution after reaction with a) acetone, b) carbon dioxide, and c) carbon monoxide. Initial distributions were all similar to that shown earlier (Figure 4.8.a). Acetone additions [$\text{Al}_n(\text{OC}(\text{CH}_3)_2)^-$] are labeled with red numbers, and oxygen losses [$\text{Al}_n\text{C}(\text{CH}_3)_2^-$] are labeled with green numbers. Additional reactivity with acetone is present due to the methyl leaving group. In (b) and (c), no reactivity is observed two contaminant peaks in (c) can be attributed to (\dagger) $\text{Fe}(\text{CO})_4^-$ and (\ddagger) $\text{Fe}(\text{CO})_5^-$; two common contaminants in bottled carbon monoxide. 131
- Figure 5.1. Scanning tunneling microscopy images of a) a hydroxyl-terminated self-assembled monolayer (SAM) and b) & c) Al_{17}^- clusters. The clusters were stable to repeated imaging, indicating covalent attachment to the SAM.⁴⁵ (a) $V_s = 1 \text{ V}$, $I_t = 15 \text{ pA}$, $800 \text{ \AA} \times 800 \text{ \AA}$; (b) $V_s = 1.5 \text{ V}$, $I_t = 15 \text{ pA}$, $320 \text{ \AA} \times 320 \text{ \AA}$; (c) $V_s = 2 \text{ V}$, $I_t = 10 \text{ pA}$, $1300 \text{ \AA} \times 1300 \text{ \AA}$ 140

- Figure 5.2. Scanning tunneling microscopy image ($V_s = 2$ V, $I_t = 8$ pA, $400 \text{ \AA} \times 400 \text{ \AA}$) of an Al_{17}^- cluster adsorbed to a hydroxyl-terminated self-assembled monolayer (SAM). Tunneling spectra were acquired over the SAM (magenta) and cluster (blue) over ± 2.5 V. A region of zero conductance can be seen in the $I(V)$ spectrum acquired over the cluster. The measured HOMO-LUMO gap is 1.4 eV. No further gaps were observed beyond ± 1.0 V, and so the spectra is condensed accordingly for clarity. 141
- Figure A.1. a) Aluminum and b) copper spectra acquired with custom magnetron gas aggregation source. It can be observed in both spectra that there exists a certain degree of contamination, which in most cases is a combination of carbon and oxygen addition to each cluster. 158
- Figure B.1. Diagram of standard cavity ringdown setup where R_n is the reflectivity of the mirrors, L is the length of the cavity, and L/c is the round trip time for light in the cavity. The intensity of the light exiting the cavity after each round trip follows a natural logarithmic decay, as shown in Figure B.2. 171
- Figure B.2. Simplified example of a ringdown, where the grey curves represent the actual light escaping the cavity and the black line represents the solution for the ringdown. The red dashed line indicates the ringdown time, τ 171
- Figure B.3. Custom-built ultra-high vacuum mirror mounts for cavity ringdown spectroscopy. Dimensions are in inches. The mirror holder can be swapped to hold any mirror size smaller than 2 inches. The Gimbal-style mount is adjusted via two magnets powerful enough to penetrate the 0.25 inch steel flange. 180
- Figure B.4. a) Percent of total cavity light at the exit mirror with respect to the number of round trips. It can be seen that, for varying substrate transmissions, the number of round trips will eventually reach 50%. The percent of light at the entrance mirror can be represented by mirroring the curve across the x -axis at 50%. b) Comparison of ringdowns from an empty cavity (green) and a cavity with a 93% transmissive substrate (blue). Although the non-empty cavity appears to have a faster ringdown time, they are actually the same once the non-empty cavity has equalized on either side of the substrate, approximately 20 round trips. The consequent difference in I_0 has no effect on the ringdown time. 187
- Figure B.5. a) Ringdown of empty cavity, $L = 1.055$ m. Predicted period of 200 nm can be seen, caused by fluctuations in focus of light exiting the cavity. b) Ringdown of cavity with sapphire window orthogonal and centered. A possible bi-exponential decay is traced, with the addition of both red and green decays forming the blue decay which is in good agreement with the experiment. 189

ACKNOWLEDGEMENTS

The author would first and foremost like to acknowledge the incalculable generosity of Professor Castleman, who consistently made readily available his unfathomable oceans of wisdom for the purpose of the scientific progress presented herein. No short amount of words could outline Professor Castleman's generosity or acumen, and so these few will have to suffice. The author would also like to thank his friends and colleagues in the Castleman group; our friendly yet professionally critical dynamic has allowed for some interesting chemistry, some of which would definitely not exist without their *arguendo*. The author would also like to thank the many collaborators that he had the pleasure of working with: Shiv Khanna and Art Reber at the Virginia Commonwealth University; Al Viggiano, Nicole Eyet, and Nick Shuman at Hanscom Air Force Base; and Paul Weiss and Meghan Blake at the Pennsylvania State University. Finally, the author would like to thank the members of his committee, who have all provided valuable discussions relating to this dissertation at some point over the past five years.

The experimental work presented in this dissertation was funded by the Air Force Office of Scientific Research, grants FA 9550-07-1-0151 and FA 9550-10-1-0071 and through an Army MURI grant, ARO W911NF-06-1-0280. The theoretical work discussed herein was funded by the Air Force Office of Scientific Research, grant FA 9550-04-1-0066 and through the same Army MURI grant, ARO W911NF-06-1-0280. The author is very grateful for this funding and for all past and future support involving these projects and their long-term goals.



Chapter 1

Introduction

Die Geschichte der Wissenschaften ist eine große Fuge,
in der die Stimmen der Völker nach und nach zum Vorschein kommen.

The history of the sciences is a great fugue,
in which the voices of the nations come one by one into notice.

—Johann von Goethe¹

1. All-Metal Clusters: A Brief Pre-History

The purpose of this chapter is to introduce the concept of metallic clusters and outline the contents of the rest of this dissertation. However, in order to provide a comprehensive understanding of this work, we must first review the history of this field. It will shortly be seen that cluster science, which is today a large field with several sub-disciplines, is a result of more than a century of chemical and physical research, both experimental and theoretical. The backgrounds of each individual responsible for major breakthroughs in the field vary by large amounts, and this chapter outlines the major historical achievements and motivations both so that this text will exist as a stand-alone work and so that the reader may gain an appreciation for the creation of this field of science, which is not attributable to one individual but rather to all of the scientific community, the world, and mankind as a whole.

The entirety of the work presented herein involves the size-selective reactivity of aluminum clusters. Therefore, due to the ambiguity of the word “cluster” (the word is commonly applied over an extensive range of size regimes, from galaxies to molecules to breakfast cereals),

the most beneficial initial topic of discussion involves defining what a cluster is, in the present context. For the purposes of this dissertation, let us define a cluster as a molecule composed of no more than one hundred metal atoms. As is revealed in the following chapters, this number is dependent on the metal(s) being considered, but let us first discuss why there is any consideration of size at all, as bulk metals are generally considered to have characteristics that are independent of their size.

At the beginning of the twentieth century, when the study of solids was transforming from an art (e.g. metallurgy) into a science (i.e. solid-state physics), much was still unknown about the inner-workings of molecules.² The earliest use of theory to explain various solid-state phenomena was pioneered by the German physicist Paul Drude, then at the University of Leipzig, and the Dutch Nobel laureate Hendrik Lorentz at the University of Leiden, who proposed that a metal could be considered a uniform mass of equally distributed positive charge, and that electrons occupying this mass and negating this charge were free to move about as dictated by exterior forces.^{3,4} This model treated electrons as an ideal gas, and the terms “electron gas” and “free-electron metal” which originated from these theoretical studies are still used today. While this early model had many flaws due to its ideal nature, it persisted for nearly three decades as the prominent explanation for many phenomena observed in solids, both electronic and optical. In 1926 and 1927 Wolfgang Pauli and Arnold Sommerfeld had repaired many of the inadequacies inherent in the Drude–Lorentz theoretical model (Austrian and German physicists, respectively; the brilliant Pauli was a student of Sommerfeld’s at the Ludwig-Maximilians University in Munich before Pauli became a lecturer at the University of Hamburg in 1923 where he developed his exclusion principle that won him the Nobel Prize in physics).⁴⁻⁶ It was also in 1926 that the legendary Austrian physicist Erwin Schrödinger, then at the University of Zürich, published his historical paper “Quantization as an Eigenvalue Problem” [Quantisierung als Eigenwertproblem],⁷ the first of four papers that forever changed the world via the gift of

quantum mechanics. In 1928 Felix Bloch, the Swiss physicist who later earned the Nobel Prize in 1952 for his role in the development of nuclear magnetic resonance, obtained a doctorate from the University of Leipzig in Germany. His doctoral dissertation, “On the Quantum Mechanics of Electrons in Crystal Lattices” [Über die Quantenmechanik der Elektronen in Kristallgittern], was the first to treat electrons in a metal not as a gas but as waves.⁸ This development began a timeline involving rapidly successive contributions and developments that subsequently made solid-state physics a breathtakingly massive field, full of numerous achievements, several Nobel Prizes, and endless sub-disciplines.^{2,9} One of these sub-disciplines is the physical chemistry of small clusters and how they differ from their bulk metals.

Metals are, in the simplest sense, infinitely large molecules. With the earliest understandings of molecular bonding and quantum mechanics came the concept that for each occupied electronic orbital an atom contributes toward a molecule, there is a corresponding number of bonding and antibonding orbitals that define that molecule’s electronic structure (Figure 1.1a).¹⁰ In the case of metals, incalculably large numbers of atoms create a series of orbitals that are so abundant and so nearly degenerate that they can be considered continuous. This molecular structure is called a band (Figure 1.1b), and there should be no doubts that it is, in fact, a molecule, albeit of the largest possible scale. Metals, having partially filled atomic orbitals, create a partially filled lowest band, which allow for the excitation of electrons with minimal (i.e. thermal) energy. This explanation reveals why metals and insulators behave as they do; insulators have a fully filled lowest band, and it takes large amounts of energy to promote electrons from the filled band to the next highest, unoccupied band, which is created by empty atomic orbitals.

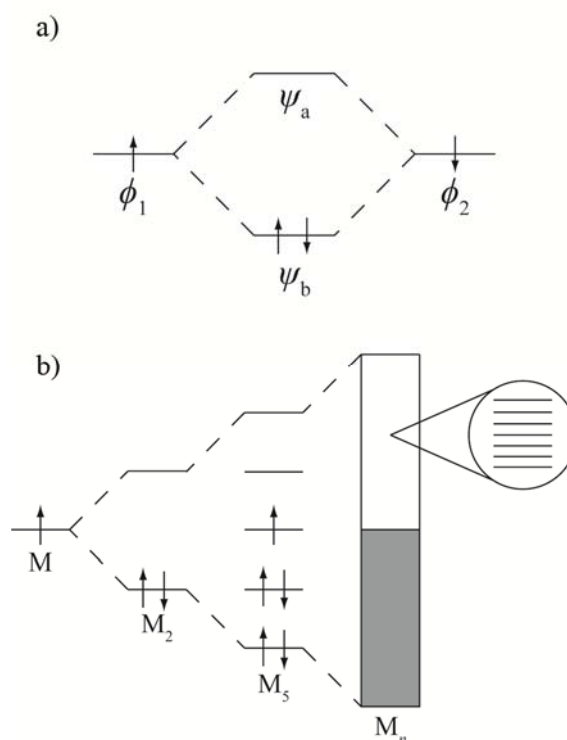


Figure 1.1. a) Example of a basic diatomic molecule, wherein the atomic orbitals form bonding and antibonding orbitals. b) Conceptual drawing of the growth of a metallic band, wherein the partially filled atomic orbitals create a partially filled band of nearly degenerate orbitals.

The theory of energy bands in solids was developed by the British physicist Alan Wilson in 1931.^{11,12} It was then that Wilson briefly left Cambridge University to visit Leipzig, which at the time was home to both Bloch and the German theoretician Werner Heisenberg who was to win the delayed 1932 Nobel Prize in Physics two years later (as a humorous aside; Wilson developed band theory because Heisenberg had asked him to give a lecture on the German-born British physicist Rudolph Peierls's then-recent work relating to the topic, and Wilson was required to re-think and simplify the standard explanation partly due to his lack of confidence in his German speaking skills and partly due to his desire to speak as lucidly as the brilliant Heisenberg).² The importance of Wilson's discovery was that in some three-dimensional solids these bands can overlap, yielding what is now a classical understanding of metals, semiconductors, and insulators.¹³

Amazingly, this broad understanding of solids persisted for over five decades. Metals were considered infinitely large molecules, and it was assumed that, as the molecules became ever smaller, the band(s) of the metal would break down into evenly spaced orbitals that would behave less like an electron gas and more like traditional molecular energy levels. Various studies exploring small metal nanoparticles (hundreds of atoms) yielded interesting results suggesting size-specific characteristics, although these were mostly attributed to the increased ratio of surface atoms (and their dangling bonds) to interior atoms (of the stable lattice).¹⁴ Then, in a groundbreaking yet highly controversial study in 1984 by Walter Knight, Keith Clemenger, Walt de Heer, Winston Saunders, Mei-Yin Chou, and Marvin Cohen at the University of California, Berkeley, observations of small gas-phase sodium molecules (< 100 atoms) suggested that specific clusters display unique physical properties as even a single atom is added or removed (Figure 1.2).¹⁵ This seminal experimental work marked the birth of what is now a field of science that spans several disciplines and even has its own sub-disciplines: the study of metal clusters.¹⁶

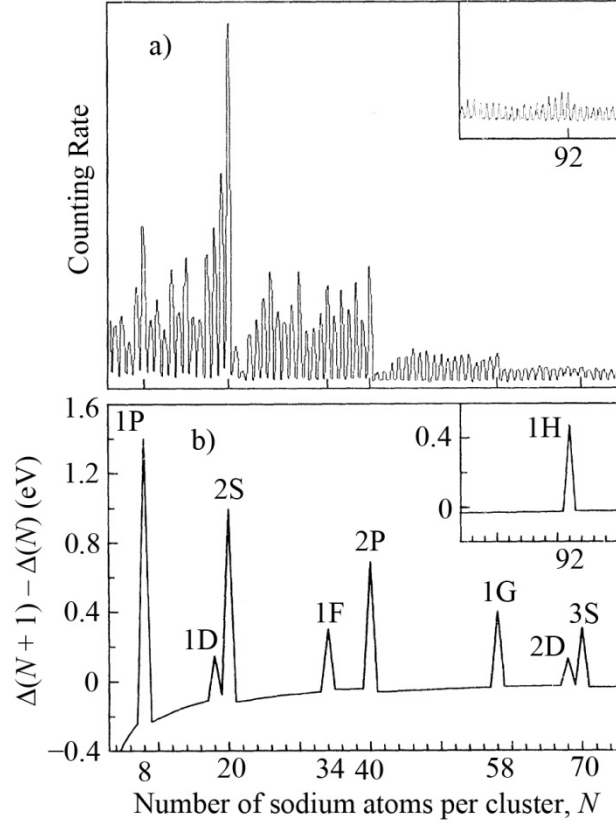


Figure 1.2. a) Mass spectrum of sodium clusters, $N < 100$. b) The calculated change in the electronic energy difference versus N . The labels of the peaks correspond to “magic” clusters (i.e. closed-shell jellium orbitals). Adapted from Reference 15.

2. Size Dependant Characteristics of Clusters: The Jellium Model

If one considers the Hamiltonian of a many-electron atom for use in the time-independent Schrödinger equation (assuming an independent electron approximation):

$$\hat{H} = \underbrace{\frac{\hbar^2 \nabla_\alpha^2}{2M}}_{\text{Nuclear Kinetic Energy}} + \sum_i \underbrace{\frac{\hbar^2 \nabla_i^2}{2m}}_{\text{Electronic Kinetic Energy}} - \sum_i \underbrace{\frac{|Ze|}{4\pi\epsilon_0 |\mathbf{r}_i - \mathbf{R}_\alpha|}}_{\text{Electron-Nucleus Potential Energy}} - \frac{1}{2} \sum_{i \neq j} \underbrace{\frac{e^2}{4\pi\epsilon_0 |\mathbf{r}_i - \mathbf{r}_j|}}_{\text{Electron-Electron Potential Energy}} \quad (1.1)$$

it quickly becomes clear that this formula is unsolvable for all but the simplest of the elements (the Hamiltonian function is named after Sir William Hamilton, who was a famous nineteenth-

century Irish mathematician/physicist; his function is the starting point of all quantum mechanics).¹⁷ However, in 1927 Max Born and J. Robert Oppenheimer, a German and an American physicist working together at the University of Göttingen in Germany (Born was the young Oppenheimer's Ph.D. supervisor), published a paper that introduced the Born–Oppenheimer approximation to the world.¹⁸ This approximation shows that electrons move blazingly fast when compared to nuclei, due to their large difference in size, which allows one to separate the nuclear and electronic aspects of the Schrödinger equation, thereby reducing it.

$$\hat{H}_e = \sum_i \frac{\hbar^2 \nabla_i^2}{2m} - \sum_i \frac{|Ze|}{4\pi\epsilon_0 |\mathbf{r}_i - \mathbf{R}_\alpha|} - \frac{1}{2} \sum_{i \neq j} \frac{e^2}{4\pi\epsilon_0 |\mathbf{r}_i - \mathbf{r}_j|} \quad (1.2)$$

This equation was further simplified via the self-consistent field approximation, which was developed by the British mathematician and physicist Douglas Hartree, also in 1927, as part of his doctoral dissertation at Cambridge.^{19,20} This approximation simplifies the inter-electronic potentials into a single wavefunction. However, the original self-consistent field approximation was flawed, as it did not consider symmetrical aspects of electronic orbitals (i.e. the restriction that only two electrons of opposite spin may occupy a single orbital). By 1935 the self-consistent field approximation had been re-tooled to include a single Slater determinant (John Slater was an American physicist at Harvard), which satisfied the Pauli Exclusion Principle.²¹ The most significant contributions to this work were performed by the Soviet physicist Vladimir Fock, and the current form of the approximation is known as the Hartree–Fock method. The self-consistent field approximation is the simplest practical form of an exchange-correlation energy, although today several other approaches exist (e.g. density functional theory). When incorporated into the Hamiltonian discussed above, it becomes:

$$\hat{H}_e = \sum_i \frac{\hbar^2 \nabla_i^2}{2m} - \sum_i \frac{|Ze|}{4\pi\epsilon_0 |\mathbf{r}_i - \mathbf{R}_\alpha|} - \sum_i \tilde{V}(\mathbf{r}_i) \quad (1.3)$$

an equation that, when used to find the normalized wavefunctions of an atom:

$$\psi_{n,\ell,m_\ell} = R_{n,\ell}(r)Y_{\ell,m_\ell}(\theta, \phi) \quad (1.4)$$

allows one to fully utilize the time-independent Schrödinger equation and thereby approximate both the energy and the probability density (i.e. average electron density) for each orbital of the multi-electron system.^{17,22-24}

$$\hat{H}\psi_{n,\ell,m_\ell} = E\psi_{n,\ell,m_\ell} \quad (1.5)$$

$$P(r) = \psi_{n,\ell,m_\ell}^2 \quad (1.6)$$

The traditional principal quantum numbers n , ℓ , and m_ℓ from (Danish) Niels Bohr's model of the atom, (German) Friedrich Hund's and (American) Robert Mulliken's orbital theory, and Hund's rules of electron configuration, respectively.

If one were to then consider the Hamiltonian operator for a molecule:

$$\hat{H} = \underbrace{\sum_{\alpha} \frac{\hbar^2 \nabla_{\alpha}^2}{2M}}_{\text{Nuclear Kinetic Energy}} + \underbrace{\sum_i \frac{\hbar^2 \nabla_i^2}{2m}}_{\text{Electronic Kinetic Energy}} - \underbrace{\sum_{\alpha \neq \beta} \frac{1}{2} \frac{Z^2}{4\pi\epsilon_0 |\mathbf{R}_{\alpha} - \mathbf{R}_{\beta}|^2}}_{\text{Nucleus-Nucleus Potential Energy}} - \underbrace{\sum_{\alpha,i} \frac{|Ze|}{4\pi\epsilon_0 |\mathbf{r}_i - \mathbf{R}_{\alpha}|}}_{\text{Electron-Nucleus Potential Energy}} - \underbrace{\frac{1}{2} \sum_{i \neq j} \frac{e^2}{4\pi\epsilon_0 |\mathbf{r}_i - \mathbf{r}_j|}}_{\text{Electron-Electron Potential Energy}} \quad (1.7)$$

it becomes clear that, even with the Born–Oppenheimer approximation and the self-consistent field approximation, the multitude of electron-nucleus interactions still presents an unsolvable equation.

$$\hat{H}_e = \sum_i \frac{\hbar^2 \nabla_i^2}{2m} - \sum_{\alpha,i} \frac{|Ze|}{4\pi\epsilon_0 |\mathbf{r}_i - \mathbf{R}_{\alpha}|} - \sum_i \tilde{V}(\mathbf{r}_i) \quad (1.8)$$

We now return to the work of Knight *et al.*, published in June of 1984, where an unusual experimental observation required a novel explanation (Figure 1.2). This required the use of a new assumption in the Hamiltonian: the jellium approximation.

The term “jellium” has been used for many years to describe the simplistic theory behind the free-electron characteristics of metals. It was first coined by (American) Conyers Herring,²⁵ then of Bell Telephone Laboratories, in a discussion following a chapter by (German) Paul Ewald

and Hellmut Juretschke, of the Polytechnic Institute of Brooklyn, in a review of a conference titled “Structure and Properties of Solid Surfaces” held at Lake Geneva, Washington in September, 1952. In this obscure epilogue of a little-known publication, Herring writes:

It is to be emphasized that the wave-mechanical calculation...applies not to a real metal but to a fictitious metal and that the fictitious metal...consists, as has been explained, of a medium with a uniform distribution of positive charge—we may call it a “positive jelly”—and a compensating number of electrons. This metal, which we may call “jellium” to distinguish it from real metals such as sodium, may be conceived to be made up of “jellium atoms,” that is, of cubes of positive jelly of such size as to contain one electronic unit of charge, with one electron attached to each atom.

While the context here specifically refers to the theoretical treatment of bulk metals, we will shortly see how it applies to clusters. The first theoretical studies to truly use a jellium model to predict the behavior of small all-metal molecules were performed by Walter Ekardt at the Fritz Haber Institute in Germany in February of 1984,²⁶ although the use of a jellium model in relation to molecules had been suggested earlier.²⁷ In Ekardt’s approach, the electrostatic part of Equation 1.7 is simplified when each nucleus (N in total) *and* its core electrons are encompassed in a spherical, homogeneous density of positive charge. This concept is, of course, contingent on the assumption that the valence electrons are truly delocalized from their atomic nuclei, and are instead merely confined to the molecule as a whole. This allows us to only consider the coulombic energy of each *valence* electron with the jellium core, with respect to every other valence electron:

$$V_c(\mathbf{r}_i) = \sum_{\alpha=1}^N V_p(|\mathbf{r}_i - \mathbf{R}_\alpha|) \quad (1.9)$$

which then simplifies the Hamiltonian into a manageable (although still quite cumbersome) level:

$$\hat{H}_e = \sum_{i=1}^{wN} \frac{\hbar^2 \nabla_i^2}{2m} - \sum_{i=1}^{wN} V_c(\mathbf{r}_i) - \sum_{i=1}^{wN} \tilde{V}(\mathbf{r}_i) \quad (1.10)$$

with w valence electrons per atom.

A striking similarity is observed when one compares Equations 1.3 and 1.10, and indeed when the energy levels are solved for a metal cluster, atom-like electronic shells are found, which directly contradict the assumptions presented in §1.1 and Figure 1.1. Differences in the jellium model yield particular differences from the elements, most notably the absence of all angular spin dependence. There is still an “azimuthal quantum number” subshell, but due to the absence of a radial function there are no apparent nodes, and therefore no $\ell < n$ restriction. These subshells are sometimes labeled with capital letters in order to distinguish them from atomic orbitals (e.g. $1S^2$, $1P^6$, $1D^{10}$, etc.). It is also obvious that the absence of the azimuthal quantum number restriction creates different orderings of the shells, some of which can be seen in Figure 1.3, where three examples of Ekardt’s study (using sodium) are provided.

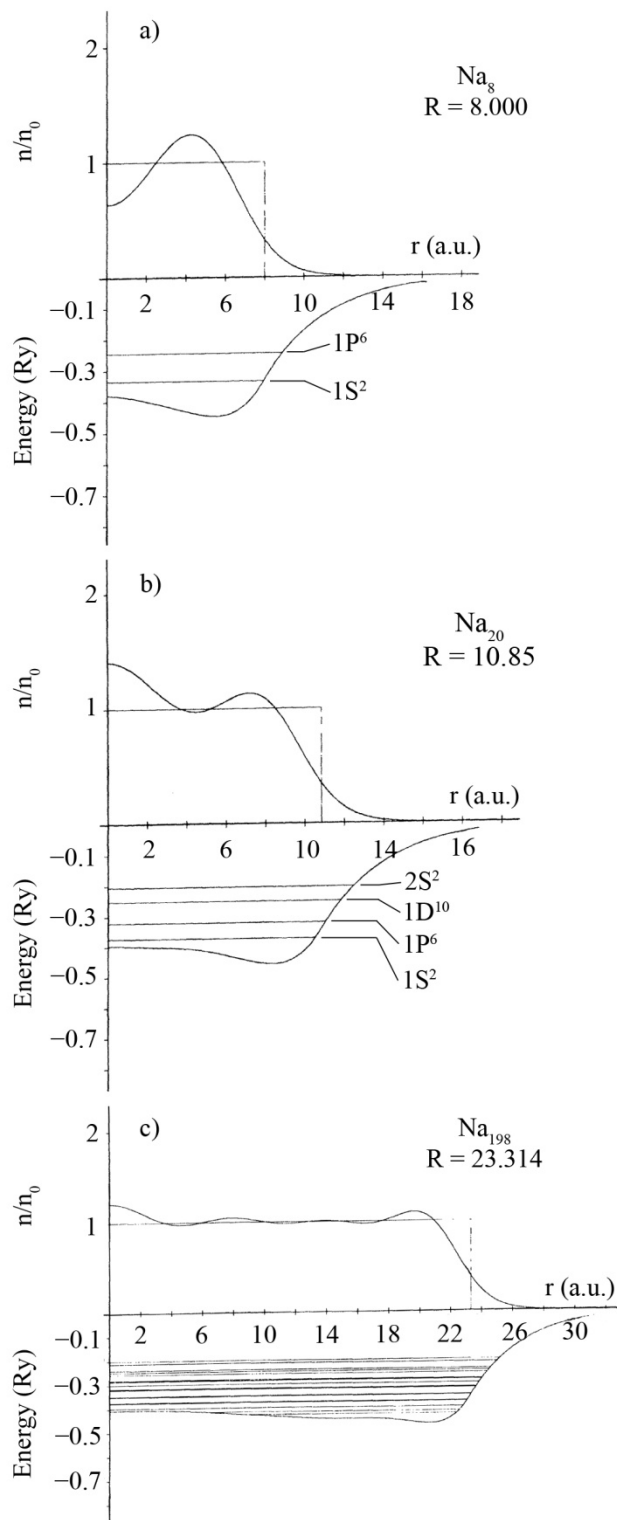


Figure 1.3. Electronic jellium shells for sodium clusters of a) 8, b) 20, and c) 198 atoms. R is the calculated outer radius of the lowest energy shell and n/n_0 is the ratio of jellium electron density versus the average electron density of the bulk. Adapted from Reference 26.

These examples also provide occupied electronic energy levels, estimated average radii of the molecules, and average charge density at a given distance from the core. It is interesting to note that, although the jellium core is homogenous in charge density throughout, the electronic self-consistent field is not, and in fact can even penetrate the outer radius of the jellium core (which is not to be thought of as a hard sphere). It can be seen in this example that the potential well of the smaller clusters is seen to exhibit a “wine bottle” shape, which becomes increasingly harmonic as the cluster size approaches the bulk. It can also be seen that, with larger cluster sizes, the average density becomes increasingly linear, and the electronic shells become near-continuous, allowing one to observe the formation of the band structure proposed by Wilson.

To be sure, Ekardt’s treatment (and final Hamiltonian) was more detailed than in this explanation, and this is to be considered only a simplified example for the purposes of lucidity. Ekardt used a self-consistent approach, using the potential energy terms to exactly solve for the kinetic part of the equation, which is very similar to modern Kohn-Sham equations (developed by Walter Kohn and Lu Sham at the University of California, San Diego in 1965) used in density functional theory.²⁸ Finally, by separating the equation into individual electrons and then adding the achieved solutions, the wavefunctions and energy levels for the molecule could be determined. One must provide a radius for the spherical jellium core, which Ekardt did by using the density of the bulk metal to calculate the radius of a sphere with a volume equal to that of N atoms of said density, and the result is a potential well that is quite complex and varying from cluster to cluster, as was seen in Figure 1.3. However, today it is typical to simplify Ekardt’s results by assuming a Woods–Saxon potential well which produces shell closings that closely match experimental results up to at least one hundred atoms (Roger Woods and David Saxon developed their equation at the University of California in Los Angeles in 1954).²⁹ The energy spacings will, of course, depend on the size of the jellium nucleus and the shape of the Woods–Saxon well (which is analogous to a harmonic oscillator with a flattened base and steeper sides,

both of which can be customized along with the depth), and for the most part have been empirically determined.³⁰

We now have a basic theory which helps explain the experimental observations of Knight, Clemenger, and de Heer. The sodium clusters which appeared to be more stable were so because of their closed electronic jellium shells, just as noble gases are more stable in their neutral elemental form than other elements. Almost thirty years later this discovery was well-summarized by Philip Ball, former editor of *Nature*, when he said, “superatoms reinforce the notion that chemistry is more about electrons than elements.”³¹ One additional consideration to note involves the assumption of a *spherical* jellium core. Although this model helps explain experimental phenomena rather well, one need not forget the truth: that the nucleus of the cluster is a molecule, not a homogenous sphere, and as such is susceptible to Jahn–Teller distortion, an effect proposed in 1937 by (German) Hermann Jahn and (Hungarian) Edward Teller to describe the separation of degenerate molecular orbitals to maximize the number of fully occupied energy levels).³² This potential error in the jellium model was corrected by Clemenger in 1985 who, using a traditional model developed by Sven Nilsson in 1955, proposed a distortion parameter which could be used to predict the shape of the jellium core, given a particular number of valence electrons (this is now known as the Clemenger–Nilsson model, and is demonstrated in Figure 1.4).^{33,34} Clemenger uses a modified harmonic oscillator potential well instead of the now common Woods–Saxon potential, but the results are nearly identical and the shell closings in Figure 1.4 are now considered canon.

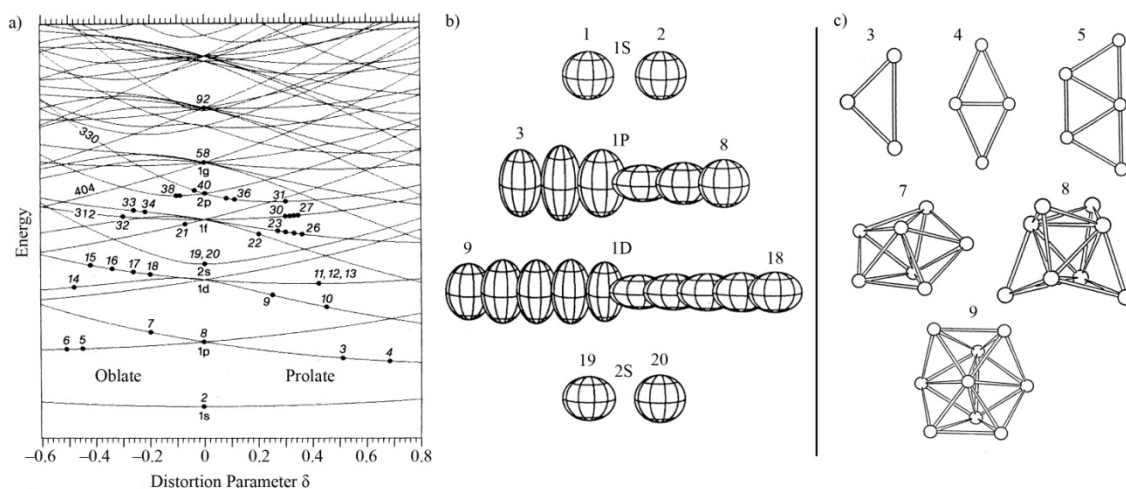


Figure 1.4. a) Distortion parameter (used to determine spheroidal shape) of a cluster predicted by full and partial shell closings using the Clemenger-Nilsson model. b) Geometric representations of shell closings and c) theoretical structures for select sodium clusters are shown for reference. a), b) and c) are adapted from References 34, 30, and 41, respectively.

Once the electronic jellium shell model was established, countless studies followed, with many other elements being examined. Stable jellium shell closings were found to exist for nearly every metal, not just sodium, and it was confirmed that it is the valence electrons, not the number of atoms, that determines stability.³⁵⁻³⁹ Sodium, donating a single valence electron, allows for the filling of each jellium shell closing. Aluminum contains three valence electrons, and so it should have shell closings at, for example, Al_6^0 (18 electrons; $1\text{S}^21\text{P}^61\text{D}^{10}$), Al_7^+ (20 electrons; $[\text{Al}_6^0]2\text{S}^2$), Al_{13}^- (40 electrons; $[\text{Al}_7^+]1\text{F}^{14}2\text{P}^6$), etc. Clusters which exhibited unique physical stability were dubbed “magic,” a term first coined in 1981 by Echt, Sattler, and Recknagel, three physicists at the University of Konstanz in Germany.⁴⁰

Further developments provided more accurate theoretical ionization potentials and electronic energy levels (e.g. the use of a configuration interaction to more accurately approximate electron-electron interactions),^{41,42} but considerably large changes in cluster theory occurred in the late 1980s and early 1990s with the rapid improvement of computing speed.⁴²⁻⁴⁴ With this new technological power came a theoretical method that was both more accurate and more cost-effective than the jellium-based Hartree-Fock model: density functional theory.⁴⁵

Briefly, this method focuses more on the probability density rather than the specific wavefunction, where the energy of the orbital is a function of the total electron density (the density is itself a function of the electron's position; a function of a function is called a functional). Using an initial orbital approximation (first-principles studies typically use the superimposed base atomic orbitals for each atom), the electron density is determined. This is then used to calculate the electron-correlation potential, which is then used to calculate a new electron density. Once a desired stability is reached, the electron density is used to calculate the energy levels. An amazing example of the application of this method to metal clusters is given in Figure 1.5, in which undeniable similarities can be observed between the degenerate orbitals and traditional atomic orbitals (note that at no point in the density functional theory calculations is the self-consistent jellium model considered, and countless other non-metallic molecules can be calculated using the same method that do not produce these atom-like orbitals). With our story nearly complete, it would seem that the jellium model was well verified both experimentally and theoretically. However, these “magic numbers” remained as physical phenomena. It was not until 1989 that A. Welford Castleman, Jr. at The Pennsylvania State University demonstrated that the jellium model could be applied toward chemical interactions as well.⁴⁶

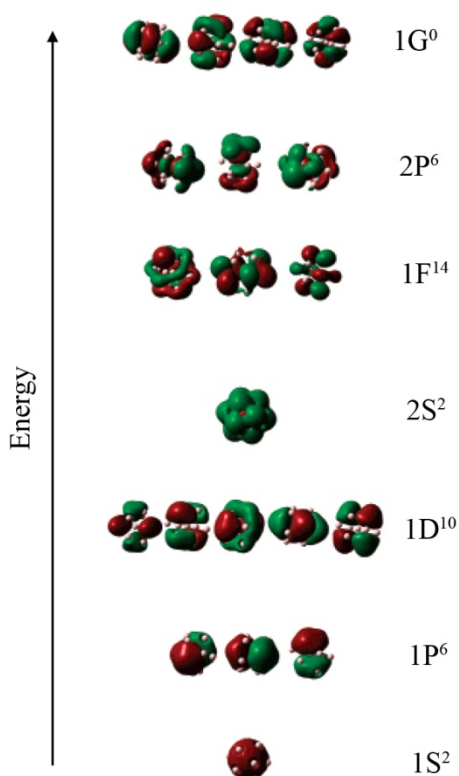


Figure 1.5. Select examples of predicted occupied and unoccupied molecular orbitals for Al_{13}^- (40 electrons) determined using density functional theory. Predicted jellium S, P, D, and F orbitals are labeled, which show remarkable resemblance to atomic s, p, d, and f orbitals, respectively. Adapted from Reference 43.

3. Aluminum Clusters: Past Developments and Current Motivations

Study of the electronic or physical properties of gas-phase aluminum clusters had been performed prior to 1989 in order to better understand how the characteristics of atoms translated into the properties of bulk metals.^{47,48} However, in a pair of papers (the second in 1991),^{46,49} Castleman demonstrated that the reactivity of specific aluminum cluster ions with oxygen was in strong accordance with the jellium model. These clusters, dubbed “unified atoms” as a reference to their similarity to inert noble gas atoms, quickly attracted the interest of the cluster community, particularly Al_{13}^- (Castleman also discovered metallocarbohedrenes one year later, organometallic molecules that also showed inherent stability, similar to fullerenes).⁵⁰ A

succeeding paper by Shiv Khanna and Puru Jena at the Virginia Commonwealth University posed the following question: “What would the electronic structure of a ‘supercrystal’ assembled out of clusters be like and how would it differ from a crystal assembled out of atoms?”⁵¹ This thought process suggests that these aggregated “unified atoms” can bond to each other, other atoms, and/or other clusters and thus create a material with properties different from a bulk of the same atomic constituents. This hypothetical medium was dubbed a “cluster-assembled crystal,” although today the broader term “cluster-assembled material” is exclusively used. In 2004 and 2005 two studies in the Castleman lab delivered the first experimental evidence that cluster-assembled materials could be created.^{52,53} It was discovered that Al_{13}^0 , a cluster one electron shy of a jellium shell closing (39 electrons), behaved strongly like a halogen (following the Aufbau principle developed by Bohr, Stoner, and Pauli)⁵⁴⁻⁵⁶ and was able to bond to iodine atoms as a chlorine atom does. These studies gave birth to the well-known term “superatom,” which is literally the same concept as a unified atom, but has become the more popular term. It is very important to realize, however, that the term superatom does not carry with it any inherent connotation of inertness for the cluster; it merely suggests that the cluster can form molecular bonds without sacrificing its own geometric or electronic structure. In fact, it is the labile characteristics of these non-magic clusters that would allow the formation of atom-like bonds. It then followed that by using the jellium model to count the valence electrons of a cluster (which is by no means limited to sodium and aluminum, the only two elements discussed here), one could predict superatom reactivity, and theoretically use this knowledge to predict clusters that mimic virtually all other elements of the periodic table of the elements, similar to what Dmitri Mendeleev was able to do in 1869. This theory, known as the “three dimensional periodic table,” was first coined by Castleman in 2006 (Figure 1.6).^{57,58}

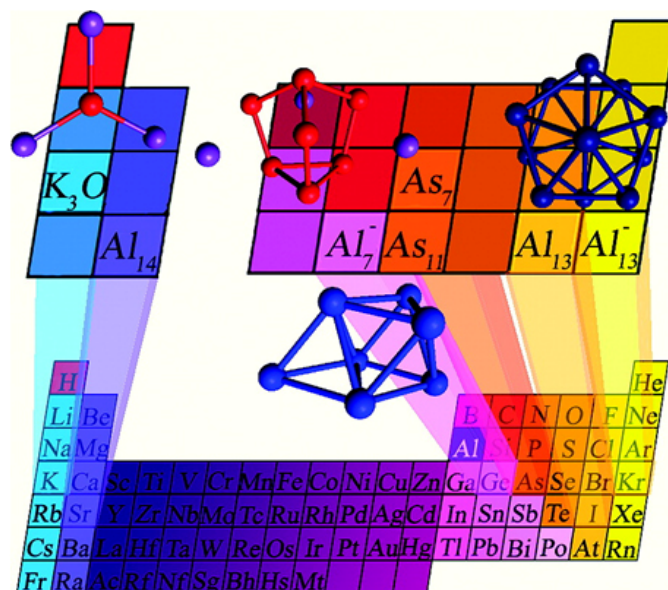


Figure 1.6. Artistic representation of the three dimensional periodic table with select examples. In reality, multiple clusters could be conceived which mimic the same element, giving rise to a truly three-dimensional aspect. Adapted from Reference 57.

In fact, other clusters have since been discovered that display properties unique from any element.⁵⁹ These include energy storage properties and catalytic properties, and with enough fundamental knowledge on clusters it could be possible to build a cluster-assembled material with any number of desirable, customizable characteristics. It is at this point that we must now consider the true value of this potential ability with respect to materials science and, in particular, to aluminum as an element.

Aluminum is probably one of the most common elements within arm's reach at any given moment today. Its low cost and light weight have made it an ideal material for countless everyday applications from soda cans to electronics casings, and air travel could not exist without it (even at the beginning; the Wright brothers' plane had an aluminum engine block and crankcase).^{60,61} It is the third most abundant element in the Earth's crust (behind silicon and oxygen), and it is therefore surprising for some to hear that a little over a century ago bulk aluminum metal did not exist. Aluminum is not found naturally anywhere on the planet (it is refined from minerals), and prior to 1886 it was not available in any appreciable quantity and was

more valuable than silver (humorously, the Washington Monument was completed only two years earlier with an aluminum cap to showcase the strength of the United States of America. Today the cap is worth about seven dollars).⁶² The reason for this lack of abundance is due to aluminum's ability to form a strong bond with oxygen. It is therefore very difficult to create aluminum instead of aluminum oxide (Al_2O_3), also known as alumina, which is a well-known ceramic material.⁶³ The history of processed aluminum is quite complex, with mixed stories of triumph and heartbreak.

Its name is derived from the mineral alum (Latin for bitter salt), a chalky mineral which for thousands of years has found use in various medicinal and industrial applications. The famous British chemist Sir Humphrey Davy gave the element its name when in 1808 he hypothesized that alum contained an unknown metal,⁶⁴ and it was first isolated in any reasonable quantity by the French chemist Henri Etienne Sainte-Clair Deville in 1854 (the process was quite costly and thus aluminum was too expensive to be used as anything other than a precious metal). Then, in 1886, Charles Martin Hall, a student at Oberlin College in Ohio, was intrigued when his professor mentioned that anyone who could invent a better way to produce aluminum would find fame and fortune.^{62,65} Working in a backyard woodshed with the help of his sister, Hall successfully developed a process wherein alumina, dissolved in molten cryolite, could be used to isolate aluminum via electrolysis, a method pioneered by Davy in 1807. In July of that year a US patent was filed, and Hall began to look for business partners. For six months he worked with the American businessmen Alfred and Eugene Cowles, until they decided his process was not worth pursuing, leaving him back at square one. Hall eventually partnered with Alfred Hunt to form the Pittsburgh Reduction Company in 1888, which later became the Aluminum Company of America and still exists today as Alcoa Inc. The early history of the company is a somewhat jaded one. In 1886, the same year Hall developed his process, a French chemist named Paul Heroult made the exact same discovery. He filed for a US patent in May: two months before Hall. However, since

Hall had filed a provisional patent (thanks to his sister's meticulous note taking) and could prove that his discovery was in February, Heroult was awarded nothing (although today the method is known as the Hall-Heroult process). Hall's new business was also threatened by the Cowles brothers, who had improved upon Hall's original process without proper licensing. A settlement was not reached until 1909, and just three years later the company was under attack for violating anti-trust laws. Nevertheless, Hall received the fame and fortune he was promised, dying in 1914, the same year as Heroult, who did not enjoy nearly as much success.

Pure aluminum, assuming one has the means to acquire it, reacts spontaneously with oxygen to form alumina. This is the reason for aluminum's strong resistance to weathering, as this alumina layer protects the interior aluminum from further reaction and degradation.⁶³ As a comparison, bulk iron will form iron oxide, also known as rust, but this will flake off, thus exposing the pure iron underneath for further oxidation. It is interesting, then, that the enthalpy of combustion of aluminum is higher (more negative) than any other element—which is directly related to the large amounts of energy required to purify aluminum from alumina. Theoretically, this makes aluminum one of the greatest energy storage mediums known, although (thankfully) the formation of an alumina layer around bulk aluminum renders it incombustible. However, a hypothetical high-energy density material composed of pure aluminum would contain about three times as much energy by weight as today's more popular carbon- and nitrogen-based explosives.⁶⁶ Extensive studies have determined that the ability for bulk aluminum to “burn” involves the ignition of a chain reaction wherein enough residual energy from the continuous combustion is available to melt the newly formed surface alumina, thus sustaining the core aluminum fuel supply for further reaction (this chain reaction is often difficult to quench once started, even when the aluminum in question is the superstructure of a large naval vessel, as we are reminded by some poignant historical events in the 1970s).⁶⁷ It stands to reason that smaller

aluminum particles will burn faster, due to their having a larger surface area-to-volume ratio (Figure 1.7).

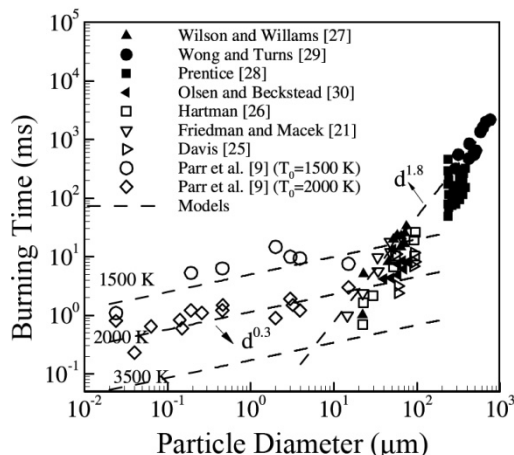


Figure 1.7. Aluminum particle burning times over varying size. Adapted from Reference 67.

A large amount of research has been devoted to aluminum combustion and, in particular, aluminum nanoparticle combustion, and this field is only briefly discussed here. The main point of interest, however, is that, while small aluminum nanoparticles burn faster than larger ones, the alumina surface layer, which is about 3 nm regardless of particle size, will sacrifice a considerable amount of volume and weight. Eventually, the advantage of rapid combustion gained from small size will be outweighed by the energy lost due to this inherently pre-oxidized fuel. The optimal ratio is reachable by today's technological means, and some modern research has been devoted to the passivation of unoxidized aluminum nanoparticles (and even small aluminum clusters) in order to waste as little volume and weight as possible;^{68,69} but even passivated nanoparticles will not burn as efficiently as a hypothetical pure aluminum fuel would. Nevertheless, the science has reached a point where aluminum nanoparticles are used as fuel additives, and recently a rocket fuel was developed by Steven Son and Richard Yetter (at Purdue University and the Pennsylvania State University, respectively) which is comprised of aluminum nanoparticles and ice (Figure 1.8).⁷⁰

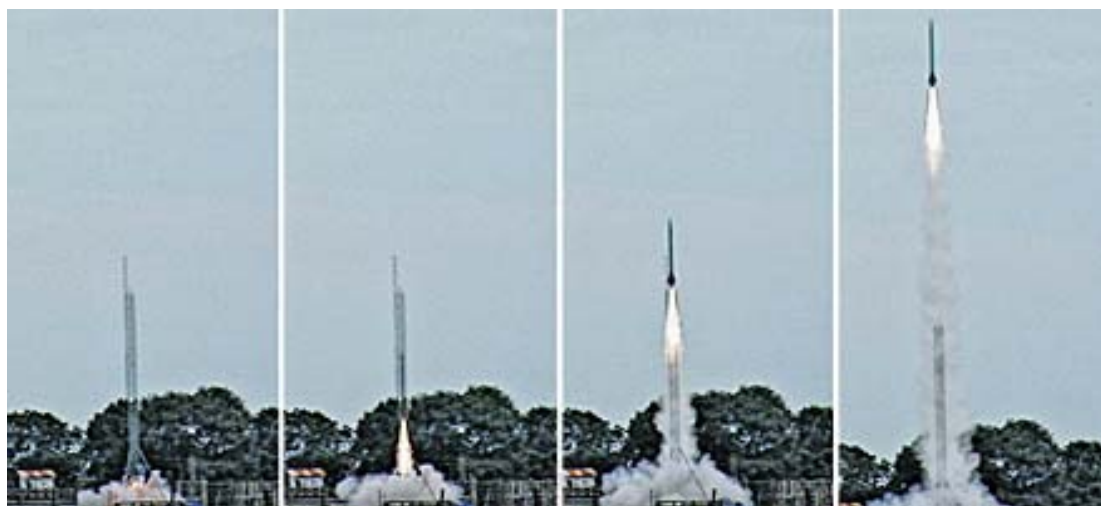


Figure 1.8. Example of an aluminum nanoparticle/ice-based rocket fuel. Photograph (Eric Barlow) adapted from Reference 70.

Our thought process now returns to aluminum clusters and the three-dimensional periodic table. Gas-phase research has already shown that specific aluminum clusters (i.e. Al_{13}^- , Al_{23}^- , etc.) do not react with oxygen, and that these clusters have the potential to form molecular bonds. Is it not feasible, then, that an aluminum-based cluster-assembled material could be created which does not react with oxygen? A crystalline form of these aluminum clusters would theoretically maximize the amount of energy available, and although no such material has been created to date, theoretical materials have already been suggested using density functional theory computations (Figure 1.9).⁷¹

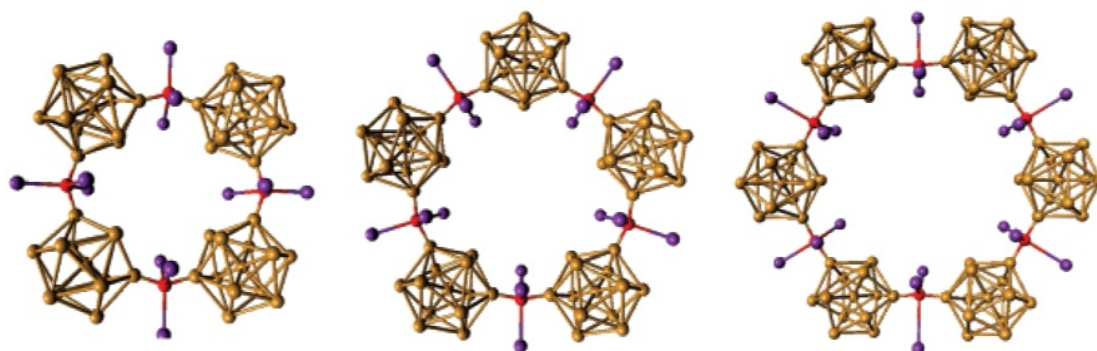


Figure 1.9. Examples of cyclical cluster-assembled materials consisting of Al_{13} superatoms and K_3O ligands, similar to a repeating or multidecker sandwich structure. Adapted from Reference 71.

In this specific example, the aluminum cluster “superhalogens” are paired with a cation to create a stable species that is rich in aluminum and oxygen yet stable. The combustion of such a material would be impressive, as the oxygen is already available within the crystal itself; a requirement of high-velocity explosives for use in demolition materials and some munitions. Other alternatives with no oxygen would be applicable in slower-burning energetic materials, such as fuels and thermobaric explosives. Therefore, gas-phase research along these lines has continued, and although no such cluster-assembled material has yet been created in any quantity, recent developments presented herein have bridged the gap between the gas-phase and the condensed-phase, hopefully bringing cluster science one large step closer to achieving this long-term goal.

4. Clusters and Catalysis: Understanding Catalytic Mechanisms

Almost all biological and industrial chemical processes rely on catalysts in order to function. It should be granted that catalysis (a term coined in 1836 by the Swedish chemist Jöns Berzelius) is a stand-alone field of chemistry, and that any kind of review of catalysis or its history would yield a text entirely too large for the present discussion.⁷² For one to appreciate the importance of catalysis on modern life, one should look no further than the Haber-Bosch process. In need of producing ammonia for fertilizer (and munitions), in 1909 Fritz Haber developed a process that could create large quantities from nitrogen, a gas which we have unlimited quantities due to its composing nearly eighty percent of our atmosphere (the strong triple bond of nitrogen gas is what led to so many failures before Haber’s success). While this story is well known, what is not is the fact that Haber quickly sold his process to the Badische Anilin- und Soda-Fabrik (today known simply as BASF SE) before any consideration had been given to its large-scale industrialization.⁷³ The process used osmium and ruthenium as a catalyst, which were quite

expensive, and the chemical reaction required dangerously high pressures to operate, which when scaled up would equate to a bomb the size of a warehouse. It was due to the experimental tinkering of an experienced German engineer named Carl Bosch which allowed the process to be industrialized in 1913 (the first few attempts did explode, but with proper precautions taken there were no fatalities). The main contribution to this process was the discovery of an iron-based catalyst, which greatly reduces the cost of the process. Today the Haber-Bosch process single-handedly supports our overstretched global population, and if one compares the global production of ammonia with population increase, one observes a direct correlation.⁷⁴ The Haber-Bosch process is one of the most significant discoveries of modern science, arguably even outweighing penicillin and semiconductors, and so it is surprising that the exact catalytic mechanism was not known until the 1980s (earning the German physicist Gerhard Ertl a Nobel Prize in Chemistry).⁷⁵ The iron catalyst used today was discovered experimentally, via careful trial and error, and indeed this is the case for most catalysts (although one treads lightly and chooses words carefully on this topic when catalytic chemists are in the room). This is a large motivation for gas-phase cluster research: the elucidation and optimization of catalytic mechanisms for industrialization.

Just as catalysis is a massive field of chemistry, so is it also a large sub-field of cluster science.⁷⁶ The specific regions of study span across the breadth of cluster chemistry, from gas-phase reactivity to deposited surface studies to theoretical studies, and the motivation for this research follows a simple train of logic: 1) catalytic mechanisms of simple, gas-phase clusters are easy to control and easier to model with theoretical calculations than bulk surfaces. 2) Gas-phase clusters have been shown to mimic defect sites on bulk surfaces.^{77,78} 3) Catalytic reactivity of controlled defect sites is seen to match that of gas-phase clusters,⁷⁹ and therefore 4) controlling/maximizing the number of active defect sites on a bulk surface via initial gas-phase cluster studies will improve catalysts and, in many cases, provide the first true insights as to how the specific catalytic mechanism works (Figure 1.10).

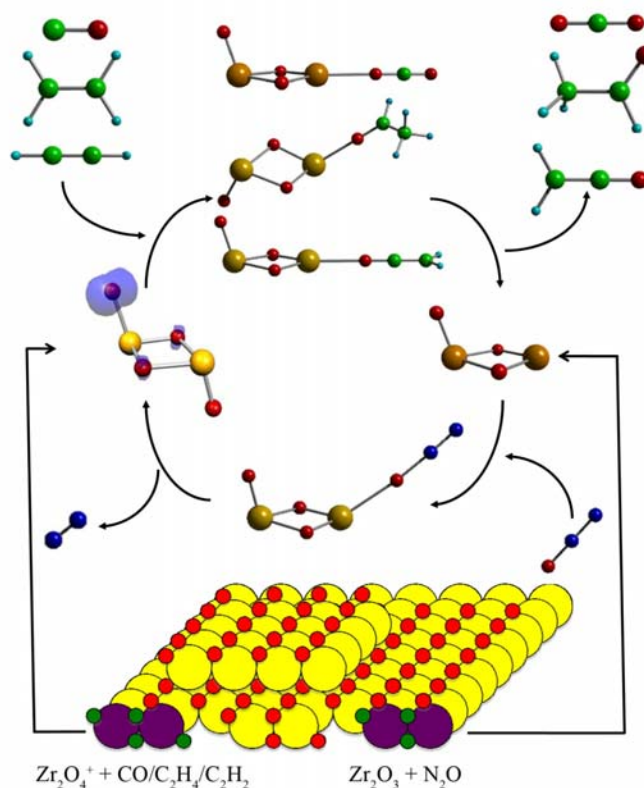


Figure 1.10. Example drawing of a gas-phase zirconium-oxide cluster catalytic oxidation mechanism and its theoretical transfer to defect sites (step edges) on a surface. Adapted from Reference 78.

In 2009 Castleman and group discovered a catalytic mechanism involving aluminum clusters wherein water is decomposed and hydrogen gas is formed.⁸⁰ The exact mechanism was determined using first-principles theory (outlined in the beginning of Chapter 4),⁸¹ and further studies have shown that this mechanism can be applied to other polar molecules as well, namely carbonyl groups. Various simple carbonyls (e.g. acetone, formaldehyde, etc.) are precursors in the formation of fine chemicals; however, much of the industrialized catalytic chemistry is still performed in a solution.⁸² Recently, much attention has been devoted to the possibility of surface catalysts that would activate a carbonyl group for specific reactions, although none have yet been implemented.^{83,84} The mechanisms discovered and presented herein could potentially be used to create such a catalyst, either on a surface as described above or in a cluster-assembled material.

5. Present Research

The information above has hopefully served its purpose in outlining the major historical achievements and motivations of cluster research to the reader. Over a century of experimental and theoretical work performed by many scientists has brought us to a point where the eventual development of cluster-assembled materials seems truly feasible. To be sure, there are many other aspects of cluster research not mentioned here that have also brought the scientific community closer to this goal, and the development of the theory behind the jellium model and first-principles density functional theory is far more complex than outlined above (both historically and conceptually), but it is the author's intent to only provide the reader with a review of cluster science sufficiently deep enough that the research presented in this dissertation can be well understood. A comprehensive history of the theory and applications of all-metal clusters does not yet exist, although there are many review papers and books that, when combined, provide detailed insights into many of the significant developments in the field, and the author has provided these as references for the interested reader.^{2,16,30}

The research presented in this dissertation is a continuation of past aluminum cluster reactivity, with some interesting discoveries and developments. First, aluminum cluster reactivity with oxygen has been re-examined using new singlet oxygen techniques (Chapter 3). Several insights have recently been published regarding the odd-even effect of aluminum cluster reactivity, and this is outlined in detail before the new work is discussed. Second, aluminum cluster reactivity with various polar functional groups (alcohols and carbonyls) is explored (Chapter 4). Expanding on the recent discovery of hydrogen formation from aluminum cluster reactivity with water, new experiments have been performed which provide a complete understanding of the mechanism involved. Possible catalytic applications are also discussed. Finally, a novel experimental technique involving the size-selective deposition of aluminum

clusters onto a surface is presented (Chapter 5). This is the first example of aluminum clusters being bonded to a surface in a predictable manner, and suggests real progress toward the long-term goal of clusters bonded to surfaces, atoms, and/or other clusters in a manner which does not destroy their desirable properties. In addition, a new instrumental technique being developed dubbed “matrix isolation cavity ringdown spectroscopy” is presented (Appendix B), which could provide the experimental means of studying individual cluster-cluster interactions as a first step toward the tailored construction of cluster-assembled materials. The entirety of this dissertation is concluded (Chapter 6) where the author uses this research to make several predictions as to the future progress of aluminum cluster research with regard to energetic materials and catalysts.

6. References

- (1) *Goethe's World: As Seen in Letters and Memoirs*; Biermann, B., Ed.; Books for Libraries Press: Freeport, NY, 1971.
- (2) *Out of the Crystal Maze: Chapters from the History of Solid-State Physics*; Hoddeson, L., Braun, E., Teichmann, J., Weart, S., Eds.; Oxford University Press: New York, 1992.
- (3) Drude, P. *Ann. Phys.* **1900**, *1*, 566-613.
- (4) Lorentz, H. A. *Proc. R. Acad. Sci. Amsterdam* **1904**, *6*, 809-831.
- (5) Pauli, W. *Z. Phys. A: Hadrons Nucl.* **1927**, *41*, 81-102.
- (6) Sommerfeld, A. *Naturwissenschaften* **1927**, *15*, 825-832.
- (7) Schrödinger, E. *Ann. Phys.* **1926**, *79*, 361-376.
- (8) Bloch, F. *Z. Phys. A: Hadrons Nucl.* **1928**, *52*, 555-600.
- (9) Ibach, H.; Lüth, H. *Solid-State Physics: An Introduction to Principles of Materials Science*, 4th ed.; Springer Publishing: New York, 2009.
- (10) Housecroft, C. E.; Constable, E. C. *Chemistry: An Introduction to Organic, Inorganic, and Physical Chemistry*; Prentice Hall: New York, 2006.

- (11) Wilson, A. H. *Proc. R. Soc. London, Ser. A* **1931**, *133*, 458-491.
- (12) Wilson, A. H. *Proc. R. Soc. London, Ser. A* **1931**, *134*, 277-287.
- (13) Atkins, P. W.; de Paula, J. D. *Physical chemistry*, 9th ed.; Oxford University Press: New York, 2002.
- (14) Robbins, E. J.; Leckenby, R. E.; Willis, P. *Adv. Phys.* **1967**, *16*, 739-744.
- (15) Knight, W. D.; Clemenger, K.; de Heer, W. A.; Saunders, W. A.; Chou, M. Y.; Cohen, M. L. *Phys. Rev. Lett.* **1984**, *52*, 2141-2143.
- (16) Ekardt, W. *Metal Clusters*; Wiley & Sons: New York, 1999.
- (17) Lowe, J. P.; Peterson, K. A. *Quantum Chemistry*, 2nd ed.; Academic Press: New York, 2006.
- (18) Born, M.; Oppenheimer, R. *Ann. Phys.* **1927**, *84*, 457-484.
- (19) Hartree, D. R. *Proc. Cambridge Philos. Soc.* **1928**, *24*, 89-110.
- (20) Hartree, D. R. *Proc. Cambridge Philos. Soc.* **1928**, *24*, 111-132.
- (21) Fock, V. *Z. Phys.* **1930**, *61*, 126-148.
- (22) Bohr, N. *Nature* **1923**, *112*, 29-44.
- (23) Mulliken, R. S. *Rev. Mod. Phys.* **1932**, *4*, 1-86.
- (24) Hund, F. *Z. Phys.* **1927**, *40*, 742-764.
- (25) *Structure and Properties of Solid Surfaces*; Gomer, R., Smith, C. S., Eds.; University of Chicago Press: Chicago, IL, 1953.
- (26) Ekardt, W. *Phys. Rev. B* **1984**, *29*, 1558-1564.
- (27) Martins, J. L.; Car, R.; Buttet, J. *Surf. Sci.* **1981**, *106*, 265-271.
- (28) Kohn, W.; Sham, L. J. *Phys. Rev.* **1965**, *140*, A1133-A1138.
- (29) Woods, R. D.; Saxon, D. S. *Phys. Rev.* **1954**, *95*, 577-578.
- (30) de Heer, W. A. *Rev. Mod. Phys.* **1993**, *65*, 611-676.
- (31) Ball, P. Column: The Crucible. *Chemistry World*, March 2010, 7.
- (32) Jahn, H. A.; Teller, E. *Proc. R. Soc. London, Ser. A* **1937**, *161*, 220-235.

- (33) Mottelson, B. R.; Nilsson, S. G. *Phys. Rev.* **1955**, *99*, 1615-1617.
- (34) Clemenger, K. *Phys. Rev. B* **1985**, *32*, 1359-1362.
- (35) Chou, M. Y.; Cleland, A.; Cohen, M. L. *Solid State Commun.* **1984**, *52*, 645-648.
- (36) Katakuse, I.; Ichihara, T.; Fujita, Y.; Matsuo, T.; Sakurai, T.; Matsuda, H. *Int. J. Mass Spectrom. Ion Processes* **1985**, *67*, 229-236.
- (37) Phillips, J. C. *J. Chem. Phys.* **1985**, *83*, 3330-3333.
- (38) Katakuse, I.; Ichihara, T.; Fujita, Y.; Matsuo, T.; Sakurai, T.; Matsuda, H. *Int. J. Mass Spectrom. Ion Processes* **1986**, *69*, 109-114.
- (39) Li, X.; Wu, H. B.; Wang, X. B.; Wang, L. S. *Phys. Rev. Lett.* **1998**, *81*, 1909-1912.
- (40) Echt, O.; Sattler, K.; Recknagel, E. *Phys. Rev. Lett.* **1981**, *47*, 1121-1124.
- (41) Bonačić-Koutecký, V.; Fantucci, P.; Koutecky, J. *J. Chem. Phys.* **1989**, *91*, 3794-3795.
- (42) Barnett, R. N.; Landman, U.; Nitzan, A.; Rajagopal, G. *J. Chem. Phys.* **1991**, *94*, 608-616.
- (43) Han, Y.; Jung, J. *J. Am. Chem. Soc.* **2008**, *130*, 2-3.
- (44) Rothlisberger, U.; Andreoni, W. *J. Chem. Phys.* **1991**, *94*, 8129-8151.
- (45) Foresman, J. B.; Frisch, A. E.; Gaussian, I. *Exploring Chemistry with Electronic Structure Methods*, 2nd ed.; Gaussian, Inc.: Wallingford, CT, 1996.
- (46) Leuchtner, R. E.; Harms, A. C.; Castleman, A. W., Jr. *J. Chem. Phys.* **1989**, *91*, 2753-2754.
- (47) Cox, D. M.; Trevor, D. J.; Whetten, R. L.; Kaldor, A. *J. Phys. Chem.* **1988**, *92*, 421-429.
- (48) Jarrold, M. F.; Bower, J. E. *J. Chem. Phys.* **1986**, *85*, 5373-5375.
- (49) Leuchtner, R. E.; Harms, A. C.; Castleman, A. W., Jr. *J. Chem. Phys.* **1991**, *94*, 1093-1101.
- (50) Guo, B. C.; Kerns, K. P.; Castleman, A. W., Jr. *Science* **1992**, *255*, 1411-1413.
- (51) Khanna, S. N.; Jena, P. *Phys. Rev. Lett.* **1992**, *69*, 1664-1667.
- (52) Bergeron, D. E.; Castleman, A. W., Jr.; Morisato, T.; Khanna, S. N. *Science* **2004**, *304*, 84-87.
- (53) Bergeron, D. E.; Roach, P. J.; Castleman, A. W., Jr.; Jones, N.; Khanna, S. N. *Science* **2005**, *307*, 231-235.

- (54) Bohr, N. *Z. Phys.* **1923**, *13*, 117-165.
- (55) Stoner, E. C. *Philos. Mag.* **1924**, *48*, 719-736.
- (56) Pauli, W. *Z. Phys.* **1925**, *31*, 765-783.
- (57) Castleman, A. W., Jr.; Khanna, S. N. *J. Phys. Chem. C* **2009**, *113*, 2664-2675.
- (58) Reveles, J. U.; Khanna, S. N.; Roach, P. J.; Castleman, A. W., Jr. *Proc. Natl. Acad. Sci. U.S.A.* **2006**, *103*, 18405-18410.
- (59) Claridge, S. A.; Castleman, A. W., Jr.; Khanna, S. N.; Murray, C. B.; Sen, A.; Weiss, P. S. *ACS Nano* **2009**, *3*, 244-255.
- (60) Howard, F. *Wilbur and Orville: A Biography of the Wright Brothers*; Dover Publications: Mineola, NY, 1998.
- (61) Farndon, J. *Aluminum*; Benchmark Books: Pelham, NY, 2000.
- (62) Asimov, I. *Asimov's New Guide to Science*; Basic Books: New York, 1984.
- (63) Housecroft, C. E.; Sharpe, A. G. *Inorganic Chemistry*, 2nd ed.; Prentice Hall: New York, 2005.
- (64) Davy, H. *Elements of Chemical Philosophy: Part 1*; Bradford and Inskeep: Philadelphia, 1812.
- (65) Smith, G. D. *From Monopoly to Competition: The Transformations of Alcoa, 1888-1986*; Cambridge University Press: New York, 2003.
- (66) Dlott, D. D. *Mater. Sci. Technol.* **2006**, *22*, 463-473.
- (67) Yetter, R. A.; Risha, G. A.; Son, S. F. *Proc. Combust. Inst.* **2009**, *32*, 1819-1838.
- (68) Dohmeier, C.; Robl, C.; Tacke, M.; Schnöckel, H. *Angew. Chem., Int. Ed. Engl.* **1991**, *30*, 564-565.
- (69) Schnöckel, H.; Kohnlein, H. *Polyhedron* **2002**, *21*, 489-501.
- (70) Halford, B. *Chem. Eng. News* **2009**, *87*, 32.
- (71) Reber, A. C.; Khanna, S. N.; Castleman, A. W., Jr. *J. Am. Chem. Soc.* **2007**, *129*, 10189-10194.
- (72) Somorjai, G. A.; Li, Y. *Introduction to Surface Chemistry and Catalysis*; Wiley & Sons: New York, 2010.

- (73) Coffey, P. *Cathedrals of Science: The Personalities and Rivalries That Made Modern Chemistry*; Oxford University Press: New York, 2008.
- (74) Smil, V. *Enriching the Earth: Fritz Haber, Carl Bosch, and the Transformation of World Food Production*; MIT Press: Cambridge, MA, 2004.
- (75) Ertl, G.; *J. Vac. Sci. Technol. A* **1983**, *1*, 1247-1253.
- (76) Rioux, R. M.; Rioux, R. *Model Systems in Catalysis: Single Crystals to Supported Enzyme Mimics*; Springer Publishing: New York, 2009.
- (77) Zemski, K. A.; Justes, D. R.; Castleman, A. W., Jr. *J. Phys. Chem. B* **2002**, *106*, 6136-6148.
- (78) Johnson, G. E.; Mitric, R.; Bonačić-Koutecký, V.; Castleman, A. W., Jr. *Chem. Phys. Lett.* **2009**, *475*, 1-9.
- (79) Fialko, E. F.; Kikhtenko, A. V.; Goncharov, V. B.; Zamaraev, K. I. *J. Phys. Chem. B* **1997**, *101*, 5772-5773.
- (80) Roach, P. J.; Woodward, W. H.; Castleman, A. W., Jr.; Reber, A. C.; Khanna, S. N. *Science* **2009**, *323*, 492-495.
- (81) Reber, A. C.; Khanna, S. N.; Roach, P. J.; Woodward, W. H.; Castleman, A. W., Jr. *J. Phys. Chem. A* **2010**, *114*, 6071-6081.
- (82) Hagen, J. *Industrial Catalysis: a Practical Approach*; Wiley & Sons: New York, 2006.
- (83) Delbecq, F.; Sautet, P. *Langmuir* **1993**, *9*, 197-207.
- (84) Gomes, J. R. B.; Gomes, J. A. N. F.; Illas, F. *J. Mol. Catal. A: Chem.* **2001**, *170*, 187-193.

Chapter 2

Experimental Techniques and Applications

1. Overview of Instrumentation

The purpose of this chapter is to outline the experimental techniques used in this dissertation. The reasons for utilizing specific methodologies are outlined, and any minor differences from cited materials are covered to some extent. There are many details regarding the nuances of this instrumentation that are neither necessary in order to understand the experiment nor are they always purely logical (some aspects of successfully acquiring data involve more of an artistic approach than a scientific one). However, because this information applies to this instrument specifically and is only of interest to a limited audience, the best efforts have been made to remove these experimental aspects to Appendix A, for those who are interested. Additionally, the matrix isolation-cavity ringdown spectroscopy technique, which is an entirely new experimental technique developed by the author, is presented in detail in Appendix B and so is not discussed here. Before we proceed any farther, it is important to note that all metallic clusters are created, observed, and only stable in the gas-phase; specifically, in high vacuum molecular beams. While the lifetimes of the beams suggest that the clusters are stable for extended periods of time, they cannot be collected in a condensed- or even a gas-phase, as the clusters are destroyed as soon as they interacted with the surface of a containment vessel. The topic of cluster-substrate interactions is covered in detail in §2.6.c—which covers novel cluster deposition methods—and in Chapter 5.

The instrument used in all of the studies presented herein is a result of decades of scientific research. This statement is both figurative and literal; the experimental techniques used

were developed over many years and for a broad range of chemistry, and also some of the steel that comprises the instrument as it exists today is recycled from similar instruments used in the Castleman lab over twenty-five years ago. What this brings about is a unique instrument that is capable of performing experimental studies exclusive from any other in the world, but also consequently means that reasoning behind its specific design and functionality are necessary in order to understand the contents of this dissertation, as opposed to a commonly available instrument that could be easily and succinctly referenced. To be sure, many of the individual components or techniques presented in this chapter are neither unique to this dissertation nor invented by the author. However, just as Chapter 1 attempted to outline cluster science in order to provide stand-alone text that a reader could easily use as a base for further research, so this chapter attempts to do the same for the experimental techniques and applications utilized in the following chapters.

An illustration of the instrument is presented in Figure 2.1. We review its individual components in turn, but as an overview it is only necessary to understand that metal clusters are created in a source (Figure 2.1.a), transported through a reaction vessel (Figure 2.1.b) where a reactant gas may be introduced, and the reactants/products are sampled through a series of ion optics that culminate in a quadrupole mass spectrometer (Figure 2.1.c through g). In addition to simply sampling the masses of the species, this instrument possesses the ability to deposit clusters on a surface for transport to another instrument for surface studies (this deposition capability is nearly identical to the one used for matrix-isolation cavity ringdown spectroscopy, Appendix B). The following sections describe the details of this experimental technique, following the order of the clusters' path through the instrument, and so we often return to Figure 2.1.

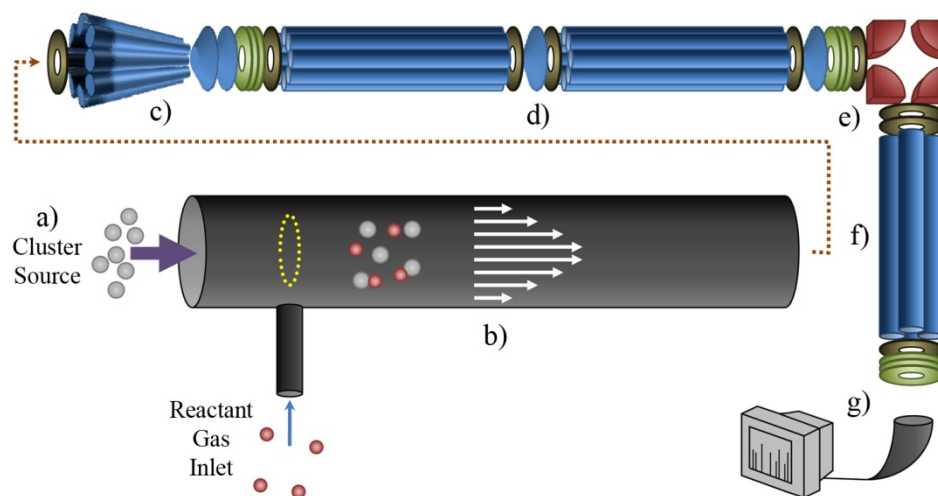


Figure 2.1. Primary experimental apparatus. a) Aluminum clusters are created in a cluster source and b) carried into a laminar flow reaction vessel where they can be exposed to a reactant gas. c) The reactants and products are then focused via a conical octopole into d) the differential pumping region. e) The ions were transported around a bend via a quadrupole energy deflection filter to eliminate neutral species, and g) mass selected via a quadrupole mass spectrometer and channeltron electron multiplier. The entire system is controlled using a personal computer.

2. Cluster Sources

The first step in any experiment involving metal clusters is to create a cluster distribution over a desired range of sizes. Several techniques exist in the production of cluster sources; for a broad overview the author recommends the commonly cited comprehensive review of clusters by Walt de Heer.¹ Although nearly twenty years old at the time of this writing, this review is still quite valuable as a reference to the experimental techniques and early history of metal cluster science. What is difficult to research, however, is the difficulty at which specific metals form clusters larger than the dimer. Early cluster research involved sodium mostly,² possibly because it was a prime candidate for jellium model studies (sodium has one valence electron which cause its clusters to fill every electronic shell as size increases), but more likely because it was easy to create sodium clusters (copper, for example, would have worked just as well, but early studies

could only produce up to the trimer³). The reason for this is that sodium has a low boiling point, and so creating clusters requires little more than a high heat source and an expansion nozzle.^{4,5}

More specifically, the production of metal clusters requires the aggregation of gas-phase atoms into molecules, and such processes will depend on the concentration of the gaseous metal and the cooling of the burgeoning clusters (to prevent, but sometimes aided by, single-atom evaporation). As is discussed below in §2.3.b, the specifics of this process are still not entirely known, but it can be safely stated that metals with low boiling points are easier to evaporate, and thus it is easier to create larger concentrations in the gas-phase. Most metals are incompatible with seeded supersonic nozzle sources and gas-aggregation cluster sources due to their high boiling points, and so other higher-power sources are needed. Popular solutions to this problem include the pulsed-arc cluster-ion source (PACIS),⁶ various forms of inert-gas sputtering sources,^{7,8} and the laser vaporization (LaVa) source.

a. Laser Vaporization Source

The LaVa source was developed by Richard Smalley at Rice University in the early 1980s as a method for creating large (tens of atoms) clusters of high-boiling point metals.^{9,10} This method was shortly thereafter used to ablate graphite, leading to the discovery of buckminsterfullerene¹¹ which subsequently earned Smalley and his coworkers the Nobel Prize in Chemistry in 1996. Later the overall design of the LaVa source was greatly improved by de Heer (Figure 2.2).¹² The construction of a LaVa source is in many ways an art form, and this author has never seen two sources that are exactly alike, although he has seen several that work improperly for no discernable reason. Therefore, the details of the specific source used in the work discussed herein is reserved for Appendix A, and we instead briefly outline the basics of the LaVa source

and list its advantages and disadvantages when considering the alternatives in order to elucidate why this type of source was used.

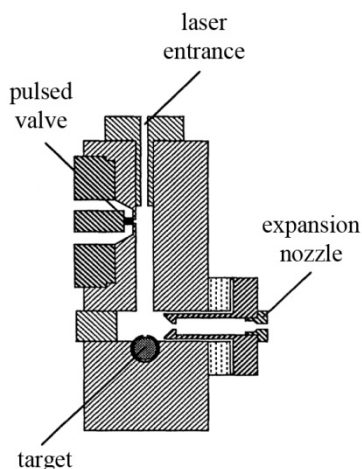


Figure 2.2. Standard laser vaporization source. Focused laser light is used to ablate a target, which is typically a rotating/translating rod. Pulsed gas then carries the nascent clusters through the expansion nozzle into the vacuum instrument. Adapted from Reference 12.

The principle idea behind a LaVa source is the use of a focused high-power laser beam to ablate a source and create a gaseous form of the target material. The target is typically a rod which is rotated and translated to increase material availability, although rotating discs have also been employed.^{13,14} The gas then condenses into small molecules of the ablated material, and these molecules (i.e. clusters) are then carried into the vacuum apparatus via a backing/carrier gas. The target material does not have to be metallic, and can in fact be composed of more than one element in order to create bi-elemental species.^{15,16} Additionally, the focused power of a common pulsed laser (e.g. Nd:YAG, 532 nm, 30 Hz, 150 mJ/pulse) is enough to create a plasma around the target material, which can be used to dissociate almost any gas which is concomitantly introduced through the back of the source (the focused laser beam can also be used to dissociate a gas without a target material).¹⁷ In this manner it is possible to create a gaseous medium containing several elements, which will agglomerate to form clusters of varying amounts of each element.^{18,19} This versatility regarding the source material, as well as the reliability of modern

lasers, makes the LaVa source a very attractive option when considering metal cluster research (assuming one has the required space for a high-power laser and table). When comparing the LaVa source to its close relative, the PACIS, most of these advantages are retained, although one does require the source material to be conductive in order to achieve the high-voltage arc necessary to form the plasma.⁶ Similarly, some inert-gas sputtering sources also require a conductive material,⁸ although there are exceptions.^{20,21}

It is worthwhile to note here that the use of a continuous-wave laser is not forbidden, although it is impractical for three reasons. First, it is much easier to achieve the powers necessary to evaporate metals with a Q-switched laser. Second, the backing gas used to transport the burgeoning clusters out of the source must be continuously pumped out of the vacuum instrument, which is much easier to manage when the laser and thus the gas is pulsed. Finally, the formation of a plasma around the target area briefly shields the material, since tailing light is absorbed by the hot, opaque blowoff material.²² The shielded material, which momentarily exists as a liquid interface around the area of ablation, cools while the plasma fully dissociates, which can take several milliseconds (Figure 2.3). In fact, too long of a laser pulse (longer than a few tenths of a millisecond) can create a laser-supported absorption wave that essentially wastes the excess energy, and so one generally does not have to worry about the upper limits of laser intensity when designing a LaVa source. Roughly, any laser faster than 200 Hz (including continuous-wave lasers), stronger than 10^8 W/cm², or with a pulse duration longer than 10^{-4} s will actually reduce the amount of material evaporated, which will directly affect the intensity of the clusters produced.²³

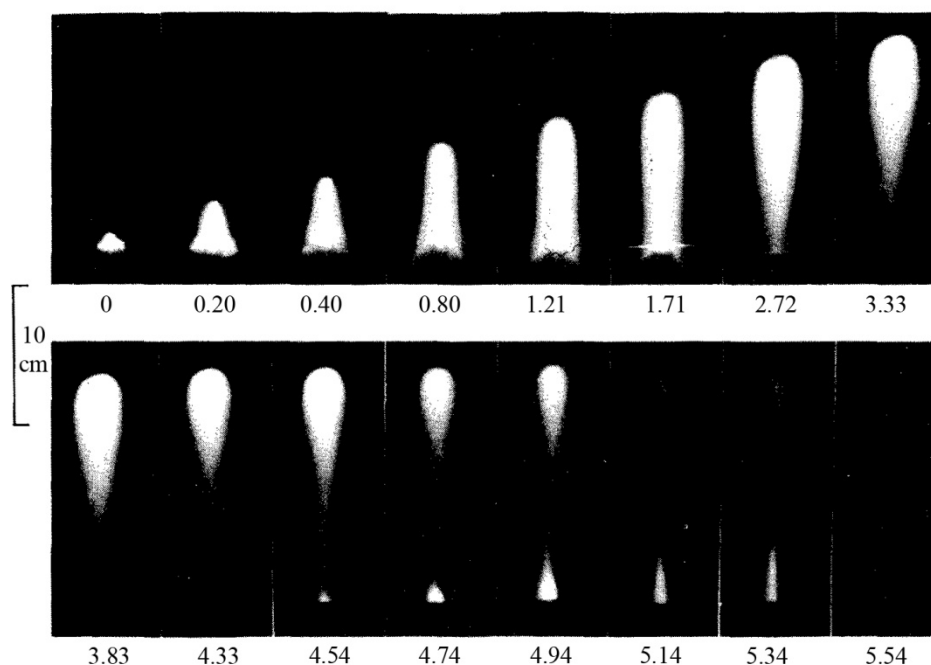


Figure 2.3. High-speed photographic images of a high-power laser pulse striking aluminum. Units of time are in ms, exposure time is 6 μ s. Adapted from Reference 22.

Once a gaseous medium has been created, the atoms begin to condense into clusters. Although much is still not known about this process, it is considered to be very similar for various sources and whether the monomers being considered are atoms or molecules (e.g. the study of water²⁴ or carbon dioxide clusters²⁵), although in the later case a cold or low-energy source is needed to prevent atomization. Briefly, three monomers collide and bond to each other to form a trimer. In order to quench the large amount of energy gained in this process and thereby conserve energy and momentum, one monomer immediately leaves, with subsequent monomer additions creating a cluster.



The three-body collisional growth of the dimer can also be assisted by a heavy inert carrier gas (e.g. argon instead of helium), although this is not recommended with LaVa sources due to the predominant formation of argon clusters and argon additions on the metal clusters^{26,27}

(additionally, the use of a carrier *molecule* with rotational and vibrational degrees of freedom would be optimal if the source did not atomize the molecule). The traditional backing gas used in LaVa sources is helium, which does not sufficiently aid cluster growth, and so this topic is reserved for the magnetron gas aggregation source discussed in §2.2.b. Once the ratio of monomers to polymers reaches a certain point, cluster growth can continue via cluster-cluster collisions, which can result in a twin-peaked mass distribution.^{25,28} In the case of a hot cluster source, the nascent cluster, which will already have large internal energies due to its hot formation,²⁷ must quench this energy somehow, or it will spontaneously dissociate by evaporating atoms into vacuum.^{29,30} This quenching is performed by a combination of thermalization with the backing gas in the source and the ensuing adiabatic expansion into the vacuum chamber. Oftentimes, this expansion will occur simultaneously with evaporation, leading to the formation of a non-uniform cluster distribution with step edges at jellium shell closings, due to those specific molecules having a greater stability and thus a higher boiling point (e.g. Figure 1.2).³¹ The evaporation of atoms into vacuum is dependent on the element being studied, but can broadly be represented by the following equation:

$$d^* = \frac{4\sigma m}{kT\varrho} \cdot \frac{1}{\ln(\Phi_k)} \quad (2.3)$$

where clusters with a diameter smaller than d^* will evaporate and larger ones will grow. In this equation, σ is the surface tension of the liquid cluster, m is the mass of the monomer, k is Boltzmann's constant, T is the temperature of the cluster, ϱ is the density of the cluster, and Φ_k is the supersaturation level of the liquid/vapor interface, represented by the ratio of the partial pressure of the monomer over the vapor pressure of the cluster, P_k/P_∞ . While it is immediately obvious that this equation presents no useful application in the laboratory, as many of the variables are difficult to control and measure, it does help explain why a cluster distribution is usually seen as a normal or an inverse gamma distribution, as opposed to a logarithmic decay

(i.e. the monomer being more intense than the dimer being more intense than the trimer, etc.). It also helps explain why metals with high boiling points tend to create smaller clusters under the same experimental conditions (due to the reduced partial pressure of the monomer, and therefore Φ_k). Of course, it stands to reason that Equation 2.3 is time-independent, and once the cluster has exited the source it will no longer grow. The time allowed for cluster formation is called the aggregation time, and will be dependent on the parameters of the source and the speed/pressure of the backing gas. Attempts have been made to quantify the aggregation time,³²⁻³⁴ but ultimately each source will behave differently and so the concept of an aggregation time should be treated as a qualitative effect which can be modified easily but never characterized rigorously. The cluster distribution created by specific sources (i.e. LaVa³² or magnetron gas aggregation²⁸) has also been attributed to the Smoluchowski rate equations for particle aggregation,^{35,36} although this does not account for the twin-peaked mass distribution. It should be reasonably safe to state, therefore, that studies have failed to determine the exact kinetic mechanism for cluster formation.

The process of formation of clusters via gas aggregation is similar for nearly every cluster source, and so most of what is stated above presents neither advantages nor disadvantages for the LaVa source. However, the average mass of a cluster distribution will increase if the time allowed for aggregation is increased, and that whichever source allows for the maximum customizability here, without the need for time-consuming disassembly/reassembly, would hold a strong advantage. The “aggregation time” is determined by the space immediately between the target material and the exit of the source, called the “waiting room,” and the pressure of the backing gas. While it is difficult, but possible, to design a LaVa source wherein the size of the waiting room is adjustable, typically the pressure of the backing gas is the easier of the two parameters to adjust. Simply increasing the flow of the gas is usually insufficient, as the gas is expanding into vacuum and therefore small changes in flow will do little to change the pressure in the source, as is approximated by the following hydrodynamic equation:

$$Q \cdot P_0 = (P_1 - P_2) C; P_1 > P_2 \quad (2.4)$$

where the throughput of the system is represented by the flow, Q , multiplied by the backing pressure at the inlet, P_0 ; P_1 and P_2 are the pressures before and after the source, respectively; and C is the conductance, which is determined by the size and shape of the source exit.³⁷ As the conductance does not change before and after a pressure change, one can see that if P_2 is very small, small changes in Q will have an equally small effect on P_1 .

In the case of a pulsed gas, as is traditional for a PACIS or LaVa source, the delay between the laser shot and the pulse can be adjusted. This pulse will create a normal distribution of pressure in the source, and by adjusting the delay one can adjust the pressure in the source at the exact moment the laser strikes. However, in the experiments conducted herein, it was quite important that the gas flow be continuous, as is discussed below. Therefore, the only practical means of adjusting the pressure of the gas in the waiting room is by adjusting the exit nozzle. As the conductance of a tube is inversely proportional to its length and directly proportional to the fourth power of its diameter ($C \propto L^{-1}$; $C \propto D^4$; see §2.3.a),³⁷ one can easily see how different exit nozzle parameters will affect the pressure in the source (as mentioned previously, exact parameters are specific to the exact LaVa source used, and so are reserved for Appendix A). Unfortunately, to the author's knowledge there is no LaVa, PACIS, or similar source that allows the user to modify or change the exit nozzle without disassembling the source. The magnetron gas aggregation source (MagGAS), however, does have this capability, although not without its own disadvantages.

b. Magnetron Gas Aggregation Source

The magnetron sputtering source, which was originally developed for thin-film deposition, has quite a long history³⁸ (not to be confused with cavity magnetrons found in every

microwave). Simple chemical vapor deposition, which has existed in some form for over a century and was first commercialized by Thomas Edison, is disadvantageous in that it requires large amounts of energy to evaporate the target medium. In the late 1930s, however, Frans Penning, a Dutch physicist, discovered that a magnetic field could confine a plasma to a target surface and amplify the rate of evaporation. Early “Penning traps” consisted of a linear magnetic field inside a cylindrical target, but in 1974 John Chapin, an American inventor, developed the modern planar magnetron sputtering source. This design created a toroid-shaped magnetic field on a flat surface, and is the predominant design today (Figure 2.4.a).³⁹

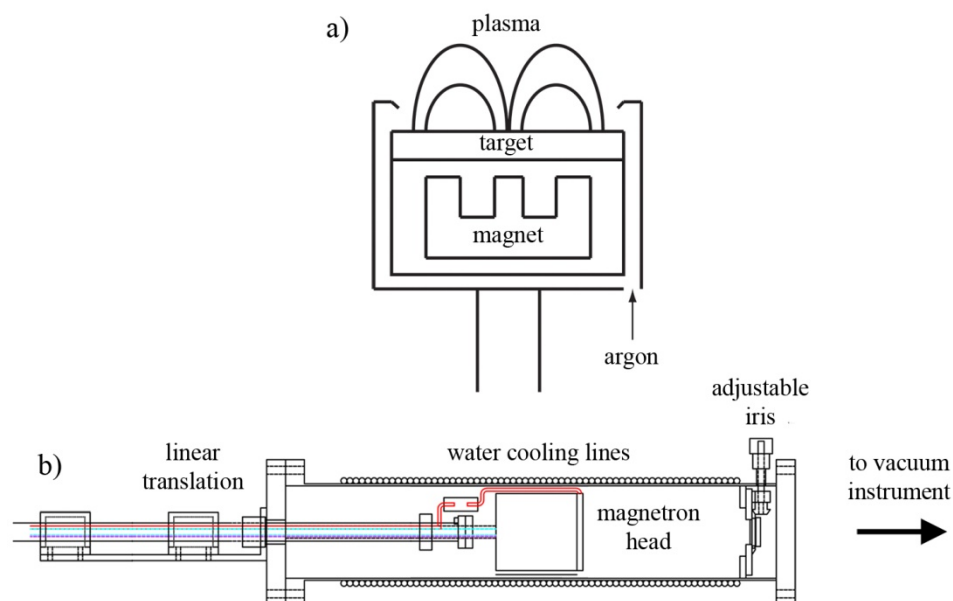


Figure 2.4. a) Illustration of magnetron head depicting magnetic field lines and argon inlet. b) Illustration of custom magnetron gas aggregation source depicting adjustable iris and water cooling lines. Illustrations are not to scale. Clusters are condensed from the plasma formed by the magnetron head before escaping into the vacuum instrument. Linear translation allows the adjustment of the distance between the magnetron head and the iris, helium backing gas (inlet not shown) and argon pressures can be freely adjusted.

Briefly, a magnetron sputtering source works in the following way: a negative potential is applied to the target surface, which is encircled by the magnetic field. An inert gas, typically argon, is allowed to flow over the surface. When one of the argon atoms spontaneously ejects an electron due to quantum effects or background radiation, the positively charged atom suddenly feels a

large Coulombic attraction towards the target. As it impacts the surface at high speed, enough energy is transferred to eject some atoms and electrons. The electrons from the surface and from the argon then collide with additional argon atoms, causing further ionization and surface sputtering, and therefore maintaining the process. This sustained effect creates a plasma that is constricted by the magnetic field, reducing losses. Due to this magnetic field, the region of prime impact is a circle around the center of the magnetic field, dubbed the “race track.” The ablation of the surface will quickly eat away at the target, creating a circular trench that exactly reveals the magnetic field. The ejected target material then expands outward in a pattern that depends on the magnetic field,⁴⁰ depositing onto and coating the desired surface. Magnetrons utilizing this design are now commercially available, and with a radio frequency power supply the ability to ablate non-conductive target surfaces is gained.⁴¹

In the early 1990s Helmut Haberland of the University of Freiburg utilized the plasma created by the magnetron sputtering source to develop the world’s first MagGAS.^{8,42} The clustering process is identical to that of a LaVa or other cluster source, wherein the aggregation time is limited in order to control the size of the particles. Haberland’s original design was improved in 1994,⁴³ and similar sources can today be found in countless labs around the globe (several are even available commercially).^{21,44-48} Although nearly all published MagGAS designs involve the creation of large nanoparticles (hundreds or thousands of atoms), the MagGAS had three desirable properties that suggested it would be ideal in a cluster deposition instrument such as the one discussed here. First, it had the potential to create several orders of magnitude more species per second than any other cluster source. Second, Haberland’s design allowed for *in situ* tuning of the aggregation time, allowing one to easily adjust the cluster distribution without disassembly. Finally, being constructed of many rugged, commercially available components, it had the potential to prove more reliable than LaVa sources, which require regular cleaning cycles in addition to depending on the fault-free operation of a complex high-powered laser. A MagGAS

was therefore conceived and built for the purposes of future deposition studies; its overall design is outlined below, while operational guidelines and early performance studies are reserved for Appendix A.

The MagGAS is depicted in Figure 2.4.b. The source is most directly influenced by Haberland's⁴³ and a similar design by Richard Palmer at the University of Birmingham.²¹ The clusters are created in a similar fashion as described in §2.2.a. Briefly, the plasma of metal atoms created by the magnetron head causes the aggregation of clusters before they exit the source via the adjustable iris. The size of the clusters is determined by the aggregation time and the speed of initial aggregation (Equation 2.1), which is accelerated by the presence of argon.



The aggregation time can be adjusted by increasing or decreasing the flow inside the source, which can be achieved in several ways. First, there is a backing flow of helium that can be adjusted. Second, the distance between the magnetron head and the exit iris can be adjusted. Finally, the size of the iris can be adjusted. In a study of a similar setup, it was determined that the predominant factors which adjust cluster size distribution are the partial pressure of argon and the distance between the magnetron head and the exit.²⁸ What separates the MagGAS presented herein and all others are two major differences: 1) the adjustable iris (described in Appendix A) allows for the adjustment of the total pressure in the source while maintaining the ratio of argon and helium, and 2) the entire source is surrounded by water lines to cool the gasses (all other published sources use a liquid nitrogen cooling jacket). This is an enormous advantage when size/cost is considered, as the common setup requires cryogenic equipment as well as a surrounding vacuum chamber to prevent excess heat absorption.

Although the MagGAS seems to have several advantages over other cluster sources, it has two major disadvantages. First, the large plasma in a small enclosure has a tendency to etch unwanted metal off of the magnetron head and the enclosing steel chamber, thus adding

detectable amounts of iron, copper, carbon, oxygen, and hydrogen into the mass distribution. For mass-selected deposition studies this may not be an issue, but for reaction studies it is inconvenient and sometimes unacceptable. Second, it creates large amounts of gas flow. This requires additional differential pumping in a system where the source is coupled directly to the high vacuum part of the instrument. This latter disadvantage is not an issue here, however, as large amounts of gas flow are in fact required in order to maintain laminar flow in the reaction vessel. Therefore, whether clusters are created in the LaVa source or the MagGAS, large amounts of carrier gas are also expanded into the flow tube, where reaction studies can then be performed.

3. Multiple-Ion Laminar Flow Tube

Once clusters have been created, they are then transported by the carrier gas into the instrument, which is of a significantly lower pressure. In the specific case of this instrument, the next chamber is a laminar flow reaction vessel (Figure 2.1.b). In this vessel the clusters can be reacted with any number of reactant gasses before being sampled by the mass spectrometer for analysis, either in qualitative reactivity or quantitative rate constant measurements. The use of laminar flow for the determination of ion-molecule reaction rate constants was predominantly developed by Eldon Ferguson and coworkers of the Environmental Science Services Administration in Boulder, Colorado in 1963.⁴⁹ However, the use of a laminar flow tube for cluster research is somewhat uncommon today, when compared to other techniques.^{50,51} Therefore, it is necessary to now outline the concepts behind the laminar flow reaction vessel and discuss its advantages and disadvantages.

a. The Importance of Laminar Flow

As is discussed in the next section, the main purpose of using a laminar flow tube as opposed to other gas-phase ion reaction techniques involves the ability to determine rate constants and activation energies for various reactions where the constraints of a vessel would normally compromise the reactants due to their being extremely labile under normal circumstances. However, experiments involving the determination of these kinetic values using typical laminar flow tube techniques have not been performed in any of the experiments presented herein. This fact produces an obvious question: Why still use a laminar flow tube? To answer this, we must first define laminar flow.

The best real-world analogy of laminar flow is the surface of a slow-moving (non-turbulent) river or stream. It is quickly observed while standing on the bank that the water towards the middle of the water is flowing faster than the water at the shore. This is due to viscosity, or the friction between the unmoving shoreline and the flowing water, which was proposed by Isaac Newton in 1687 and further developed in 1822 by Claude-Louis Navier and George Stokes.⁵² This layman's analogy applies equally well to gases in a circular tube, provided certain conditions are met. Strictly speaking, laminar flow in a tube is defined as a static state of flow wherein velocity is represented by a parabolic distribution of layers, or streamlines, and this general effect is illustrated in Figure 2.1.b. This produces two important restrictions on the flow medium and any entrained objects: 1) diffusion toward the outside of the tube is resisted and 2) the transfer of energy from the tube walls towards the center of the flow is enhanced due to the frictional effects (i.e. the temperature of the entire medium is the same as the flow tube walls). More quantitatively, the viscosity of an ideal gas can be represented by the following equation:

$$\mu = \frac{2}{3\pi^{2/3}} \frac{\sqrt{mkT}}{d^2} \quad (2.6)$$

which was developed in part by James Maxwell in 1860.⁵² Here all variables are the same as in Equation 2.3 and d is the diameter of the molecule. As μ is independent of temperature, it suggests that the viscosity of a gas is analogous to that of a liquid, and this is found to be true experimentally for gasses at pressures below ten atmospheres (the temperature dependence of $T^{0.5}$ is an oversimplification, and thus empirically determined values of μ typically are used). Additionally, it can be shown that the radial-dependent velocity of the gas in the tube is represented by:

$$v_z(r) = \frac{(P_0 - P_L)R^2}{4\mu L} \left[1 - \left(\frac{r}{R} \right)^2 \right] \quad (2.7)$$

and the laminar flow is represented by:

$$Q = \frac{\pi(P_0 - P_L)R^4}{8\mu L} \quad (2.8)$$

where P_0 and P_L are pressures at the beginning and end of the flow region of length L ($P_0 > P_L$) and R is the radius of the tube. Note that Equation 2.8 is equal to the product of the average velocity $\langle v_z \rangle$ and the area of the tube, πR^2 . This is known as the Hagen–Poiseuille law after Gotthilf Hagen and Jean Louis Poiseuille, who independently derived it around 1840.⁵² It is important to know that this is only true for laminar flow, and systems with transient or turbulent flow will not follow this simple equation nor will imperfect shapes due to there being eddies along the tube at defect sites (e.g. ports for inlets or pressure gauges).⁴⁹ It is possible, however, to assume laminar flow by considering the Reynolds number (named after Osborne Reynolds) of a system (Re) and defining laminar flow to exist in any system:

$$Re = 2R\langle v_z \rangle \rho / \mu \quad (2.9)$$

where ρ is the density of the gas, which is constant across the entire length L , and $Re < 2100$. The restriction of this unitless number is an empirically determined estimation, but considering the assumptions made thus far and the fact that no tangible tube will be perfect, we can be satisfied

with this requirement. Using this information, we can therefore estimate the force of the gas flow on an object at a given radial position along a laminar flow tube:

$$\begin{aligned}
 F_z(r) &= -v_z \cdot Q \cdot \rho = -\frac{\pi R^2 \rho}{2} \left[1 - \left(\frac{r}{R} \right)^2 \right] \left[\frac{(P_0 - P_L) R^2}{4\mu L} \right]^2 \\
 &= -\text{Re} \frac{\pi R \langle v_z \rangle \mu}{4} \left[1 - \left(\frac{r}{R} \right)^2 \right]
 \end{aligned} \tag{2.10}$$

which will prove relevant in §2.3.c. It is also important to mention here that Re is inversely proportional to the square of the viscosity, and therefore inversely proportional to the mass of the gas ($\text{Re} \propto \mu^{-2}$ for a given ΔP ; $\text{Re} \propto m^{-1}$ assuming a constant ρ). This is an argument for the use of argon rather than helium, as it is ten times the mass of helium it will reduce the Reynolds number of a given system by an order of magnitude. It was revealed in §2.2.a that argon is not ideal in a LaVa source, but it was also explained how the MagGAS requires argon flow to operate. We will shortly see (§2.3.c) that the real reason this experimental setup utilizes helium instead of argon is due to the former's lower ionization energy.

We now have an adequate definition of laminar flow, but we have not yet discussed any of its inherent advantages or disadvantages. In §2.2.a it was mentioned that a nascent cluster must lose energy or risk evaporating into the vacuum, and that one way for it to accomplish this is via adiabatic expansion out of the source and into the vacuum instrument. When the clusters escaping the source do so faster than the speed of sound this is called supersonic expansion (the speed of sound in a vacuum is relative: as the mean free path is usually longer than the chamber length it literally means that no cluster exits the source faster than those ahead of it, and therefore no cluster-cluster interactions occur in the vacuum). The degree of expansion is represented by the Mach number, which is represented by the following equation (developed by John Anderson and John Fenn in 1965):

$$M_T = \frac{v_T}{a} = \frac{v_T}{\sqrt{\frac{\gamma RT}{m}}} = k \left(\frac{Kn_0}{\varepsilon} \right)^{-(\gamma-1)/\gamma} \quad (2.11)$$

where v_T is the terminal velocity, a is the local speed of sound, R is the gas constant, ε is the collision effectiveness (1/4 for an ideal gas), γ is the heat capacity ratio (5/3 for an ideal gas), and Kn_0 is the Knudsen number:

$$Kn_0 = \frac{\lambda_0}{D} \quad (2.12)$$

where λ_0 is the mean free path in the source and D is the diameter of the nozzle.⁵³ The Mach number is named after Ernst Mach and the Knudsen number is named after Martin Knudsen; both were physicists who pioneered gas and fluid characteristics at the turn of the twentieth century. These equations make it possible to calculate the temperature of a molecule after expansion, but none of this is relevant here as combining Equations 2.9 and 2.11 demonstrates that to achieve supersonic expansion the average velocity, $\langle v_z \rangle$, must be higher than the local speed of sound, which is unrealistic for a laminar flow tube. As an example, expanding helium into a 0.035 m radius tube at 300 K ($Re = 2100$; $M_T = 1$) would require a density in the tube of 6.12×10^{-4} kg/m³. Applying this to Equations 2.9 and 2.8 results in a flow of 3.93 m³/s and a pressure drop of 1 Torr/m (This corresponds to a standard temperature and pressure pumping speed greater than 310 liters per minute, which while not impossible is quite impractical). By further pursuing this *ad nauseam* it can be shown that when $M_T = 1$, $Kn_0 = 1.48$, which, when combined with our previous assumptions for density and flow, yield unfeasible values for P_0 , D , and/or L (from §2.2.a). Therefore the Mach number for a system with laminar flow is *less* than one, leading to subsonic expansion. To be sure, the clusters exiting the source are much, much heavier than the helium backing gas and therefore are less inclined to expand faster than the preceding helium atoms (the collision effectiveness of larger clusters in the presence of helium can be calculated, but is not relevant here), but it is equally obvious that this lack of equilibrium

would lead to collisions from behind. We discuss the possibility of cluster-cluster interactions shortly. What affect this would have on the cooling of the nascent clusters is unclear, but it can be shown that the “steps” at jellium shell closings are much less pronounced (Figure 2.5).^{31,50,54} This suggests that the subsonic helium expansion plays some enhanced role in collisional cooling, but it is unknown whether this effect occurs after the expansion nozzle or in the source, as the subsonic expansion would lead to a pressure wave effect that travels an indeterminable distance back into the source. Thus, the main advantage of the laminar flow reaction vessel emerges: temperature control. The clusters are never cooled beyond the temperature of the flow tube walls (this undefined temperature is known as being “thermal”).

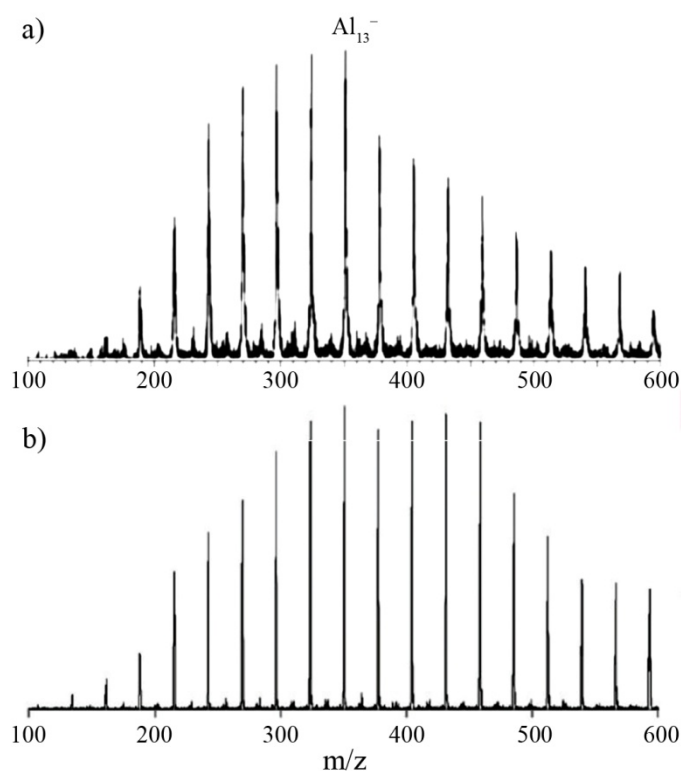


Figure 2.5. Examples of two aluminum cluster anion distributions created a) with and b) without supersonic expansion. A strong step edge at the jellium shell closing Al_{13}^- can be observed in (a) due to the concomitant evaporation of clusters with expansion cooling. (a) Adopted from Reference 50.

Shortly after exiting the source they reach the same temperature as the entraining helium gas and, with a simple experimental setup, this can be controlled with supreme precision over a wide

temperature range (from tens to hundreds of Kelvin).^{49,55} The exact distance at which the cluster becomes thermal is difficult to calculate, but was empirically explored by Ferguson early on using a quartz flow tube which could be penetrated by infrared spectroscopy, thus providing an absorption spectrum of an excited species and therefore the temperature.⁴⁹ With his flowing afterglow system, he determined that excited helium reached thermal temperatures “a few centimeters after the excitation region.” Therefore, the introduction of any reactant gas after these few centimeters would be reacting with clusters at a well-defined temperature, thus allowing for kinetics studies (which are discussed below; briefly, this allows one to determine activation energy and the Arrhenius prefactor).

How does this compare to other experimental reactivity studies? To answer this, we very briefly outline the two most popular candidates for gas-phase cluster reactivity studies: tandem mass spectrometry^{56,57} and Fourier transform ion cyclotron resonance (FT-ICR) mass spectrometry.⁵⁸ In tandem mass spectrometry, a multipole is used as the reaction vessel, and the ions successively lose energy due to nonreactive collisions with any background gasses and the adiabaticity of the multipole.^{59,60} Additionally, the clusters are supersonically expanded into the apparatus, which implies that their temperature is less than room temperature to begin with (as discussed above, final temperature is relative to the Mach number, but could be as high as one hundred Kelvin²⁷). Temperature-controlled tandem mass spectrometers do exist, although the technique is not as precise as the laminar flow tube and generally can only be controlled when lower than room temperature.⁶¹ Contrastingly, FT-ICR mass spectrometry *adds* resonance excitation to the trapped species’ internal energy distributions.^{62,63} This creates an environment where the temperature is non-thermal and difficult to control, although lower-temperature techniques involving nonreactive collisions with a quenching gas do exist.⁶⁴ In comparison with a laminar flow reaction vessel, neither of these techniques offers the control or, quite frankly, the simplicity. There are, however, two strong disadvantages of the flow tube that both of the above

alternative techniques do not possess. The first is the large amount of carrier gas that must be pumped before the high vacuum mass spectrometer. This is typically handled by a Roots blower coupled to a high-volume vacuum pump. A Roots blower is very similar in design to a supercharger (invented by Philander and Francis Roots in 1860 for use primarily in blast furnaces, followed by airplane engines, and today muscle cars). It cycles large amounts of air very quickly into the intake of a pump which is usually several times the size of modern high vacuum pumps and can take up an entire room, which could certainly become an issue if space is a consideration. The second disadvantage of the flow tube is the lack of mass selection before the reaction vessel. This is inherent in both of the alternative techniques considered here (tandem mass spectrometers typically have a quadrupole before the reaction vessel, allowing for preliminary mass selection). To be sure, laminar flow tubes have been employed where a quadrupole mass spectrometer feeds selected reactants into a flow tube. This style of “selective ion flow tube” (pioneered by Nigel Adams and David Smith at the University of Birmingham in 1976) will be at a much higher pressure, and so a Venturi inlet must be used.⁵⁵ However, mentioning this disadvantage here only serves as a prologue to the following section (and also Chapter 4), where it shall be argued that no such mass selection is necessary for the studies presented herein or for any studies in the near future.

b. Kinetic Theory and Rate Constants

In Ferguson’s original analysis of laminar flow reaction vessels he developed an oversimplified but approachable model for reaction kinetics where he assumes the basic reaction:



and derives an equation for the rate constant:

$$k(T) = \frac{\pi R^2 \langle v_z \rangle^2}{Q_B L} \ln \left(\frac{[A]}{[A]_0} \right) \quad (2.14)$$

where Q_B is the rate of introduction of reactant B, in units of flow.⁴⁹ With the laminar flow reaction vessel also comes the ability to control temperature, and thus a temperature-dependent study will yield both the Arrhenius prefactor and the activation energy of a chemical reaction. The simplicity of Equation 2.14 stems from the fact that it ignores non-ideal flow tube conditions such as radial diffusion, eddies in the flow due to imperfections and inlet/outlet flanges, and the initial non-uniformity of Reactant B. Theoretical models accounting for these aspects do exist, to some extent, although it is much easier to determine an empirical end correction factor by first determining a well-characterized rate constant. In 1987 Castleman performed such a study on several variables of the flow tube, including the shape and size of the reactant gas inlet.⁶⁵ The physical steel flow tube used in that study (for one of the radii examined) was literally the same piece of steel used in the studies presented in this dissertation. Therefore the facts presented in the 1987 study are conveniently transferable to present-day work.

It was mentioned above that the lack of mass selection before the flow tube creates a disadvantage for this technique. This becomes evident when one considers the initial assumption made: that Equation 2.13 is the sole chemical interaction that causes a change in $[A]$ over time. In a multiple-species flow tube other reactions may exist, most notably any reactions which cause the *formation* of Species A.



As is demonstrated in Chapter 3, this is a concern when there is substantial evidence for Equation 2.15 to be a contributing factor in $\frac{d[A]}{dt}$, which is not the case for many reactions. One additional concern is cluster-cluster interactions in the flow tube. While also present in similar techniques, it nevertheless requires brief attention. The fact of the matter is that the concentration of clusters in the flow tube (positive, negative, and neutral) is entirely too small, and their separate mean free

path is on the order of several kilometers (for specific empirical details of the laminar flow tube used herein; see Appendix A).

c. Conical Octopole Ion Guide

Once the clusters/products have reached the end of the flow tube, they must then be sampled into the high vacuum portion of the instrument. Traditionally this can be achieved using a skimmer, which is quite literally an outward-facing coned orifice which allows a small fraction of the laminar flow to pass through while deflecting the large remainder to be pumped away. As the majority of the clusters are located towards the center of the flow tube due to the laminar flow, a large percentage of the total concentration would be sampled. However, this is obviously not ideal as much of the total cluster count is still lost. Therefore it is desirable to focus the incoming clusters so that as much of the signal is transported through the skimmer as possible. As the final species to be sampled are always ions, there are multiple ways to achieve this, and to be consistent with our approach thus far, we shall compare alternative techniques while we outline the one utilized: the conical octopole (Figure 2.1.c). In order to keep this discussion as brief as possible, the author would first recommend two worthwhile books on basic multipole theory.^{60,66} The author also recommends two papers for insights into the idea of the conical octopole and ion funneling in general. The first is the undisputed origin of the conical octopole concept, designed and built in 2006 by Ueli Heiz for the focused deposition of clusters onto a surface.⁶⁷ This paper is discussed further below. The second paper is a review on the ion funnel, but discusses other options as well, namely alternative radio frequency (RF) focusing devices, including this conical octopole.⁶⁸

The invention of the quadrupole mass analyzer is largely credited to Wolfgang Paul, a German physicist who was to win the Nobel Prize for his work in 1989, although the history of

multipoles is quite a long and complicated one.⁶⁹ Skipping the history lesson then, it is worthwhile to understand that, from the second of Newton's laws of motion ($F = m \cdot a$), it is possible to derive immensely complicated equations which accurately describe the motion of an ion in a multipole:

$$\frac{d^2u}{d\xi^2} = -(a_u - 2q_u \cos 2\xi)u, \quad q_u = \frac{n-1}{n} \frac{qV_0}{\varepsilon}, \quad a_u = 2 \frac{n-1}{n} \frac{qU_0}{\varepsilon}; \quad (2.16)$$

$$\varepsilon = m\Omega^2 r_0^2$$

This equation is called the Mathieu Equation in mass spectrometry circles, after the mathematician Émile Mathieu who first introduced it in 1868, although he introduced several other equations that are now used to characterize various ponderomotive effects including the Stark effect and paramagnetic resonance. Of the myriad of variables discussed above and below, the important ones to consider are the peak-to-peak RF voltage, V_0 , the mass of the ion, m , the charge of the ion, q , and the effective radius between poles, r_0 ($2n$ is the number of rods, a_u is the DC potential, and $\Omega = 2\pi f$, all of which are a constant for any given non-mass discriminating system, conical or not). It is important to note before we proceed that there are a few requirements that will ultimately create a less-than-perfect solution for the effective potential (and later the adiabaticity parameter). The first is that the multipole, conical or not, is infinitely long. Although clearly impossible, this really only comes into play at the ends of the optic, and so is a reasonable assumption for the time being. However, we must eventually replace r_0 with $R_0(z)$, since in a conical octopole the radius of the optic varies along its length. The second requirement is that the infinitely long individual poles consist of perfectly constructed, infinitely thick, parallel, superconducting parabolas. This could not be more impossible; however, approximating the field created by such perfect poles with cylindrical ones is possible using the following equation:

$$r_0 = (n - 1)d/2 \quad (2.17)$$

where $2n$ is the number of poles and d is the individual pole diameter. Note that an exact realization of these perfect circles is difficult when a conical octopole is considered. It has been explored using theory and experiment that the size and position of cylindrical poles is fairly forgiving when it comes to approximating the field of an ideal optic,⁶⁶ and so it can be assumed that poles in the shape of cones will approximate these circles to a satisfying extent; in reality an orthogonal cross section of the optic at a given point will yield eight inward-pointing ellipses. The third requirement is that the field generated by the poles is uniform at any angle around the axis down the pole, z . This is impossible not only for a practical system, but for an ideal one as well. Because of the existence of the poles and the oscillating RF voltage, there will always be a time- and radial-dependant gradient of the effective potential with regards to the angle. Most of the literature assumes a time- and angle-averaged value for both of these variables, since in any true system their initial values are impossible to control (as the charged particle arrives at a random point in the oscillation). However, since in a conical octopole the effective potential will vary along the z axis when all other variables are held constant, it must not be forgotten completely (in the seminal paper by Heiz the radial-dependent aspect is never ignored⁶⁷). However, considering all of the other impossible assumptions made, it is reasonable to assume a time- and angle-averaged value for both of these variables after some initial derivations, which will ultimately make the final analysis much easier to perform.

With Equation 2.16 one can determine the effective potential, V^* , and the adiabaticity parameter, η for a given system. The effective potential is quite simply the amount of energy transferred to an ion by the multipole while it is inside of the optic. Using Coulomb's law, we know this to be dependent on V_0 , m , q , and the radial position of the ion, r :

$$V^* = \frac{q^2 E_0^2}{4m\Omega^2} + q\Phi_s \approx 4 \frac{q^2}{m\Omega^2} \frac{V_0^2}{r_0(z)^8} \left[r^6 + \frac{r^8}{2z^2} \right] \quad (2.18)$$

The final equation on the right is specific to a conical octopole, although it is easily simplified if one assumes r_0 to be independent of z . It is interesting to note here that, because the charge of the ion is squared, this is where we prove that the optic will work equally well for anions *and* cations. We can now concentrate on the adiabaticity parameter. Adiabaticity (the process of *not* adding or removing energy with respect to a closed system) in a multipole is similar to balancing a broomstick on one's finger. An ion in the multipole will swing wildly around the x - and y -axes (ignore the z -axis), eventually tracing a circle where it has been. If the ion overcompensates with each swing, energy is being inserted into the system (resonant energy build-up), and the circle will get larger and wider until the ion eventually strikes a pole and “crashes out.” Alternatively, if energy is being removed, the circle will shrink until the ion is at a dead stop in the center of the optic (the third option, of course, is a perfect system which will continue to trace the same circle forever). It should be pointed out here that, although a given system may be adiabatic, the ion can still crash out if the effective potential is too weak to compensate for the starting angle of the ion. Thankfully, we need not use the broomstick analogy for long, as we develop an equation to quantify this term:

$$\eta = \frac{2qV_0|E_0|}{m\Omega^2} = 24 \frac{q}{m\Omega^2} \frac{V_0}{r_0(z)^4} r^2 \quad (2.19)$$

Again, the final equation is for a conical octopole. Unfortunately, exploring the principles of this equation does not yield a strict range where the system is stable. However, a reasonable estimate, supported by empirical evidence, is that $|\eta|$ must be less than 0.3 for ions to not crash out. It is this equation which determines the mass limitations for any given multipole, as m_{\max} (when $|\eta| = 0.3$) is inversely proportional to frequency and radius, and it is this equation which explains the high-pass filter effects of an RF multipole, since m_{\max} is directly proportional to V_0 . Additionally, it is

here that we see why the oscillations must be in the radio frequency range for any practical values of V_0 , r_0 , and m_{\max} .

It is immediately clear that $V^* \propto r^6$, and $\eta \propto r^2$. Also, if $r_0(z)$ is re-defined as $z \cdot \tan(\theta)$, where θ is the opening angle of the octopole, $V^* \propto z^{-8}$, and $\eta \propto z^{-4}$. It is easy to see from this observation that, for any given $r \neq 0$, there will be a steep increase in V^* and η towards the narrow end of the optic.⁶⁷ However, what is not abundantly clear is the role that V^* plays in determining whether or not an ion possesses the energy required to pass through the optic. One can imagine a 2-dimensional cross section of the optic as a cone on its side: for a marble to roll through the funnel it will need an appropriate initial vector that allows for this to happen, which, when the geometry of the cone is known, is easy to calculate using classical physics. However, for any cross-section determined by a given z , V^* will always reach zero as r crosses the origin. This means that any cation or anion with the slightest initial vector down the center of the optic will pass through. That being said, there is a net force in the z -direction when $r > 0$, although this force will be orders of magnitude less than the force towards the center. This directly contrasts classical multipole theory, where there is zero force in the z -direction.

For more than a quantitative approach to this scenario, we must treat our equation for V^* as a Cartesian gradient, where the x - and y -axes are represented by r and z , respectively. From here it is trivial to calculate the direction and magnitude of force on a given ion at point (r, z) :

$$\nabla V^*(r, z) = \left(\beta \left[\frac{6r^5}{z^8} + \frac{4r^7}{z^{10}} \right], \beta \left[\frac{r^6}{8z^9} + \frac{r^8}{20z^{11}} \right] \right); \beta = \frac{4q^2}{m\Omega^2} \frac{V_0^2}{\tan^8 \theta} \quad (2.20)$$

which allows us to estimate vector fields and, with computational support, plot the movement of a hypothetical ion of initial position and velocity through the optic (Figure 2.6). Note that, for illustrative purposes, the r - and z -direction force magnitudes are irrespectively and logarithmically represented. In actuality all vectors near the poles would be much longer than the page, and so Figure 2.6 makes it much easier to observe the net force in the positive z -direction.

From here on in (including the above example), we are required to finally define all variables in order to draw any useful conclusions.

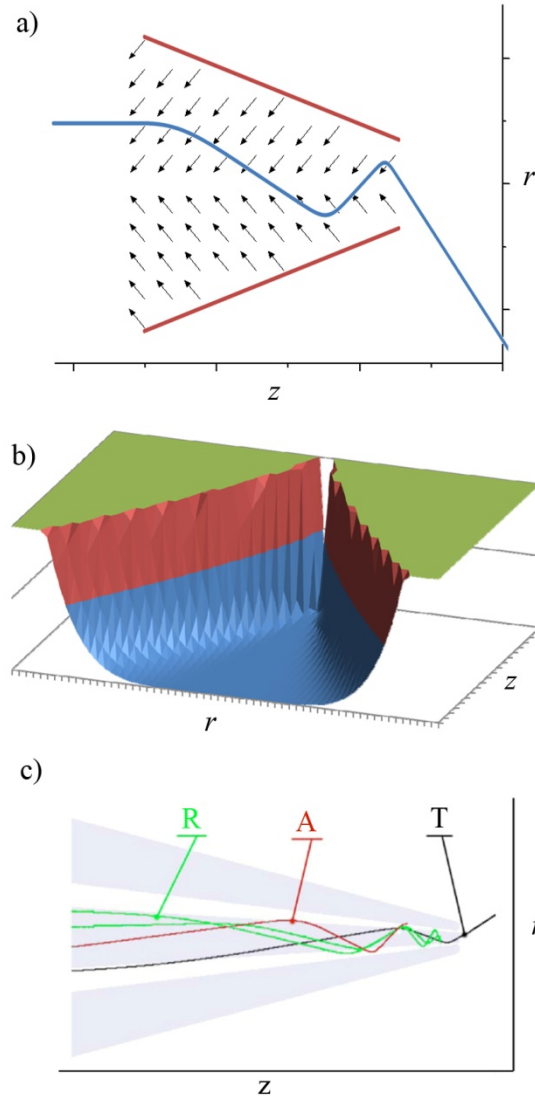


Figure 2.6. a) Illustration of field lines in a conical octopole predicted by Equation 2.20 ($V(r)$ and $V(z)$ are shown logarithmically and irrespective of each other for clarity). Red lines indicate physical poles, blue line indicates hypothetical ion trajectory (left to right). Note the wide exit angle. b) Three-dimensional depiction of the same field lines, for clarity. One can imagine the difficulty in rolling a marble through the slit at the end, and how large initial velocities would be required. c) Possible conical octopole ion trajectories in a vacuum environment: R) reflected, A) absorbed, and T) transmitted. (c) Adapted from Reference 67.

Ideally one would expect the above information to provide an answer to the primary question when designing a conical octopole: What are the best parameters to use for maximizing ion

transmission? The difficulty in answering this question should be obvious, given the complexity of the equations. In a traditional linear octopole, ions of varying mass are the only serious variable to consider (assuming average r_0 and x,y vectors are small), and can be compensated for by varying V_0 . In a conical octopole, one must seriously consider the initial vector of the ion, the mass of the ion, and the angle of the poles. Assuming an average initial velocity is known for a system, the ideal angle of the poles can be calculated, since the mass of the ion can be compensated for by varying V_0 just as in a linear octopole. This approach is described to some extent Heiz's work,⁶⁷ where it is described that an ion can either crash out, reverse direction, or travel through the optic, depending on initial parameters (Figure 2.6.c). Of specific importance here is the fact that 1) the ions are effectively travelling uphill, and therefore become less focused as they exit the optic, leading to a wide exit angle, and 2) the ions require a high initial velocity, especially towards the outside of the optic, which is impossible when exiting a temperature-controlled laminar flow tube. This is where similarities between the conical octopole developed by Heiz and that which is described herein cease.

The purpose of Heiz's conical octopole is to focus ions onto a surface for soft-landing vacuum deposition. The disadvantage of his design is that the optic does not focus well over appreciable distances, due to the wide exit angle, and subsequently the exit velocities are not well defined. His solution is to allow the ions barely enough energy to travel through the optic, and to place the surface as close to the exit of the octopole as possible. In a similar situation one could also utilize an einzel lens stack (see §2.4.a), which is a simple, well-defined method of focusing ions and can produce near-zero exit energies for soft-landing studies. The purpose of our design is to focus ions from a large-radius laminar flow tube through an aperture into a high vacuum mass spectrometer. This introduces one important variable: laminar flow. Collisions between the backing gas and the ions create a net force in the z -direction that modifies our equation above:

$$\nabla V'(r, z) = \left(\beta \left[\frac{6r^5}{z^8} + \frac{4r^7}{z^{10}} \right], \beta \left[\frac{r^6}{8z^9} + \frac{r^8}{20z^{11}} \right] + F_z \right); \beta = \frac{4q^2}{m\Omega^2} \frac{V_0^2}{\tan^8 \theta} \quad (2.21)$$

where F_z is from Equation 2.10. This of course assumes perfect elastic collisions between the ion and the carrier gas. With a sufficiently high gas flow, this provides us with a vector field considerably different from the one derived from a conical octopole in vacuum (Figure 2.7) and would appear to behave much more like a funnel.

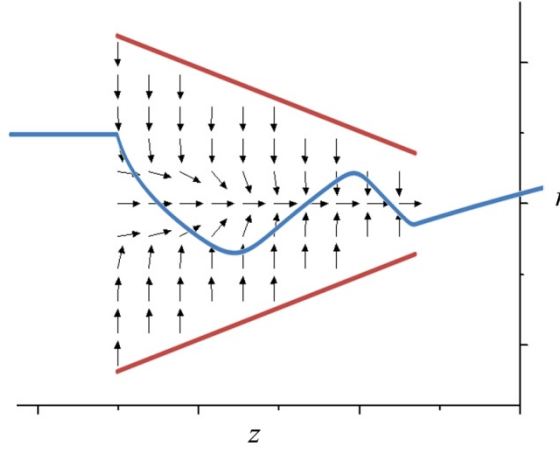


Figure 2.7. Illustration of field lines in a conical octopole predicted by Equation 2.21, where a laminar flow backing gas is present ($V(r)$ and $V(z)$ are shown logarithmically and irrespective of each other for clarity). Note the funnel shape in the z -direction.

The most important advantage here is that, with a net force in the positive z -direction, initial ion momentum plays far less of a role, and thus the system is much more forgiving over varying values of V_0 . In fact, since ions will experience the greatest amount of influence in the r -direction towards the outside of the pole where z -direction push is smallest, ions are able to relax towards the center of the pole where successful transmission is more favorable, and this in turn produces an effect of a focused ion output (and lower exit angle). In a vacuum, where there is an opposing force in the z -direction, this effect does not occur.

When all of the assumptions that have led to this point are considered (and if we assume the carrier gas, which is typically noble, behaves like an ideal gas), it is theoretically possible to calculate the transmission of an ion of defined mass and charge with initial velocity and radius

equal to v_z and r , respectively and backing mass flow rate $Q \cdot \rho_L$ for a defined conical octopole. Thus, we arrive at the true disadvantage of the conical octopole. Changes in ∇V^* and F_z will affect the successful transmission of an ion for a given V_0 to different extents. Because the backing gas is paramount to the successful transmission of ions due to momentum transfer in the z -direction, the mass range of a strictly defined system will no longer be entirely dependent on η . Lower values of V_0 will not allow heavier ions to focus correctly, and will lead to their crashing into the optic. Ultimately this will yield the desire to maximize V_0 , which in turn will increase the filtered masses of the optic. Usually, however, V_0 will reach a limit as the high voltage triggers a self-sustaining plasma to form in and around the optic, effectively destroying all ion signal. The voltage at which this plasma forms can be estimated by Paschen's law and is dependent on P_L and R_L (the radius of the octopole at its far end, which for optimal focusing should be as small as possible).⁷⁰ Paschen's law, named after the German physicist Friedrich Paschen who developed it in 1889, allows one to predict the breakdown voltage of a particular system (distance, pressure, gas, and electrode material), which is when a plasma will spark. At the pressures and practical distances of the end of a conical octopole in a laminar flow tube, helium will always have a higher breakdown voltage than argon. This further complicates the design, as argon is used in the MagGAS but not the LaVa source (the astute reader may have noticed that all of the reasons for using helium rather than less-costly argon in a LaVa source are discredited by the use of a laminar flow tube; however, in this system helium is used specifically to prevent the formation of a plasma in the conical octopole). Additionally, tuning the MagGAS causes a change in the source pressure, and therefore changes the flow. Therefore, the use of a conical octopole in a laminar flow tube in conjunction with a MagGAS is difficult at best.

Although the conical octopole has a large disadvantage in its sensitivity to variations in flow, it has the following advantages: it is reliable, not susceptible to charging, easy to clean, and operates well at relatively high pressures (~ 1 Torr). The single greatest advantage, however, is its

ability to funnel ions in a consistent manner, as opposed to the ion funnel, which relies on Brownian-type motion to transport ions across the optic (recent advances have improved this aspect of ion funnels with a DC potential gradient).⁶⁸ With this advantage it is possible to utilize a conical octopole in systems which rely on consistent motion in the z -direction, such as ion mobility spectrometry. In fact, the greatest disadvantage of the optic is its sensitivity to variations in flow, and in a consistent laboratory setup this is not an issue. For readers interested in the design and construction of a conical octopole, the author recommends the following steps: 1) Identify or define the parameters of a laminar flow tube; 2) Use these parameters to determine a minimum value for r_L and maximum value for V_0 ; 3) Using mathematical analysis software, define all other variables but m , r_0 , and θ in order to determine which value of θ gives the highest ion transmission rate over a desirable mass range (several values for Ω can also be used, but typically the highest practical frequency is chosen); 4) Use this value to calculate the final size and shape of the optic.

4. Differential Pumping

The state-of-the-art vacuum instrument utilized for much of the research in this dissertation is a dual-purpose instrument. It was specifically designed to allow the continuation of past gas-phase temperature-controlled metal cluster reactivity while concurrently beginning a series of deposition experiments where clusters are deposited and examined both on a surface and in a matrix of a frozen inert species. These deposition experiments (see §2.6) require lower pressures than standard gas-phase research due to the necessary elimination of contaminants. For this reason, some of the experimental aspects pertaining to the gas-phase research seem overly complicated and even detrimental to maximum reactant/product signal sampling. The primary example of this exists in the differential pumping of several chambers after the reaction vessel,

where a level of vacuum is reached that is unwarranted for the experiment performed. Because of this excessive pumping and the requisite ion optics that must be used to transport the ions from the reaction vessel to the detector at the far end, the state-of-the-art quadrupole mass spectrometer and channeltron electron multiplier are severely limited in their end results (due to the fact that no ion optic is 100% transmissive, and so some signal intensity is lost for each unnecessary optic used). It can be confidently said, however, that the resolution and intensity of this instrument, using the same laser, LaVa source, and laminar flow tube as were used in several past studies, has improved by several orders of magnitude due to the modern quadrupole and associated electronics, even with the addition of these new optics.

a. Ion Optics and Vacuum Pumps

Full details regarding the origin of the ion optics and vacuum pumps, which were predominantly acquired from Extrel Core Mass Spectrometers, LLC and Pfeiffer Vacuum, GmbH, are provided in Appendix A. Detailed descriptions of the science and techniques behind differential pumping can be found elsewhere,^{37,71} as well as the science and applications behind electrostatic lenses and RF multipoles.^{60,71} This section exists, then, only as a philosophical treatment of the use of these lenses, as the author feels their use is slipping steadily further into the realm of “black box” instrumentation, where the user does not fully understand the design and function of an instrument or technique. It can be seen in Figure 2.1 that the various electrostatic lenses are colored differently. This is to illustrate this point: electrostatic lenses have a purpose, and that purpose is to guide an expanding ion beam further down the instrument with minimal losses due to collisions with the lenses themselves or deflections out into the walls of the chamber. Extensive electrostatic lens use, such as in this example, exists because of the single most important requirement of a differential pumping system: large flange sizes to maximize

conductance into the pumps and small orifices to reduce gas flow into the lower pressure regions. By successfully directing a large percentage of the original ion beam through the small orifices it is therefore possible to maximize ion intensity at the end while minimizing residual gas pressure. It is therefore important to realize that there are ways of maximizing this transmission percentage, and that the lenses used in the present system were chosen carefully, not arbitrarily, and that their functionality should be fully understood by every user. Lens settings will change on a day-to-day basis depending on a large number of variables, most of which are indeterminable, and so blindly tuning the ion optics to maximize signal on any given day is dangerous as it could slowly lead to a poorly tuned system that is difficult to fix. However, if one understands the purpose of each optic, one can resist the urge to simply maximize signal intensity on any given day and instead focus on the long-term reliability of a vacuum instrument. Careful maintenance of lens settings includes not the constant improvement of signal, but rather the desire to reduce the potential on each lens to as near ground as possible. This reduces the kinetic energy of the ions in the system and subsequently encourages a much more stable beam path that is forgiving to day-to-day fluctuations in many variables. Such mentality has produced a custom-built vacuum instrument that is more reliable than any other that this author has seen.

The ion optics used here as seen in Figure 2.1 can be separated into five groups: 1) single lenses/orifices, 2) einzel stacks, 3) RF octopoles, 4) a quadrupole energy deflection filter, and 5) a quadrupole mass spectrometer. After exiting the conical octopole, the ions are rather sharply focused and will quickly pass their focal length and begin to rapidly expand. It is therefore necessary to quickly collimate the beam. This is accomplished with a combination orifice and shield, which are the first two blue lenses in Figure 2.1. The orifice/shield combination is a well-characterized system wherein the orifice is allowed an attractive charge which serves to reduce the angle of the ion beam. This attractive charge would also cause the loss of much of the outer limits of the ion beam, however, and so a lens with a shielding charge is used to prevent the

attractive charge from penetrating out past the immediate front of the optic. This shielding charge can be zero or repulsive, and effectively creates a potential funnel wherein the ions are directed through the orifice, which also serves to deflect the large amounts of helium carrier gas exiting the flow tube. The beam is then somewhat collimated, but not sufficiently enough to satisfy the strict entrance angle requirements of the upcoming octopole, and so further lenses are necessary. An einzel stack, colored green in Figure 2.1, is a popular method for focusing a somewhat collimated ion beam. The advantage of an einzel stack is that typically the first and third lenses are kept at the same potential, which reduces the number of power supplies required as they can be easily connected. When one of the two potentials used is locked at ground, this further reduces the power supply requirements to one for each stack. The first einzel stack has the ability to place a separate potential on each of the three lenses, but nevertheless should be considered and treated as a focusing einzel stack. The isolated fourth (brown) lens in the series serves to commit a final defocusing potential, which finally collimates the beam. Once the beam is collimated, it is then transported through an RF octopole. The reason for using an octopole rather than more electrostatic lenses is simple: a properly functioning octopole can be considered as a single, flat lens. It can be shown using multipole theory that an ion beam successfully entering and exiting an octopole of a given pole bias will have similar entrance and exit angles as a single electrostatic lens. Because the ions must cover a distance large enough to incorporate a vacuum pump, the best way to guide them along such a distance is with an RF octopole, even though the electronics required to power the octopole seem much more complicated than a simple high voltage power supply. After exiting the octopole, the ions travel through a second orifice and a second octopole. Single lenses at the front and back of each thick optic ensure the minimization of the beam spread, and a potential can also be applied to the orifice. After exiting the final octopole, the ions are focused again using another einzel stack into a quadrupole deflector energy filter, colloquially known as a “quad bender” (despite the similarity in name, the quad bender bears no similarities to

a RF quadrupole and in fact is electrostatic; the name applies only to the four-poled electrostatic field it creates). Initially developed in order to fan an ion beam of varying kinetic energies, often today it is simply used as a means to achieve a ninety degree turn in a series of ion optics, and this is precisely its purpose here. Although the first orifice effectively eliminates all ions of the oppositely desired charge; it in no way removes neutrals, either in the form of the carrier gas, the reactant, or neutral clusters. The quad bender effectively eliminates these neutral species as the desired ions are turned. However, because the packet of ions is of varying mass but similar speed, heavier ions will curve slower than lighter ones and thus the preliminary focusing by the einzel stack is necessary to prevent the clipping of the upper and lower masses. The final step is a quadrupole mass spectrometer, which allows for mass selection for final analysis of gas-phase reactivity results or for single species deposition (see §2.6). However, in order to place a surface in the path of the mass selected ion beam for deposition, a larger than usual space must exist between the quadrupole and the detector. Therefore, a final einzel stack must be employed to focus the ion beam across the distance and into the detector or onto the surface. One final important topic remains: the impact velocity, covered in §2.6, is very important. Clusters can pick up tremendous amounts of kinetic energy while traveling through these systems, and this can easily lead to their destruction upon impact with a surface. However, it can be shown that a series of ion optics, just like those of light optics, can be treated as “thick lenses” wherein they are summarized as a single lens. It can also be shown that the kinetic energy of an ion entering and exiting an einzel stack where the initial and final potentials are zero will maintain its original energy. Therefore, one can assume that if the first and last optic of this extensive ion optic system is grounded, then the ions will exit the system with the same energy as they entered (the reader is also reminded of the fact that every optic should have as little a potential on it as possible to encourage stability and reliability). This is easily controlled here, and therefore the ions exiting the system have the same kinetic energy as they did in the flow tube, which is easily calculated

using the average speed of the flow tube. Specifically, soft-landing molecules requires less than 1 eV per atom. Typical flow tube conditions yield approximately 0.1 eV of kinetic energy, suggesting that the combination of a laminar flow tube with vacuum deposition is a viable way to safely soft-land clusters. There is one final consideration that the author would like to make: nowhere in this description of the instrument has it been suggested that the system is limited to the study of cations or anions. It is trivial to realize that both will work equally well in this experimental setup, although every system studied in this dissertation has composed of anionic species.

5. Detection Methods

The clusters exiting the quadrupole mass spectrometer are focused to a point where their attraction onto the dynode of a channeltron electron multiplier is maximized (Figure 2.1.g). The setup used is very traditional, and so can be easily referenced here.^{37,72} However, there are many instances where it is necessary to measure the ion current before this point. First and foremost, on the rare occasion that a malfunction requires the disassembly of any part of the instrument, there is always a large risk that tiny changes will require a full re-tuning of the optics. This must be performed in steps, as there will likely be no detectable ion signal at the channeltron electron multiplier. It is very easy to detect the amount of ions striking an electronically isolated metal surface (i.e. a Faraday plate), and each of the ion optics can be used as such. Unfortunately, the amount of current created by ions striking these optics, even if an attractive potential is placed on them, is entirely too small for a standard ammeter to read (typically on the order 10^{-9} to 10^{-12} amps; $1\text{ A} \approx 6.24 \times 10^{18}$ ions per second). Therefore, a highly sensitive picoammeter is employed (Kiethley 6487). A simple LabVIEW program allows the user to slowly move down the line of optics, adjusting the earlier lenses each time to re-tune the system. Once the optics are tuned to

such an extent as signal is detected at the multiplier, then it may be used to finish the process. The picoammeter can also be used to test cluster deposition, where the ions striking an isolated metal disc of appropriate diameter indicate the amount of cluster being deposited, and a biased repulsive potential can indicate the kinetic energy of the ions, as the Coulombic potential reaches a point where the ions are just deflected away from the surface rather than reaching it. Finally, on several of the earlier lenses before a well-collimated ion beam is achieved, there is some loss around the inside edge of the lens. The biased picoammeter behaves just as a lens would; however it also reads the current of crashed ions, and if the ratio of crashed ion current to final deposition current is known, the amount of ions deposited over a period of time can be very accurately estimated (a necessary action, as the intensity of the cluster sources presented above have some tendency to fluctuate over time). Therefore, the picoammeter is a very valuable tool in the laboratory.

6. Deposition Methods and Considerations

In Chapter 5 we discuss the deposition of Al_{17}^- on a self-assembled monolayer (SAM). The importance of the cluster/surface pair chosen for deposition is covered in detail there, but the broad experimental methodologies regarding the deposition and subsequent analysis are appropriately outlined here. Specifically, details are given with regard to the difficulties inherent in depositing clusters onto a surface, and what evidence these studies have produced which suggest that the deposited clusters are stable.

a. Vacuum Suitcase

For many years, modular vacuum transfer systems have been utilized for the safe transport and manipulation of air-sensitive samples between ultra high vacuum systems.⁷³⁻⁷⁶ The rationale required for controlling sample transfer between analysis chambers varies, but typically involves the limitations imposed by both the immobility and the pre-existence of one or more desired vacuum apparatuses for various surface science studies. Although containing several major differences, most vacuum transfer systems share three requirements: 1) a volume-minimized steel chamber with stand-alone pumping capabilities; 2) an interlock system for maintaining vacuum after removal of the transfer device; and 3) a mechanism for moving the sample into and out of the transfer device. With the exception of these three parameters, other design constraints (e.g. chamber size, flange diameter, transfer arm stroke, etc.) often result in their specificity for a particular technique, experiment, or system.

The deposition of clusters on a self-assembled monolayer required the design and implementation of a versatile vacuum suitcase for use in transporting air-sensitive samples between two vacuum instruments: the cluster instrument discussed throughout this chapter (Figure 2.1) and a scanning tunneling microscope used to image the deposited clusters. This system is easily adaptable to a wide variety of applications involving sample preparation and analyses where two or more of the procedural steps occur in separate vacuum chambers. The advantages of our system include portability, the stability with which the sample is transferred into the final vacuum chamber, and the ease of adaptability of this transfer device to other vacuum systems.

The vacuum suitcase is shown in Figure 2.8. The construction of the vacuum suitcase interlock enables rough evacuation of the space between the apparatus and the suitcase via a bellows valve, and thus it is not necessary to vent either in order to connect the two.

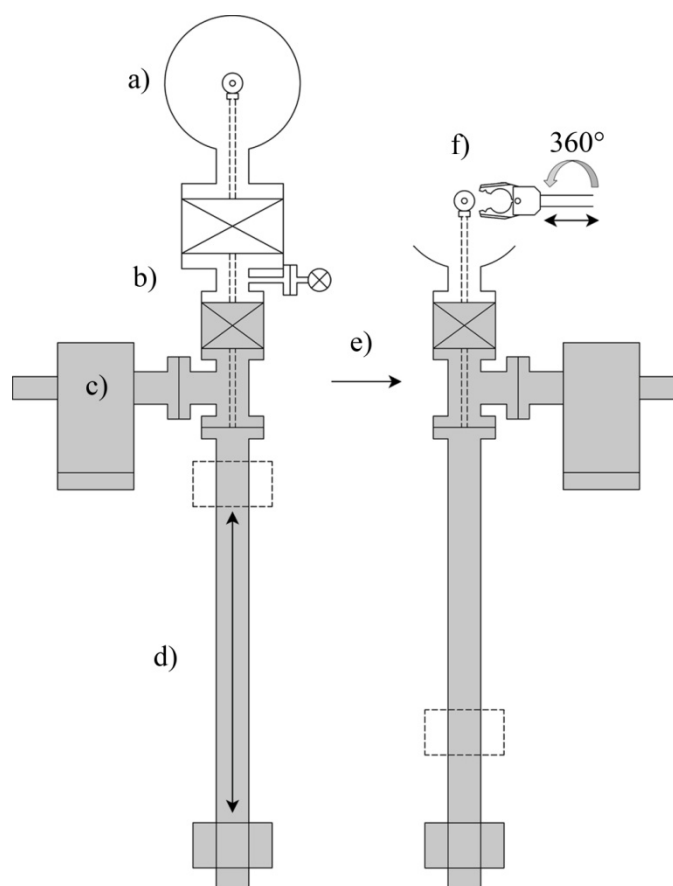


Figure 2.8. Diagram of the custom-built vacuum suitcase (to scale). a) The air-sensitive sample is prepared in a sample holder that is attached to the linear translator of the suitcase via a fixed screw thread. b) The suitcase is attached to the vacuum instrument via two gate valves, with a vent that enables both initial evacuation of the suitcase volume and, following deposition, venting of the small chamber between the instrument and the suitcase. c) Vacuum inside the chamber is maintained by a battery-powered ion pump (controller not shown). d) After sample preparation, the holder is linearly translated into the suitcase where the gate valve can be closed and e) the entire suitcase can be detached and transported. f) Once the suitcase is connected to the next vacuum apparatus, the sample can be securely removed by a wobble stick with modified jaws.

The sample holder is affixed to a magnetically coupled rotary-linear translator (Figure 2.8.d) via a threaded rod that engages a tapped hole on the outer perimeter of the sample holder. Following sample preparation, the sample holder is lowered into the suitcase. After locking the linear translator in place with two shaft collars, both gate valves separating the suitcase from the deposition instrument were closed and the small load-lock region between the suitcase and vacuum instrument is vented through a bellows valve (Figure 2.8.b). The ion pump (Figure 2.8.c) is controlled by a battery-powered portable controller assembled inside of a water-resistant

“suitcase.” The suitcase is attached to the ion pump by a long enough cable to allow a single person to carry both comfortably.

Once the suitcase is attached to the load-lock of the second vacuum instrument, the load-lock chamber is evacuated. To minimize atmospheric contamination, dry nitrogen is leaked into the load-lock before the pressures are fully equilibrated. In order to remove and to transfer the sample holder, a rotary pincer wobble stick is locked onto the sample holder while the magnetic translator is rotated (Figure 2.8.f). As shown in Figure 2.9, grooves were cut in the wobble stick jaws to ensure that the sample holder is grasped firmly and that the claw can fit around the threaded end of the translator. This modification was made on a machining mill and provided a simple means of modifying the claw. Once the rotary-linear translator is rotated to unscrew the sample holder from the vacuum suitcase, it is secure in all three axes and the sample cannot be released without opening the jaws. It can then be safely maneuvered inside the chamber for further treatment. Replacement of the sample holder onto the linear translator of the suitcase is less straightforward, but possible. Three tapped holes spaced apart by 120° around the circumference of the sample holder facilitate the alignment of a tapped hole with the threaded rod.

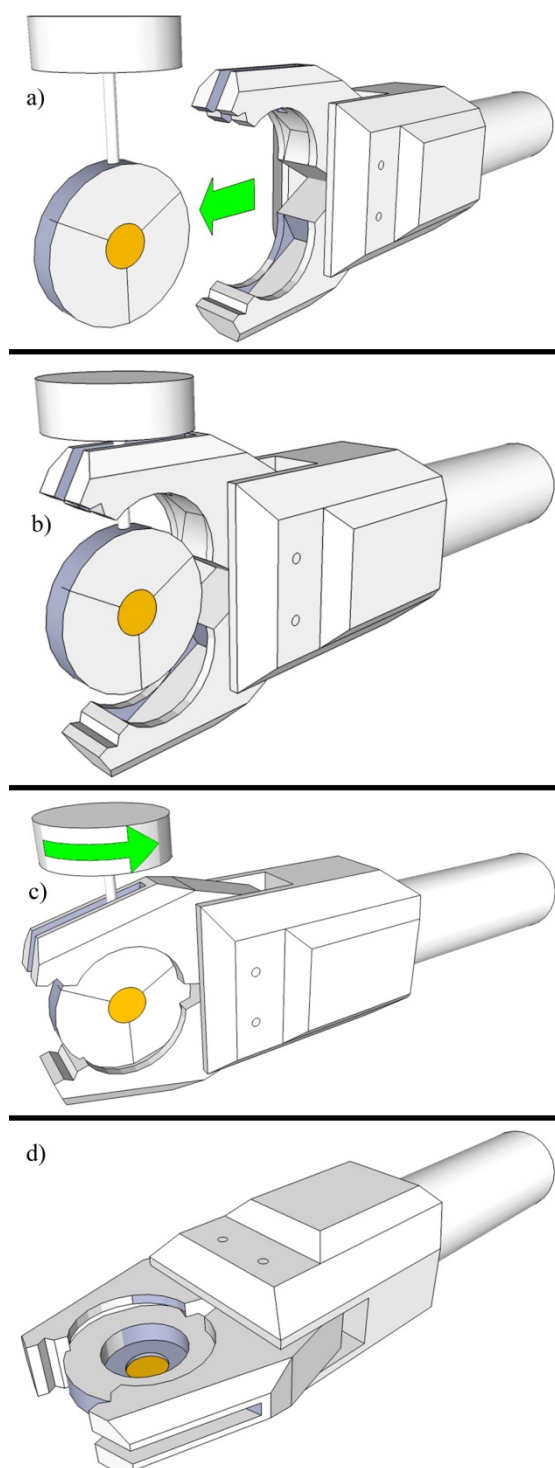


Figure 2.9. Diagram of sample transfer. a) The slot in the top jaw allows the claw to b) encompass the sample while allowing access to the tapped holes by the threaded coupling rod. c) Once the jaws are secured around the sample, the linear translator can be rotated to unscrew the thread from the sample. d) With the sample separated from the vacuum suitcase, it can be rotated and translated freely inside of the UHV chamber.

This vacuum suitcase is constructed to deposit gas-phase molecules/clusters onto a surface and to facilitate the transfer of samples between instrumentation located in distant laboratories. The necessity of a vacuum suitcase stemmed from the pre-existence of the two sophisticated instruments (in different buildings), the details of which are not pertinent to the design of the suitcase. Here, we discuss the three UHV sample transfer system commonalities mentioned earlier: the vacuum chamber, the method of suitcase-to-instrument attachment, and the transfer mechanism. The “T” shaped design of the stainless steel vacuum chamber forming the suitcase is easily constructed from off-the-shelf stainless steel flanged components and therefore enables an inexpensive and portable solution; our completed design weighs 23 kg and 13.5 kg with and without the battery-operated controller, respectively, and can be carried by a single individual or placed inside of a vehicle. In previous examples, the pump used to maintain vacuum varied among a turbomolecular pump, which requires a permanent power supply,⁷⁷ an ion pump, which requires no backing pump and may be battery operated,^{78,79} or a getter pump, which has a large advantage in that it requires no electricity once started.⁸⁰ The current embodiment employs a battery-operated ion pump, because it also functions as a pressure gauge, simplifying the overall design while minimizing size, weight, and power requirements. It has the ability to use an external power source to pump continuously, unlike the getter pump. The latter undergoes intermittent recharging in normal use, a process that may contaminate the sample.³⁷ Our system is capable of maintaining a vacuum of $< 1 \times 10^{-7}$ Torr for a 48 hr period under battery power, and indefinitely while an electrical connection is provided.

In addition to the pumping mechanism and overall shape, the reported methods of coupling the suitcase to each vacuum instrument vary. The most commonly used method is a gate valve; however, other options are available that utilize all-metal valves in order to maintain minimal pressures throughout the transfer.⁷⁹ When considering the components necessary to maintain vacuum conditions for an extended period of time, we determined that a standard gate

valve with a Viton o-ring carriage assembly would maintain a pressure of $< 1 \times 10^{-7}$ Torr without the need for a baking cycle.³⁷ Transfer of the sample into and out of the suitcase is accomplished with a linear translator, and in at least one example the translator is detached to minimize the size of the transfer device.⁸¹ For our purposes, this additional step was not necessary, since our final design was already sufficiently compact (approximately 75 cm \times 30 cm \times 30 cm) without the ion gauge controller, and was capable of maintaining acceptable pressures. If considering this alternative, it is important to consider the pumping requirements of both options, which will vary depending on the targeted pressure, the internal surface area of the translator, the permeation rate increase that may occur upon adding a second Viton-sealing gate valve, and whether a bake-out process will be utilized. In order to reduce the length and weight of the vacuum suitcase, the linear translator was custom built to enable a maximum travel distance of 33 cm, although it is noted that costs can be reduced by using an off-the-shelf translator with a linear travel distance greater than or equal to their minimum requirement.

The significant advantage of this design is in its ability to transfer samples to and from the vacuum suitcase. While not detailed in previous publications on vacuum suitcases, separating the sample from the transfer device is a key requirement when adapting an existing analytical instrument. Our technique introduces an inexpensive means of modifying an off-the-shelf wobble stick for reliable, controlled sample transfers. This modification can be made to accommodate a large range of sample holder sizes. The only limitation of the current instrumentation is that two flanges be available near each other in the instrument; this is a common feature on load-lock chambers present on many vacuum instruments used in surface studies. Additionally, since the sample holder is attached to the suitcase only through a threaded rod, it is possible to isolate the sample electronically by constructing a sample holder and/or rod of insulating materials. The electrically isolated sample then can be wired to a feedthrough in the wall of the vacuum suitcase. This technique was shown to be very useful in our laboratory for the optimization of our sample

preparation technique. Two limitations imposed by this design are the inability to maintain the sample at cryogenic temperatures⁸² and the inability to transfer more than one sample at a time.⁷⁸ However, these limitations did not impact our specific experimental requirements. In summary, this design has the advantages of being both versatile and reliable. While our specific application involved surface studies of deposited species, this design could be modified easily for a large number of applications with minimal engineering time and cost.

b. Cluster Deposition

As discussed in §2.4.a, extensive differential pumping allows the pressure in the end chamber to reach 1×10^{-8} Torr, while the experiment is being performed at a gas pressure of about 1 Torr. These pressures can be attributed predominantly to the He carrier gas, and thus the chance of undesirable depositions or additional reactions with deposited clusters is minimized. Lenses are tuned to maximize the desired cluster's signal, at which point the quadrupole settings are adjusted to filter all other ions. It is important to note that the initially thermal clusters maintain an effective birth potential of < 1 eV, and the initial and final electrostatic lenses have no applied potential, thus allowing the entire system to emulate a large unipotential lens.⁷¹ It has been reported that deposition energies above 1 eV per atom leads to destructive landings (e.g. fragmentation, deformation, implantation, etc.), and so this ensured deposition energies similar to other soft-landing techniques.^{83,84}

With the vacuum suitcase attached to the deposition instrument, the sample can be moved into and out of the path of the ion beam. As detailed above, construction of the vacuum suitcase interlock enables it to be put under vacuum via a bellows valve so that it is not necessary to vent the entire deposition apparatus. The detector is positioned 8 cm from the last lens so that the deposition surface has sufficient clearance. In order to optimize the focus of the final einzel lens

stack, a provisional sample was constructed with an electronically floating surface that could be connected to a bias-able picoammeter (§2.5); however it was found that by optimizing signal with the detector, the radius of the ion beam at the sample was nearly ideal. Immediately following deposition, the sample is lowered into the vacuum suitcase and transported under battery power to the scanning tunneling microscope chamber. The total time required to transfer the sample is approximately 3 hrs.

Simply depositing the clusters onto any surface for study, however, is not feasible. It was suggested in Chapter 1 that select clusters with jellium shell closings are inert, but it has been alluded throughout this chapter that “inert” is not a particularly accurate adjective to use. While it is true that, in the gas-phase, these “magic” clusters exhibit extraordinary stability over large periods of time, they still have free-electron properties that will cause them to dissociate in the presence of a metallic surface. As an example, theoretical studies have shown that metal clusters deposited on a metal surface with *zero* kinetic energy (0 eV, 0 K) may still dissociate as soon as they land (Figure 2.10).⁸⁵ Other theoretical studies have shown, not surprisingly, that at greater-than-zero energies, clusters will distort upon landing.⁸⁶ Once successfully soft landed onto a surface, clusters have been shown to diffuse until they bind to defect sites, step edges, or reactive sites. Depending on their abundance, these clusters can then agglomerate into large islands that, due to the strongly size-dependent properties of smaller clusters, no longer exhibit their original properties.⁸⁷

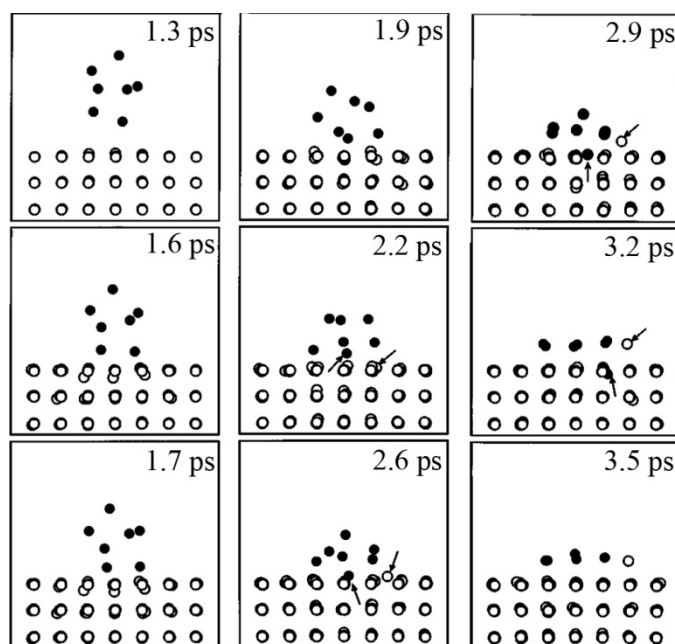


Figure 2.10. Theoretical deposition of Ag_7 cluster onto a $\text{Pd}(100)$ surface at 0 eV and 0 K. Filled circles represent Ag atoms and hollow circles represent Pd atoms. Arrows are used to identify when atoms undergo a site exchange. Adapted from Reference 85.

To be sure, there are a number of published examples of deposited cluster systems that display characteristics so interesting that they have prompted the growth of an entire sub-field of cluster science involving clusters on diverse surfaces, including metals, metal oxides, graphite, and silicon.^{74,83,88-100} However, it should be acknowledged that in most examples the electronic and geometric structures of the deposited metal clusters were found to be notably different than the same clusters in the gas-phase, with few exceptions.^{74,90,101,102} Clusters can also be grown on a surface using controlled defect sites,¹⁰³ although this will likely lead to a size distribution instead of cluster sizes with an exact number of atoms, which is not optimal for size-specific cluster reactivity. Therefore, in order to utilize the unique properties of specific small metal clusters on surfaces, they must either be deposited such that their structure on the surface leads to desired properties and characterized *ex post*,^{104,105} or they must selectively react with the surface in a manner predicted using gas-phase reactivity studies. The latter is precisely what was attempted here, where clusters were deposited onto a SAM in order for them to selectively and

instantaneously bond to the surface, thus preserving their gas-phase properties. Similar studies have been performed with the soft landing of organic molecules on SAMs,^{106,107} the deposition of pre-tethered assemblies onto a surface,¹⁰⁸ and even of peptide ions onto SAMs.¹⁰⁹ In the latter case, the ions not only bind as predicted, but they also retain their charge. This is important here, as only ionic clusters can be selectively deposited. However, no study has ever been performed where fragile, metallic clusters are bound to the SAM in a predictable manner.

c. Self-Assembled Monolayers

Self-assembled monolayers have become widely used in chemistry and require only a brief discussion here, being easily cited and not the focus of this dissertation.^{110,111} The invention of the self-assembled monolayer is largely credited to William Zisman at the Naval Research Laboratory in 1946,¹¹² although the now-common thiol-on-gold SAM morphology (the one used in this study) was pioneered in 1983 by Ralph Nuzzo and David Allara, then at Bell laboratories.¹¹³ Basic structure of a SAM, in the present context, involves a hydrocarbon chain “backbone” with a terminal functional “headgroup” that has a specific affinity towards a substrate. The spontaneous adsorption of the chains onto the surface creates an ordered layer over time, due to the affinity of the headgroup to the substrate being strong enough to overcome the initial disorder or the randomly splayed backbones. Given enough time, a uniform monolayer of neatly ordered chains develops (Figure 2.11). When a terminal functional “endgroup” is added to the opposite side of the molecule, the surface can take on the characteristics of that functional group. In this dissertation, eleven-carbon chains with thiol headgroups and hydroxyl endgroups were utilized to predictably bond clusters to the SAM using cluster-hydroxyl group reactivity previously characterized in the gas-phase. These clusters were then imaged using scanning tunneling microscopy. The reasons for the development of this technique are covered in detail in

Chapter 5, although the inherent difficulty of depositing clusters onto surfaces (and hence the necessity for the SAM) was discussed in §2.6.b.

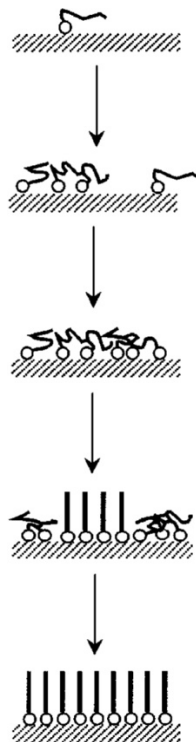


Figure 2.11. Example of liquid-phase self-assembled monolayer construction. Two-dimensional organization is promoted by the strong adsorption of the “headgroups” to the substrate. Adapted from Reference 111.

7. Scanning-Tunneling Microscopy/Spectroscopy

The use of scanning tunneling microscopy (STM) and scanning tunneling spectroscopy (STS) was made possible via collaborations with the research group of Paul Weiss, now at the University of California, Los Angeles. Because the design and implementation of this instrumentation was not a result of the author’s intellectual pursuits, it is not covered in any detail here, although the best effort has been made to include every reference necessary for an interested reader to pursue all additional details. Scanning tunneling microscopy was invented by Gerd Binnig and Heinrich Rohrer at IBM in Zürich in 1982,^{114,115} a discovery which was to earn them

the Nobel Prize in 1986. The basic idea behind STM is that a charged electronic probe, held a specific distance from a conducting surface, will transfer electrons through the interface and through the surface. This interface can arguably consist of any material (or no material, i.e. vacuum) and can be of any thickness, but the rate of electron transfer (current) will be directly related to its conductivity (resistance) and the potential placed on the probe tip (electromotive force). This is exactly the same as Ohm's law, which is named after the German physicist Georg Ohm. In the case of high vacuum STM, such as is utilized here, the vacuum interface classically allows no electron transfer, and so all current is a result of quantum tunneling through the void. This tunneling is quite sparse ($\sim 10^{10} \Omega$), and so only a minor current is observed. When piezoelectric translators are employed, the tip can be moved across the surface and raised up and down (in actuality the surface sample holder is being moved, but this description is harder to picture). When a computer is used to maintain a constant resistance between the surface and the tip as the probe is scanned across the surface, the distance between the tip and the surface exactly mimics the topography of the electron density of the surface, and thus an image is obtained (Figure 2.12). One additional consideration is that lower temperatures will inherently yield stable surfaces with less noise, diffusion, etc., and so it is common for STM setups to utilize a liquid helium cryostat, which can reach temperatures below 4K. To be sure, this is quite a simplified description of STM, covering only the broad details pertinent to this dissertation, but comprehensive accounts are readily available and easily referenced here.^{116,117}

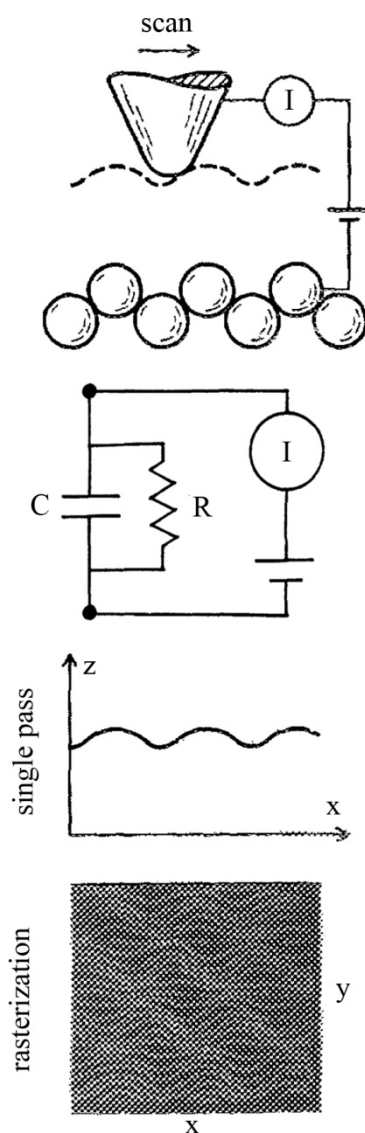


Figure 2.12. Illustration of constant-current STM imaging with a basic circuit diagram representation. As the tip is scanned across the conductive surface it is raised or lowered by a computer to maintain a constant current through the interface. This procedure can be used to rasterize across a 2-D surface, thus producing an image of the electronic density of the surface. Cartoon and graphs adapted from Reference 118. Circuit diagram adapted from Reference 119.

The development of STS almost immediately followed STM. Using the same conceptual tunneling mechanism, it is possible to imagine that, as the electromotive force is adjusted and the tip height is held, the electrons will tunnel into different “bands” of the solid surface. In this manner it is possible to explore the local density of electronic states of a conductor or semiconductor, and the band gap of a solid can be determined.¹¹⁷ This method was expanded

when it was realized that an isolated molecule between two insulating media would create a “double-barrier tunnel junction” (Figure 2.13.a).¹¹⁹ This situation would allow the investigation of the electronic energy levels of the molecule, both occupied and unoccupied, via single-electron tunneling. In 2006, Paul Weiss at the Pennsylvania State University used this method to examine the energy levels of ligand-stabilized Au₁₁ clusters on a SAM (Figure 2.13.b),¹²⁰ wherein the molecule is isolated by the vacuum between itself and the tip and the insulating hydrocarbon SAM. The observed “region of zero conductance” was evidence that the gold clusters retained their metallic nature, yet still exhibited molecular energy levels.

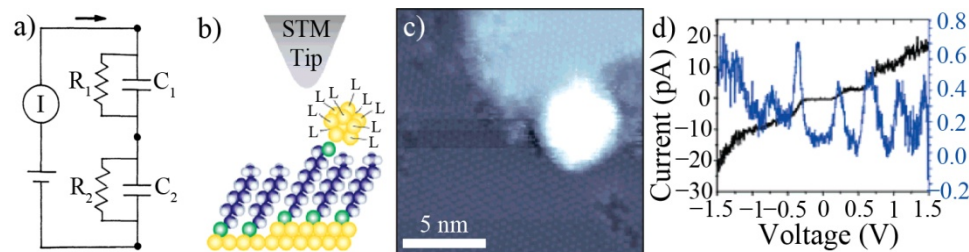


Figure 2.13. a) Representative circuit diagram of a double barrier tunnel junction. b) Illustration of a cluster on a self-assembled monolayer. c) Actual scanning tunneling microscopy image of cluster. d) Scanning tunneling spectroscopy data for metallic cluster, where the double barrier tunnel junction can be seen. The current versus voltage graph (black) shows step-edges where additional electronic levels are tunneled to and from, and the derivative of this (indigo) produces a spectrum similar to that of absorption spectroscopy. Although not shown here, a current versus voltage graph of a single tunnel junction would imitate a sloped line as predicted by Ohm’s law. (a) is adapted from Reference 119; (b), (c), and (d) are adapted from Reference 120.

This method was also utilized by Peter Lievens at the Katholieke Universiteit Leuven to examine larger gold nanoparticles (average diameter of 2 nm; ~250 atoms),¹⁰¹ and it was confirmed that small metal particles allow single-electron tunneling and exhibit a double-barrier tunnel junction. In a later example with slightly larger nanoparticles (~350 atoms), the deposited species appeared to settle into the SAM and agglomerate onto the underlying gold surface, creating hills on the otherwise flat SAM surface.¹²¹ While these studies will prove quite important for comparison purposes in the characterization of aluminum clusters deposited on a SAM, the author would like to point out that in none of these situations are clusters predictably bonded to a surface, and that the work presented in this dissertation is unique in that respect.

The custom-built, ultrastable, extreme high vacuum cryogenic scanning tunneling microscope used in this study has been described in detail previously.^{122,123} Briefly, the microscope is contained within a cryogenic vacuum chamber and consists of a beetle-style design enabling a coarse approach to a field-sharpened Pt-Ir tip. Tunneling spectra were acquired simultaneously using a lock-in amplifier. Specific details of the instrumentation, currents, and voltages used are outlined, where pertinent, in Chapter 5.

8. First-Principles Density Functional Theory

The methods to be attributed to the author of this dissertation were entirely experimental, although the conclusions reached from this work were greatly improved by the addition of theoretical calculations performed by Arthur Reber and Shiv Khanna at the Virginia Commonwealth University. While the full details of the theoretical work performed are beyond the scope of this dissertation, being easily cited and not at all a result of the author's own intellectual pursuits, a summary of the methods used are necessary in order to briefly outline the origin of the results and what considerations must be taken when reading the following chapters. These include much discussion pertaining to the combination of the theoretical and experimental work, and are very much the result of the author's efforts. The theoretical studies were carried out using a first-principles molecular orbital approach within a gradient corrected density functional framework.¹²⁴ The molecular orbitals are expressed as a linear combination of atomic orbitals that were, in turn, formed via a linear combination of Gaussian functions located at the atomic sites. The exchange correlation contributions are included within the GGA-PBE gradient corrected density functional formalism.¹²⁵ The calculations were carried out, at an all-electron level, using deMon2K.¹²⁶ The basis sets used are listed in the experimental section of Chapter 3.

As described in §1.2, density functional theory is a powerful computational method for estimating the electron density of a particular molecule, and has been widely shown to reproduce experimental results with great accuracy. However, it is very important to realize how easily one can abuse this technique's impressive abilities. It must be stated immediately that theoretical calculations are not educated guesses. When Erwin Chargaff, the American biochemist, wrote "...an ounce [*sic*] of proof still weighs more than a pound of prediction,"¹²⁷ he was not referring to mathematically-based theoretical predictions. However, because of the vast complexity of the mathematics contained within these calculations, many variables can lead to results that are quite wrong. As an example, let us consider Al_4 . A quick literature search will provide no less than thirty-five lowest energy structures for this simple molecule.¹²⁸⁻¹³⁸ The obvious question—which is correct?—is controversial; although some more costly basis sets probe further into the deep electronic structure of a molecule than others, many are considered advantageous in entirely separate ways. In order to answer the question, then, one need look little farther than at an experimental study which confirms the theoretical predictions.¹³⁹ In fact, once a viable basis set is found, it can be used to predict the structures of similar molecules with reasonable confidence, and in this situation a pound of prediction is nearly worth its weight in proof.

With this example in mind, the author would like to point out that even Schrödinger was cautious when considering theoretical predictions without experimental support: "The claims of theory...are so vague, that you should instead try to adapt the relationship or weights to the data of observations..." [Die Forderungen der Theorie sind aber in diesem Punkte, wie man weiß, so ungewiß, daß lieber versucht wurde, die Gewichtsverhältnisse den Beobachtungsdaten möglichst gut anzupassen...].¹⁴⁰ However, the author would like to reiterate how important first-principles density functional theory has been to the studies presented herein and indeed to all of chemistry. The symbiotic combination of experimental results and theoretical calculations is vital to the progression of cluster science. In addition to theory providing insights as to experimental cluster

stability and reaction mechanisms, theoretical calculations often suggest structures or mechanisms that are later confirmed experimentally. The only restrictions, therefore, are when theory does not agree with experimental results, or when theoretical methods are extrapolated too far past the experimental boundaries.

Natural Philosophy, as invented by Aristotle of Stagira in the fourth century B.C., involves the use of basic, infallible axioms to deduce every aspect of the universe, and strictly speaking can be equally applied to ethics and theology as to science. This manner of “philosophy,” which literally translates to “the desire to know,” persisted for nearly two thousand years until Galileo Galilei’s methods of empirical deduction convinced the scientific community to embrace the concept of Scientific “Theory,” which literally translates to “viewing” or “beholding.” Today we live in an empirical society, where a single experimental observation can overthrow any theory, and no theoretical model is to be considered absolute or axiomatic.^{141,142} To be sure, there are many examples of theoretical cluster calculations that have yet to be confirmed or disproven experimentally, and in many cases it is this author’s hope that the former prevails (e.g. Figure 1.9). However, as this dissertation is for a doctorate of *philosophy* in a natural science, the author hopes that he has cogently expressed his thoughts regarding the importance of empiricism versus rationalism, and to point out that theory, by definition, is dependent on experiment exactly as experiment is dependent on theory in the modern laboratory.

9. References

- (1) de Heer, W. A. *Rev. Mod. Phys.* **1993**, *65*, 611-676.
- (2) Knight, W. D.; Clemenger, K.; de Heer, W. A.; Saunders, W. A.; Chou, M. Y.; Cohen, M. L. *Phys. Rev. Lett.* **1984**, *52*, 2141-2143.
- (3) Preuss, D. R.; Pace, S. A.; Gole, J. L. *J. Chem. Phys.* **1979**, *71*, 3553-3560.

- (4) de Heer, W. A.; Knight, W. D.; Chou, M. Y.; Cohen, M. L. *Solid State Physics* **1987**, *40*, 93-181.
- (5) Sattler, K.; Muhlbach, J.; Recknagel, E. *Phys. Rev. Lett.* **1980**, *45*, 821-824.
- (6) Siekmann, H. R.; Luder, C.; Faehrmann, J.; Lutz, H. O.; Meiwesbroer, K. H. *Z. Phys. D: At., Mol. Clusters* **1991**, *20*, 417-420.
- (7) Begemann, W.; Meiwesbroer, K. H.; Lutz, H. O. *Journal de Physique* **1989**, *50*, 133-139.
- (8) Haberland, H.; Karrais, M.; Mall, M.; Thurner, Y. *J. Vac. Sci. Technol., A* **1992**, *10*, 3266-3271.
- (9) Dietz, T. G.; Duncan, M. A.; Powers, D. E.; Smalley, R. E. *J. Chem. Phys.* **1981**, *74*, 6511-6512.
- (10) Powers, D. E.; Hansen, S. G.; Geusic, M. E.; Puiu, A. C.; Hopkins, J. B.; Dietz, T. G.; Duncan, M. A.; Langridgesmith, P. R. R.; Smalley, R. E. *J. Phys. Chem.* **1982**, *86*, 2556-2560.
- (11) Kroto, H. W.; Heath, J. R.; Obrien, S. C.; Curl, R. F.; Smalley, R. E. *Nature* **1985**, *318*, 162-163.
- (12) Milani, P.; de Heer, W. A. *Rev. Sci. Instrum.* **1990**, *61*, 1835-1838.
- (13) Maruyama, S.; Anderson, L. R.; Smalley, R. E. *Rev. Sci. Instrum.* **1990**, *61*, 3686-3693.
- (14) Heiz, U.; Vanolli, F.; Trento, L.; Schneider, W. D. *Rev. Sci. Instrum.* **1997**, *68*, 1986-1994.
- (15) Roach, P. J.; Woodward, W. H.; Reber, A. C.; Khanna, S. N.; Castleman, A. W., Jr. *Phys. Rev. B* **2010**, *81*, 195404.
- (16) Melko, J. J.; Ong, S. V.; Gupta, U.; Reveles, J. U.; D'Emidio, J.; Khanna, S. N.; Castleman, A. W., Jr. *Chem. Phys. Lett.* **2010**, *500*, 196-201.
- (17) Peppernick, S. J.; Gunaratne, K. D. D.; Castleman, A. W., Jr. *Int. J. Mass Spectrom.* **2010**, *290*, 65-71.
- (18) Leskiw, B. D.; Castleman, A. W., Jr. *Chem. Phys. Lett.* **2000**, *316*, 31-36.
- (19) Roach, P. J.; Reber, A. C.; Woodward, W. H.; Khanna, S. N.; Castleman, A. W., Jr. *Proc. Natl. Acad. Sci. U.S.A.* **2007**, *104*, 14565-14569.
- (20) Fayet, P.; Wolf, J. P.; Woste, L. *Phys. Rev. B* **1986**, *33*, 6792-6797.
- (21) Pratontep, S.; Carroll, S. J.; Xirouchaki, C.; Streun, M.; Palmer, R. E. *Rev. Sci. Instrum.* **2005**, *76*, 045103.

- (22) Stegman, R. L.; Schriemp, J.; Hettche, L. R. *J. Appl. Phys.* **1973**, *44*, 3675-3681.
- (23) Ready, J. F. *Industrial Applications of Lasers*; Academic Press: New York, 1997.
- (24) Shi, Z.; Ford, J. V.; Wei, S.; Castleman, A. W., Jr. *J. Chem. Phys.* **1993**, *99*, 8009-8015.
- (25) Soler, J. M.; Garcia, N.; Echt, O.; Sattler, K.; Recknagel, E. *Phys. Rev. Lett.* **1982**, *49*, 1857-1860.
- (26) Haberland, H. *Clusters of Atoms and Molecules: Theory, Experiment, and Clusters of Atoms*; Springer-Verlag: New York, 1994.
- (27) Milani, P.; de Heer, W. A. *Phys. Rev. B* **1991**, *44*, 8346-8348.
- (28) Morel, R.; Brenac, A.; Bayle-Guillemaud, P.; Portemont, C.; La Rizza, F. *Eur. Phys. J. D* **2003**, *24*, 287-290.
- (29) Breaux, G. A.; Neal, C. M.; Cao, B.; Jarrold, M. F. *Phys. Rev. Lett.* **2005**, *94*, 173401.
- (30) Li, Z. H.; Truhlar, D. G. *J. Phys. Chem. C* **2008**, *112*, 11109-11121.
- (31) Ganteför, G.; Meiwesbroer, K. H.; Lutz, H. O. *Phys. Rev. A* **1988**, *37*, 2716-2718.
- (32) Huang, R. B.; Zhang, Q.; Chen, H.; Zheng, L. S. *Eur. Phys. J. D* **1999**, *9*, 253-256.
- (33) Chaiken, J.; Goodisman, J. *J. Chem. Phys.* **1993**, *98*, 4610-4625.
- (34) Yamamuro, S.; Sumiyama, K.; Suzuki, K. *J. Appl. Phys.* **1999**, *85*, 483-489.
- (35) von Smoluchowski, M. *Phys. Z.* **1916**, *17*, 557-571.
- (36) von Smoluchowski, M. *Z. Phys. Chem.* **1917**, *92*, 129-168.
- (37) Moore, J. H.; Davis, C. C.; Coplan, M. A.; Greer, S. C. *Building Scientific Apparatus*; Cambridge University Press: Cambridge, MA, 2009.
- (38) Mattox, D. M. *The Foundations of Vacuum Coating Technology*; Noyes Publications/William Andrew Publishing: Norwich, NY, 2003.
- (39) Chapin, J. S. *Research/Development* **1974**, *25*, 37-40.
- (40) Window, B.; Savvides, N. *J. Vac. Sci. Technol., A* **1986**, *4*, 196-202.
- (41) Davidse, P. D.; Maissel, L. I. *J. Appl. Phys.* **1966**, *37*, 574-579.
- (42) Haberland, H.; Karrais, M.; Mall, M. *Z. Phys. D: At., Mol. Clusters* **1991**, *20*, 413-415.

- (43) Haberland, H.; Mall, M.; Moseler, M.; Qiang, Y.; Reiners, T.; Thurner, Y. *J. Vac. Sci. Technol., A* **1994**, *12*, 2925-2930.
- (44) Imanaka, M.; Arai, H.; Nakagawa, T.; Ohshiro, Y.; Watanabe, S. I. *Int. J. Mod. Phys. B* **2005**, *19*, 2327-2332.
- (45) Majumdar, A.; Koepp, D.; Ganeva, M.; Datta, D.; Bhattacharyya, S.; Hippler, R. *Rev. Sci. Instrum.* **2009**, *80*, 095103.
- (46) Momin, T.; Bhowmick, A. *Rev. Sci. Instrum.* **2010**, *81*, 075110.
- (47) Ayesh, A. I.; Qamhieh, N.; Ghamlouche, H.; Thaker, S.; El-Shaer, M. *J. Appl. Phys.* **2010**, *107*, 034317.
- (48) Lightstone, J. M.; Patterson, M. J.; White, M. G. *Chem. Phys. Lett.* **2005**, *413*, 429-433.
- (49) Ferguson, E. E.; Fehsenfeld, F. C.; Schmeltekopf, A. L. *Adv. At. Mol. Phys.* **1969**, *5*, 1-56.
- (50) Grubisic, A.; Li, X.; Gantefoer, G.; Bowen, K. H.; Schnoeckel, H.; Tenorio, F. J.; Martinez, A. *J. Chem. Phys.* **2009**, *131*, 184305.
- (51) Noessler, M.; Mitric, R.; Bonačić-Koutecký, V.; Johnson, G. E.; Tyo, E. C.; Castleman, A. W., Jr. *Angew. Chem., Int. Ed. Engl.* **2010**, *49*, 407-410.
- (52) Bird, R. B.; Stewart, W. E.; Lightfoot, E. N. *Transport Phenomena*; Wiley & Sons: New York, 2007.
- (53) Anderson, J. B.; Fenn, J. B. *Phys. Fluids* **1965**, *8*, 780-787.
- (54) Reber, A. C.; Khanna, S. N.; Roach, P. J.; Woodward, W. H.; Castleman, A. W., Jr. *J. Phys. Chem. A* **2010**, *114*, 6071-6081.
- (55) Adams, N. G.; Smith, D. *Int. J. Mass Spectrom. Ion Process.* **1976**, *21*, 349-359.
- (56) Douglas, D. J.; Frank, A. J.; Mao, D. M. *Mass Spectrom. Rev.* **2005**, *24*, 1-29.
- (57) Ervin, K. M.; Armentrout, P. B. *J. Chem. Phys.* **1985**, *83*, 166-189.
- (58) Marshall, A. G.; Hendrickson, C. L.; Jackson, G. S. *Mass Spectrom. Rev.* **1998**, *17*, 1-35.
- (59) Bell, R. C.; Zemski, K. A.; Justes, D. R.; Castleman, A. W., Jr. *J. Chem. Phys.* **2001**, *114*, 798-811.
- (60) Dawson, P. H. *Quadrupole Mass Spectrometry and Its Applications*; American Institute of Physics: Woodbury, NY, 1976.

- (61) Hess, H.; Kwiet, S.; Socaciu, L.; Wolf, S.; Leisner, T.; Woste, L. *Appl. Phys. B* **2000**, *71*, 337-341.
- (62) Guan, S. H. *J. Chem. Phys.* **1992**, *96*, 7959-7964.
- (63) Guan, S. H.; Kim, H. S.; Marshall, A. G.; Wahl, M. C.; Wood, T. D.; Xiang, X. Z. *Chem. Rev.* **1994**, *94*, 2161-2182.
- (64) Balaj, O. P.; Berg, C. B.; Reitmeier, S. J.; Bondybey, V. E.; Beyer, M. K. *Int. J. Mass Spectrom.* **2009**, *279*, 5-9.
- (65) Upschulte, B. L.; Shul, R. J.; Passarella, R.; Keesee, R. G.; Castleman, A. W., Jr. *Int. J. Mass Spectrom. Ion Process.* **1987**, *75*, 27-45.
- (66) Ng, C. Y.; Baer, M.; Prigogine, I.; Rice, S. A. *State-Selected and State-to-State Ion-Molecule Reaction Dynamics*; Wiley & Sons: New York 1992.
- (67) Röttgen, M. A.; Judai, K.; Antonietti, J. M.; Heiz, U.; Rauschenbach, S.; Kern, K. *Rev. Sci. Instrum.* **2006**, *77*, 013302.
- (68) Kelly, R. T.; Tolmachev, A. V.; Page, J. S.; Tang, K.; Smith, R. D. *Mass Spectrom. Rev.* **2010**, *29*, 294-312.
- (69) Finnigan, R. E. *Anal. Chem.* **1994**, *66*, A969-A975.
- (70) Hassouba, M. A.; Elakshar, F. F.; Garamoon, A. A. *Fizika A* **2002**, *2*, 81-90.
- (71) Harting, E.; Read, F. H.; Brunt, J. N. H. *Electrostatic Lenses*; Elsevier Science: New York: 1976.
- (72) Skoog, D. A.; Holler, F. J.; Nieman, T. A. *Principles of Instrumental Analysis*, 5th ed.; Sounders College/Harcourt Brace: Philadelphia, 2007.
- (73) Crider, C. A.; Cisneros, G.; Mark, P.; Levine, J. D. *J. Vac. Sci. Technol.* **1976**, *13*, 1202-1205.
- (74) Messerli, S.; Schintke, S.; Morgenstern, K.; Sanchez, A.; Heiz, U.; Schneider, W. D. *Surf. Sci.* **2000**, *465*, 331-338.
- (75) Schouteden, K.; Lando, A.; Janssens, E.; Van Haesendonck, C.; Lievens, P. *New J. Phys.* **2008**, *10*, 083005.
- (76) Hayderer, G.; Cernusca, S.; Schmid, M.; Varga, P.; Winter, H. P.; Aumayr, F. *Phys. Scr.* **2001**, *T92*, 156-157.
- (77) Osaka, F.; Ishikawa, T.; Tanaka, N.; Lopez, M.; Matsuyama, I. *J. Vac. Sci. Technol., B* **1994**, *12*, 2894-2900.

- (78) Wang, X. S.; Huang, C.; Bresslerhill, V.; Maboudian, R.; Weinberg, W. H. *J. Vac. Sci. Technol., A* **1993**, *11*, 2860-2862.
- (79) Jiricek, P.; Cukr, M.; Kolarik, V.; Koc, S. *Rev. Sci. Instrum.* **1998**, *69*, 2804-2805.
- (80) Firpo, G.; de Mongeot, F. B.; Boragno, C.; Valbusa, U. *Rev. Sci. Instrum.* **2005**, *76*, 026108.
- (81) Gomlak, G.; Kelly, M. C.; Panayotov, V. G.; Koplitz, B. *Rev. Sci. Instrum.* **1999**, *70*, 3701-3706.
- (82) Sik, M. J.; Ferrier, R. P. *J. Phys. E: Sci. Instrum.* **1973**, *6*, 749-750.
- (83) Meiwes-Broer, K. H. *Metal Clusters at Surfaces: Structure, Quantum Properties, Physical Chemistry*; Springer Publishing: New York, 2000.
- (84) Bromann, K.; Félix, C.; Brune, H.; Harbich, W.; Monot, R.; Buttet, J.; Kern, K. *Science* **1996**, *274*, 956-958.
- (85) Nacer, B.; Massobrio, C.; Félix, C. *Phys. Rev. B* **1997**, *56*, 10590-10595.
- (86) Cleveland, C. L.; Landman, U. *Science* **1992**, *257*, 355-361.
- (87) Francis, G. M.; Goldby, I. M.; Kuipers, L.; von Issendorff, B.; Palmer, R. E. *J. Chem. Soc. Dalton Trans.* **1996**, 665-671.
- (88) Jensen, P. *Rev. Mod. Phys.* **1999**, *71*, 1695-1735.
- (89) Yamaguchi, W.; Yoshimura, K.; Tai, Y.; Maruyama, Y.; Igarashi, K.; Tanemura, S.; Murakami, J. *Chem. Phys. Lett.* **1999**, *311*, 341-345.
- (90) Claeysens, F.; Pratontep, S.; Xirouchaki, C.; Palmer, R. E. *Nanotechnology* **2006**, *17*, 805-807.
- (91) Yasumatsu, H.; Hayakawa, T.; Koizumi, S.; Kondow, T. *J. Chem. Phys.* **2005**, *123*, 124709.
- (92) Lee, S.; Lee, B.; Mehmood, F.; Seifert, S.; Libera, J. A.; Elam, J. W.; Greeley, J.; Zapol, P.; Curtiss, L. A.; Pellin, M. J.; Stair, P. C.; Winans, R. E.; Vajda, S. *J. Phys. Chem. C* **2010**, *114*, 10342-10348.
- (93) Kandel, S. A.; Weiss, P. S. *J. Phys. Chem. B* **2001**, *105*, 8102-8106.
- (94) Kushmerick, J. G.; Weiss, P. S. *J. Phys. Chem. B* **1998**, *102*, 10094-10097.
- (95) Kuk, Y.; Jarrold, M. F.; Silverman, P. J.; Bower, J. E.; Brown, W. L. *Phys. Rev. B* **1989**, *39*, 11168-11170.
- (96) Kaden, W. E.; Wu, T.; Kunkel, W. A.; Anderson, S. L. *Science* **2009**, *326*, 826-829.

- (97) Lee, S.; Molina, L. M.; Lopez, M. J.; Alonso, J. A.; Hammer, B.; Lee, B.; Seifert, S.; Winans, R. E.; Elam, J. W.; Pellin, M. J.; Vajda, S. *Angew. Chem., Int. Ed. Engl.* **2009**, *48*, 1467-1471.
- (98) Lee, S. S.; Fan, C. Y.; Wu, T. P.; Anderson, S. L. *J. Am. Chem. Soc.* **2004**, *126*, 5682-5683.
- (99) Lightstone, J. M.; Patterson, M. J.; Liu, P.; Lofaro, J. C., Jr.; White, M. G. *J. Phys. Chem. C* **2008**, *112*, 11495-11506.
- (100) Woodruff, D. P. *Atomic Clusters: From Gas Phase to Deposited*; Elsevier Science: New York, 2007.
- (101) Schouteden, K.; Vandamme, N.; Janssens, E.; Lievens, P.; van Haesendonck, C. *Surf. Sci.* **2008**, *602*, 552-558.
- (102) Duffe, S.; Irawan, T.; Bielecki, M.; Richter, T.; Sieben, B.; Yin, C.; von Issendorff, B.; Moseler, M.; Hoevel, H. *Eur. Phys. J. D* **2007**, *45*, 401-408.
- (103) Brune, H.; Giovannini, M.; Bromann, K.; Kern, K. *Nature* **1998**, *394*, 451-453.
- (104) Sanchez, A.; Abbet, S.; Heiz, U.; Schneider, W. D.; Hakkinen, H.; Barnett, R. N.; Landman, U. *J. Phys. Chem. A* **1999**, *103*, 9573-9578.
- (105) Chrétien, S.; Buratto, S. K.; Metiu, H. *Curr. Opin. Solid State Mat. Sci.* **2007**, *11*, 62-75.
- (106) Shen, J. W.; Evans, C.; Wade, N.; Cooks, R. G. *J. Am. Chem. Soc.* **1999**, *121*, 9762-9763.
- (107) Nagaoka, S.; Ikemoto, K.; Fujio, K.; Hiehata, K.; Sasahara, A.; Mitsui, M.; Onishi, H.; Nakajima, A. *Eur. Phys. J. D* **2009**, *52*, 103-106.
- (108) Peng, W.; Johnson, G. E.; Fortmeyer, I. C.; Wang, P.; Hadjar, O.; Cooks, R. G.; Laskin, J. *Phys. Chem. Chem. Phys.* **2011**, *13*, 267-275.
- (109) Laskin, J.; Wang, P.; Hadjar, O. *Phys. Chem. Chem. Phys.* **2008**, *10*, 1079-1090.
- (110) Schreiber, F. *Prog. Surf. Sci.* **2000**, *65*, 151-256.
- (111) Schwartz, D. K. *Annu. Rev. Phys. Chem.* **2001**, *52*, 107-137.
- (112) Bigelow, W. C.; Pickett, D. L.; Zisman, W. A. *J. Colloid Sci.* **1946**, *1*, 513-538.
- (113) Nuzzo, R. G.; Allara, D. L. *J. Am. Chem. Soc.* **1983**, *105*, 4481-4483.
- (114) Binnig, G.; Rohrer, H.; Gerber, C.; Weibel, E. *Appl. Phys. Lett.* **1982**, *40*, 178-180.
- (115) Binnig, G.; Rohrer, H. *Surf. Sci.* **1983**, *126*, 236-244.

- (116) Chen, C. J. *Introduction to Scanning Tunneling Microscopy*; Oxford University Press: New York, 1993.
- (117) *Scanning Probe Microscopy and Spectroscopy: Theory, Techniques, and Applications*, 2nd ed.; Bonnell, D. A., Ed.; VCH Publishers: New York, 2001.
- (118) Hansma, P. K.; Tersoff, J. *J. Appl. Phys.* **1987**, *61*, R1-R23.
- (119) Amman, M.; Wilkins, R.; Benjacob, E.; Maker, P. D.; Jaklevic, R. C. *Phys. Rev. B* **1991**, *43*, 1146-1149.
- (120) Smith, R. K.; Nanayakkara, S. U.; Woehrlle, G. H.; Pearl, T. P.; Blake, M. M.; Hutchison, J. E.; Weiss, P. S. *J. Am. Chem. Soc.* **2006**, *128*, 9266-9267.
- (121) Lando, A.; Lauwaet, K.; Lievens, P. *Phys. Chem. Chem. Phys.* **2009**, *11*, 1521-1525.
- (122) Stranick, S. J.; Kamna, M. M.; Weiss, P. S. *Rev. Sci. Instrum.* **1994**, *65*, 3211-3215.
- (123) Blake, M. M.; Nanayakkara, S. U.; Claridge, S. A.; Fernandez-Torres, L. C.; Sykes, E. C. H.; Weiss, P. S. *J. Phys. Chem. A* **2009**, *113*, 13167-13172.
- (124) Perdew, J. P.; Burke, K.; Ernzerhof, M. *Phys. Rev. Lett.* **1996**, *77*, 3865-3868.
- (125) Koster, A. M.; Calaminici, P.; Casida, M. E.; Flores-Moreno, R.; Geudtner, G.; Goursot, A.; Heine, T.; Ipatov, A.; Janetzko, F.; del Campo, J. M.; Patchkovskii, S.; Reveles, J. U.; Salahub, D. R.; Vela, A. *deMon2k*, ver. 2.3.6, The deMon Developers: Cinvestav, Mexico, 2010. Available at <http://www.deMon-software.com>.
- (126) del Campo, J. M.; Koester, A. M. *J. Chem. Phys.* **2008**, *129*, 024107.
- (127) Chargaff, E. *Experientia* **1950**, *6*, 201-209.
- (128) Jones, R. O. *Phys. Rev. Lett.* **1991**, *67*, 224-227.
- (129) Upton, T. H. *J. Chem. Phys.* **1987**, *86*, 7054-7064.
- (130) Alipour, M.; Mohajeri, A. *J. Phys. Chem. A* **2010**, *114*, 12709-12715.
- (131) Zhao, Y. L.; Zhang, R. J. *J. Phys. Chem. A* **2007**, *111*, 7189-7193.
- (132) Schultz, N. E.; Staszewska, G.; Staszewski, P.; Truhlar, D. G. *J. Phys. Chem. B* **2004**, *108*, 4850-4861.
- (133) Rao, B. K.; Jena, P. *J. Chem. Phys.* **1999**, *111*, 1890-1904.
- (134) Calaminici, P.; Russo, N.; Toscano, M. Z. *Phys. D: At., Mol. Clusters* **1995**, *33*, 281-288.

- (135) Fournier, R. *J. Chem. Theory Comput.* **2007**, *3*, 921-929.
- (136) Zhan, C. G.; Zheng, F.; Dixon, D. A. *J. Am. Chem. Soc.* **2002**, *124*, 14795-14803.
- (137) Sun, J.; Lu, W. C.; Wang, H.; Li, Z. S.; Sun, C. C. *J. Phys. Chem. A* **2006**, *110*, 2729-2738.
- (138) Drebov, N.; Ahlrichs, R. *J. Chem. Phys.* **2011**, *134*, 124308.
- (139) Li, X.; Wu, H. B.; Wang, X. B.; Wang, L. S. *Phys. Rev. Lett.* **1998**, *81*, 1909-1912.
- (140) Schrodinger, E. *Z. Phys.* **1924**, *30*, 341-349.
- (141) Asimov, I. *Asimov's New guide to science*; Basic Books: New York, 1984.
- (142) Popper, K. R. *The Logic of Scientific Discovery*; Routledge, Chapman & Hall: New York, 2002.

Chapter 3

Energetic Materials

Reprinted with permission from the *Journal of Physical Chemistry C* **2011**, 115, 9903-9908.

Copyright 2011 American Chemical Society.

1. Introduction

It was outlined in Chapter 1 how all-metal cluster reactivity with oxygen has been a continuing topic of interest over the past twenty years due to the potential use of such clusters in high energy density materials.¹⁻⁵ Aluminum is of particular interest because of its outstanding energy storage capabilities. In terms of combustion, the enthalpy of combustion of pure aluminum with oxygen is more exothermic than any other element of the periodic table,⁶ and aluminum-based energetic materials have the potential for storing three times as much energy as traditional carbon- and nitrogen-based materials by weight.⁷⁻⁸ Unfortunately, aluminum reacts readily with oxygen, a detrimental trait which becomes increasingly apparent in aluminum nanoparticles, whose small size maximizes surface area for increased combustion rate, due to their increased ratio of pre-oxidized surface aluminum to non-oxidized interior aluminum.⁷⁻⁸ However, as particle diameter is decreased even further, the cluster size regime is eventually reached wherein specific aluminum clusters exhibit properties unique from the bulk, one of which is resistance to reactivity with ground state oxygen ($X^3\Sigma_g^-$).⁹⁻¹⁰

It was first discovered in 1989 that free-electron metal clusters exhibit unique reactivities governed by their jellium electronic shell closings;¹⁻² a finding which suggested that this model could be used to describe both the physical and chemical properties of individual clusters, which

behave like isolated atoms. These properties change as even a single atom is added or removed, leading to a “unified atom” theory where specific clusters with desirable properties different from their bulk constituents could potentially allow the construction of cluster-assembled materials which preserve these properties.¹¹⁻¹² One example of such a desirable cluster is Al_{13}^- , which was identified early on as being resistant to reactions with oxygen. Subsequent theoretical work suggested that Al_{13}^0 clusters have the potential to be incorporated into cluster-assembled materials with oxygen-containing ligands.¹³ Such a tunable substance would allow the development of high energy density materials that burn at a desirable rate, governed by the initial presence or absence of oxygen.

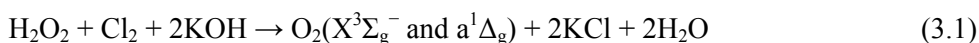
More recent work involved examination of the spin-dependence of aluminum cluster reactivity, wherein aluminum clusters containing an even number of electrons appeared more resistant to oxygen etching (production of smaller clusters) than those with an odd number of electrons, and all species were found to be susceptible to reaction with singlet oxygen ($\text{a}^1\Delta_g$).⁹⁻¹⁰ These results, which are supported by the Wigner-Witmer correlation rules coupled with spin conservation,¹⁴ suggest that even Al_{13}^- , which has previously been viewed as an inert species, is susceptible to reaction. Past studies were performed either by the addition of hydrogen atoms to a particular aluminum cluster,⁹ which essentially adds single electrons to the electronic structure, or by using a size-selective Fourier-transform ion cyclotron resonance (FT-ICR) mass spectrometer to selectively isolate and react aluminum clusters with $\text{O}_2(\text{a}^1\Delta_g)$.¹⁰ In the later reference, however, the $\text{O}_2(\text{a}^1\Delta_g)$ was generated via microwave discharge, which is also known to produce O_3 as well as O atoms.¹⁵ While the presence of these species was excluded as being responsible for the findings reported in the earlier publication, herein we re-examine the reactivity of pure aluminum cluster anions with $\text{O}_2(\text{a}^1\Delta_g)$ via a new approach—multiple-ion flow tube mass spectrometry coupled to a chemical $\text{O}_2(\text{a}^1\Delta_g)$ generator (which does not produce O atoms). We report the

previously unobserved resistance of Al_9^- to reaction with triplet oxygen as well as relative rate constants for the reactivity of individual aluminum clusters with $\text{O}_2(a^1\Delta_g)$ and $\text{O}_2(X^3\Sigma_g^-)$.

2. Experimental

The experimental setup is discussed in Chapter 2,¹⁶⁻¹⁸ but specific details are provided here. Clusters were produced in a laser vaporization source consisting of a rotating and translating aluminum rod (99.999%, Puratronic, Inc.) ablated by the second harmonic of a Nd:YAG laser. The clusters are transported out of the source via a helium carrier gas (High Purity, Praxiar, Inc.) into a room temperature (293 K) laminar flow reaction vessel maintained at 0.56 Torr by a high volume pump. Reactant gasses were introduced to the clusters approximately 30 cm downstream from the source and allowed to react with the clusters over a distance and time of 60 cm and 7.8 ms, respectively, after which the products were extracted into a differentially pumped ion guide vacuum system where a spectrum was obtained via quadrupole mass spectrometry (Extrel CMS).

The reactant gasses used were $\text{O}_2(X^3\Sigma_g^-)$ (Praxiar, Inc.) and $\text{O}_2(a^1\Delta_g)/\text{O}_2(X^3\Sigma_g^-)$ created in an $\text{O}_2(a^1\Delta_g)$ generator and detector, which has been thoroughly described previously.¹⁹ Briefly, Cl_2 was bubbled through a basic solution of hydrogen peroxide to produce both ground and excited states of O_2 — $\text{O}_2(X^3\Sigma_g^-)$ and $\text{O}_2(a^1\Delta_g)$ —as shown by Equation 3.1:



One hundred percent of the Cl_2 reacted to form one of the states of O_2 . Water byproduct was collected in a trap submerged in a methanol-liquid nitrogen slush maintained at -60 to -70 °C. $\text{O}_2(a^1\Delta_g)$ emissions at 1270 nm were monitored in a calibrated cell to determine its concentration.¹ Using this technique, the gas entering the flow tube was predominantly He, $\text{O}_2(X^3\Sigma_g^-)$, and $\text{O}_2(a^1\Delta_g)$. In the current experiments the fraction of O_2 as $\text{O}_2(a^1\Delta_g)$ varied from 7 to 17 percent.

In order to compare the reactivity of aluminum clusters with $O_2(X^3\Sigma_g^-)$ and $O_2(a^1\Delta_g)$, mass spectra were taken with 1) no reactant, 2) $O_2(X^3\Sigma_g^-)$, and 3) an equal amount of $O_2(a^1\Delta_g)$ plus $O_2(X^3\Sigma_g^-)$ (i.e. the Cl_2 flow equaled the $O_2(X^3\Sigma_g^-)$ flow). Both the $O_2(X^3\Sigma_g^-)$ and Cl_2 were introduced using a gas flow meter (MKS Instruments). Mass spectra with no reactants were taken before and after those with reactants and showed no appreciable change in the Al_n^- distribution with time. The rate constants were derived from the mass spectra as described below.

3. Results and Discussion

The experiment was repeated three times on separate days. Typical mass spectra are shown in Figure 3.1. Aluminum cluster anion reactivity with $O_2(X^3\Sigma_g^-)$ (Figure 3.1.a) is similar to past studies where Al_{13}^- is shown to increase appreciably due to etching reactions of higher order clusters.¹⁻⁴ Additionally, Al_{23}^- , which was also previously observed to be resistant to oxygen reactivity, does not appear to decrease, and other odd-numbered aluminum clusters decrease less than their even-numbered neighbors. The spectra depicting aluminum cluster anion reactivity with a mixture of $O_2(a^1\Delta_g)$ and $O_2(X^3\Sigma_g^-)$ (Figure 3.1.b) differs in a number of respects.

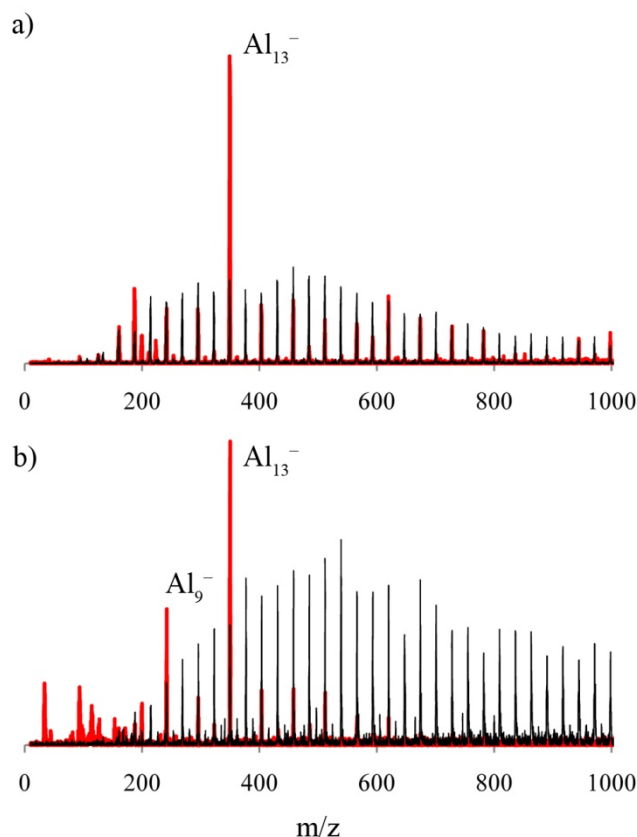


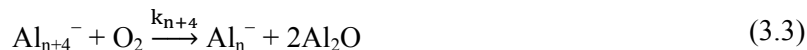
Figure 3.1. Observed Al_n^- mass spectrum (black) before and (red) after introduction of a) 42.5 sccm $\text{O}_2(\text{X}^3\Sigma_g^-)$ and b) 42.5 sccm of a 12% $\text{O}_2(\text{a}^1\Delta_g)/\text{O}_2(\text{X}^3\Sigma_g^-)$ mixture. Intensities between (a) and (b) are arbitrary.

What is particularly intriguing is that Al_9^- appears to increase in a manner similar to Al_{13}^- . The pattern of odd-numbered clusters compared to even-numbered clusters is also clearly different. In order to determine the causes for differences, we derived rate constants for individual aluminum clusters reacting with both $\text{O}_2(\text{a}^1\Delta_g)$ and $\text{O}_2(\text{X}^3\Sigma_g^-)$. Details of the derivation are discussed below.

Past experimental work with aluminum cluster anions and oxygen has identified the most likely product to be Al_2O .^{3-4,10} This suggests the following reaction dominates Al_n^- loss:



As there is no preliminary mass selection such as in a selective ion flow tube or FT-ICR, Al_n^- is formed in a similar reaction from larger aluminum clusters throughout the duration of the reaction time:



The result of Reactions 3.2 and 3.3 is that individual clusters that are resistant to oxygen etching ($k_n \ll k_{n+4}$) will stand out in the spectrum as dominant peaks, and in some cases will even increase (i.e. Al_{13}^-). However, the amount of aluminum clusters etched and the amount of Al_n^- product formed is indeterminable, and therefore the observed change is in the concentration of Al_n^- , represented by the equation:

$$\frac{d[\text{Al}_n^-]}{dt} = -k_n[\text{Al}_n^-][\text{O}_2] + k_{n+4}[\text{Al}_{n+4}^-][\text{O}_2] \quad (3.4)$$

The kinetics involves multiple such equations, as large clusters are progressively etched to smaller ones, and thus Equation 3.4 does not provide us with an analytical means of calculating k_n for any given cluster.²⁰ The complexity increases when a reactant mix of $\text{O}_2(a^1\Delta_g)$ and $\text{O}_2(X^3\Sigma_g^-)$ is considered:

$$\begin{aligned} \frac{d[\text{Al}_n^-]}{dt} = & -k_{na}[\text{Al}_n^-][\text{O}_2(a^1\Delta_g)] + k_{(n+4)a}[\text{Al}_{n+4}^-][\text{O}_2(a^1\Delta_g)] \\ & - k_{nx}[\text{Al}_n^-][\text{O}_2(X^3\Sigma_g^-)] + k_{(n+4)x}[\text{Al}_{n+4}^-][\text{O}_2(X^3\Sigma_g^-)] \end{aligned} \quad (3.5)$$

To circumvent this, we have solved the equations numerically in order to estimate rate constants for each cluster using the individual relative abundances for the initial and final aluminum cluster spectra.

This approach requires three considerations. First, in addition to cluster anions, a laser vaporization source also produces a similar number of cations and neutrals;²¹ however, past studies suggest that no aluminum cluster anions are formed from neutral reactions with oxygen, and cluster-cluster collisions in the flow tube are negligible. Therefore, these species can be

effectively ignored as possible contaminants. Second, it has been suggested that for smaller Al_n^- clusters ($n < 7$), significant amounts of AlO^- and AlO_2^- may be formed in reactions with O_2 .⁴ As is shown below, these potential variables affect only the smallest aluminum clusters in our spectrum. Additional possible products are therefore ignored, and our results at these smaller sizes may contain a systematic error if this occurs. Lastly, there is the possibility that specific aluminum cluster reactions (Reactions 3.2 and 3.3) will produce an appreciable amount of residual energy (ΔH_{rxn}). If this energy is high enough it could cause the evaporation of one or more aluminum atoms from the cluster, causing additional Al_n^- loss or formation:



as well as the potential loss of an Al^- or e^- :



This effect was explored in detail by Cooper *et al.*,⁴ and is discussed in further detail below.

With these three considerations, rate constants for the reaction of individual aluminum cluster anions with $\text{O}_2(a^1\Delta_g)$ and $\text{O}_2(X^3\Sigma_g^-)$ were derived as follows: The initial Al_n^- cluster distribution was extrapolated to higher values than the maximum observed in the experiment ($n = 37$) by a decaying exponential fit to the tail of the observed distribution; the extrapolated distribution quickly approaches zero and was truncated at $n = 54$. Due to the use of a conical octopole and a quadrupole deflector energy filter (i.e. quad bender), the experimental mass discrimination was not exactly known. This uncertainty was explored by modifying our observed distribution via: 1) no mass discrimination, 2) a Gaussian mass discrimination function with maximum detection efficiency at $n = 20$ or $n = 30$ and of varying widths, or 3) a smooth initial cluster distribution peaking at $n = 20$, $n = 30$, or $n = 40$. Mass discrimination factors for each cluster size were determined by the ratio of the observed distribution to the smooth distribution,

assuming that the different mass discrimination functions had only small effects on the determined rate constants, which are included in the reported uncertainties.

Rate constants were determined through a Monte Carlo optimization in which the 100 reaction rate constants (k_{na} , k_{nx} ; $n = 5-54$) were randomly and independently selected between a value too small to observe on the time scale of the reaction ($10^{-15} \text{ cm}^3 \text{ s}^{-1}$) and an assumed collision rate constant ($10^{-9} \text{ cm}^3 \text{ s}^{-1}$). Final peak intensities assuming a given set of rate constants were calculated from the known initial conditions for both the $\text{O}_2(\text{X}^3\Sigma_g^-)$ -only and $\text{O}_2(\text{a}^1\Delta_g)/\text{O}_2(\text{X}^3\Sigma_g^-)$ conditions by iteratively solving the set of coupled differential equations (Equations 3.4 and 3.5 for $n = 5-54$) in sufficiently small time steps throughout the experimental reaction time. The resulting calculated Al_n^- relative abundances were compared to the experimental abundances via a weighted least squares goodness-of-fit. The randomly guessed rate constants were varied in a simple, downhill optimization until a local minimum in the goodness-of-fit was reached. The procedure was continuously repeated, starting from different randomly selected sets of rate constants to find another local minimum, until the large parameter space defined by the 100 unknown rate constants was mapped out. Finally the best-fit values and uncertainty limits for each individual rate constant were determined by viewing the goodness-of-fit as a function of that rate constant (Figure 3.2). Some reaction rate constants are well-defined by the data as shown by a distinct minimum (Figure 3.2.a); some rate constants have only upper or lower limits defined (Figure 3.2.b); some rate constants, particularly those for cluster sizes above $n = 37$ for which no data was measured, are completely undefined (Figure 3.2.c).

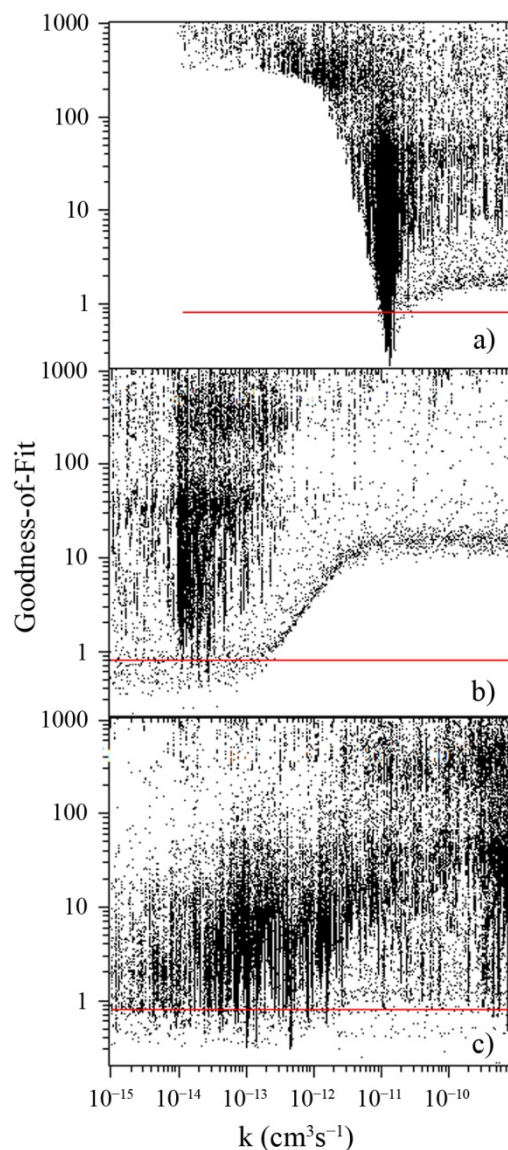


Figure 3.2. Modeling results for rate constants of selected Al_n^- clusters with $\text{O}_2(\text{X}^3\Sigma_g^-)$. a) $n = 16$; b) $n = 13$; c) $n = 41$. The red line at a goodness-of-fit of 0.8 indicates the determined threshold above which the calculated abundances do not fit the experimental data within uncertainty.

At first glance it may appear unlikely that any information can be gleaned when varying 100 different parameters in the model; however, we emphasize that the full parameter space has been explored through the Monte Carlo procedure (all rate constants are varied in concert, *not* independently of each other) and, within the assumptions of the model, the data do define a large number of rate constants. Under the considerations above, in which only reactions with $\text{O}_2(\text{a}^1\Delta_g)$

or $O_2(X^3\Sigma_g^-)$ to reduce Al_n^- to Al_{n-4}^- are considered, the full reaction network consists of just eight reaction chains. An assumed rate constant for the reaction of cluster size n largely dictates the rate constants for reaction of cluster sizes $n-4$, $n-8$, etc., that can provide an acceptable fit to the data. Although this is not explicitly assumed in the modeling, the 100 parameters are effectively reduced to just 8 independent parameters.

Results for the calculations are shown in Figures 3.3 and 3.4. Figure 3.3 compares the experimental mass spectra with predictions using the determined rate constants. It can be seen in Figure 3.3 that the fitting procedure reproduces the data exceptionally well.

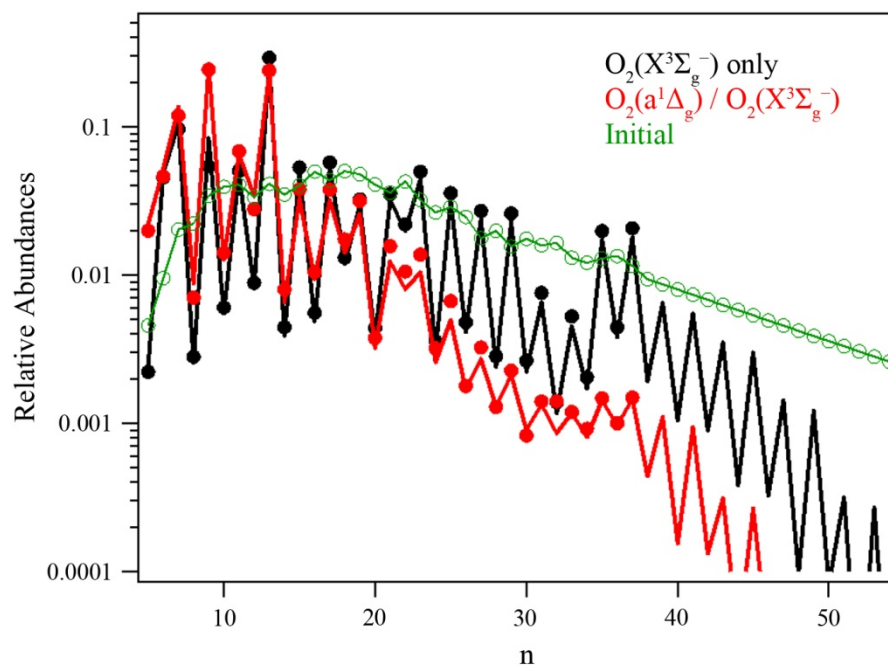


Figure 3.3. Observed and calculated branching ratios for (green) initial and final aluminum distributions with (black) $O_2(X^3\Sigma_g^-)$ and (red) $O_2(a^1\Delta_g)/O_2(X^3\Sigma_g^-)$. Observed values are represented by circles. Calculated values are represented by colored lines.

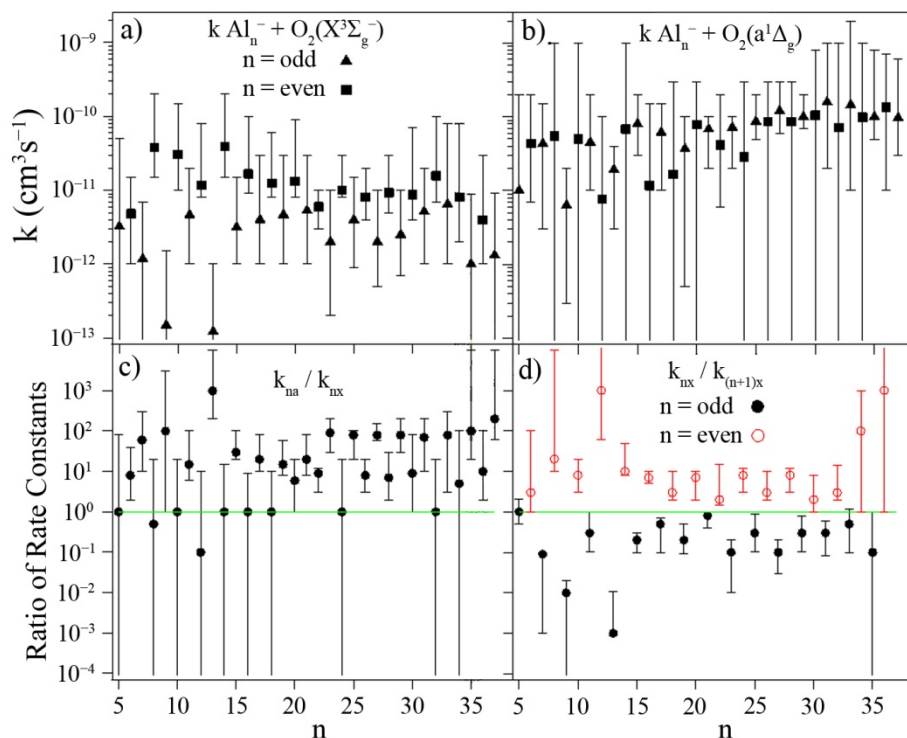


Figure 3.4. Fitted rate constants for a) $\text{Al}_n^- + \text{O}_2(\text{X}^3\Sigma_g^-)$ and b) $\text{Al}_n^- + \text{O}_2(\text{a}^1\Delta_g)$. c) Relative rate constants for $\text{Al}_n^- + \text{O}_2(\text{a}^1\Delta_g)$ to $\text{Al}_n^- + \text{O}_2(\text{X}^3\Sigma_g^-)$ for each cluster size and d) for adjacent cluster sizes.

Figures 3.4.a and 3.4.b display the fitted rate constants and their errors for $\text{Al}_n^- + \text{O}_2(\text{X}^3\Sigma_g^-)$ and $\text{Al}_n^- + \text{O}_2(\text{a}^1\Delta_g)$, respectively. The error bars do not include potential systematic errors caused by the assumptions discussed above.

Several trends are immediately obvious. For most values of n , $\text{O}_2(\text{a}^1\Delta_g)$ reacts considerably faster than $\text{O}_2(\text{X}^3\Sigma_g^-)$; typically about 10 to 20 times faster. This is best observed in Figure 3.4.c, where the ratio of the $\text{O}_2(\text{a}^1\Delta_g)$ to $\text{O}_2(\text{X}^3\Sigma_g^-)$ rate constants are plotted. Note that the error bars for the ratios are considerably smaller than the individual ones. The $\text{O}_2(\text{a}^1\Delta_g)$ rate constants are mainly similar to each other with rates of about 20 to 40 percent of the collision value ($\sim 5.4 \times 10^{-10} \text{ cm}^3 \text{ s}^{-1}$). The lack of lower limits on the $\text{O}_2(\text{a}^1\Delta_g)$ rate constants for many even n clusters is a consequence of large $\text{O}_2(\text{X}^3\Sigma_g^-)$ rate constants for those clusters. While data do not unambiguously distinguish in these cases between etching due to $\text{O}_2(\text{a}^1\Delta_g)$ and etching due to a

large $O_2(X^3\Sigma_g^-)$ rate constant, the best-fits to the data in all cases imply $O_2(a^1\Delta_g)$ rate constants in agreement with previous studies.^{2,4} For $O_2(X^3\Sigma_g^-)$, there is an even-odd variation with even-numbered n reacting two to three times faster than odd-numbered n for most values and greater for some of the lower values of n . Again this is shown more clearly as a ratio, k_n/k_{n+1} is plotted in Figure 3.4.d. All even n are above the 1:1 line, indicating that in all cases that even n clusters react more quickly than similarly-sized odd n clusters. Again one should note that the relative error bars are much smaller than the absolute ones. The uncertainty in the rate constant includes values too low to measure in the current experiment. Rate constants in cluster sizes at the extremes ($n < 5$; $n > 30$) of the observed distribution also include immeasurably small values; this is due to the uncertainty in fitting the data at the outskirts of our experimental cluster distribution and previously observed reactivity suggesting that our product assumption (Reaction 3.3) is less reliable when $n < 7$;³⁻⁴ we do not believe that these clusters should be considered less reactive than previously observed “magic” species such as Al_{13}^- and Al_{23}^- . For $n = 9$ and 13, k_{nx} are very slow and the error includes zero. Alternatively, k_{nx} for 8, 10, and 14 are somewhat faster than other values. However, Al_{13}^- and Al_{23}^- do not appear to be much different than other values of n when reacted with $O_2(a^1\Delta_g)$, which is in agreement with previous spin-dependent etching studies.⁹⁻¹⁰

For any Al_n^- to erroneously appear more or less reactive using our method, its production rate must be lower or higher, respectively, than allowed by Reaction 3.2 alone. This may be explained by Reactions 3.6, 3.7, and/or 3.8 (i.e. the exothermicity of the reaction may lead to loss of an Al^0 , Al^- , or e^- , respectively). When considering Al_9^- with the four-aluminum loss mechanism (Reaction 3.2), this would imply that Al_{14}^- reacts with O_2 and then loses an additional aluminum atom. Previous aluminum cluster reactivity studies by Cooper *et al.* have suggested that Al_{14}^- reacts with oxygen in such a way that 100% of its Al_{10}^- products eject an Al atom to create Al_9^- , which could explain some of the abundance of this peak in our observed spectrum.⁴

This argument, however, is in direct disagreement with a more recent spin-dependent etching study performed by Burgert *et al.*, which found that Al_{13}^- and Al_{14}^- reacts with $\text{O}_2(\text{X}^3\Sigma_g^-)$ to form only Al_9^- and Al_{10}^- , respectively.¹⁰ In our experiment, reactions with excited-state $\text{O}_2(\text{a}^1\Delta_g)$ would inherently contain 0.98 eV more enthalpy than with ground-state $\text{O}_2(\text{X}^3\Sigma_g^-)$,²² and this energy difference may cause ΔH_{rxn} to cross the aluminum removal energy barrier (Reaction 3.6). However, even if the 0.98 eV from the $\text{O}_2(\text{a}^1\Delta_g)$ is considered, the studies by Burgert *et al.* were performed in a FT-ICR, which adds resonance excitation to the cluster's internal energy distribution, while the present study was performed under multiple collision conditions in a laminar flow tube maintained at 293 K. Both of these effects would lead to colder clusters in the present experiments. Also, as noted above, Al_9^- formation via Reaction 3.6 would result in a significant increase in the apparent Al_{10}^- reactivity, which we do not observe.

Similarly, Al_{10}^- , Al_{11}^- , or Al_{12}^- could be reacting with O_2 to form AlO_2 , Al_2O_2 , or Al_3O_2 neutrals, respectively, and Al_9^- . However, no previous experimental evidence supporting these products exists, and if any one of the reactions leading to them were uniquely predominant we would observe a large rate constant for Al_6^- , Al_7^- , and Al_8^- , respectively, which we do not. Thus, we conclude that Al_9^- growth can be considered predominantly a product of Al_{13}^- etching by $\text{O}_2(\text{a}^1\Delta_g)$ and not Al_{14}^- etching under our conditions. The presence of a large Al_9^- peak after $\text{O}_2(\text{a}^1\Delta_g)/\text{O}_2(\text{X}^3\Sigma_g^-)$ introduction is therefore attributed to being a product of the large amounts of Al_{13}^- present, and the absence of a large Al_9^- peak after pure $\text{O}_2(\text{X}^3\Sigma_g^-)$ introduction is explained by the lack of Al_{13}^- reactivity to form Al_9^- . In fact, this is supported by the argument that, if Al_9^- were reactive, it would be the smallest peak in the $\text{O}_2(\text{X}^3\Sigma_g^-)$ -only product spectrum, as all other aluminum clusters demonstrate some degree of product formation (Equation 3.2). The discovery of a large abundance of Al_9^- is not explained by Clemenger-Nilsson ellipsoidal shell structures, as this species has 28 electrons: Al_9^- has an approximate distortion parameter of -0.5 , whereas an electronic shell closing at 28 e^- would require a value of approximately 0.33.²³⁻²⁴ However, note

that even if Jahn-Teller distortion created a closed shell the gap between the highest occupied molecular orbital and the lowest unoccupied molecular orbital would still not be large enough to suggest any unusual stability, and past theoretical calculations probing this gap, the electron detachment energy, the aluminum binding energy, the global hardness value of Al_9^- , etc., do not suggest it to be particularly stable.²⁴⁻²⁶ This is the first time Al_9^- has been observed to exhibit such strong resistance to oxygen etching, although Cooper *et al.* did identify this species as having a lower rate constant than neighboring clusters.⁴

4. Conclusions

The unique finding of Al_9^- stability was enabled by the use of a multiple-ion flow tube following $\text{O}_2(a^1\Delta_g)$ addition. Past mass-selective techniques have not produced this effect because Al_{13}^- is unreactive with $\text{O}_2(X^3\Sigma_g^-)$ and therefore Al_9^- is not formed in the etching reaction. We have used a Monte Carlo procedure to estimate rate constants for reactions of Al_n^- with both $\text{O}_2(a^1\Delta_g)$ and $\text{O}_2(X^3\Sigma_g^-)$. However the assumption inherent in the method suggests that the present observations warrant further investigation. Our findings confirm that aluminum cluster anions are susceptible to etching by $\text{O}_2(a^1\Delta_g)$, regardless of electronic or geometric stabilities. We believe that Al_9^- has been newly identified as resistant to oxygen etching for reasons that cannot be explained using the jellium model. This unusual reactivity would benefit from first-principles theory, and future studies will include the kinetics of mass-selected clusters in order to further explore the extent of this resistivity.

5. References

- (1) Leuchtner, R.E.; Harms, A. C.; Castleman, A. W., Jr. *J. Chem. Phys.* **1989**, *91*, 2753-2754.

- (2) Leuchtner, R. E.; Harms, A. C.; Castleman, A. W., Jr. *J. Chem. Phys.* **1991**, *94*, 1093-1101.
- (3) Hettich, R. L. *J. Am. Chem. Soc.* **1989**, *111*, 8582-8588.
- (4) Cooper, B. T.; Parent, D.; Buckner, S. W. *Chem. Phys. Lett.* **1998**, *284*, 401-406.
- (4) Roach, P. J.; Woodward, W. H.; Reber, A. C.; Khanna, S. N.; Castleman, A. W., Jr. *Phys. Rev. B* **2010**, *81*, 195404.
- (5) When examining the enthalpy of formation of common oxides for each element, Al_2O_3 is the highest per mole of initial standard-state element.
- (6) Dlott, D. D. *Mat. Sci. Tech.* **2006**, *22*, 463-473.
- (7) Yetter, R. A.; Risha, G. A.; Son, S. F. *Proc. Combust. Inst.* **2009**, *32*, 1819-1838.
- (8) Reber, A. C.; Khanna, S. N.; Roach, P. J.; Woodward, W. H.; Castleman, A. W., Jr. *J. Am. Chem. Soc.* **2007**, *129*, 16098-16101.
- (9) Burgert, R.; Schnöckel, H.; Grubisic, A.; Li, X.; Stokes, S. T.; Bowen, K. H.; Ganteför, G. F.; Kiran, B.; Jena, P. *Science* **2008**, *319*, 438-442.
- (10) Claridge, S. A.; Castleman, A. W., Jr.; Khanna, S. N.; Murray, C. B.; Sen, A.; Weiss, P. S. *ACS Nano* **2009**, *3*, 244-255.
- (11) Castleman, A. W., Jr.; Khanna, S. N.; *J. Phys. Chem. C* **2009**, *113*, 2664-2675.
- (12) Reber, A. C.; Khanna, S. N.; Castleman, A. W., Jr. *J. Am. Chem. Soc.* **2007**, *129*, 10189-10194.
- (13) Bellary, V. P.; Balasubramanian, T. K.; Shetty, B. J. *Ind. Acad. Sci.* **1998**, *51*, 445-452.
- (14) Ahlrichs, R.; Ehrhardt, C.; Lakenbrink, M.; Schunck, S.; Schnöckel, H. *J. Am. Chem. Soc.* **1986**, *108*, 3596-3602.
- (15) Roach, P. J.; Woodward, W. H.; Castleman, A. W., Jr.; Reber, A. C.; Khanna, S. N. *Science* **2009**, *323*, 492-495.
- (16) Guo, B. C.; Wei, S.; Chen, Z.; Kerns, K. P.; Purnell, J.; Buzza, S.; Castleman, A. W., Jr. *J. Chem. Phys.* **1992**, *97*, 5243-5245.
- (17) Castleman, A. W., Jr.; Weil, K. G.; Sigsworth, S. W.; Leuchtner, R. E.; Keesee, R. G. *J. Chem. Phys.* **1987**, *86*, 3829-3835.
- (18) Midey, A.; Dotan, I.; Viggiano, A. A. *J. Phys. Chem. A* **2008**, *112*, 3040-3045.
- (19) Ferguson, E. E.; Fehsenfeld, F. C.; Schmeltekopf, A. L. *Adv. Atom. Molec. Phys.* **1969**, *5*, 1-56.
- (20) de Heer, W. A. *Rev. Mod. Phys.* **1993**, *65*, 611-676.

- (21) O₂(a¹Δ_g) energy from NIST Chemistry Web Book.
- (22) Clemenger, K. *Phys. Rev. B* **1985**, 32, 1359-1362. Distortion parameter estimated from theoretical Al₉⁻ structure in Reference 24.
- (23) Sun, J.; Lu, W. C.; Wang, H.; Li, Z.-S.; Sun, C.-C. *J. Phys. Chem. A* **2006**, 110, 2729-2738.
- (24) Fournier, R. *J. Chem. Theory Comput.* **2007**, 3, 921-929.
- (25) Rao, B. K.; Jena, P. *J. Chem. Phys.* **1999**, 111, 1890-1903.

Chapter 4

Catalysts

1. Introduction

In Chapter 1 it was discussed how the gas-phase reactivity of clusters is valuable in the understanding of catalytic mechanisms on a surface. It is well accepted that many factors influence the reactivity of a molecule and govern the rate of product formation and the selectivity of products formed. Among these, bond activation plays the primary role. In particular, the reactivity of a metal cluster is influenced by its electronic structure and can be modified through controlled variations in size, support, solvation, and atomic substitution.¹⁻¹⁰ One manifestation of the effect of electronic structure on cluster reactivity is the formation of active sites, which are analogous to specific locations on a reactant or catalyst that bind a reagent and lower the activation energy. Gas-phase chemistry of size-selected metal clusters serves as a method of interrogating specific reactant-site interactions with high levels of precision and control, providing detailed information that serves to explain and predict reaction mechanisms, and is ideal for identifying active sites.^{11,12} Recent work in the Castleman laboratory has addressed the role of active sites on aluminum cluster anions in breaking polar bonds. In particular, their size-selective reactivity with water has been previously identified as being due to the existence of adjacent complementary active sites where one site serves as a Lewis acid and the other site serves as a Lewis base.^{13,14} A Lewis acid site accepts electrons from the oxygen atom and a neighboring Lewis base site donates electrons to the hydrogen, which stabilizes the transition state for bond cleavage. The reactivity is not governed by the electronic shell closures which is the usual explanation for cluster reactivity with oxygen,^{1,15-19} but rather is due to the existence of

these complementary active sites. Surprising control of the reactivity is possible, and specific aluminum clusters with two or more adjacent active sites have been shown to selectively release hydrogen gas, via a cooperative mechanism that could potentially be useful in fuel cells. In fact, bulk aluminum had been previously shown to mysteriously react with water to form hydrogen,²⁰ which, in lieu of our current understanding, suggests that this reactivity indeed extends to bulk surfaces. In a continuation of this research, aluminum cluster anions have been reacted with other species containing polar bonds, including alcohols (i.e. methanol and *t*-butanol), thiols (hydrogen sulfide), amines (ammonia), and carbonyls (formaldehyde and acetone).

2. Semi-Empirical Rules for Nucleophilic Attack

At first glance it might seem unlikely that electrons can be donated to negatively charged anionic cluster, but in actuality this is quite possible, provided that certain conditions are met. In 2004 Horia Metiu and coworkers proposed a set of semi-empirical rules governing the likelihood that propene would donate electrons to gold cluster anions.²¹ These rules, worded here as to be unspecific to propene or gold, are as follows: 1) The donation of electrons exists as a bond forming between the reactant and the cluster, whereby the reactant always donates electrons to an unoccupied molecular orbital (the lowest of which is technically designated LUMO, the second lowest LUMO+1, etc., but here for simplicity LUMO is used to describe any unoccupied orbital susceptible to attack); 2) This electron donation will only occur at a site where the LUMO protrudes into vacuum (i.e. there is no appreciable electron density from an occupied orbital protecting it); 3) The energy released in this bond formation is relative to the energy of the LUMO (i.e. the lowest orbital which satisfies Rule 2 is generally the most favored); and 4) in the case of multiple sites for the same LUMO, the reactant will bind more strongly to the site with the lowest coordination (i.e. corner sites are more preferred).

In 2009 these rules were tested using aluminum cluster anions reacting with water.^{13,14}

Theoretical calculations suggest that nearly all clusters possess LUMOs that protrude into vacuum, including to some extent Al_{13}^- and Al_{23}^- (Figure 4.1).

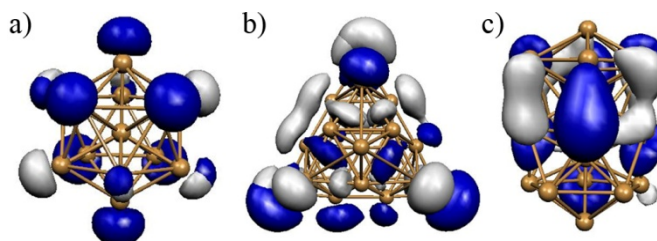


Figure 4.1. Lowest fully unoccupied molecular orbitals for a) Al_{13}^- , b) Al_{23}^- , and c) Al_{20}^- . Metiu’s semi-empirical rules for nucleophilic attack (Reference 21) suggest that those orbitals protruding into vacuum will be most susceptible to attack.

This is interesting, as Al_{13}^- and Al_{23}^- contain jellium shell closings. As a converse example, Al_{20}^- is shown in Figure 4.1.c. Note that Al_{20}^- (and indeed all even-numbered aluminum cluster anions) has an odd number of electrons, and so its LUMO+1 is considered instead of its LUMO, since the oxygen donates two electrons to the cluster and cannot do this to a partially filled LUMO. Al_{20}^- does not have a jellium shell closing, and previous studies with oxygen have shown this to be the most important concept in predicting their reactivity. When tested, the rules do not exactly predict the reactivity of these three clusters (Figure 4.2.b), with Al_{13}^- and Al_{20}^- appearing “magic” while Al_{23}^- reacts readily.

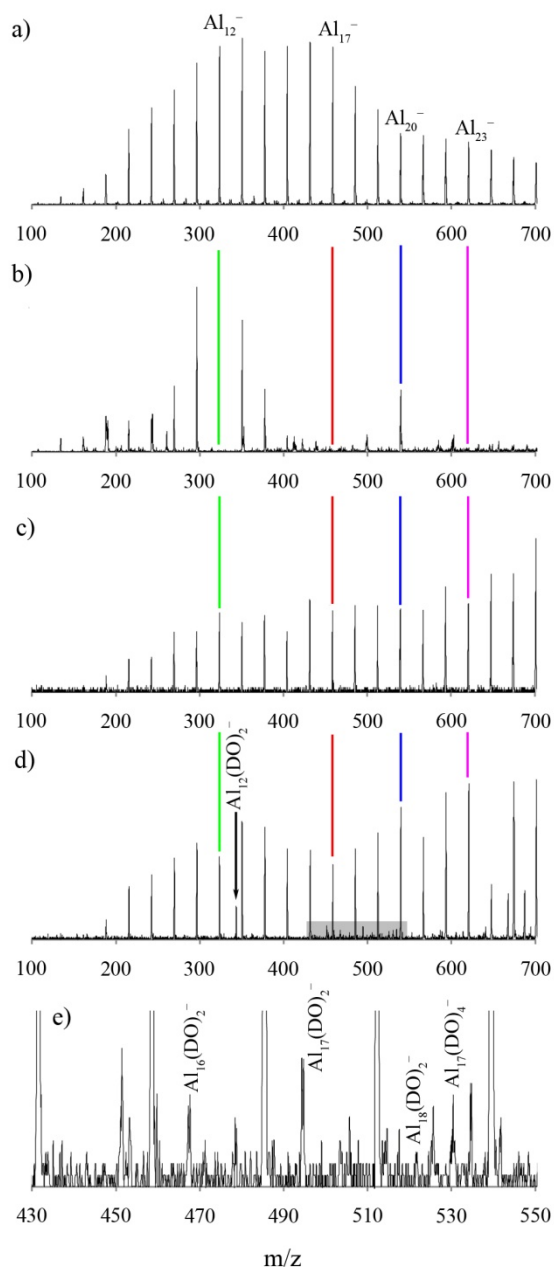


Figure 4.2. Experimental mass spectra of aluminum cluster reactivity with water. a) Aluminum cluster distribution before introducing water; b) Aluminum cluster distribution after introducing a large amount of water; c) retuned aluminum cluster distribution before d) introducing a small amount of heavy water. e) Zoomed-in section of grayed box in (d) focusing on D_2 loss; D_2O and H_2O were used interchangeably with no discernible difference in reactivity. The specific mass spectra shown were acquired using D_2O for (c), (d), and (e), and H_2O for (a) and (b). The colored lines are to aid the reader in identifying aluminum cluster peaks, with Al_{12}^- , Al_{17}^- , Al_{20}^- , and Al_{23}^- represented by green, red, blue, and purple lines, respectively. Adapted from Reference 14.

Therefore, since all aluminum clusters exhibit LUMOs which protrude into vacuum, the rules suggested that the oxygen on the water would be most able to donate electrons to those clusters with the lowest LUMO energies (Figure 4.3).

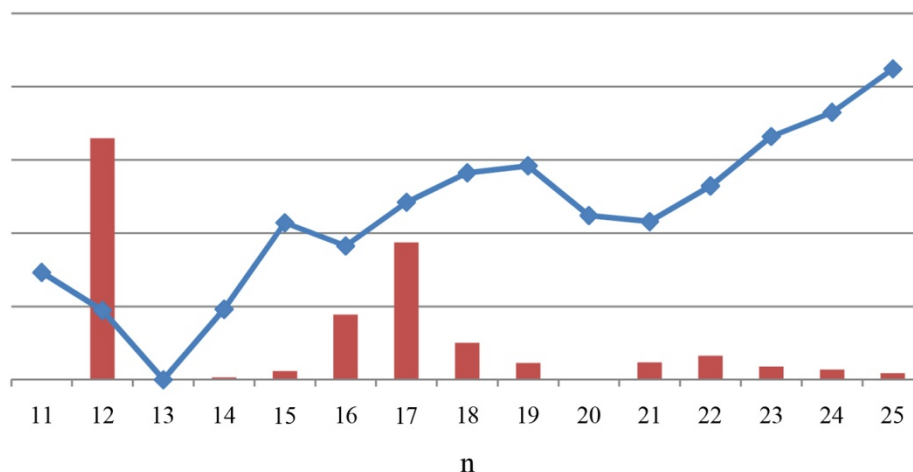


Figure 4.3. Graph comparing theoretically determined LUMO energies (blue) to experimentally observed aluminum cluster anion (Al_n^-) intensities after reaction with water (red) from $n = 11$ -25. Intensities between the two are normalized to Al_{13}^- to allow for comparison. The post-reaction intensities were acquired from the same data used in Figure 4.2.e. For even-numbered clusters the LUMO+1 was used, as is described in the main text.

Oddly, this was not found to be the case, as the aluminum clusters appeared to follow a seemingly random pattern of reactivity (defined as water additions) when interacting with water. It was postulated that the formation of an Al–O bond was only the first step in a complicated mechanism, and that this step was quite reversible at room temperature. Theoretical calculations provided the answer: once the initial intermediate was formed, a second reaction could occur involving the donation of electrons from the highest occupied molecular orbital (HOMO) of the complex to the hydrogen on the water molecule. This interaction resulted in the formation of an Al–H bond, which allowed the bond between the H atom and the O atom to stretch and subsequently break. Once this process occurs, the total energy released from the cleavage of the O–H bond is eventually quenched in the laminar flow tube, resulting in an irreversible chemical reaction. An example of this mechanism is illustrated in the first half of Figure 4.4.

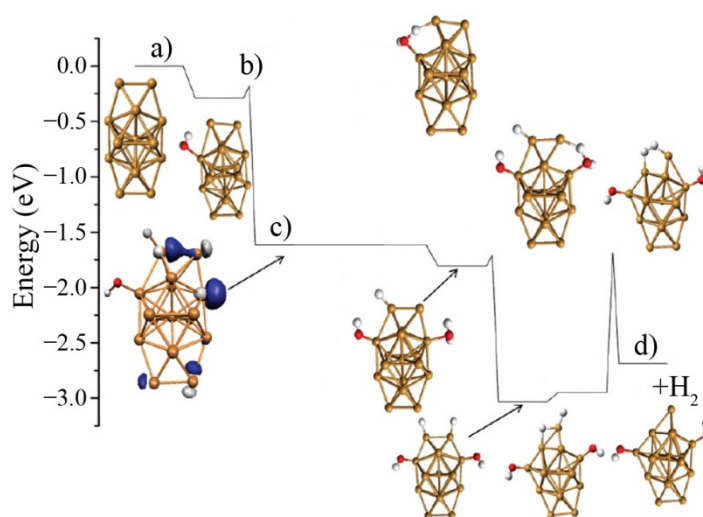


Figure 4.4. Reaction coordinate diagram for the reaction of Al_{17}^- with water. a) Water attacks the intact cluster, bonding to the LUMO. b) The resultant bond formation between the adjacent Al atom and the H atom requires sufficient energy to overcome a barrier. c) The LUMO of the final product is then susceptible to further nucleophilic attack, d) eventually leading to the liberation of a hydrogen molecule. Adapted from Reference 14.

It can be theoretically determined that Al_{13}^- , experimentally observed to not react with water, has a barrier for breaking the O–H bond that is higher than the energy available, and so eventually the water will be able to leave in a reversal of the first half of the mechanism. On the other hand, Al_{12}^- and Al_{17}^- are both shown to exhibit these complementary adjacent active sites, and so the mechanism proceeds to completion. The idea that no water molecules adsorb onto the “magic” clusters Al_{13}^- and Al_{20}^- is a misinterpretation of the experimental results. In fact, these clusters simply do not undergo any appreciable irreversible chemical reactivity before the end of the flow tube is reached, and thus no change in their intensity is observed. The concept of the complementary active sites can also be thought of as the aluminum atom behaving like a Lewis acid, accepting the electrons from the oxygen, and the neighboring aluminum atom behaving like a Lewis base, donating electrons to the hydrogen.

With this in mind, it became quite simple to predict which aluminum cluster anions would exhibit the most reactivity. It was found that Al_{12}^- , which exhibits a large LUMO and an ideally located subsequent HOMO, was the most reactive of all. It is worth mentioning that,

according to Metiu's rules for nucleophilic attack, the most likely site of attack is a corner site.²¹ This quickly explains the reactivity of Al_{23}^- , which maintains a jellium shell closing. Density functional theory has suggested the symmetry of this cluster to be D_{3h} .^{16,22} Although the cluster may resist oxygen etching, it is still susceptible to nucleophilic attack. In fact, seemingly all aluminum cluster anions larger than Al_{20}^- will have at least one corner,²² suggesting that the cluster regime *ends* at this point and not at 100 atoms as previously stated. After Al_{20}^- the nanoparticle size regime is effectively reached, wherein clusters will exhibit internal structure similar to bulk aluminum. Finally, it was also found that specific clusters (i.e. Al_{16}^- , Al_{17}^- , and Al_{18}^-) had more than one pair of complementary active sites. When these active sites were neighboring each other, the resulting proximate H atoms could bond to each other and release as hydrogen gas (Figure 4.2.e and Figure 4.4.d) in a Langmuir-Hinshelwood type mechanism.^{14,23} This discovery attracted some attention in the fields of hydrogen fuel cells and energy alternatives, as hydrogen gas was seemingly being liberated from water in a catalytic mechanism.²⁴ This is not entirely accurate, however, as such a catalyst would quickly become poisoned with hydroxyl groups, but the alternative uses for such a mechanism is discussed at the end of this chapter and in Chapter 6.

3. Extension of the Mechanism

It has likely not escaped the notice of some readers that this mechanism is not dependent on water at all, but rather just the O–H bond or, hypothetically, merely a polar bond. With this in mind, experiments continued in order to explore the limitations of this mechanism. These experiments included not only simple alcohols but also simple thiols, amines, and carbonyl compounds as well (as a non-polar control, simple ethers were shown to exhibit no reactivity with aluminum cluster anions, and so is not discussed beyond this brief mention). In the sections that

follow the results of these experiments are discussed after a brief outline of the experimental conditions related to each individual reactant studied.

a. Alcohols

Much of the experimental details have already been outline in Chapter 2 and in published literature.^{13,25,26} Clusters were produced from an aluminum rod (99.999%, Puratronic) in a laser vaporization source with the presence of a continuous flow of helium (High Purity, Praxiar, Inc.). The clusters were carried out of the source through an expansion nozzle and into a laminar flow tube that was maintained at a pressure of 0.56 Torr by a high volume pump. The clusters were thermalized via collisions with the helium carrier gas before being exposed to a selected reactant introduced through a reactant gas inlet. The three reactants used in these experiments were heavy water (99.9%, Cambridge Isotope Laboratories, Inc.), methanol-d (99.5%, Alfa Aesar), and *t*-butanol (99.5%, Baker). Although all mass spectra involving water and methanol are of deuterated species, similar results were obtained with H₂O and CH₃OH, respectively. In order to control the flow of these reactant gasses into the reaction vessel, they were heated or cooled to a point where their vapor pressure was approximately 100 Torr. Flow was controlled using a medium-flow needle valve (SS-4MG-MH, Swagelok Co.). Reactants and products were sampled through a 2 mm extraction orifice via a custom conical octopole²⁷ and guided through a series of differentially pumped radio frequency octopoles and electrostatic lenses before being analyzed via a quadrupole mass spectrometer (Extrel, CMS).

Product spectra are shown in Figure 4.5, while the normalized product intensities are shown in Figure 4.6. It can be seen that the reactivity of individual aluminum clusters is quite independent of the reactant, as Al₁₃⁻ and Al₂₀⁻ appear less reactive in all cases. The overall reactivity of all clusters with water appears less reactive, although this can be attributed to the low

vapor pressure of water. The condensation of water in the reactant gas inlet and onto the flow tube walls after the needle valve would cause the flow rate and therefore the concentration to be less than the other two reactants.

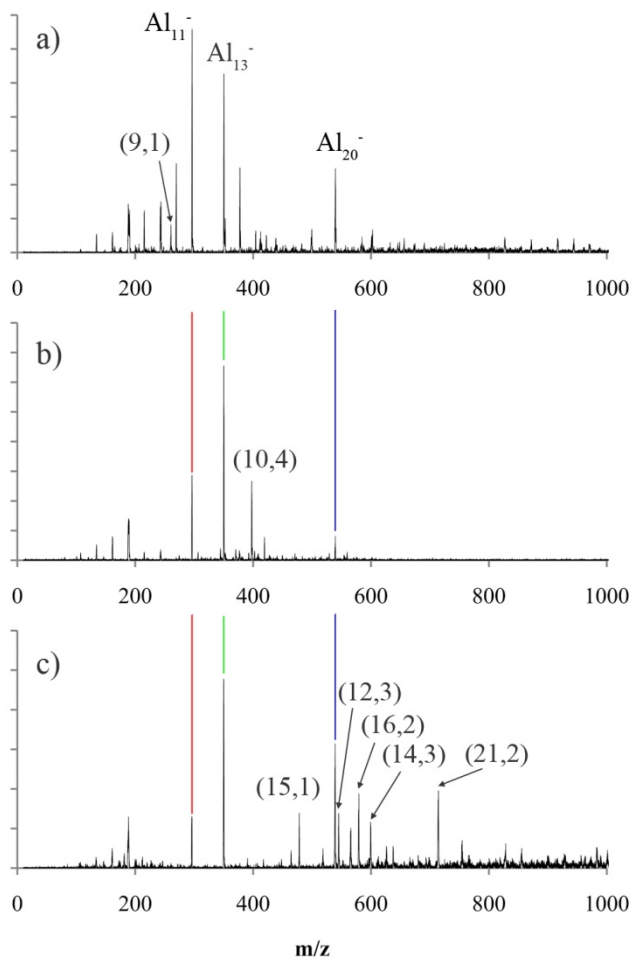


Figure 4.5. Full etching spectra with non-pure aluminum peaks $\text{Al}_n\text{ROH}_m^-$ labeled as (n,m) . a) $R = \text{H}$; b) $R = \text{CH}_3$; c) $R = \text{C}(\text{CH}_3)_3$. The colored lines are to aid the reader in identifying aluminum cluster peaks, with Al_{11}^- , Al_{13}^- , and Al_{20}^- represented by red, green, and blue lines, respectively.

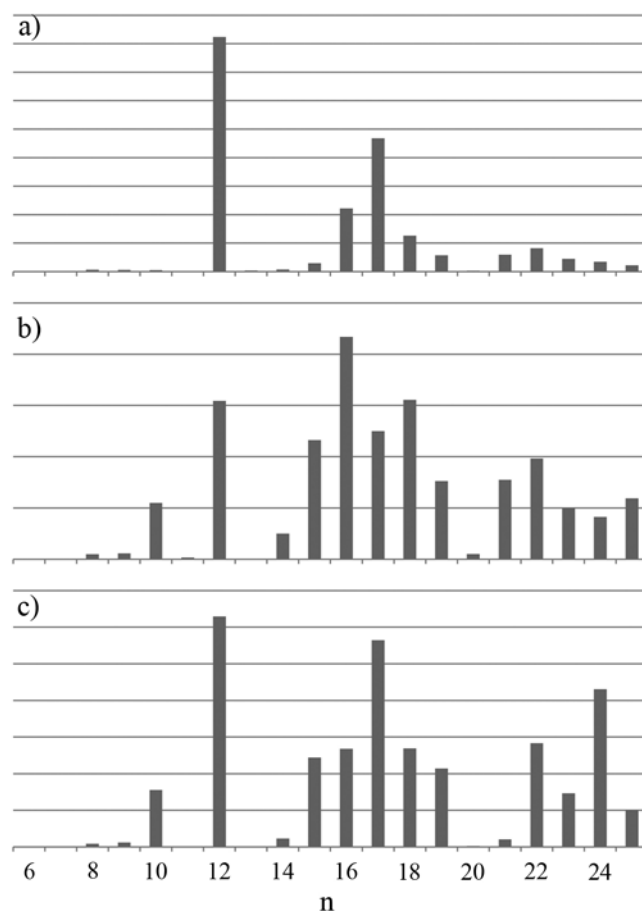


Figure 4.6. Relative reactivities of a) water, b) methanol, and c) *t*-butanol with aluminum cluster anions (Al_n^-). Values determined by dividing final aluminum cluster intensities by initial intensities. Relative reactivity intensities are arbitrary.

It is interesting to note that Al_{11}^- appears less reactive than its neighbors; this is likely due to a large transition state energy for this cluster, as was observed theoretically for water reactivity.¹⁴ It is also interesting to note that clusters smaller than Al_8^- appear much less reactive. This is likely due to the electronic charge density of the anionic clusters finally becoming localized enough to resist the initial nucleophilic attack. One additional point of interest is the existence of “magic” clusters with specific numbers of alcohol additions (water seemingly has none of these). The reason for this stability is unknown, although it could be due to steric protection by the R group of the attached molecule. As the complementary active sites are subjected to further reactions, the R groups eventually surround the cluster, protecting it from further attack in a similar fashion to

thiol ligands protecting a gold nanoparticle. This information could prove useful in the future construction of stable aluminum clusters and cluster-assembled materials.

b. Hydrogen Sulfide and Ammonia

The experiments for the reaction of aluminum cluster anions with H_2S and NH_3 were conducted in a manner very similar to that described in §4.3.a. The gasses were leaked into the flow tube via the same reactant gas inlet, and product spectra were obtained (Figure 4.7). Although these studies were performed at lower concentrations of reactants than with the alcohols, it can be seen that the reactivity is similar. Firstly, Al_{12}^- always appears very reactive, which is explained by its very prominent complementary active sites. Secondly, Al_{13}^- and Al_{20}^- appear less reactive than their neighboring clusters. This suggests that the same mechanism is occurring here with the polar S–H and N–H bonds. The author would like to point out that the reactivity of aluminum cluster anions with ammonia has been examined in the past,²⁸ and although similar results were observed (i.e. Al_{12}^- reacting fastest, while Al_{13}^- and Al_{20}^- resist reaction), a somewhat different mechanism was proposed. Briefly, density functional theory is used to determine the lowest energy conformation in order to determine how many, if any, N–H bonds are broken, and the reactivity is attributed to the energy barrier of reorienting the adsorbed ammonia molecule (i.e. rotation or undergoing an umbrella flip) wherein the electronegative nitrogen is forced closer to the anionic cluster. Here, no theoretical calculations are provided to support our complementary active site mechanism; however, similarities in the product spectra both here (Figure 4.7) and in the earlier publication²⁸ suggest that there is some validity to our proposed mechanism with regard to ammonia reactivity, and it should be considered an alternative explanation.

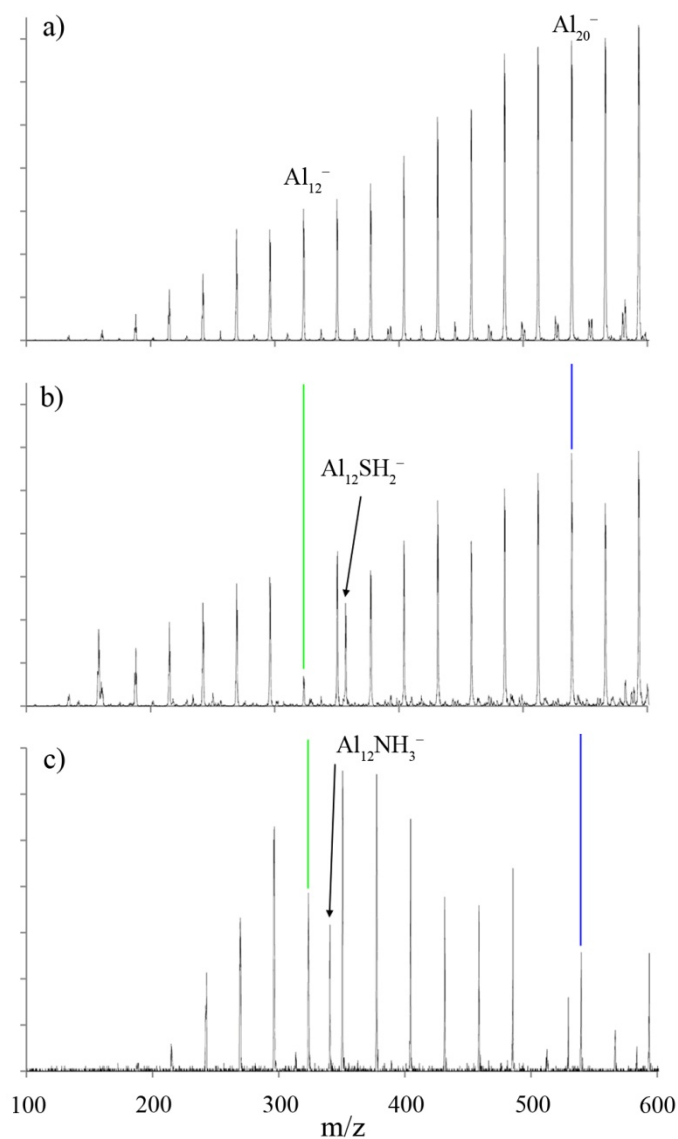


Figure 4.7. Etching spectra of Al_n^- cluster anions a) before and after reacting with b) H_2S and c) NH_3 . The colored lines are to aid the reader in identifying aluminum cluster peaks, with Al_{12}^- and Al_{20}^- represented by green and blue lines, respectively.

4. Carbonyl Bond Cleavage

Of particular interest was the prospect of discovering alternative reactants and clusters/metal surfaces that would exhibit this mechanism for species with large bond energies. It was therefore essential that research along this path continued, both in order to determine strong

bonds that may be broken in this manner but also to identify what surfaces and clusters may possess the well-patterned Lewis acid/Lewis base sites optimal to promote this type of reactivity,²⁰ be it metal oxides, bimetallic interfaces, customized defect sites and step edges, or cluster-assembled materials.^{3,29-33} One example of particular interest is the dissociation of the carbonyl group in formaldehyde, a bond which is involved in many chemical processes but is difficult to break. The polar C=O double bond has a bond dissociation energy of 751.5 kJ/mol versus only 498.8 kJ/mol for the O–H bond in water, which suggests that the C=O bond will be harder to cleave using the same mechanism.³⁴ Formaldehyde has a resonance hybrid structure, with positive and negative charges on the C and O atoms, respectively. We hypothesized that the canonical C–O single bond structure may be stabilized by the complementary active sites and subsequently promote the weakening of the C=O double bond, thereby allowing the splitting of such a strong interaction. As the controlled formation and dissociation of simple carbonyl group-containing compounds is an important aspect in the creation of complex chemicals, the utilization of this mechanism could lead to important developments in catalysis. In fact, formaldehyde-surface interactions have already been the focus of various theoretical studies involving metal surfaces.^{35,36}

a. Formaldehyde

Reactions between formaldehyde and anionic aluminum clusters were observed and investigated under multicollisional conditions in a fast flow reactor.^{13,14,25,26} Clusters were produced in a laser vaporization source consisting of an aluminum rod (99.999%, Puratronic) which was rotated and translated as it was ablated by a focused laser beam. The clusters were then carried out of the source through an expansion nozzle via a helium carrier gas. Clusters were cooled to room temperature in a laminar flow tube, which was maintained at approximately 0.56

Torr. Formaldehyde was introduced approximately 60 cm downstream from the source through a reactant gas inlet. The formaldehyde was created by heating paraformaldehyde (97%, Alfa Aesar),³⁷ which was previously dried in a nitrogen hood, and was then passed through a low-flow needle valve (SS-SS4-VH, Swagelok) to control reactant gas concentration. Products were sampled through a differentially pumped vacuum apparatus before being mass selected using a quadrupole mass spectrometer (Extrel CMS).

Reactivity spectra are shown in Figure 4.8. The intensity of Al_{12}^- shows the largest decrease for clusters in its size range upon exposure to formaldehyde, while Al_{13}^- reveals virtually no reactivity. Both of these observations are similar to the previously observed reactivity with water.^{13,14} By contrast, Al_{11}^- diminishes in intensity when exposed to formaldehyde, yet is resistant to etching with water. Al_{14}^- shows some resistance to formaldehyde etching; its intensity continually decreases, but it is the second largest pure aluminum peak suggesting a relatively slow reaction. Due to the tendencies of formaldehyde to polymerize on surfaces³⁷ it was not possible to determine the exact amount of formaldehyde introduced to the aluminum cluster distribution, and so rate constants are not reported here. Previously, the products of Al_n^- reactions with water produced peaks corresponding to $\text{Al}_n(\text{H}_2\text{O})^-$ in which the water dissociatively coupled to the cluster, while etching experiments with molecular oxygen (Chapter 3) produced smaller Al_n^- clusters corresponding to the loss of two neutral Al_2O species. Here, peaks were observed in the product spectrum corresponding to $\text{Al}_n(\text{CH}_2)^-$ complexes (+14 m/z) for where $n = 6-10, 13-17$ (green labels in Figure 4.8.b) and $\text{Al}_n(\text{OCH}_2)^-$ complexes (+30 m/z) for $n = 12, 18$ and larger clusters (red labels in Figure 4.8.b).

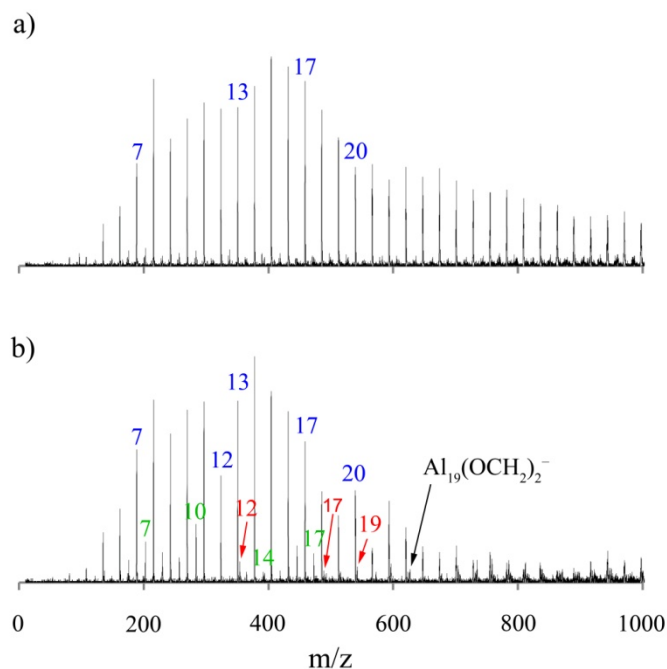
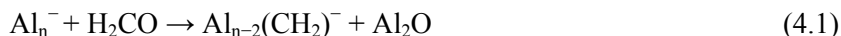


Figure 4.8. Aluminum cluster anion distribution a) before and b) after reaction with formaldehyde. Aluminum clusters (Al_n^-) are labeled with blue numbers, formaldehyde additions $[\text{Al}_n(\text{OCH}_2)]^-$ are labeled with red numbers, and oxygen losses $[\text{Al}_n(\text{CH}_2)]^-$ are labeled with green numbers. Anomalies are labeled in black. Intensities are arbitrary.

Methylene complexes are due to the adsorbed formaldehyde molecule losing an oxygen atom through reaction with each aluminum cluster. Al_2O is the most energetically favorable leaving group of an aluminum cluster-oxygen atom complex, being greater than 1.5 eV more exothermic than the loss of O, AlO , or Al_3O .^{19,38,39} This suggests that each $\text{Al}_n(\text{CH}_2)^-$ product peak observed corresponds to the loss of a single Al_2O from an $\text{Al}_{n+2}(\text{OCH}_2)^-$ complex as shown in Equation 4.1.



The largest methylene peak is $\text{Al}_{10}(\text{CH}_2)^-$ and the most diminished pure aluminum peak is Al_{12}^- confirming the loss of Al_2O . Also, the absence of an $\text{Al}_{11}\text{CH}_2^-$ peak confirms the inactivity of Al_{13}^- . This reaction, combined with the Al_{12}^- and Al_{13}^- reactivity described above, supports our initial hypothesis, as it suggests that the $\text{C}=\text{O}$ bond is being cleaved in a manner quite similar to the $\text{O}-\text{H}$ bond of past studies, thus initially creating an $\text{Al}_n(\text{OCH}_2)^-$ complex. Additionally, the nearly complete absence of $\text{Al}_{12}(\text{CH}_2)^-$ suggests that Al_{14}^- has reduced reactivity, although we

believe that a secondary product of Al_{13}^- with the loss of $[\text{AlOCH}_2]$ —due to the Al_{13}^- being a more energetically favorable product—may explain the weak $\text{Al}_{12}\text{CH}_2^-$ signal. Al_n^- ($n \leq 6$) clusters did not react, which is consistent with past observations and is likely due to the concentration of the excess charge protecting the smaller clusters from nucleophilic attack.

Formaldehyde additions without oxygen loss at larger cluster sizes are most likely due to the larger molecules (more atoms) containing more vibrational degrees of freedom over which the energy released by the aluminum-oxygen bond formation may be redistributed. We note that this does not imply that the carbonyl bond is intact in these clusters. Al_{23}^- reacted with formaldehyde, despite having a closed electronic shell that makes it resistant to etching by oxygen, a result which was also observed with water. In summary, the experimental results presented here unambiguously show that the carbonyl bond in formaldehyde is being size-selectively cleaved by the aluminum cluster anions.

To support the proposed mechanism, we have studied the reactions with first principles density functional theory.⁴⁰ The calculations were carried out, at an all electron level, using the deMon2K.⁴¹ The DZVP basis set was used for Al, and TZVP was used from Oxygen, Carbon, and Hydrogen. Transition states were found using a hierarchical transition state search algorithm.⁴² We first examined the reaction pathway of Al_9^- with formaldehyde (Figure 4.9.a). The red and blue charge density on the Al_9^- cluster indicates the HOMO and LUMO of the clusters which serve as Lewis base and Lewis acid active sites, respectively. Formaldehyde binds most favorably when the O atom binds to the Lewis acid site, and the C atom binds to the Lewis base site. Once the oxygen has donated charge to the Lewis acid site, the single bond resonance structure is favored, leading to a more weakly bonded C–O intermediate.

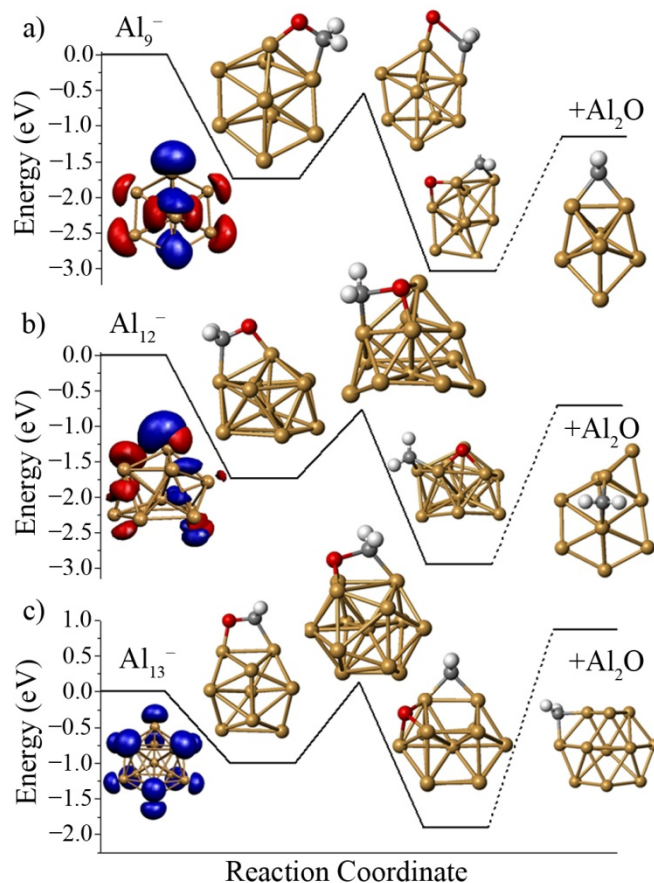


Figure 4.9. Theoretically determined reaction coordinate diagrams of $\text{Al}_n^- + \text{OCH}_2$ for a) $n = 9$, b) $n = 12$, and c) $n = 13$. For each initial structure, the HOMO and LUMO (LUMO+1) are shown in red and blue, respectively. The results reveal that Al_9^- and Al_{12}^- will react readily at the complementary active sites and subsequently lose an Al_2O , while Al_{13}^- does not have active sites and has both a barrier to carbonyl cleavage and Al_2O release is endothermic. This is in agreement with experimental observations.

The large binding energy between the formaldehyde molecule and the aluminum cluster (1.76 eV) indicates that a covalent bond has formed. The C–O bond has stretched from 1.22 Å to 1.46 Å, and the O–C–H bond angle changes from 121.8° in the formaldehyde molecule to 109.5° after binding to the cluster, all of which confirms that the C–O single bond is present, and that the C atom has moved from sp^2 to sp^3 hybridization. The formaldehyde molecule bonds in a manner similar to an $\eta^2\text{-H}_2\text{CO}$ conformation with a bulk surface.³⁵ The barrier to cleave the C–O bond is 1.22 eV (117.7 kJ/mol); however there is sufficient energy from the binding to affect this transformation. There is some distortion of the cluster at the transition state, although the large

binding energy provides the cluster with enough energy for reconstruction. Finally, once the carbonyl bond is cleaved, 3.04 eV of energy is released, which is enough to eject an Al_2O molecule from the surface of the cluster, confirming the proposed origin for the observed Al_7CH_2^- peak. Additionally, we examined the reaction pathway between Al_{12}^- and formaldehyde, with similar results (Figure 4.9.b). The barrier for splitting the carbonyl is even lower than the barrier on Al_9^- which is consistent with Al_{12}^- reacting more readily, and the cleavage of the C–O bond releases 3.03 eV of energy, which is sufficient to release an Al_2O molecule.

In the case of Al_{13}^- , the activation energy required to break the C=O bond designated by the peak in the reaction coordinate diagram (Figure 4.9.c) is greater than the binding energy gained from the initial interaction. Thus, the reaction does not proceed, agreeing with our experimental results. Al_{13}^- is an icosahedral cluster, with a closed electronic shell, whose electron density is uniformly distributed on all of the surface atoms, which means that no atom serves as a superior Lewis acid or base, so the cluster is uniquely deficient of active sites. We also note that Al_{23}^- reacts with formaldehyde while having a closed electronic shell showing that the reduced reactivity of Al_{13}^- is due to the absence of active sites and not entirely because of its closed electronic shell. The absence of active sites on Al_{13}^- and the lack of observed reactivity confirm that active sites are necessary to promote carbonyl cleavage of formaldehyde on aluminum cluster anions.

Several active sites on aluminum cluster anions which cleave formaldehyde do not cleave water, making formaldehyde less sensitive than water to the strength of the active sites. As an example, Al_{11}^- reacts with formaldehyde despite being resistant to water etching, with two energetically favorable pathways for Al_2O release (Figure 4.10).

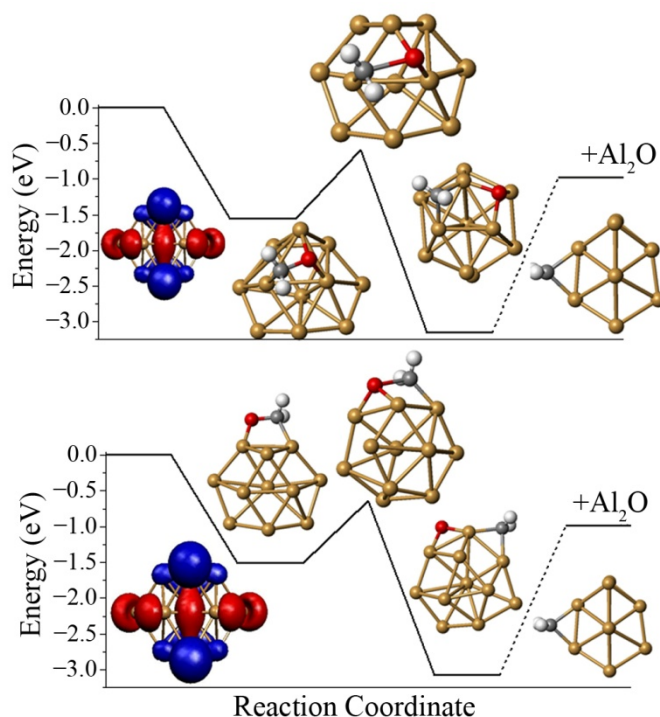


Figure 4.10. Theoretically determined reaction pathways for $\text{Al}_{11}^- + \text{OCH}_2$. The LUMO and LUMO+1 are shown in blue and aqua, respectively, while the HOMO and HOMO-1 are shown in red and orange, respectively. In the upper diagram, the oxygen attacks the LUMO and the carbon bonds to the HOMO, while in the lower pathway the O atom binds to a second site with significant LUMO density, and the C atom binds to the HOMO-1. In both cases, there is sufficient energy available for the reaction to proceed and an Al_2O is lost.

In the first pathway, the O atom interacts with the Lewis acid site of the Al_{11}^- cluster, and the C atom interacts with the HOMO in a manner similar to Al_9^- and Al_{12}^- . There is enough energy to cleave the C–O bond, and then release an Al_2O molecule forming the observed Al_9CH_2^- peak. The second pathway, in which the carbonyl is split along an edge site, differs in that the O atom binds to a site with LUMO density serving as a Lewis acid site, and the C atom binds to a site with HOMO-1 charge density serving as a Lewis base. The barrier of this second pathway is only 0.04 eV higher in energy than the first, and both are energetically plausible. In comparison, the transition state for C=O cleavage on Al_{12}^- is 0.4 eV higher in energy at the edge site of Al_{12}^- than the pathway shown in Figure 4.9.b. This indicates that the strong binding, due to the singly

bonded resonance contributor of formaldehyde being stabilized by bonding to the cluster, reduces the threshold for reactivity.

b. Acetone, Carbon Dioxide, and Carbon Monoxide

To test the limitations of this chemical activity, experiments were carried out in which aluminum cluster anions were reacted with three carbonyl-containing species of differing bond strength: acetone (771.4 kJ/mol); carbon dioxide (532.2 kJ/mol); and carbon monoxide (1076.4 kJ/mol).³⁴ In these experiments, similar reactivity was observed with acetone, while carbon dioxide and carbon monoxide showed no reactivity, even though carbon dioxide has a lower bond dissociation enthalpy than formaldehyde and acetone (Figure 4.11). The absence of any noticeable change in the intensity of clusters distribution for the reactivity with CO and CO₂ suggests that there is no unobserved reactivity wherein the C atom and CO dimer favorably leave the cluster once the bond is broken (i.e. Al₁₃⁻ does not increase).^{17,18} This reactivity is interesting, as it suggests that these two must be more reactive because the methylene and 2-propylene allow a greater tendency to the canonical resonance structure of fully charged C and O atoms. In the case of carbon dioxide, the highly electronegative oxygen atom is likely to resist the localization of electrons on the neighboring carbon atom, preventing the weakening of the C–O bond. In the case of carbon monoxide, a canonical double-bonded resonance structure is feasible; however even with such a system there still exists a double bond that is likely too strong to break.

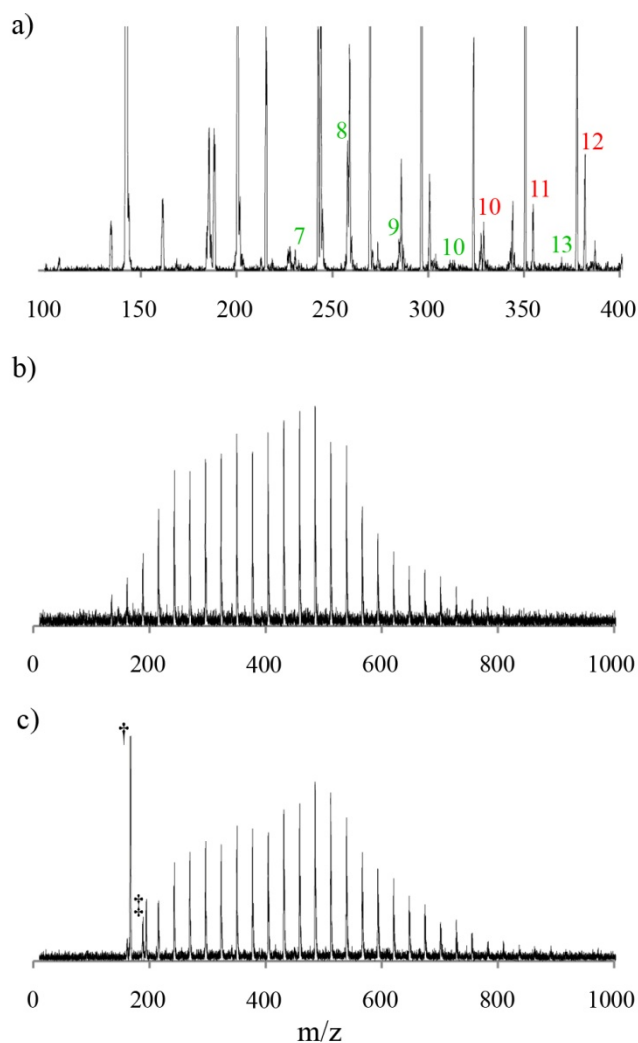


Figure 4.11. Aluminum cluster anion distribution after reaction with a) acetone, b) carbon dioxide, and c) carbon monoxide. Initial distributions were all similar to that shown earlier (Figure 4.8.a). Acetone additions $[\text{Al}_n(\text{OC}(\text{CH}_3)_2)]^-$ are labeled with red numbers, and oxygen losses $[\text{Al}_n\text{C}(\text{CH}_3)_2]^-$ are labeled with green numbers. Additional reactivity with acetone is present due to the methyl leaving group. In (b) and (c), no reactivity is observed two contaminant peaks in (c) can be attributed to (†) $\text{Fe}(\text{CO})_4^-$ and (‡) $\text{Fe}(\text{CO})_5^-$; two common contaminants in bottled carbon monoxide.

5. Conclusions

In conclusion, these experiments have demonstrated that the reactivity of aluminum cluster anions with polar/covalent species has a different fundamental origin than reactions with oxygen. The reactivity is size-selective and entails complementary active sites that can even

cleave the strong C=O bond of formaldehyde. In the reactions with alcohols, the primary products are reactant additions, whereas in the reactions with formaldehyde the primary products are the $\text{Al}_{n-2}\text{CH}_2^-$ species after an Al_2O molecule is released from the cluster. It was discovered that Al_{11}^- was reactive with formaldehyde but not water or alcohols, which is consistent with the strong binding due to the cluster stabilizing the singly bonded C-O resonance structure. Although much of the reactivity in all of these studies is likely due to the large amount of energy gained from aluminum oxide formation, similar complementary active sites on a different surface material could prove to be catalytically active in the cleavage of polar bonds. This cracking mechanism could find wide applications in the formation of fine chemicals, using either bulk surfaces or assemblies of clusters with the desired Lewis-acid/Lewis base sites. Further exploration of gas-phase metal cluster chemistry is necessary to identify additional metals and combinations to fully understand the mechanisms promoted by these active sites as well as their usefulness in their application to large-scale catalysis, but optimistically this research could lead to a material that generates hydrogen from water or catalyzes the activation of polar bonds for the production of fine chemicals. Even if this material is not a true catalyst and requires some form of regeneration via heating or other chemical means, it is reasonable to suppose that it could still demonstrate significant economic value.

6. References

- (1) Castleman, A. W., Jr.; Bowen, K. H. *J. Phys. Chem.* **1996**, *100*, 12911-12944.
- (2) Castleman, A. W., Jr.; Khanna, S. N. *J. Phys. Chem. C* **2009**, *113*, 2664-2675.
- (3) Claridge, S. A.; Castleman, A. W., Jr.; Khanna, S. N.; Murray, C. B.; Sen, A.; Weiss, P. S. *ACS Nano* **2009**, *3*, 244-255.
- (4) Bohme, D. K.; Schwarz, H. *Angew. Chem., Int. Ed. Engl.* **2005**, *44*, 2336-2354.

- (5) Arenz, M.; Landman, U.; Heiz, U. *ChemPhysChem* **2006**, *7*, 1871-1879.
- (6) Parent, D. C.; Anderson, S. L. *Chem. Rev.* **1992**, *92*, 1541-1565.
- (7) Romero, C. P.; Avila, J. I.; Trabol, R. A.; Wang, H.; Vantomme, A.; Van Bael, M. J.; Lievens, P.; Cabrera, A. L. *Int. J. Hydrogen Energy* **2010**, *35*, 2262-2267.
- (8) Mills, G.; Gordon, M. S.; Metiu, H. *J. Chem. Phys.* **2003**, *118*, 4198-4205.
- (9) Lei, Y.; Mehmood, F.; Lee, S.; Greeley, J.; Lee, B.; Seifert, S.; Winans, R. E.; Elam, J. W.; Meyer, R. J.; Redfern, P. C.; Teschner, D.; Schlögl, R.; Pellin, M. J.; Curtiss, L. A.; Vajda, S. *Science* **2010**, *328*, 224-228.
- (10) Das, U.; Raghavachari, K.; Jarrold, C. C. *J. Chem. Phys.* **2005**, *122*, 014313.
- (11) Zemski, K. A.; Justes, D. R.; Castleman, A. W., Jr. *J. Phys. Chem. B* **2002**, *106*, 6136-6148.
- (12) Johnson, G. E.; Mitric, R.; Bonačić-Koutecký, V.; Castleman, A. W., Jr. *Chem. Phys. Lett.* **2009**, *475*, 1-9.
- (13) Roach, P. J.; Woodward, W. H.; Castleman, A. W., Jr.; Reber, A. C.; Khanna, S. N. *Science* **2009**, *323*, 492-495.
- (14) Reber, A. C.; Khanna, S. N.; Roach, P. J.; Woodward, W. H.; Castleman, A. W., Jr. *J. Phys. Chem. A* **2010**, *114*, 6071-6081.
- (15) Reber, A. C.; Khanna, S. N.; Roach, P. J.; Woodward, W. H.; Castleman, A. W., Jr. *J. Am. Chem. Soc.* **2007**, *129*, 16098-16101.
- (16) Roach, P. J.; Woodward, W. H.; Reber, A. C.; Khanna, S. N.; Castleman, A. W., Jr. *Phys. Rev. B* **2010**, *81*, 195404.
- (17) Leuchtner, R. E.; Harms, A. C.; Castleman, A. W., Jr. *J. Chem. Phys.* **1989**, *91*, 2753-2754.
- (18) Leuchtner, R. E.; Harms, A. C.; Castleman, A. W., Jr. *J. Chem. Phys.* **1991**, *94*, 1093-1101.
- (19) Burgert, R.; Schnöckel, H.; Grubisic, A.; Li, X.; Stokes, S. T.; Bowen, K. H.; Ganteför, G. F.; Kiran, B.; Jena, P. *Science* **2008**, *319*, 438-442.
- (20) Mori, S.; Sugino, M.; Tamai, Y. *ASLE Transactions* **1982**, *25*, 261-266.
- (21) Chrétien, S.; Gordon, M. S.; Metiu, H. *J. Chem. Phys.* **2004**, *121*, 3756-3766.
- (22) Sun, J.; Lu, W.; Li, Z.; Wang, C. Z.; Ho, K. M. *J. Chem. Phys.* **2008**, *129*, 014707.
- (23) Somorjai, G. A.; Li, Y. *Introduction to Surface Chemistry and Catalysis*; Wiley & Sons: New York, 2010.

- (24) Kemsley, J. N. *Chem. Eng. News* **2009**, 87, 30.
- (25) Guo, B. C.; Kerns, K. P.; Castleman, A. W., Jr. *Science* **1992**, 255, 1411-1413.
- (26) Castleman, A. W., Jr.; Weil, K. G.; Sigsworth, S. W.; Leuchtner, R. E.; Keesee, R. G. *J. Chem. Phys.* **1987**, 86, 3829-3835.
- (27) Röttgen, M. A.; Judai, K.; Antonietti, J. M.; Heiz, U.; Rauschenbach, S.; Kern, K. *Rev. Sci. Instrum.* **2006**, 77, 013302.
- (28) Grubisic, A.; Li, X.; Gantefoer, G.; Bowen, K. H.; Schnoeckel, H.; Tenorio, F. J.; Martinez, A. *J. Chem. Phys.* **2009**, 131, 184305.
- (29) Guevara-Garcia, A.; Martinez, A.; Ortiz, J. V. *J. Chem. Phys.* **2005**, 122, 214309.
- (30) Bonačić-Koutecký, V.; Burda, J.; Mitric, R.; Ge, M. F.; Zampella, G.; Fantucci, P. *J. Chem. Phys.* **2002**, 117, 3120-3131.
- (31) Sanchez, A.; Abbet, S.; Heiz, U.; Schneider, W. D.; Hakkinen, H.; Barnett, R. N.; Landman, U. *J. Phys. Chem. A* **1999**, 103, 9573-9578.
- (32) Anderson, J. A.; García, M. F. *Supported Metals in Catalysis*; Imperial College Press: London, 2005.
- (33) Carley, A. F.; Roberts, M. W. *Surface Chemistry and Catalysis*; Kluwer Academic Publishers: Norwell, MA, 2002.
- (34) Chase, M. W. *NIST-JANAF Thermochemical Tables*, 4th ed.; *J. Phys. Chem. Ref. Data*, **1998**, Monograph 9.
- (35) Delbecq, F.; Sautet, P. *Langmuir* **1993**, 9, 197-207.
- (36) Gomes, J. R. B.; Gomes, J. A. N. F.; Illas, F. *J. Mol. Catal. A* **2001**, 170, 187-193.
- (37) Helander, K. G. *Biotech. Histochem.* **2000**, 75, 19-22.
- (38) Ruatta, S. A.; Anderson, S. L. *J. Chem. Phys.* **1988**, 89, 273-286.
- (39) Cooper, B. T.; Parent, D.; Buckner, S. W. *Chem. Phys. Lett.* **1998**, 284, 401-406.
- (40) Perdew, J. P.; Burke, K.; Ernzerhof, M. *Phys. Rev. Lett.* **1996**, 77, 3865-3868.
- (41) Köster, A. M.; Calaminici, P.; Casida, M. E.; Flores-Moreno, R.; Geudtner, G.; Goursot, A.; Heine, T.; Ipatov, A.; Janetzko, F.; del Campo, J. M.; Patchkovskii, S.; Reveles, J. U.; Salahub, D. R.; Vela, A. *deMon2k*, ver. 2.3.6, The deMon Developers: Cinvestav, Mexico, 2010. Available at <http://www.deMon-software.com>.

(42) del Campo, J. M.; Köster, A. M. *J. Chem. Phys.* **2008**, *129*, 024107.

Chapter 5

Deposition

Reprinted with permission from the *Journal of Physical Chemistry C* **2011**, 115, 5373-5377.

Copyright 2011 American Chemical Society.

1. Introduction

It was outlined in Chapter 1 how, in the past decade, the potential use of all-metal clusters in forming cluster-assembled materials has generated great interest in the behavior of clusters on surfaces.¹⁻⁴ In the gas-phase, small clusters have been shown to exhibit properties substantially different from bulk materials as well as from each other as even a single atom is added or removed.^{5,6} Some of these properties find potential use in large-scale applications, such as the catalytic properties of particular gold clusters (with bulk gold proving relatively unreactive),^{7,8} the resistance to oxygen etching exhibited by particular aluminum clusters and the production of energetic materials,⁹⁻¹¹ or the selectivity of the band gap and optical properties based on specific precise clusters.¹² Unfortunately, due to the free-electron characteristics and thus reactivity of metal clusters, precisely controlled deposition onto surfaces has proven difficult. Assuming a cluster can be successfully soft landed without implanting, embedding, or fragmenting, theoretical studies suggest that in many cases the cluster will deform on the surface, thus losing its desirable electronic and geometric structure.^{13,14} Once successfully soft landed onto a surface, clusters have been shown to diffuse until they bind to defect sites, step edges, or reactive sites, and depending on their abundance, can then agglomerate into large islands that, due to the strongly size-dependent properties of smaller clusters, no longer exhibit their original properties.¹⁵

To be sure, there are a number of published examples of deposited cluster systems that display characteristics so interesting that they have prompted the growth of an entire sub-field of cluster science involving clusters on diverse surfaces, including metals, metal oxides, graphite, and silicon.¹⁶⁻²⁸ However, it should be acknowledged that in most examples the electronic and geometric structures of the deposited clusters were found to be notably different than the same clusters in the gas-phase, with few exceptions.^{17,19,29,30} Clusters can also be grown on a surface using controlled defect sites,³¹ although this will likely lead to a size distribution instead of cluster sizes with an exact number of atoms, which is not optimal for size-specific cluster reactivity. Therefore, in order to utilize the unique properties of specific small metal clusters on surfaces, they must either be deposited such that their structure on the surface leads to desired properties and characterized *ex post*,^{32,33} or they must selectively react with the surface in a manner predicted using gas-phase reactivity studies.

Recently, Roach *et al.* characterized the size-selective gas-phase reactivity of aluminum cluster anions with water.³⁴ This initial study has since been expanded upon,³⁵ and through a combination of experiment and theory, it is now understood that much of a particular aluminum cluster's size dependence stems from complementary active sites on its surface. The first active site behaves as a Lewis acid, accepting electrons from a nucleophile, such as the oxygen in a water molecule. The second active site subsequently acts as a Lewis base, bonding to a hydrogen atom on the same water molecule, causing the O–H bond to stretch and eventually break. Several different aluminum clusters exhibit strong tendencies for this type of chemisorption due to these complementary active sites, including Al_{12}^- , Al_{16}^- , Al_{17}^- , Al_{18}^- , and Al_{23}^- . Additionally, it has recently been confirmed that, as the second hydrogen plays no role, this identified reactivity applies to any molecule with a hydroxyl group, not just water.³⁶

Of the reactive clusters mentioned above, Al_{17}^- is unique in that it exhibits *several* active sites, one on each face of its structure. It can then be surmised that an Al_{17}^- cluster approaching a

hydroxyl group would have a high probability of interacting in this manner to form a chemisorbed product. Further, it can be conjectured that a self-assembled monolayer (SAM) consisting of only hydroxyl-terminated molecules would present a continuous surface of nucleophiles, each able to donate electrons to the approaching cluster and thus link the cluster covalently to the substrate. At low kinetic energies, this reaction could occur before the cluster fully impacted the surface. Presently, it is unclear whether any of the other three active sites on the Al_{17}^- would bind to other hydroxyl groups on the surface (because of geometric constraints). Similar studies have been performed with the soft landing of organic molecules on SAMs,³⁷ the deposition of pre-tethered assemblies onto a surface,³⁸ and even of peptide ions onto SAMs where the ions not only bind as predicted, but they also retain their charge.³⁹ However, since Al_{17}^- and Al_{17}^0 clusters have similar structures and metallic characteristics, the charge of such a deposited species would be irrelevant when using standard microscopic techniques.^{40,41}

Here, we present a study in which we soft land Al_{17}^- clusters onto hydroxyl-terminated SAMs using reactivity previously characterized in the gas-phase before imaging the deposited clusters via scanning tunneling microscopy (STM). This is a novel deposition scheme where fragile all-metal clusters are deposited in a predictable fashion, and is an important first step in the bottom-up construction of substrate-supported clusters. While the interactions of metal nanoparticles on surfaces and their subsequent catalytic behavior have yielded interesting and valuable chemistry in the past, here we are specifically referring to size-dependent cluster reactivity with a surface as a proof-of-concept experiment, and not as a proposed catalytically active surface. In addition to size-selective cluster deposition, this study furthers the concept of clusters covalently-bonded in a predictable manner that will eventually enable the formation of cluster-assembled materials wherein the clusters retain their desirable size-selective properties.

2. Results and Discussion

Experimental details on cluster creation and the deposition process are outlined in §2.2 and §2.6, respectively. Gas-phase aluminum cluster size distributions were characteristic of those previously observed using this apparatus,^{34,35} and are not shown here. Once an acceptable ion signal was achieved, the sample was moved into the path of the ion beam. Throughout the deposition the sample was periodically moved in order to re-tune the ion optics and to confirm the ion signal. Cluster production steadily decreased over time, eventually disappearing altogether; restoring the LaVa source required an extensive cleaning procedure. Similar studies have shown that SAMs at room temperature degrade somewhat.⁴² Therefore, the deposition time was limited to the lifetime of the source, ~7 hrs. Although the signal intensity fluctuated, a rough estimate for calculating ion current is $\sim 2 \times 10^8 \text{ Al}_{17}^-$ clusters deposited per second, or ~32 pA. With a surface diameter of 0.75 cm and a deposition time of 7 hrs, this would yield approximately 1×10^5 clusters per square micron. Thus, we expected to observe small quantities of well-separated clusters in most STM images, but further expected that toward the center of the focusing region there would be greater areal densities of clusters. Immediately following deposition, the sample was transferred to the STM held at 4 K via the vacuum suitcase.

Experimental details on the STM are outlined in §2.7. Over a period of several days, multiple images were collected that each contained at least one Al_{17}^- cluster (Figure 5.1). While the cluster's apparent diameters are greater than any estimates for the physical dimensions of isolated gas-phase clusters deduced by density functional theory,^{35,41} STM images convolute sample geometric structure and electronic structure and tip structure such that apparent sizes are typically substantially larger than actual physical dimensions.^{29,43,44} Protruding features on surfaces have the effect of “imaging” the probe tip and can appear convoluted with the size and shape of the tip.^{45,46}

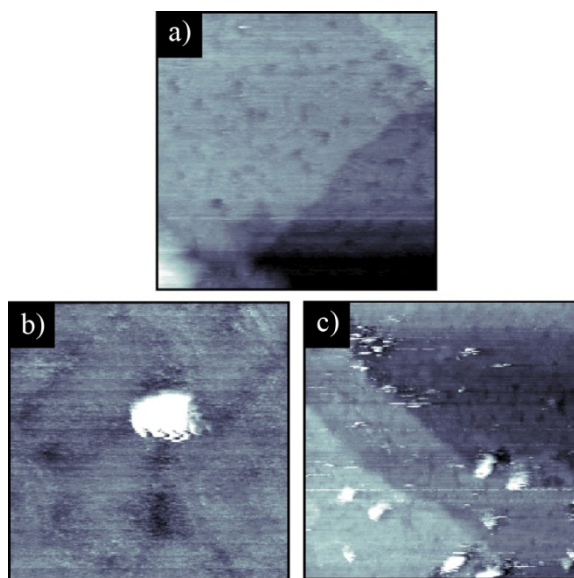


Figure 5.1. Scanning tunneling microscopy images of a) a hydroxyl-terminated self-assembled monolayer (SAM) and b) & c) Al_{17}^- clusters. The clusters were stable to repeated imaging, indicating covalent attachment to the SAM.⁴⁵ (a) $V_s = 1 \text{ V}$, $I_t = 15 \text{ pA}$, $800 \text{ \AA} \times 800 \text{ \AA}$; (b) $V_s = 1.5 \text{ V}$, $I_t = 15 \text{ pA}$, $320 \text{ \AA} \times 320 \text{ \AA}$; (c) $V_s = 2 \text{ V}$, $I_t = 10 \text{ pA}$, $1300 \text{ \AA} \times 1300 \text{ \AA}$.

Clusters deposited directly onto surfaces with no covalent attachment are easily displaced by the STM tip.^{45,47,48} During data acquisition, the clusters were stable over repeated scans; thus, we conclude that the clusters were covalently bound to the surface. In order to test whether the clusters retain free-electron behavior, scanning tunneling spectroscopy was performed on isolated, stable clusters and also on the surrounding SAM surface, as shown in Figure 5.2. The $I(V)$ and dI/dV spectra acquired over the SAM (magenta) are typical of *n*-alkanethiolate SAMs.⁴⁹ The $I(V)$ and $dI/dV(V)$ acquired over the cluster (blue) shows a region of zero conductance. Spectra acquired over metal clusters exhibit zero-conductance behavior.^{45,50-52} This is expected if the clusters retain their free-electron behavior. By averaging several spectra, the measured gap between the highest occupied molecular orbital and the lowest unoccupied molecular orbital (HOMO-LUMO gap) was found to be 1.4 eV. However, this is not a comprehensive average of a sufficient number of independent clusters to elucidate systematic variations in this value.^{45,53} Rather, the observed gap, which qualitatively suggests a double-barrier tunneling junction, confirms that the observed species are, in fact, metal clusters.

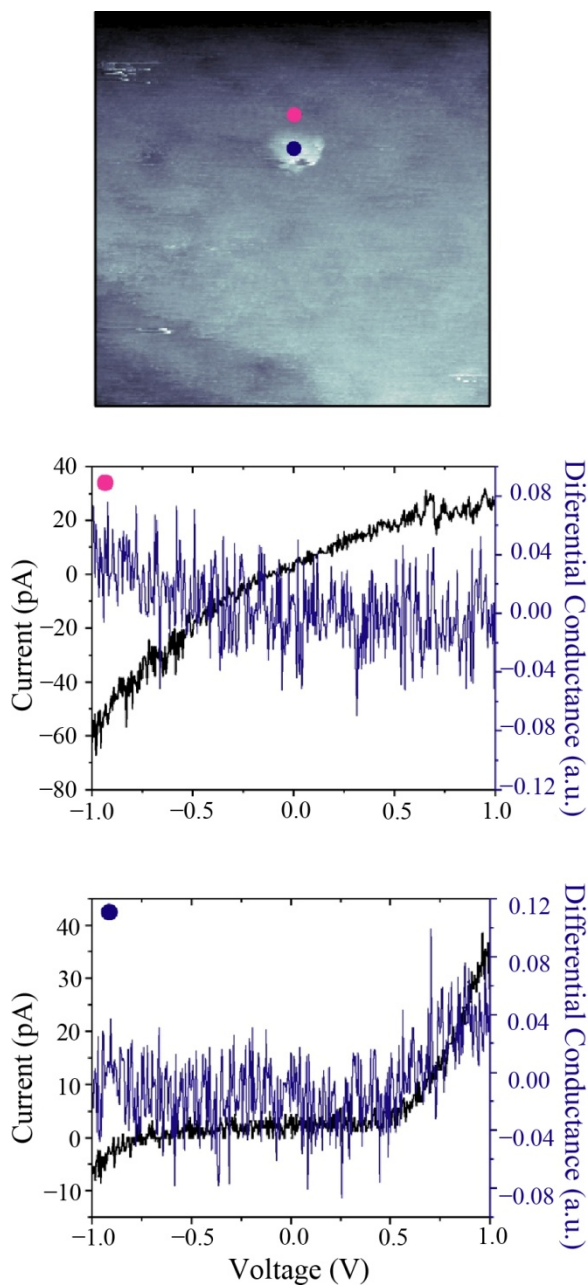


Figure 5.2. Scanning tunneling microscopy image ($V_s = 2$ V, $I_t = 8$ pA, $400 \text{ \AA} \times 400 \text{ \AA}$) of an Al_{17}^- cluster adsorbed to a hydroxyl-terminated self-assembled monolayer (SAM). Tunneling spectra were acquired over the SAM (magenta) and cluster (blue) over ± 2.5 V. A region of zero conductance can be seen in the $I(V)$ spectrum acquired over the cluster. The measured HOMO-LUMO gap is 1.4 eV. No further gaps were observed beyond ± 1.0 V, and so the spectra is condensed accordingly for clarity.

As in our earlier work, the *combined* spectra are consistent with what one might expect for such tethered clusters in terms of zero-conductance regions whereas individual spectra give many different values.⁴⁵ The origins of this spectral diffusion remain unknown.

It would be naïve to assume that the deposited Al_{17}^- clusters, which have previously been shown to react readily with oxygen,⁹ would not become contaminated over time, as minute amounts of oxygen are present in any vacuum apparatus.⁴⁵ Once at low temperature, the oxygen partial pressure is indeed negligible and the tethered clusters were stable; and although the clusters are likely to be partially oxidized, their stability and the existence of a double-barrier tunneling junction suggests a covalent bond of the $\text{Al}_{17}\text{O}_n^-$ cluster with the surface and not the full oxidation of the clusters into an agglomeration of aluminum oxide, which would behave as an insulator. This observation, combined with the cleanliness of the surface and the absence of small defect sites, supports our claim that the clusters are not merely agglomerated islands of aluminum or aluminum oxide, but are individually deposited metallic clusters.

This work has demonstrated that, using previously characterized gas-phase reactivity, it is possible to soft land mass-selected clusters on a chemically functionalized surface by having them covalently bond in a predictable fashion. Using the massive collection of gas-phase cluster reactivity known, this technique can now be adapted such that the resulting reaction product forms a complex with desired and predictable properties, such as resistance to oxygen etching.

3. Conclusions

We have successfully deposited size-selected aluminum cluster anions onto a SAM employing reactivity previously determined in the gas-phase. This is an important step in the use of gas-phase data in the controlled, chemically selective deposition of cluster-assembled materials and supports the importance of continued gas-phase research. Due to the high reactivity of

aluminum clusters with oxygen and the finite lifetime of the SAM, it would be desirable to utilize this technique on a more resilient surface with a cluster-reactant complex that appears “magic” in the gas-phase, thus creating surface-bound clusters that are stable under ambient conditions. This initial proof-of-concept experiment enabled us to test our hypothesis regarding cluster reactivity with surfaces. Future studies will further expand this idea to enable the deposition of clusters on surfaces that can withstand standard atmospheric conditions for extended periods, and with size-selective cluster production techniques constantly improving, the possibility of selective cluster deposition for use in catalysis or the construction of cluster-assembled materials may someday become a reality.

4. References

- (1) Castleman, A. W., Jr.; Khanna, S. N. *J. Phys. Chem. C* **2009**, *113*, 2664-2675.
- (2) Claridge, S. A.; Castleman, A. W., Jr.; Khanna, S. N.; Murray, C. B.; Sen, A.; Weiss, P. S. *ACS Nano* **2009**, *3*, 244-255.
- (3) Woodruff, D. P. *The Chemical Physics of Solid Surfaces*, Vol. 12; Elsevier Science: New York, 2007.
- (4) Meiwes-Broer, K. H. *Metal Clusters at Surfaces: Structure, Quantum Properties, Physical Chemistry*; Springer: New York, 2000.
- (5) Bergeron, D. E.; Roach, P. J.; Castleman, A. W., Jr.; Jones, N.; Khanna, S. N. *Science* **2005**, *307*, 231-235.
- (6) Roach, P. J.; Reber, A. C.; Woodward, W. H.; Khanna, S. N.; Castleman, A. W., Jr. *Proc. Natl. Acad. Sci. U.S.A.* **2007**, *104*, 14565-14569.
- (7) Yoon, B.; Hakkinen, H.; Landman, U.; Worz, A. S.; Antonietti, J. M.; Abbet, S.; Judai, K.; Heiz, U. *Science* **2005**, *307*, 403-407.
- (8) Herzing, A. A.; Kiely, C. J.; Carley, A. F.; Landon, P.; Hutchings, G. J. *Science* **2008**, *321*, 1331-1335.
- (9) Leuchtner, R. E.; Harms, A. C.; Castleman, A. W., Jr. *J. Chem. Phys.* **1989**, *91*, 2753-2754.

- (10) Reber, A. C.; Khanna, S. N.; Roach, P. J.; Woodward, W. H.; Castleman, A. W., Jr. *J. Am. Chem. Soc.* **2007**, *129*, 16098-16101.
- (11) Burgert, R.; Schnöckel, H.; Grubisic, A.; Li, X.; Stokes, S. T.; Bowen, K. H.; Ganteför, G. F.; Kiran, B.; Jena, P. *Science* **2008**, *319*, 438-442.
- (12) Leuchtner, R. E.; Harms, A. C.; Castleman, A. W., Jr. *J. Chem. Phys.* **1991**, *94*, 1093-1101.
- (13) Cleveland, C. L.; Landman, U. *Science* **1992**, *257*, 355-361.
- (14) Nacer, B.; Massobrio, C.; Félix, C. *Phys. Rev. B* **1997**, *56*, 10590-10595.
- (15) Francis, G. M.; Goldby, I. M.; Kuipers, L.; von Issendorff, B.; Palmer, R. E. *Dalton Transactions* **1996**, 665-671.
- (16) Jensen, P. *Rev. Mod. Phys.* **1999**, *71*, 1695.
- (17) Messerli, S.; Schintke, S.; Morgenstern, K.; Sanchez, A.; Heiz, U.; Schneider, W. D. *Surf. Sci.* **2000**, *465*, 331-338.
- (18) Yamaguchi, W.; Yoshimura, K.; Tai, Y.; Maruyama, Y.; Igarashi, K.; Tanemura, S.; Murakami, J. *Chem. Phys. Lett.* **1999**, *311*, 341-345.
- (19) Claeysens, F.; Pratontep, S.; Xirouchaki, C.; Palmer, R. E. *Nanotechnology* **2006**, *17*, 805-807.
- (20) Yasumatsu, H.; Hayakawa, T.; Koizumi, S.; Kondow, T. *J. Chem. Phys.* **2005**, *123*, 124709.
- (21) Lee, S.; Lee, B.; Mehmood, F.; Seifert, S.; Libera, J.; Elam, J.; Greeley, J.; Zapol, P.; Curtiss, L.; Pellin, M.; Stair, P.; Winans, R.; Vajda, S. *J. Phys. Chem. C* **2010**, *114*, 10342-10348.
- (22) Kandel, S. A.; Weiss, P. S. *J. Phys. Chem. B* **2001**, *105*, 8102-8106.
- (23) Kushmerick, J. G.; Weiss, P. S. *J. Phys. Chem. B* **1998**, *102*, 10094-10097.
- (24) Kuk, Y.; Jarrold, M. F.; Silverman, P. J.; Bower, J. E.; Brown, W. L. *Phys. Rev. B* **1989**, *39*, 11168-11170.
- (25) Kaden, W. E.; Wu, T. P.; Kunkel, W. A.; Anderson, S. L. *Science* **2009**, *326*, 826-829.
- (26) Lee, S.; Molina, L. M.; Lopez, M. J.; Alonso, J. A.; Hammer, B.; Lee, B.; Seifert, S.; Winans, R. E.; Elam, J. W.; Pellin, M. J.; Vajda, S. *Angew. Chem., Int. Ed. Engl.* **2009**, *48*, 1467-1471.
- (27) Lee, S. S.; Fan, C. Y.; Wu, T. P.; Anderson, S. L. *J. Am. Chem. Soc.* **2004**, *126*, 5682-5683.
- (28) Lightstone, J. M.; Patterson, M. J.; Liu, P.; Lofaro, J. C.; White, M. G. *J. Phys. Chem. C* **2008**, *112*, 11495-11506.

- (29) Schouteden, K.; Vandamme, N.; Janssens, E.; Lievens, P.; Van Haesendonck, C. *Surf. Sci.* **2008**, *602*, 552-558.
- (30) Duffe, S.; Irawan, T.; Bielecki, M.; Richter, T.; Sieben, B.; Yin, C.; Issendorff, B.; Moseler, M.; Hovel, H. *Eur. Phys. J. D* **2007**, *45*, 401-408.
- (31) Brune, H.; Giovannini, M.; Bromann, K.; Kern, K. *Nature* **1998**, *394*, 451-453.
- (32) Sanchez, A.; Abbet, S.; Heiz, U.; Schneider, W. D.; Hakkinen, H.; Barnett, R. N.; Landman, U. *J. Phys. Chem. A* **1999**, *103*, 9573-9578.
- (33) Chrétien, S.; Buratto, S. K.; Metiu, H. *Curr. Opin. Solid State Mater. Sci.* **2007**, *11*, 62-75.
- (34) Roach, P. J.; Woodward, W. H.; Castleman, A. W., Jr.; Reber, A. C.; Khanna, S. N. *Science* **2009**, *323*, 492-495.
- (35) Reber, A. C.; Khanna, S. K.; Roach, P. J.; Woodward, W. H.; Castleman, A. W., Jr. *J. Phys. Chem. A* **2010**, *114*, 6071-6081.
- (36) Roach, P. J.; Woodward, W. H.; Reber, A. C.; Khanna, S. K.; Castleman, A. W., Jr. *In Press*. **2010**.
- (37) Shen, J. W.; Evans, C.; Wade, N.; Cooks, R. G. *J. Am. Chem. Soc.* **1999**, *121*, 9762-9763.
- (38) Peng, W. P.; Johnson, G. E.; Fortmeyer, I. C.; Wang, P.; Hadjar, O.; Cooks, R. G.; Laskin, J. *Phys. Chem. Chem. Phys.* **2011**, *13*, 267-275.
- (39) Laskin, J.; Wang, P.; Hadjar, O. *Phys. Chem. Chem. Phys.* **2008**, *10*, 1079-1090.
- (40) Ma, L.; Issendorff, B.; Aguado, A. *J. Chem. Phys.* **2010**, *132*, 104303.
- (41) Chuang, F. C.; Wang, C. Z.; Ho, K. H. *Phys. Rev. B* **2006**, *73*.
- (42) Poirier, G. E. *Langmuir* **1999**, *15*, 1167-1175.
- (43) Eigler, D. M.; Weiss, P. S.; Schweizer, E. K.; Lang, N. D. *Phys. Rev. Lett.* **1991**, *66*, 1189-1192.
- (44) Weiss, P. S.; Eigler, D. M. *Phys. Rev. Lett.* **1993**, *71*, 3139-3142.
- (45) Smith, R. K.; Nanayakkara, S. U.; Woehle, G. H.; Pearl, T. P.; Blake, M. M.; Hutchison, J. E.; Weiss, P. S. *J. Am. Chem. Soc.* **2006**, *128*, 9266-9267.
- (46) Cygan, M. T.; Dunbar, T. D.; Arnold, J. J.; Bumm, L. A.; Shedlock, N. F.; Burgin, T. P.; Jones, L.; Allara, D. L.; Tour, J. M.; Weiss, P. S. *J. Am. Chem. Soc.* **1998**, *120*, 2721-2732.
- (47) McCarty, G. S.; Love, J. C.; Kushmerick, J. G.; Charles, L. F.; Keating, C. D.; Toleno, B. J.; Lyn, M. E.; Castleman, A. W., Jr.; Natan, M. J.; Weiss, P. S. *J. Nanoparticle Res.* **1999**, *1*, 459-466.

- (48) Moore, A. M.; Dameron, A. A.; Mantooth, B. A.; Smith, R. K.; Fuchs, D. J.; Ciszek, J. W.; Maya, F.; Yao, Y. X.; Tour, J. M.; Weiss, P. S. *J. Am. Chem. Soc.* **2006**, *128*, 1959-1967.
- (49) Blake, M. M.; Nanayakkara, S. U.; Claridge, S. A.; Fernandez-Torres, L. C.; Sykes, E. C. H.; Weiss, P. S. *J. Phys. Chem. A* **2009**, *113*, 13167-13172.
- (50) Amman, M.; Wilkins, R.; Benjacob, E.; Maker, P. D.; Jaklevic, R. C. *Phys. Rev. B* **1991**, *43*, 1146-1149.
- (51) Dorogi, M.; Gomez, J.; Osifchin, R.; Andres, R. P.; Reifenberger, R. *Phys. Rev. B* **1995**, *52*, 9071-9077.
- (52) Andres, R. P.; Bein, T.; Dorogi, M.; Feng, S.; Henderson, J. I.; Kubiak, C. P.; Mahoney, W.; Osifchin, R. G.; Reifenberger, R. *Science* **1996**, *272*, 1323-1325.
- (53) McCarty, G. S.; Weiss, P. S. *Chem. Rev.* **1999**, *99*, 1983-1990.

Chapter 6

Final Considerations

1. Review of Current Aluminum Cluster Research

Throughout the course of this dissertation it has been the goal of this author to both discuss the work performed over the past five years and also to relate this work to the possibility of using this aluminum cluster research in real-world applications such as cluster-assembled materials or as the basis for a catalyst. In order to perform the research presented here, a custom-built state-of-the-art vacuum apparatus was constructed almost entirely from the ground up. It is the author's wish that this instrument not only continues to produce valuable data relating to gas-phase and deposited cluster reactivity, but also serve as an example to others wishing to build an instrument with any similar characteristics. With this instrument a novel study was performed involving the reactivity of aluminum cluster anions with singlet and triplet oxygen. With the combination of a singlet oxygen generator and a laminar flow tube, a new species (Al_9^-) was identified as being resistant to reaction with ground-state triplet oxygen. Additionally, reaction studies were carried out between aluminum cluster anions and various molecules with polar functional groups. It was found that a specific mechanism involving complementary active sites promotes the cleavage of these polar bonds. While not a catalytic mechanism in itself, this reactivity could potentially be duplicated on a surface either as a stand-alone catalyst or a regenerable one (e.g. rechargeable hydrogen fuel cells). This mechanism was also used to deposit aluminum clusters onto a surface. This unique proof-of-concept study showed that it is possible to deposit these fragile clusters onto a surface and examine them using scanning tunneling microscopy. In addition, a new spectroscopic technique, matrix isolation cavity ringdown

spectroscopy, has been developed for the controlled construction and deposition of cluster-assembled materials (Appendix B). It has been the goal of this dissertation to logically explain the design and execution of these experiments and coherently discuss the results. For a conclusion, we will now discuss future experiments that these studies could influence and hypothesize as to the long-term future of cluster-assembled materials. These prognostications should be considered the opinions of the author, but nevertheless they are based on realistic goals.

2. Future Research in Energetic Materials

It was described in Chapter 1 how specific clusters can be considered “magic” in that their inertness could allow them to exist as stable materials. In Chapter 3, however, it is concluded that Al_{13}^- , previously considered to be inert to nearly all reactivity, in fact readily reacts with singlet oxygen. This should not be considered a crippling blow to cluster-assembled materials, as singlet oxygen reacts quite readily with many things in nature that are considered stable, and its presence is quite rare under normal conditions. The truly exciting future of aluminum cluster reactivity with oxygen, then, lies in the possibility of building a cluster-assembled high energy density material with aluminum clusters. By using all-metal clusters as one component of an ionic compound, the speed at which the material burns could be controlled by the second component. Traditional explosives rely on a careful balance between their oxygen content and their unoxidized elements which, when ignited, creates their final lowest-energy oxidized formations (i.e. an oxygen balance of zero). The energy released from the initial ignition fuels a chain reaction that breaks up the compound, thus freeing the constituents for oxidation. Ideally these oxygen-fuel ratios should be as ideal as possible, but other factors such as stability and sensitivity are necessary considerations when designing such potentially dangerous matter. Alternatively, some fuels rely on the oxygen in the air to burn. These slow-burning fuels can also

be used in thermobaric explosives, where the fuel particles are distributed throughout the air before being ignited. In the function of aluminum-based cluster-assembled materials, complementary ions with large amounts of oxygen would allow the compound to explode quite quickly to form alumina, Al_2O_3 . The ideal compound would be composed of these two elements in this exact empirical ratio to minimize its density while maximizing its relative effectiveness, although in reality this is impossible and so a compromise must be reached. Alternatively, aluminum-based cluster-assembled materials with little or no oxygen content could be used in systems where the oxygen is supplied, such as in fuels or thermobaric explosives. This long-term goal of customizable high energy density materials could bring an entirely new perspective to demolition explosives, fuel, and munitions.

3. Future Research in Catalysis and Surface Deposition

In Chapter 4 it is discussed in detail how complementary active sites on select aluminum cluster anions play a crucial role in the cleavage of some polar bonds. This reactivity was demonstrated on hydroxyl, amine, thiol, and carbonyl functional groups, and could almost certainly be applied to other polar bonds as well. To be sure, no catalytic activity in any way was demonstrated, and it has likely not escaped the reader's attention that the reaction pathways may be energetically favorable only because of the irreversible redox reaction (i.e. aluminum oxidation and in some cases the formation of Al_2O). It is mentioned in §4.1 that the formation of hydrogen from water on bulk aluminum surfaces has been observed experimentally, but this is not a repetitive effect; the reaction of the water with the pure aluminum surface likely oxidizes the aluminum, forming an alumina layer. However, the research presented here outlines a mechanism that could possibly be used in a catalytic process. While large-scale catalysis was not a principle topic of this dissertation it is reasonable to propose how this could be accomplished.

Similar catalysts with complementary Lewis acid/Lewis base active sites are known to exist, both on surfaces and in the gas-phase. One such catalyst, with the active sites appropriately spaced, could be used to activate the polar bond for reaction by weakening it or breaking it. This could lead to the formation of fine chemicals or, as suggested by the first reaction investigated, hydrogen production from water. Efficiently breaking or activating the O–H bond and liberating hydrogen from the surface would require precise active site placement as freed hydrogen atoms would need to be in close proximity to bond and desorb, and the surface would likely be poisoned by residual oxygen atoms or hydroxyl groups. In this hypothetical situation, heating the surface could release oxygen, hydrogen peroxide, water, or a combination thereof and effectively regenerate the catalyst. While this is all just speculation, Chapter 4 provides some references to similar catalysts, both on surfaces and in the solution-phase. The argument for the importance of clusters in catalytic research has been made here and in many other works, but it should be somewhat convincing that this exact mechanism could find practical use in large-scale (i.e. industrial) applications.

The deposition work presented in Chapter 5 suggests some future projects that are not quite as long-term. It has been shown that aluminum cluster anions with specific complementary active sites can be bound to a surface using chemistry determined in the gas-phase. It has also been shown (Chapter 4) that individual clusters demonstrate a specific number of active sites, and that these sites can be used to sterically protect the cluster (i.e. with *t*-butanol). One cluster in particular, Al_{15}^- , was unique in that it required only a single *t*-butanol to become “magic” (Figure 4.5.c). The next step for this research, therefore, should be to attempt to deposit Al_{15}^- clusters onto a hydroxyl-terminated self-assembled monolayer using the same experimental technique. It is not entirely known why the $\text{Al}_{15}(\textit{t}\text{-butanol})^-$, or for that matter any of the other $\text{Al}_n(\textit{t}\text{-butanol})_m^-$ clusters, seem so stable, but if the cluster achieves some sort of electronic stability in addition to steric protection from the cumbersome ligand, it is reasonable to suppose that the surface would

protect the cluster in a similar manner and that the deposited cluster would be more stable than Al_{17}^- under the same conditions. The extent of this stability is not known, and theoretical studies have not yielded any answers, but it is nevertheless an interesting concept. Of course, the stable deposition of Al_{15}^- onto a hydroxyl-terminated self-assembled monolayer would be interesting, but not practical. Al_{15}^- shows no potential for use in such fields as energetic materials or catalysis, but its stability would provide a step forward in the construction of cluster-assembled materials.

Matrix-isolation cavity ringdown spectroscopy, on the other hand, could provide a true breakthrough in this field. Granted, the absorption spectra of aluminum cluster anions in a matrix will yield new insights that photoelectron spectroscopy cannot, and cavity ringdown spectroscopy of clusters in a matrix and on a surface has existed for years. The true novelty of the technique, therefore, lies in the ability to slowly react clusters with reactants and with each other. Monitoring a single absorption peak while a matrix-phase reaction takes place will, with theoretical support, provide clues as to the behavior of nascent cluster-assembled materials as they slowly grow. Ultimately, the goal will be to freeze complementary anions and cations into a matrix, then slowly evaporate the matrix away, allowing the clusters/ligands to form a salt as predicted by theoretical studies. This crystal would then settle onto a surface (repeated studies would eliminate the need for spectroscopic measurements, and so the surface material options could be limitless) where it could be examined using any number of analytical techniques, including scanning tunneling microscopy/spectroscopy, scanning/tunneling electron microscopy, X-ray crystallography, etc. The techniques and cluster sources developed in this lab were specifically built to study minute amounts of gas-phase clusters. Once a true ground-up cluster-assembled material has been created in any quantity, research will begin to be directed toward larger scales. This progression of molecular-to-bulk scale has been seen in the past with atomic isotopes and fullerenes, and the development of industrial-scale production methods is always preceded by

laboratory-scale experimentation. The creation of cluster-assembled materials on a surface using matrix-isolation should be considered a reasonable option for assisting this forward progress.

4. Closing Remarks

The field of metal clusters has been continuously growing since its birth in the latter half of the twentieth century, although its background can be traced to the nineteenth century and arguably even to medieval times, if the oft-used example of nanoparticles in colored glass is to be allowed. Gas-phase research of cluster properties continues both because these smaller species provide insights into chemistry that cannot possibly be achieved through large-scale experiments where infinite variables cloud specific mechanisms, and also because of the hope that one day cluster-assembled materials and a 3-D periodic table will allow the construction of bulk matter with a limitless range of properties. Although this goal is still quite distant, it is the sincere belief of this author that this is not a pipe dream, and that every experiment brings the world closer to these customizable materials. In the field of energetic materials, mankind has possibly reached a plateau in the amount of energy that can be stored in non-fissile materials. Metal clusters, which have the potential to store more energy than traditional carbon- and nitrogen-based molecules, could find widespread use in both slow and fast burning combustible materials such as fuel additives and munitions.

In addition, metal clusters already serve as a means of identifying active sites on bulk catalytic surfaces, but they could also become the basis for catalysts themselves. When cluster-assembled materials become a reality, it could be possible to maximize the activity of a catalyst using bottom-up chemical engineering wherein clusters are either the building blocks of a material or simply the surface structure of base matter via a deposited monolayer of “unified atoms.” The basis for many of these materials has already been explored. Indeed, the history of

clusters has been an exciting and somewhat fruitful one, but all cluster chemists should aspire to make it such that this is remembered as just the beginning.

Appendix A

Fine Experimental Details

1. Overview of Instrumentation

As discussed in Chapter 2, this Appendix serves as a reference to those actually operating the custom vacuum instrument utilized throughout all of the studies presented herein. The organization of this Appendix exactly correlates with Chapter 2 for easy navigation (e.g. §2.2 → §A.2).

2. Cluster Sources

The two clusters sources described here are both custom-made and unique from any other in existence. However, they are both greatly influenced by existing cluster sources, and so the overall principles of their operation are easily referenced (see §2.2). Specific operating conditions for each source are best learned from hands-on experience and referencing past lab notebooks, but their basic characteristics are briefly discussed here.

a. Laser Vaporization Source

The laser vaporization (LaVa) source used today is a custom-made stainless steel dual-rod source with an external motor and constant flow. The exact source was most likely designed and built by Dennis Bergeron in the early 2000s, although no record of it exists until the dissertation of Patrick Roach (2009).¹ In this dissertation the physical aspects of the source are

covered in elaborate detail, and thus no such description is necessary here. What is not discussed, however, is the relationship between this source and the laminar flow tube with respect to the cluster size distribution. The expansion nozzle most commonly utilized is constructed of Teflon and is about 0.025 m long with an inner diameter of 0.0032 m. The pressure inside the source during normal operating conditions is 40 Torr (5.33×10^3 Pa), which suggests a Knudsen number of 2.79×10^{-3} and a terminal Mach number of 12.3. As discussed in §2.3, this system does not utilize supersonic expansion, and so this value is revisited in §A.3.a.

It is interesting to note that the pressure in the source is reached several minutes after the flow of the helium backing gas has been set, and therefore using the backing gas to modify the cluster distribution requires some patience. Even then, however, little change is ever noticed for minor variations in flow, as discussed in §2.2. It is also worth noting that, using the Hagen–Poiseuille law, the conductance of the expansion nozzle can be estimated and calculated, and is typically found to exhibit viscous flow. A typical aluminum cluster anion distribution using this source and nozzle is shown in Figure 2.5.b. While other nozzles have been constructed of varying lengths and inner diameters, none were utilized in the studies presented herein and so relevant aluminum or other metal cluster spectra are not shown, suffice it to say the effects that various source parameters have on the cluster distribution as described in §2.2.a can be observed in the laboratory should one desire to explore these options. Specifically, clusters of coinage metals (e.g. copper, silver, and gold) have been particularly difficult to create with this source, potentially due to their higher melting points. Some success has been achieved with longer, narrower expansion nozzles, but never enough to produce a viable scientific study or warrant further discussion here. One last point of interest is the fact that the source, which is typically loaded with 0.00635 m rods, can accept rods half this diameter, both instead of and concurrent with the larger rod. In this way bimetallic species can be created, although once again this is never a topic of discussion in this dissertation.

b. Magnetron Gas Aggregation Source

Although directly influenced by those of Haberland and Palmer,^{2,3} no other description of the current magnetron gas aggregation source (MagGAS) designed and built by this author currently exists, and so the nuances of its design are presented here. The overall scheme of the source is presented in Figure 2.4. The magnetron head is a Torus circular sputtering source built by Kurt J. Lesker Co. (TRS2HS). The directions for its disassembly and maintenance can all be found elsewhere, but it is important to reiterate here that the source *must* be cooled with water at all times. Anything less than 4 liters per minute could be catastrophic to the magnet, which is quite costly to replace. The main difference between this source and others in the literature is its external cooling. Every other known MagGAS uses a liquid nitrogen cooling jacket, which itself requires an additional surrounding vacuum chamber to reduce heat transfer. The logic behind this design is that the cold outer walls of the source absorb heat from the enclosed gasses and reduce cluster size. Without liquid nitrogen cooling, the size of the clusters created enters the nanometer size regime, which is entirely too big for cluster research. In fact, most of the published sources use liquid nitrogen cooling in order to achieve metal molecules with thousands and even tens of thousands of atoms, and so it would initially appear that liquid nitrogen cooling is absolutely essential for smaller (< 100 atoms) clusters. However, one study found that increased temperatures actually reduced the size distribution due to cluster evaporation, and that the real disadvantage was a drastically increased birth potential (hotter clusters), leading to clusters that cannot be soft-landed. Our instrumental setup, on the other hand, utilizes a laminar flow tube, which already exists to cool the clusters to room temperature, and so it was decided that water cooling was sufficient, drastically reducing size, weight, and cost.

Another important modification is the dark space shield, which constricts the argon plasma to the front of the magnetron head. The required distance between this shield and the head

is dependent on the breakdown voltage of the argon for a given distance and pressure, and can be estimated by using Paschen's law (the same law used to estimate when a plasma will form in the conical octopole, §2.3.c). Basically, at a given pressure the distance required must be shorter than the mean free path of the gas, yet sufficiently long enough so that significant electron tunneling does not occur. The dark space shield included with the original magnetron head assumed pressures much lower than the source is operated at, and so a sleeve was constructed and inserted into the existing shield in order to shorten this distance from 0.01 m to roughly 0.003 m. One final unique aspect of the MagGAS is the adjustable exit iris. Traditional sources utilize an exit aperture that is exchangeable, but requires the venting of the instrument. The adjustable iris utilizes a rotary feedthrough which uses a bevel gear mechanism (Boston Gear GSS486Y-G and P) to turn the lever of a threaded iris (Thor Labs SM1D12SS). Although other adjustable irises have been implemented in the past, it is the opinion of this author that this presents the simplest and most reliable method available.

The rest of the source is fairly straightforward. The power supply originally purchased was a Lambda Americas GEN1500W (GEN600-2.6) which is restricted by a water flow safety. It will not turn on unless sufficient water flow is provided, which is currently supplied by a recirculating chiller (Thermo NesLab System 1) due to inadequate water pressure in the house lines. It is suggested in the literature that the two biggest variables affecting cluster size distribution are the partial pressure of argon and the distance between the head and the exit.⁴ The argon and helium gas pressures are controlled via a series of needle valves on the front of the support rack. Several bellows valves allow the shutoff and pumping of these lines without the need to adjust the needle valves so that experimental conditions can be preserved. It is possible to introduce some helium into the argon gas ring flow, although this has never been observed to affect the mass distribution and so is typically ignored. The position of the head is controlled manually, and the long (0.30 m) neck is supported by two heavy-duty linear bearing supports.

Minor adjustments can be made via a custom-built micrometer screw gauge. Specific experimental settings will vary greatly depending on the cluster distribution desired, and so individual lab notebooks should be consulted for voltages, currents, gas pressures, iris settings, and length. Some example spectra are shown in Figure A.1.

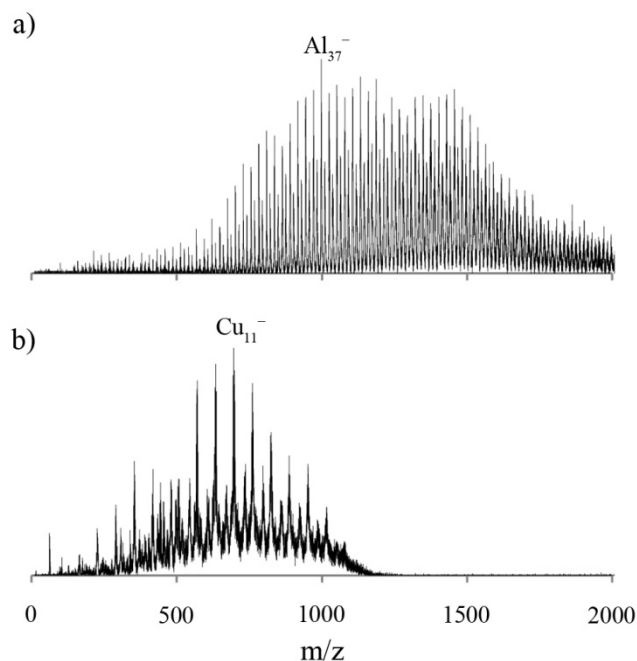


Figure A.1. a) Aluminum and b) copper spectra acquired with custom magnetron gas aggregation source. It can be observed in both spectra that there exists a certain degree of contamination, which in most cases is a combination of carbon and oxygen addition to each cluster.

It can be seen that, although smaller mass distributions are indeed possible with this design, currently there exists a degree of contamination that has thus far proven unsolvable. Because of this, the magnetron source has not yet replaced the LaVa source as originally intended, although progress continues at the time of this writing.

3. Multiple-Ion Laminar Flow Tube

For all of the studies discussed herein, the following parameters were utilized for the laminar flow tube: radius (R) of 0.032 m; distance (L) between reactant gas inlet and conical octopole of 0.60 m; exact total length of flow tube of 1.13 m; flow of helium carrier gas (S) of 2.012×10^{-4} standard cubic meters per second; pressure (P) 0.245 m from end of tube of 0.56 Torr.

a. The Importance of Laminar Flow

It was mentioned in §2.3.a that the exact flow tube used in the studies presented herein was designed, built, and characterized as early as 1987.⁵ However, certain experimental aspects have changed which have subsequently affected parameters such as the Reynolds number, average velocity, etc. The average velocity in the flow tube was measured by pulsing a high voltage on the reactant gas inlet and then measuring the time before the ion signal disappeared from the detector (9.0 ± 0.2 ms). The same process was then used at the first orifice after the conical octopole (1.2 ± 0.2 ms). The difference between the two was then taken to be the average time taken by the ions to travel between the reactant gas inlet and the orifice into high vacuum, which is effectively the reaction time (7.8 ± 0.2 ms). When divided into the distance traveled, an average velocity of 76.9 m/s is determined (the high vacuum region covers a distance of 1.15 m, yielding an average speed of 952.5 m/s). With Equation 2.7 and an assumed viscosity (μ) of 2.08×10^{-5} Pa·s (He at 300 K; Equation 2.6), an average pressure of 0.59 Torr can be estimated. From this, the density (ρ) can be estimated (1.26×10^{-4} kg/m³). Finally, using Equation 2.9, a Reynolds number of 29.8 emerges. Note that, using a flow of 2.012×10^{-4} standard cubic meters per second and Equation 2.8, the velocity can be independently determined (64.2 m/s), which

produces similar results. One final fact to consider here is that at 300 K the speed of sound is 1.02×10^3 m/s, which suggests a terminal Mach number of approximately 0.07. This number confirms that the Mach number of 12.3 calculated for the LaVa source is irrelevant, and that there will be some sort of shockwave which travels back into the LaVa source. The effect of these source conditions is unknown, as outlined in §2.3.b.

b. Kinetic Theory and Rate Constants

The classical derivation of rate constants in a laminar flow tube was outlined in §2.3.b, being pioneered by Ferguson in the late 1960s.⁶ Of the many considerations that Ferguson takes into account, one of course is the absence of an ideal system with regard to reaction time. Even minor defects in the cylindrical flow tube can cause eddies which affect this time constant. Another assumption made with regard to the reaction gas is its instantaneous laminar distribution across the radius of the tube. This is, of course, impossible for any real system, and so in 1986 Castleman attempted to determine how much various reactant gas inlets caused variations in the determined rate constant of a known reaction.⁵ His results suggest that the best reactant gas inlet is a “radial inlet,” which consists of a ring with a diameter 0.375 that of the flow tube and with three holes pointed radially inward and three holes pointed radially outward. This gas inlet was used with the current instrument for nearly all studies presented herein, however, in Chapter 3 a singlet oxygen generator was utilized, wherein all container materials must be constructed of glass to reduce the quenching of singlet oxygen to ground state triplet oxygen. In this situation, a glass finger inlet was utilized. While not as ideal as a radial inlet, the end correction factors determined by Castleman for this exact flow tube suggest that the loss of accuracy is negligible with regard the errors reported in this study.

Also in Chapter 3 it is briefly outlined how individual rate constants are derived from the entire mass distribution of aluminum clusters before and after reactions with oxygen. The computer program used to run these calculations was written by Nicholas Shuman of the Air Force Office of Scientific Research Space Vehicles Directorate. The Pascal programming language was used for the original program, but since this is not a product of this author's intellectual pursuits the many pages of script is not simply listed here as is commonplace in other dissertations. Rather, the mechanisms of the program is explained here in detail with as many layman's terms as possible in order to better help the average reader understand the mathematics involved.

The rate constant equations $\left(\frac{d[Al_n^-]}{dt}\right)$ for the entire aluminum anion series were independently solved via the Euler method, which is a common computational procedure for solving ordinary differential equations.⁷ Developed by the 18th century Swiss mathematician Leonhard Euler, this method uses an initial start point ($t = 0$) where the tangent of the equation is known (i.e. the differential of the equation at that point). This tangent is dependent on the known initial reactant concentrations and the rate constants assumed for the aluminum cluster reactivity series, which are initially placed either too fast or too slow (literally speaking, as fast as the collision rate or too slow to measure, respectively). The tangent is extended linearly by a defined time constant after which a new tangent line is determined using the recalculated reactant concentrations. This process is then repeated until the reaction time is reached, wherein the final concentrations are calculated and compared with the experimentally known final concentrations. The reaction rate constants are then adjusted and the entire process is repeated until the calculated final concentrations are within a defined goodness-of-fit to the experiment, and the estimated rate constants are thus revealed. As can be observed in Equations 3.4 and 3.5, the time-dependent concentration of Al_{n+4}^- is needed for each step. However, it was outlined in Chapter 3 that the

entire cluster distribution can be represented by no more than eight reaction pathways, as the series Al_{n+4x}^- will begin to repeat after four single atom additions, and singlet and triplet oxygen reactions result in two separate rate constants per aluminum cluster ($4 \times 2 = 8$). Therefore, the process starts with the highest available value of x (in this case there is no Al_{n+4}^- and so the equation is simplified) and continues downward until the smallest cluster is reached. Of course, this results in very inaccurate rate constants at the higher masses, but considerably accurate ones in the range of interest. It is also outlined how deviations from Equations 3.4 and 3.5 yield inaccuracies at much lower masses. Once the rate constants were determined for triplet oxygen alone (Equation 3.4), the entire process was repeated for the singlet/triplet oxygen mix (Equation 3.5) with the predetermined triplet oxygen rate constants in order to determine the singlet oxygen rate constants. The limitations of this process are clearly in its large error bars, but two points should be reiterated: 1) The rate constants for these concomitant reactions could not be determined any other way in such a laminar flow tube and 2) twenty years of previous aluminum cluster anion reactivity studies did not reveal Al_9^- as a uniquely stable species because no such studies were run in a laminar flow tube before, and that any previously utilized methods which produced more concrete rate constants never revealed Al_9^- to be worthy of further study, which is why this study was important in its own right. It is also worth mentioning that, when rate constant ratios are determined as in Figure 3.4, the error bars are significantly reduced due to the fact that many of the uncertainties cancel. While the Euler method is probably the easiest form of solving these differential equations, other methods do exist (e.g. Runge–Kutta methods, the simplest of which is actually the Euler method), and should be considered if future studies are performed which desire higher efficiency and less error.

c. Conical Octopole Ion Guide

Although no further descriptions of the conical octopole are necessary, the author would like to point out that the dissertation of Patrick Roach contains some information that was not repeated here but is still quite interesting.¹ This data was presented in poster form at the 56th annual conference of the American Society for Mass Spectrometry.⁸ Specifically, certain experimental studies were performed early in the conical octopole's implementation relating to its ion transmission effectiveness. These studies used ionized noble gasses wherein the ion current was measured before and after the optic in order to calculate loss. The total transmission of the optic was determined to be nearly 100 percent. Theoretical studies were also performed using SIMION simulation software. The results are similar to those presented in §2.3.c, although these are entirely specific to the current conical octopole's shape and therefore considerably more difficult to modify. The author would like to make the point that the equations presented in this dissertation are quite unique and will enable the curious reader to better understand the properties of this novel optic.

4. Differential Pumping

a. Ion Optics and Vacuum Pumps

Nearly all of the ion optics and vacuum pumps in use at the time of this writing were purchased from Pfeiffer Vacuum GmbH. When not in use, the flow tube is pumped via a HiPace 80. The next two chambers are pumped via a SplitFlow TMH 261-250-010 P, and the final chamber is pumped via two TMU 521 P's. These are all backed via two XtraDry™ 150-2's. The cavity ringdown chamber is pumped via a Varian, Inc. StarCell 150, which is not backed. All of

the specifications for these pumps can be easily found elsewhere. The pumps could very well be replaced at any time, and so listing them is seemingly pointless, although the author would like to point out that all of these pumps are “oil-free,” which should contribute to lower pressures. When the laminar flow tube is in use, however, a high-volume pump must be incorporated to deal with the large quantities of gas. This is handled by a Stokes 1721 Mechanical Booster Pump, which consists of a high-speed blower (Stokes 615; $0.61 \text{ m}^3/\text{s}$) coupled to a Microvac pump (Stokes 212). The oils used in each of these pumps have room temperature vapor pressures in the mTorr range, and therefore a chilled trap has been employed to reduce oil contamination in the vacuum chambers. The trap consists of coiled tubing through which a 60% by volume propylene glycol/water mix is flowed. This solution is chilled to -40°C via a recirculating chiller (Thermo NesLab RTE 740). To the author’s knowledge, no data exists regarding the vapor pressure of mechanical pump oils at this temperature, and so no real quantitative data suggests that the use of this cold trap reduces oil contamination to an appreciable degree, but since the film of oil on the walls above the trap never seems to extend to the inside of the vacuum instrument it appears to do some good. When not in use, the high volume pump is closed off from the rest of the instrument via a gate valve.

5. References

- (1) Roach, P. J. The Reactivity of Aluminum Clusters as a Function of Atom Number. Ph.D. Dissertation, The Pennsylvania State University, University Park, PA, December 2009.
- (2) Haberland, H.; Mall, M.; Moseler, M.; Qiang, Y.; Reiners, T.; Thurner, Y. *J. Vac. Sci. Technol. A* **1994**, *12*, 2925-2930.
- (3) Pratontep, S.; Carroll, S. J.; Xirouchaki, C.; Streun, M.; Palmer, R. E. *Rev. Sci. Instrum.* **2005**, *76*, 045103.
- (4) Morel, R.; Brenac, A.; Bayle-Guillemaud, P.; Portemont, C.; La Rizza, F. *Eur. Phys. J. D* **2003**, *24*, 287-290.

- (5) Upschulte, B. L.; Shul, R. J.; Passarella, R.; Keesee, R. G.; Castleman, A. W., Jr. *Int. J. Mass Spectrom. Ion Process.* **1987**, *75*, 27-45.
- (6) Ferguson, E. E.; Fehsenfeld, F. C.; Schmeltekopf, A. L. *Adv. At. Mol. Phys.* **1969**, *5*, 1-56.
- (7) Press, W.; Teukolsky, S. A.; Vetterling, W. T.; Flannery, B. P. *Numerical Recipes: The Art of Scientific Computing*, 3rd ed.; Cambridge University Press: New York, 2007.
- (8) Roach, P. J.; Kuchta, K.; Woodward, W.; Castleman, A. W., Jr. Efficiently Transporting Ions from Viscous Flow to Ultra-High Vacuum with Minimal Loss. Presented at the 56th Annual ASMS Conference on Mass Spectrometry, Denver, CO, June, 2008.

Appendix B

Matrix-Isolation Cavity Ringdown Spectroscopy

1. Introduction

Spectroscopy is an immensely powerful tool for probing the electronic characteristics of matter, and so it was an obvious step to apply one of its techniques toward determining the electronic structure of clusters and exploring the validity of the jellium model. As discussed in §2.8, photoelectron spectroscopy is a common experimental method used on clusters, and a detailed study of aluminum cluster anions was published in 1998.¹ Coupled with first-principles density functional theory, accurate electronic and geometric structures of all small aluminum clusters have been determined,² and so it would appear that the research prospects for these systems have been thoroughly explored. To be sure, aluminum cluster anion studies still emerge in the literature with some regularity and provide valuable insights regarding the unique properties of individual clusters,³ and there is still some debate regarding the emergence of the jellium model in small (< 7) aluminum clusters,⁴ but it should be granted that a considerable amount of knowledge has been stockpiled on clusters containing this one element (see, for example, §1.3 and §2.8). However, the familiarity of these clusters' electronic structure allows for further studies such as their reactivity and stability in a controlled environment. Specifically, cluster research has reached a point where predictions can be made as to the necessary components for the construction of cluster-based crystals. Cluster "salts," as discussed in §1.3, could provide a means for the first cluster-assembled materials.^{5,6} First, however, the individual components must be introduced to each other in a controlled manner so that their interactions can be thoroughly studied. Gas-phase reactivity studies do not readily allow the observation of

singular cluster-reactant interactions, but rather the culmination of thousands upon thousands of interactions. Deposition techniques are readily available which allow the study of clusters on a surface,^{7,8} but it was argued in Chapter 5 that, while extremely valuable, these techniques provide little information pertaining to the gas-phase clusters in question due to their interactions with the surface affecting their electronic structure. What is needed is a controlled environment where reactant molecules can be slowly introduced to individual clusters and the changes observed. Matrix isolation spectroscopy—which involves freezing a sample into an inert glass—could provide such an environment.

Matrix isolation spectroscopy was invented in the latter part of the nineteenth century,^{9,10} although it involved the placement of fluorescing optical samples in liquid air or nitrogen long before solid matrices due to the tendency of frozen materials to become “crazed,” or cloudy. It was not until the 1930s that G. N. Lewis developed a technique wherein organic molecules could be frozen in an optically clear matrix, allowing for spectroscopic measurements to be made.⁹ In 1954 George Pimentel proposed using solidified noble gasses instead of organic matrices, thus significantly reducing possible reactions between the matrix and the sample.¹¹ While initial studies could only use solidified xenon glasses or less-reactive hosts such as CCl₄, eventually low-temperature techniques reached a point where liquid hydrogen and helium was readily available and the matrix could be built from krypton, argon, or neon. This technique proved to be quite valuable in the observations of charged molecules, radicals, or even reaction intermediates.^{9,12} In fact, it was found that controlled diffusion through the matrix at rigorously controlled temperatures (annealing) could lead to reactivity in a controlled environment.¹³ This is exactly what is needed for cluster-based crystal construction. Today matrix isolation is a common technique applied to a large variety of samples, and many books can be found on the topic. Modern equipment can be bought with almost no customization, and so not much detail is given

here. Our attention turns, therefore, to whether or not this technique can be applied to all-metal clusters.

Matrix isolation studies of $C_{60}^{+/-}$ appeared in 1991, just six years after the discovery of fullerenes,^{14,15} due in part to the interest generated by the potential superconductivity of alkali-stabilized C_{60}^{n-} anions.^{16,17} The deposition of small mass-selected all-metal clusters requiring concurrent cluster formation, mass-selection, and deposition also appeared at about this time, involving mostly neutral noble metal clusters.¹⁸⁻²² At the time, photoelectron spectroscopy supported by theoretical calculations had not reached its full potential, and so infrared absorption spectroscopy was providing clues as to the vibrational energy levels of clusters that other techniques could not. Over the past 20 years this technique has continued to provide insights as to the structure and behavior of metal clusters.²³⁻²⁶ However, these studies report cluster densities in the matrix as high as 10^{19} cm^{-3} , and cluster sources with nA brightness. While the modern magnetron gas aggregation source developed by Palmer (§2.2.b) could provide this much cluster current for larger species, nothing available today is readily adaptable to the current deposition instrumentation and the laser vaporization source is several orders of magnitude away from this intensity. Until cluster sources improve, single-pass absorption spectroscopy of aluminum clusters in a matrix is not possible. Therefore, alternative spectroscopic techniques must be explored. Several options exist, however only one of them offers an experimental setup that is simple, reliable, and inexpensive: cavity ringdown spectroscopy.

Cavity ringdown (sometimes referred to as cavity-ringdown, cavity ring-down, cavity ring down, etc.) spectroscopy (CRDS) was developed in the 1980s as a way of accurately determining the reflectivity of fine mirrors,²⁷⁻³⁰ but has blossomed into an independent spectroscopic technique with several review papers, two comprehensive books, and annual conferences.³¹⁻³⁵ The concepts of the technique are briefly discussed in §B.2, being easily referenced yet necessary for a full understanding of the remainder of this chapter. To put it quite

tersely, CRDS is the most sensitive absorption optical spectroscopy technique available today (i.e. smallest minimum of molecules per unit volume, $< 10^{13} \text{ cm}^{-3}$). Comparable techniques include laser-induced fluorescence, intracavity laser absorption spectroscopy, and resonance-enhanced multiphoton ionization. These techniques need not be discussed here, as they are discussed in a recently published dissertation by Aras Kartouzian from the Technical University of Munich, and the author recommends this source for a detailed comparison.³⁶ Suffice it to say, cavity ringdown spectroscopy offers the best sensitivity with an experimental setup that is simple and relatively inexpensive.

Like matrix isolation spectroscopy, CRDS has previously been applied to small metal clusters with success.³⁷⁻³⁹ In these experiments, mass-selected gold and nickel clusters were deposited onto a glass substrate for spectroscopic measurements. There is much to envy regarding the sensitivity and control at which these experiments were carried out, and our experimental setup has greatly benefited from the resulting publications. However, the cavity ringdown spectroscopic measurement of such small quantities of clusters in an inert matrix has not yet been achieved, and it is this which we hope to accomplish. As a reminder, this is not because we wish to determine the electronic energy levels of these clusters, but because we wish to build cluster-based crystals via diffusion through the matrix. The application of CRDS to matrix isolation spectroscopy (or vice versa) has not been previously explored, and there are several factors which suggest that it might be too difficult to achieve any useful resolution. These factors are discussed below (§B.3). Nonetheless, the apparatus has been built and initial experiments have achieved some success. This author feels that the technique can be applied towards clusters, and hopes to now convince the reader likewise.

2. The Mathematics of Cavity Ringdown Spectroscopy

One of the largest advantages of CRDS, when compared with other highly sensitive spectroscopic techniques, is its simplicity. In addition to a relatively simple experimental setup, CRDS is also convenient for the reason that determining an absorbance spectrum is independent of several variables that are difficult to control, such as shot-to-shot fluctuations in laser intensity. This can be demonstrated through the derivation of the main equations used in CRDS, a subject too narrow for the main text of this dissertation. The following mathematical solutions are in no way meant to be claimed as original work by the author. They are only included in order to supplement the reader who is unfamiliar with the basics of CRDS so that he or she may fully understand the technique. For a comprehensive review of the technique, including an introduction to the design and application of stable passive optical cavities using ray matrices, the author recommends “Cavity-Ringdown Spectroscopy: An Ultratrace-Absorption Measurement Technique” by Kenneth and Marianna Busch.³⁴

a. Ringdown Time for an Empty Cavity

To begin, we imagine a stable two-mirror passive optical cavity in which a pulse of light enters through the back of one of the highly reflective mirrors. As the light bounces back and forth in the cavity, a small fraction exits through the front of each mirror with every reflection. The total intensity of light inside the cavity decreases over time, and the light exiting the second mirror with each reflection is measured (Figure B.1).

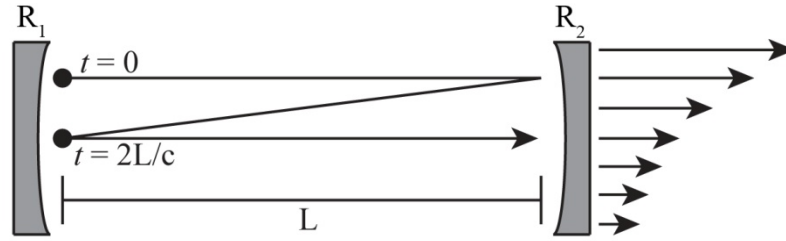


Figure B.1. Diagram of standard cavity ringdown setup where R_n is the reflectivity of the mirrors, L is the length of the cavity, and L/c is the round trip time for light in the cavity. The intensity of the light exiting the cavity after each round trip follows a natural logarithmic decay, as shown in Figure B.2.

The exact dimensions of the cavity are not important, suffice it to say that the cavity must be long enough such that the pulse of light entering the cavity is shorter than the round trip time, or otherwise tuned such that interference effects still yield a measurable ringdown (Figure B.2).

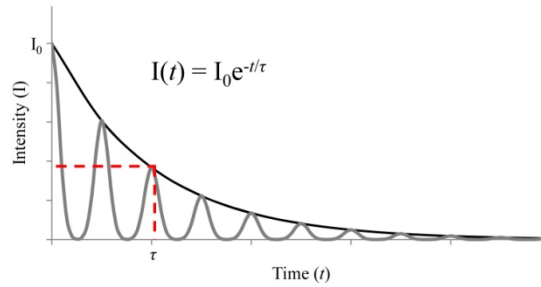


Figure B.2. Simplified example of a ringdown, where the grey curves represent the actual light escaping the cavity and the black line represents the solution for the ringdown. The red dashed line indicates the ringdown time, τ .

However, for the purposes of this exercise, we must assume that the light exits the cavity in a uniform logarithmic decay, and not as individual pulses of light that are, in fact, seen experimentally. We account for this imperfection when the ringdown is analyzed in §B.3.

Now that we have defined our cavity, it is possible to determine the percent of light lost from the empty cavity after an amount of time, dt . This can be represented by:

$$\frac{\text{Change in Light Intensity}}{\text{Original Light Intensity}} = \frac{\text{Percent Light Lost}}{\text{Reflection}} \times \frac{\text{Number of Reflections}}{\text{Round Trip}} \times \frac{\text{Round Trips}}{\text{Unit Time}} \times dt \quad (\text{B.1})$$

We must account for losses through each mirror, even though we only detect the light escaping through the one. Substituting the variables from Figure B.1a and assuming $R_1 = R_2$, Equation B.1 becomes:

$$\frac{-dI}{I} = (1 - R) \cdot 2 \cdot \frac{c \cdot dt}{2L} \quad (\text{B.2})$$

Note that dI is negative because the intensity of light in the cavity always decreases over time.

We can then develop an equation for light intensity versus time by integrating from 0 to t :

$$\int_0^t \frac{dI}{I} = \int_0^t -(1 - R) \frac{c \cdot dt}{L} \quad (\text{B.3})$$

$$\ln \frac{I_0}{I(t)} = (1 - R) \frac{c \cdot t}{L} \quad (\text{B.4})$$

$$\ln \frac{I(t)}{I_0} = -(1 - R) \frac{c \cdot t}{L} \quad (\text{B.5})$$

$$I(t) = I_0 e^{-(1-R)\frac{c \cdot t}{L}} \quad (\text{B.6})$$

We now define a ringdown time, τ , such that:

$$I(\tau) = I_0 e^{-1} \quad (\text{B.7})$$

This occurs when the intensity of light in the cavity is ~37% of the original intensity, which is true for an empty cavity when:

$$I_0 e^{-1} = I_0 e^{-(1-R)\frac{c \cdot \tau}{L}} \quad (\text{B.8})$$

Solving for τ , we find:

$$\tau = \frac{L}{c \cdot (1 - R)} \quad (\text{B.9})$$

b. Ringdown Time for a Non-Empty Cavity

A simple way of introducing an absorbing species into an empty ringdown cavity is to incorporate the Beer–Lambert law. However, before we are able to utilize it with confidence we must first make a quick digression in order to confirm that its fundamental assumptions remain valid. First, we define each absorbing species as having an absorption cross section, σ , which consists of a two-dimensional area to which the propagation of light is surface normal. Any photon intersecting with this absorption cross section will be absorbed; otherwise, it will be transmitted. This assumes that the orientation of the species is random, and therefore polarization effects can be ignored. Second, we define the number density, N , as the number of absorbing species in a three-dimensional space represented by the volume of light in the cavity. Finally, we define an arbitrary length along the axis of light propagation, $d\ell$, where absorbing species are present. We treat the time that it takes light to travel this distance as:

$$dt = \frac{d\ell}{c} \quad (\text{B.10})$$

We can therefore define the percent of light lost due to the absorbing species over the distance $d\ell$ as:

$$\frac{-dI}{I} = \sigma \cdot N \cdot d\ell = \sigma \cdot N \cdot (c \cdot dt) \quad (\text{B.11})$$

For this to be true there are two important assumptions that we must consider. The first is that no two individual absorption cross sections may overlap along the axis of light propagation. This assumption need only hold true over the distance $d\ell$, a consideration which is important for CRDS as it assumes that absorbing species may absorb multiple photons as unabsorbed light is repeatedly reflected back into the cavity. It is also important that the decay time for the excited species be less than the time it takes for the pulse of light to return, otherwise N will decrease over time. This requirement may not be true for all cavities and/or absorbing species, and so must

be considered when an experiment is performed. The second assumption is that N be an accurate *average* number density inside the entire volume of light over the distance $d\ell$. This second assumption allows Equation B.11 to hold true for uneven distributions of number density, which is especially important for the purposes of CRDS where the absorbing species are restricted to a short section of the cavity or even deposited on a surface. As is discussed below, if the absolute number of absorbing species is determined and the *average* number density is calculated using the volume of the light in the cavity, σ can be determined. This assumption also allows for $d\ell$ to be represented by the length of the cavity, L , provided that the first assumption holds true.

The rightmost side of Equation B.11 can therefore be added to the right side of Equation B.2 in order to provide the percent of light lost over time in a non-empty cavity:

$$\frac{-dI}{I} = \left[\left(\frac{1-R}{L} \right) + \left(\frac{\sigma \cdot N \cdot L}{L} \right) \right] \cdot (c \cdot dt) \quad (\text{B.12})$$

which can then be integrated in a similar fashion to Equations B.3 through B.6:

$$I(t) = I_0 e^{-[(1-R) + (\sigma \cdot N \cdot L)] \cdot \left(\frac{c \cdot t}{L} \right)} \quad (\text{B.13})$$

yielding a ringdown time of:

$$\tau = \frac{L}{c \cdot [(1-R) + (\sigma \cdot N \cdot L)]} \quad (\text{B.14})$$

From this point forward the ringdown time for a non-empty cavity (Equation B.14) is referred to as τ_1 and the ringdown time for an empty cavity (Equation B.9) is referred to as τ_2 . Solving Equations B.9 and B.14 for $(1-R)$, setting them equal to each other, and simplifying yields:

$$\sigma \cdot N = \frac{1}{c} \left(\frac{1}{\tau_1} - \frac{1}{\tau_2} \right) \quad (\text{B.15})$$

which can be used to determine $\sigma \cdot N$ when τ_1 and τ_2 are experimentally determined. Before we proceed it is important to remember that these values are dependent on the wavelength of light, λ . However, by scanning multiple wavelengths it is possible to obtain a relative absorption spectrum

of $\sigma \cdot N$ versus λ when the sample remains constant, seeing as absorbance is proportional to $\sigma \cdot N$ for an unvarying L .

c. Experimental Determination of Absorbance Spectra

As discussed in §B.2.a, these derivations assume a smooth exponential decay in the intensity of light exiting the cavity, which does not occur experimentally. In order to simulate this, we must determine the peak of each pulse of light exiting the cavity and assemble them into a set of points, thus extrapolating the exponential decay. The set of points can then be fitted to an exponential decay over time:

$$I(t) = I_0 e^{-kt} + b \quad (\text{B.16})$$

Equations B.6 and B.13 can be substituted for Equation B.16 when k is τ^{-1} and b is zero (assuming that the light in the cavity eventually decays to an intensity of zero). Thus it is possible to experimentally determine τ_1 and τ_2 from the light exiting the cavity. Since ringdown times can be acquired at the frequency of the laser, they are typically averaged over several tens of measurements. Equation B.15 then allows us to obtain experimental values of $\sigma \cdot N$ for any given λ , and plotting the former versus the later provides an absorption spectrum for an absorbing species in the cavity.

There are several acceptable methods used to determine peak sets and fit them to Equation B.16. The more convenient ones are able to process the incoming data in real time, thus allowing the user to tune the cavity and achieve the highest possible values for τ and therefore the maximum possible resolution. This can be as fast as or faster than 50 Hz for some lasers, which can prove difficult for methods such as the nonlinear Levingburg–Marquardt fit, and so the author recommends using a method of corrected successive integration.⁴⁰ The method for

determining peak sets is generally not the limiting factor, with various methods producing equivalent results at acceptable speeds.

We now have a set of considerations and assumptions that apply to all experimental CRDS studies:

- The derivations above do not consider the loss of light from the cavity due to factors other than the mirrors or the absorbing species, such as the presence of an optical window or rare gas matrix. However, it can be assumed that these factors will be present for each pass through the cavity, empty or not, and so can be considered a part of R . It is therefore necessary to carefully reproduce any and all factors in the empty cavity when determining ringdown times for a non-empty cavity. It is the goal of the experimentalist to attempt to achieve a value for R which is as close to 1 as possible, typically greater than 0.99. The minimum resolution that can be obtained with a given empty cavity can be estimated:

$$(\sigma \cdot N)_{\min} = \frac{t U_{\tau} \sqrt{\frac{2}{n}}}{c \tau_2} \quad (\text{B.17})$$

where t is the value of Student's t for $2n - 2$ degrees of freedom, n is the number of measurements taken, and U_{τ} is the relative precision of the time constant measurement ($d\tau/\tau$). The derivation of Equation B.17 can be found on pages 16-17 of Reference 34.

- The limiting factor in sensitivity is almost always the reflectivity of the cavity mirrors being used. As a specific example, let us imagine a perfect 30 cm empty cavity with 99% reflective mirrors. Using Equation B.17 and assuming a constant expected deviation and Student's t , we know that in order to reduce the minimum detectable absorption cross section by a factor of one hundred we would have to either 1) introduce 100 times the amount of absorbing species into the cavity, a factor that would potentially increase the

length of experiment preparation from hours to days (unacceptable for matrix isolation techniques); 2) increase the length of the cavity from 30 cm to 3 m (a considerable change, especially when vacuum instrumentation is involved); 3) increase the number of measurements per average by 141 times (a factor that is directly related to the total time required for the CRDS experiment, which must be as short as possible for matrix isolation techniques); or 4) increase the mirror reflectivity from 99% to 99.9%. To be sure, there is a limit to the amount you can improve each of these variables. The improvement of R , however, is usually the easiest way to improve sensitivity, and mirrors with reflectivities of 99.99% and higher are readily available. However, for highly reflective dielectric mirrors, R is extremely dependent on λ . Most mirrors that are suitable for CRDS only offer sufficient reflectivity over short spectral ranges, typically ~ 50 nm. Therefore it is necessary to use several different sets of mirrors in order to cover any significant portion of the IR, visible, and/or UV spectral regions. These mirrors are often expensive and fragile, and so careful planning must be taken before experiments are performed.

- The constants R , L , and c are not dependent on whether the cavity is empty or full. Therefore, when they are accurately reproduced between measurements of τ_1 and τ_2 , they are essentially eliminated as variables. Also, I_0 is entirely unnecessary for the determination of $\sigma \cdot N$, and so shot-to-shot fluctuations in laser intensity (arguably the hardest factor to control or measure) are effectively ignored.
- If a focusing lens is used to direct the light exiting the cavity into the detector, then the cavity need not be perfectly confocal nor concentric, and thus the proper placement of the mode-matching optics are not necessary to focus light into the cavity. This shortcut is ultimately convenient given that the “poor” mode structure fills in the gaps between the

longitudinal modes, thus providing a quasi-continuous cavity. Because of this, mode-matching optics can often be disregarded altogether.⁴¹

- As mentioned above, the absorbing species must have a relaxation time less than the time it takes for the pulse of light to reflect off of a mirror and return; however this is only an issue for fluorescing/phosphorescing molecules or for very short cavities, a problem which is not an issue in this research.

It is also mentioned above that the absorption cross section can be determined if the average number density is known. We can now explore the possibility of calculating σ for each value of λ studied.

d. Solving for the Absorption Cross Section

If a neutral species is being monitored as a stable gas, as is commonly performed in CRDS, it is possible to determine N from the partial pressure of the species in the cavity chamber by using the van der Waals equation. It is then possible to determine an absolute value for σ . Considering the experimental setup used in this research, this is not an option as the absorbing species is isolated on a surface or in a rare gas matrix, and therefore the actual number density is not accurate as applied to the derivations above. To be sure, since all particles are assumed to exist as two-dimensional absorption cross sections, any species on a surface would have a two-dimensional number density and therefore Equation B.11 would no longer be valid. However, if we are able to calculate the *average* number density for the entire cavity, knowing all the while that the absorbing species is located to a small volume or plane inside of the volume of light, we would be able to determine σ for any value of λ . This can be done by dividing the total number of species in the volume of light by the volume of light.

It is possible to estimate the number of absorbing species present in the cavity using one of two methods. First, if ions are being deposited either on a surface or into a rare gas matrix, then it is possible to determine the ion current using a conductive plate attached to a picoammeter. The plate is moved in front of the beam of ions periodically to monitor the ion current and the total number of ions can be calculated using the following equation:

$$\text{Number of Absorbing Species Deposited} = \frac{\text{Measured Ion Current (A)} \times \text{Deposition Time (s)}}{1.602 \times 10^{-19} (\text{Coulombs per Elementary Charge})} \quad (\text{B.18})$$

This method can also be used for ions that are neutralized before being deposited if the ion current is measured before the neutralization occurs. If a neutral gas is being deposited, however, current measurement is not possible. If the partial pressure of the gas is known, the number of species deposited can be determined based on the conditions of the surface or growing rare gas matrix. Once the number of absorbing species is determined, dividing it by the volume of light will yield N , which can then be used to find σ . This can be estimated for confocal cavities by treating the cavity as two cones:

$$\text{Volume of Light in Cavity} = \frac{\pi r^2}{3} \cdot L \quad (\text{B.19})$$

It is important to remember, however, that this is only true when every absorbing species is contained within the volume of light for each pass, which may be difficult to control or predict for various optical cavities or deposition methods. This method can therefore only be confidently used for well-characterized confocal or concentric cavities, where the beam diameter at the cavity center remains constant from one pass to the next.

3. Experimental Concerns

It is understandable that this experimental technique has all the experimental difficulties that are always associated with matrix isolation spectroscopy and CRDS, and so these need not be

addressed here. Minor aspects such as the sensitivity of the empty cavity with regard to different parameters and the speed at which individual ringdowns can be recorded were discussed in the previous section. We must now, however, consider any and all experimental aspects that could prevent these two techniques from being utilized together.

a. The Cavity

The coherent light source being used is a Spectra Physics MOPO-SL ($< 0.2 \text{ cm}^{-1}$ linewidth) pumped by the third harmonic of a Nd:YAG laser (Quantra-Ray PRO-250-20). It is capable of producing a nearly continuous range of wavelengths from 1800 nm to 200 nm (there is a small gap around 700 nm and wavelengths below 400 nm require a frequency doubler). The light is guided into the cavity via five mirrors (Edmund NT48-016). The light enters the vacuum chamber through a quartz window where it is introduced into the cavity through the back of one of the high-reflectivity mirrors. The cavity is adjusted via two ultra high vacuum mirror mounts (Figure B.3) that were designed and built specifically for this purpose.

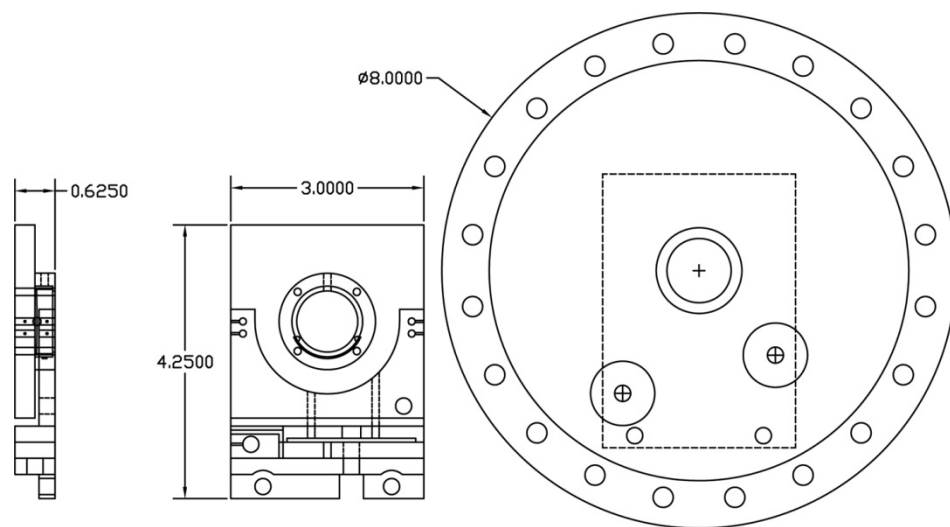


Figure B.3. Custom-built ultra-high vacuum mirror mounts for cavity ringdown spectroscopy. Dimensions are in inches. The mirror holder can be swapped to hold any mirror size smaller than 2

inches. The Gimbal-style mount is adjusted via two magnets powerful enough to penetrate the 0.25 inch steel flange.

Briefly, the mounts are similar to traditional Gimbal mounts except that they are constructed of 316L stainless steel and care has been taken to eliminate all air pockets. They are adjusted at two points by magnetic rods that are powerful enough to be turned through the steel mounting flange. The advantage of this design is its low cost, low maintenance, and reliable performance. The largest disadvantage of this design is that the entire system must be vented in order to replace the mirrors, which makes spectroscopy quite difficult but reaction studies at single wavelengths still possible. Ultimately, however, the entire setup should be replaced by one which allows multiple mirrors. The light escaping the second mirror is detected via a photomultiplier tube (Hamamatsu H6780) or a photodiode (Electro Optics Technology, Inc. ET-2020), and must be adjusted depending on the intensity of light exiting the cavity. The ringdown is analyzed at speed and stored via a custom LabVIEW program. This program also controls the output wavelength of the laser and the temperature of the cryostat in order to maximize efficiency.

There is a large amount of literature available regarding the best way to couple light into an optical cavity, but it is convenient to argue that one need not worry about mode matching optics and polarization if the cavity is specifically de-tuned.⁴¹ One of the effects of low-temperature studies is the narrowing of absorption bands due to the reduction of vibrations in the low-temperature matrix.²⁵ A mode-matched cavity may not allow a specific absorption wavelength, and if the absorption peak is narrow enough to lie between to stable wavelengths then information could be lost. In order to achieve a quasi-continuous cavity, the radius of curvature (R_n) of the mirrors and the length of the cavity (L) must be considered. The cavity is 1.055 m long, and mirrors are commonly available in sizes of $R = 1$ m and $R = 6$ m. It can be shown that the best option is the 1 m mirrors, because this would require less transverse modes to be active in order to fill the mode-spectrum. Because mode matching optics would actually hinder

low-temperature studies, no attempt is made to eliminate the mode structure of the laser or couple the light into the cavity. Furthermore, it is not possible to adjust the distance between the mirrors with the current setup. The light is passed into the cavity unfocused, which easily produces a ringdown but does have one detrimental effect. The diameter of the light exiting the cavity can be calculated using ray transfer matrix analysis:

$$\begin{bmatrix} r(z') \\ \alpha(z') \end{bmatrix} = \begin{bmatrix} 1 - \frac{2L}{R_2} & 2L - \frac{2L^2}{R_2} \\ \frac{4L}{R_1 R_2} - \frac{2}{R_1} - \frac{2}{R_2} & 1 - \frac{2L}{R_2} - \frac{4L}{R_1} + \frac{4L^2}{R_1 R_2} \end{bmatrix} \cdot \begin{bmatrix} r(z) \\ \alpha(z) \end{bmatrix} \quad (\text{B.20})$$

where $r(z)$ and $r(z')$ represent the radius of the light beam before and after a round trip, respectively, and $\alpha(z)$ and $\alpha(z')$ represent the angle of the light beam before and after a round trip, respectively. One can show that when $\alpha(z) = 0$ for an initial cavity entrance, the radius of the light exiting the cavity will fluctuate for all values of $L \neq R/2$ or R . When $R = 1$ and $L = 1.055$, this fluctuation has a period of about 29 round trips. Since a round trip in a 1.055 m cavity takes 7 ns, this would suggest a period of about 200 ns. Although the ringdown time would not be affected by this, the disadvantage here is that the light exiting the cavity would be harder to analyze. Even if a program is able to only pick out each twenty-ninth peak, according to Equation B.17 this would drastically increase the error of the calculated ringdown. We will now discuss the aspects of matrix isolation spectroscopy, but this consideration is addressed further once a substrate is introduced.

b. The Matrix

The first aspect to consider is whether or not the matrix will perturb the electronic and geometric structure of the cluster. Without this simple requirement the abundance of gas-phase data will prove much less valuable. The deposition of clusters into a matrix has previously been

explored, with experimental^{42,43} and theoretical⁴⁴ studies suggesting that the metal clusters do not deform on impact with the matrix (deposition energies similar to surface studies are required or fragmentation can occur). Additionally, studies involving C₆₀ ions and small silver clusters suggest that the clusters retain their electronic structure while enclosed within the matrix,^{16,22} although there is a shift in absorption peaks due to a combined dielectric effect (redshift) and a confinement of the outer electrons of the cluster due to the electronic density of the matrix (blueshift).^{45,46} The total shift in the spectrum was found to be dependent on the matrix material, but relatively independent of the cluster being studied.⁴⁷ Therefore, the successful deposition of clusters into a matrix should be possible, and the next consideration should be the matrix material.

Argon is quite popular, being the most inexpensive noble gas, chemically inert, and extensively studied. Forming an optically clear argon gas is somewhat tricky, due to its tendency to form globules or clusters in the gas-phase which then deposit onto a cold substrate leaving gaps in the crystal structure,⁴⁸ but these complications are easily overcome with some practice. Another consideration is the buildup of charge in the matrix due to the deposition of anions. Eventually this charge could grow to the point that the focused slow-moving clusters could be deflected or repulsed from area of the light. In studies with cations, the positive charge can be neutralized with an electron gun,³⁹ however this is likely not an issue with the density of clusters expected here (1 V of electric potential due to a point charge is achieved at approximately 1.4 nm, corresponding to a density of $3.4 \times 10^{20} \text{ cm}^{-3}$, well above our experimental limit). One final consideration with regard to the matrix material is the cost and complexity involved in a liquid helium setup. Liquid helium, while readily available, is rather expensive. Liquid nitrogen, comparatively, is not, and it is much easier to maintain liquid nitrogen temperatures than liquid helium temperatures. The obvious advantage of liquid helium is the use of noble gas matrices, which are optically clear and have no vibrational energy levels, but there are several options for

matrices that freeze at liquid nitrogen temperatures and are optically clear in the visible and UV light regions. One such option is sulfur hexafluoride, which in addition to being inexpensive and optically clear in the regions specified is also quite inert.⁴⁹ SF₆ has been used in experiments specifically for its high-temperature freezing points when IR studies are not a concern,⁵⁰ and so it was an ideal candidate for early matrix isolation cavity ringdown experiments. It also has a high ionization energy and low electron affinity, and so poses little threat toward the unwanted neutralization of cations or anions. Another advantage of SF₆ lies in its crystal structure. Although it freezes at 222 K, it passes through a second phase boundary at 95 K at low pressures.⁵¹ At this point the crystal structure changes from body centered cubic to a monoclinic structure. Ultimately what this suggests is that the matrix can be “softened” by raising the temperature above this point, which can either be used to anneal the matrix for optical clarification or to allow reactant species to diffuse, thus promoting reactivity. To accomplish matrix isolation, a cryostat was purchased and incorporated into the deposition instrument (Janis Research ST-400) which is coupled to a temperature controller (LakeShore Model 331). This allows temperature control down to liquid helium temperatures with a gold radiation shield and liquid nitrogen temperatures with a stainless steel radiation shield. We turn our attention now to the substrate, and what considerations are made when introducing a matrix into a stable optical cavity.

c. The Substrate

The placement of an optically transparent substrate into a stable optical cavity has been successfully implemented in the past, both in the study of substrate quality⁵²⁻⁵⁴ and deposited materials.^{37,38,55,56} The first consideration when placing a substrate in the cavity is angle. While a Brewster’s angle is may provide nearly 100% transmission for P-polarized light, it limits the choice of window material. On the other hand, placing the substrate orthogonal to the cavity

allows the reflected light to stay in the stable cavity, although the angle is much more sensitive to misalignment.⁵⁷ Using ray transfer matrix analysis, it is possible to prove that for a stable optical cavity to exist the following parameters must be met:

$$0 \leq \left(1 - \frac{L}{R_1}\right) \left(1 - \frac{L}{R_2}\right) \leq 1 \quad (\text{B.21})$$

As an example, when $L = 1.05$ m and $R_1 = R_2 = 1$ m this statement is true. This statement is also true, however, when $L \approx 0.5$ and $R_2 = \infty$ or when $R_1 = R_2 = \infty$ for all values of L . Therefore, introducing a substrate orthogonal to the cavity simply creates *several* cavities, one between the first mirror and the face of the substrate, one between the first mirror and the back of the substrate, one between the two faces of the substrate, two between the faces of the substrate and the back mirror, and one between the two mirrors. This has been mathematically and experimentally confirmed,^{58,59} and so the introduction of a substrate into cavity ringdown spectroscopy should not pose a threat to this study. Of course, the substrate will never be perfectly transparent, due to minor imperfections and unwanted material on its surface. We must therefore explore what experimental losses are acceptable.

It is derived in §B.2 that the ringdown time of an empty cavity can be represented by:

$$\tau = \frac{L}{c \cdot L_C(\omega)} \quad (\text{B.22})$$

where L_C is the wavelength-dependent percent of light exiting the cavity through the mirrors each round trip. When a substrate and an absorbing species are introduced (L_C and L_A , respectively), this equation becomes:

$$\tau = \frac{L}{c \cdot [L_C(\omega) + L_S(\omega) + L_A(\omega)]} \quad (\text{B.23})$$

Previous studies with various substrates have produced values of L_S on the order of 10^4 (hundreds of parts per million loss),^{54,55,60} and so this should be achievable for a similar system. This number will depend on the cleanliness of the substrate and to some extent the flatness of the substrate, and

maximizing τ will also require that the substrate be in the middle of the cavity. This is due to the simple reason that placing the substrate anywhere but the middle increases the amount of times the light interacts with the non-vacuum aspects of the cavity. Finally, while the amount of light decaying in the cavity will not change (assuming zero loss due to transmissions or reflections from the substrate), the pattern of the light exiting the cavity will. If one assumes a perfectly transparent, infinitely thin substrate in the exact center of a cavity with $R_1 = R_2 = 1$, the average density of light at each of the two mirrors can be represented by:

$$I(t) = \frac{I_0}{2} \pm I_0 \left(T - \frac{1}{2} \right) e^{-\frac{2L\beta}{c}t}$$

$$\beta = \ln \left(\frac{-\frac{I_0}{2} + 2I_0T(1-T)^2 + I_0T((1-T)^2 + T^2)}{-\frac{I_0}{2} + I_0T} \right) \quad (\text{B.24})$$

where T is the transmission of the substrate. Note that adding the two possible equations together yields I_0 for all values. Also note that after several tens of round trips in the cavity, the light on either side of the substrate will be the same, the exact length being dependant on T (Figure B.4.a). This conveniently oversimplified portrayal of the cavity allows us to draw two conclusions. First, the light will interact with the mirrors for the exact same number of times as for an empty cavity, and therefore the ringdown time should be the same.

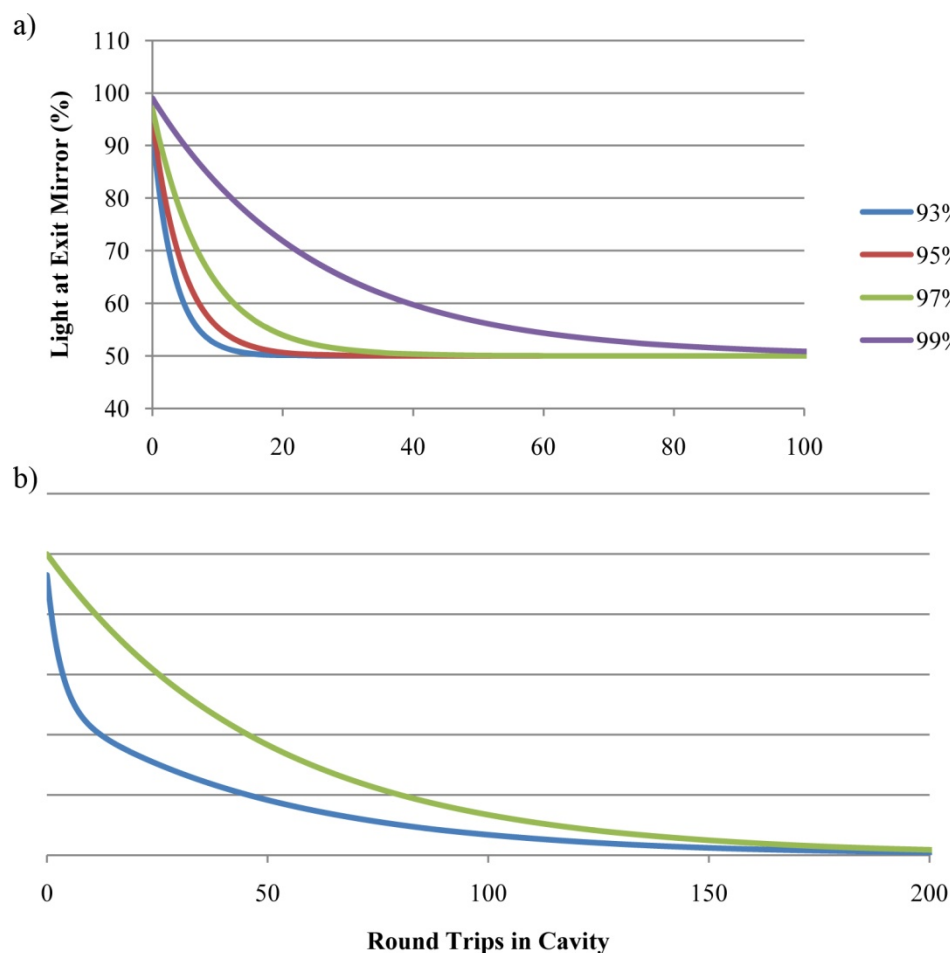


Figure B.4. a) Percent of total cavity light at the exit mirror with respect to the number of round trips. It can be seen that, for varying substrate transmissions, the number of round trips will eventually reach 50%. The percent of light at the entrance mirror can be represented by mirroring the curve across the x -axis at 50%. b) Comparison of ringdowns from an empty cavity (green) and a cavity with a 93% transmissive substrate (blue). Although the non-empty cavity appears to have a faster ringdown time, they are actually the same once the non-empty cavity has equalized on either side of the substrate, approximately 20 round trips. The consequent difference in I_0 has no effect on the ringdown time.

However, there will be a bi-exponential decay due to the equalization of the light on either side of the substrate, and while this effect should become negligible very quickly, it could lead to an underestimation of the ringdown time. Delaying the initial intensity to eliminate this effect will deliver a more accurate ringdown time, although as long as the same initial point is always chosen these effects will cancel out when determining absorption coefficients in actual experiments. Second, any values for T should work, although the amount of light exiting the

cavity is reduced for lower values, which could affect the sensitivity due to the limitations of the detector (Figure B.4.b). This is important, because the optimal substrate material for low-temperature studies in the wavelengths desired here is sapphire, which has a transmission of approximately 93% for wavelengths in the visible and near-UV ranges. It should now be reasonable to suppose that utilizing matrix isolation spectroscopy inside an optical cavity is feasible. We will now discuss what progress has been made in this regard and what experimental difficulties remain.

4. Current and Future Experiments

A sample ringdown for the empty cavity is shown in Figure B.5.a. It can be observed how the ringdown exhibits a period of approximately 200 ns, exactly as predicted. A sample ringdown for the cavity when sapphire is introduced is shown in Figure B.5.b. Here the fluctuations have ceased, and a stable, consistent ringdown remains. One of the biggest difficulties faced so far in this laboratory setup is the losses due to the sapphire. The sapphire windows (Meller Optics Inc. SCD2117-02A) have a surface finish of 10^{-5} and a crystallographic orientation of 0001, and so their losses should be minimal, yet we consistently see two to three thousand parts per million, an order of magnitude higher than allowed. Investigations here are ongoing. Low-temperature studies have begun, with some brief but promising results. When the sample is maintained at 79 K for 4 hours, a molar absorption coefficient of $1.43 \times 10^{-3} \text{ m}^{-1}$ is measured. This suggests a deposition of less volatile species in the chamber (water, oils, etc.) onto the sapphire, which corresponds to the drop in pressure (5×10^{-8} to 8×10^{-9} Torr) at low temperature. Assuming a molar absorption cross section of $3 \times 10^{-22} \text{ m}^2$, this would suggest a density of $4.8 \times 10^{18} \text{ molec./m}^3$. With a cavity volume of $3 \times 10^{-5} \text{ m}^3$, this would suggest

1.43×10^{14} molecules deposited onto the substrate (the pressure change would remove approximately 4×10^{10} molecules from this volume, which is a negligible effect).

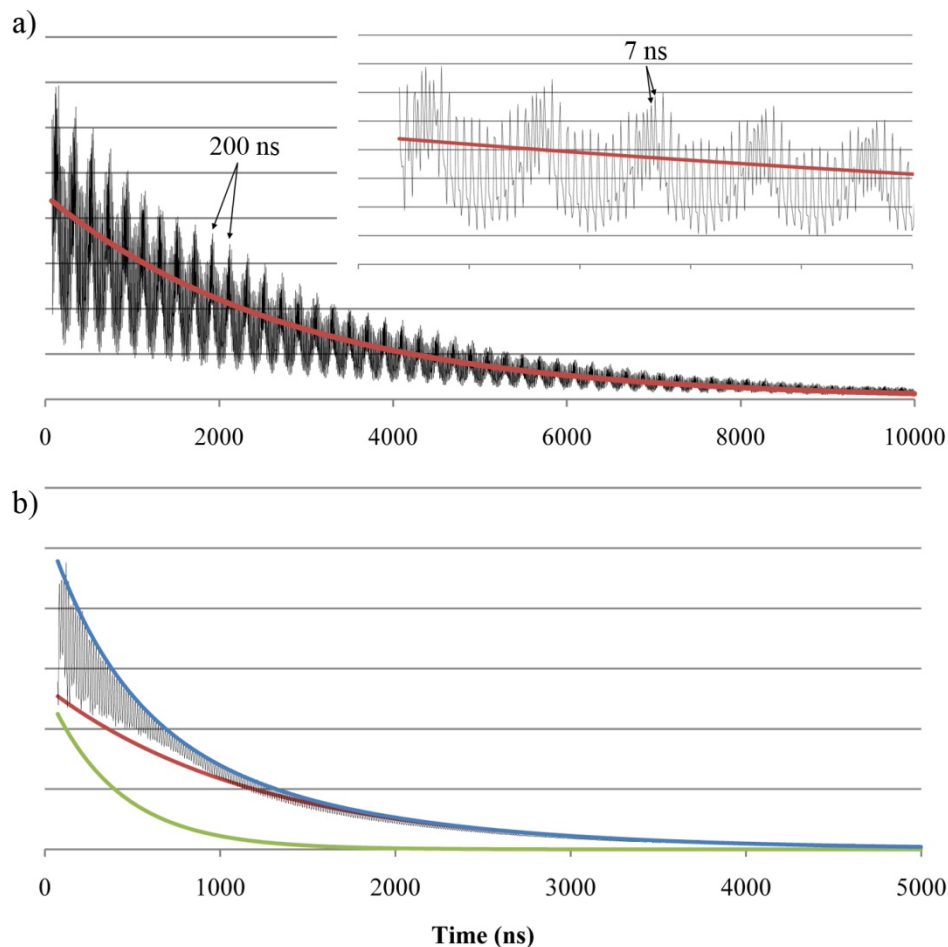


Figure B.5. a) Ringdown of empty cavity, $L = 1.055$ m. Predicted period of 200 nm can be seen, caused by fluctuations in focus of light exiting the cavity. b) Ringdown of cavity with sapphire window orthogonal and centered. A possible bi-exponential decay is traced, with the addition of both red and green decays forming the blue decay which is in good agreement with the experiment.

With an assumed mass of 100 g/mol for the deposited species, this corresponds to a pressure of 2.9×10^{-9} Torr, and although several averages were assumed this is in reasonable agreement with our observed pressures. The next step was to attempt to build a SF_6 matrix on the substrate. Similar molar absorption coefficients were observed over the course of four hours, being attributed to the volatile species freezing into the burgeoning matrix. A problem was discovered upon evaporation, however, as the gold shield was etched, sputtering gold onto the sapphire,

effectively ruining it. This is likely due to the SF_6 forming some radical sulfur-containing fluorinated species in the neighboring ion pump, which then reacts with the gold. A literature search revealed no suggestions as to the exact mechanism occurring here, but the gold shield was replaced with a stainless steel copy, and this problem was eliminated, although the gold will need to be replaced for liquid helium temperatures. At this point experiments are currently underway to deposit a readily available organic species, isatin, into the SF_6 matrix in order to prove the concept of matrix isolation cavity ringdown spectroscopy. Once this is done, stronger efforts will be made to increase ion signal out of the cluster sources, enabling the deposition and reaction of aluminum cluster anions within the matrix. Theoretical calculations have already predicted the absorption spectra of small aluminum cluster anions (Figure B.6), and similar studies of burgeoning cluster-assembled materials could provide specific wavelengths to observe over time to hint as to the production of these ionically bound dimers, tetramers, etc., and the subsequent effects on the electronic properties of the clusters.

5. Conclusions

The thought of using matrix isolation spectroscopy to study cluster interactions is not a new one; jellium shell closing of sodium clusters have been observed to form in argon matrices after annealing.⁶¹ Of course, our goal is not to create inert clusters but rather create stable cluster-assembled materials. As research continues on the development and implementation of matrix isolation cavity ringdown spectroscopy, valuable insights will be gained on the formation of minute amounts of cluster crystals. Such information could lead to the development of methods for larger-scale production of said materials. In this regard, several options already exist. First, the matrix containing the cations and anions of the salt could be evaporated away, slowly building a small amount of the crystal on the surface for further study. Larger-scale methods also exist, such

as helium nanodroplet formation⁶² and deposition and condensation/passivation methods.⁶³ Long-term goals for this research are addressed in Chapter 6, but on the shorter timescale this author is quite confident that matrix-isolation cavity ringdown spectroscopy is a viable technique for the study of metal clusters in addition to other non-cluster species of interest. Its low cost and simple experimental setup will hopefully inspire other scientists to consider its use in the spectroscopic study of minute amounts of labile species.

6. References

- (1) Li, X.; Wu, H. B.; Wang, X. B.; Wang, L. S. *Phys. Rev. Lett.* **1998**, *81*, 1909-1912.
- (2) Drebov, N.; Ahlrichs, R. *J. Chem. Phys.* **2011**, *134*, 124308.
- (3) Leuchtner, R. E.; Harms, A. C.; Castleman, A. W., Jr. *J. Chem. Phys.* **1991**, *94*, 1093-1101.
- (4) Melko, J. J. Ph.D. Dissertation, The Pennsylvania State University, University Park, PA, December 2011.
- (5) Khanna, S. N.; Jena, P. *Phys. Rev. Lett.* **1992**, *69*, 1664-1667.
- (6) Reber, A. C.; Khanna, S. N.; Castleman, A. W., Jr. *J. Am. Chem. Soc.* **2007**, *129*, 10189-10194.
- (7) Meiwes-Broer, K. H. *Metal Clusters at Surfaces: Structure, Quantum Properties, Physical Chemistry*; Springer Publishing: New York, 2000.
- (8) Woodruff, D. P. *Atomic Clusters: From Gas Phase to Deposited*; Elsevier Science: Oxford, 2007.
- (9) Dunkin, I. R. *Matrix-Isolation Techniques: A Practical Approach*; Oxford University Press: New York, 1998.
- (10) Lewis, G. N.; Lipkin, D. *J. Am. Chem. Soc.* **1942**, *64*, 2801-2808.
- (11) Whittle, E.; Dows, D. A.; Pimentel, G. C. *J. Chem. Phys.* **1954**, *22*, 1943-1943.
- (12) Cradock, S.; Hinchcliffe, A. J. *Matrix Isolation: a Technique for the Study of Reactive Inorganic Species*; Cambridge University Press: New York, 1975.

- (13) Ewing, G. E.; Thompson, W. E.; Pimentel, G. C. *J. Chem. Phys.* **1960**, *32*, 927-932.
- (14) Kato, T.; Kodama, T.; Shida, T.; Nakagawa, T.; Matsui, Y.; Suzuki, S.; Shiromaru, H.; Yamauchi, K.; Achiba, Y. *Chem. Phys. Lett.* **1991**, *180*, 446-450.
- (15) Gasyna, Z.; Andrews, L.; Schatz, P. N. *J. Phys. Chem.* **1992**, *96*, 1525-1527.
- (16) Fulara, J.; Jakobi, M.; Maier, J. P. *Chem. Phys. Lett.* **1993**, *211*, 227-234.
- (17) Varma, C. M.; Zaanen, J.; Raghavachari, K. *Science* **1991**, *254*, 989-992.
- (18) Harbich, W.; Fedrigo, S.; Meyer, F.; Lindsay, D. M.; Lignieres, J.; Rivoal, J. C.; Kreisle, D. *J. Chem. Phys.* **1990**, *93*, 8535-8543.
- (19) Harbich, W.; Fedrigo, S.; Buttet, J.; Lindsay, D. M. *Z. Phys. D: At., Mol. Clusters* **1991**, *19*, 157-159.
- (20) Harbich, W.; Fedrigo, S.; Buttet, J. *Chem. Phys. Lett.* **1992**, *195*, 613-617.
- (21) Fedrigo, S.; Harbich, W.; Belyaev, J.; Buttet, J. *Chem. Phys. Lett.* **1993**, *211*, 166-170.
- (22) Fedrigo, S.; Harbich, W.; Buttet, J. *J. Chem. Phys.* **1993**, *99*, 5712-5717.
- (23) Rabin, I.; Schulze, W.; Ertl, G.; Félix, C.; Sieber, C.; Harbich, W.; Buttet, J. *Chem. Phys. Lett.* **2000**, *320*, 59-64.
- (24) Félix, C.; Sieber, C.; Harbich, W.; Buttet, J.; Rabin, I.; Schulze, W.; Ertl, G. *Phys. Rev. Lett.* **2001**, *86*, 2992-2995.
- (25) Sieber, C.; Buttet, J.; Harbich, W.; Félix, C.; Mitric, R.; Bonačić-Koutecký, V. *Phys. Rev. A* **2004**, *70*, 041201.
- (26) Conus, F.; Lau, J. T.; Rodrigues, V.; Félix, C. *Rev. Sci. Instrum.* **2006**, *77*, 113103.
- (27) Herbelin, J. M.; McKay, J. A.; Kwok, M. A.; Ueunten, R. H.; Urevig, D. S.; Spencer, D. J.; Benard, D. J. *Appl. Opt.* **1980**, *19*, 144-147.
- (28) Herbelin, J. M.; McKay, J. A. *Appl. Opt.* **1981**, *20*, 3341-3344.
- (29) Kwok, M. A.; Herbelin, J. M.; Ueunten, R. H. *Opt. Eng.* **1982**, *21*, 979-982.
- (30) Anderson, D. Z.; Frisch, J. C.; Masser, C. S. *Appl. Opt.* **1984**, *23*, 1238-1245.
- (31) Scherer, J. J.; Paul, J. B.; O'Keefe, A.; Saykally, R. J. *Chem. Rev.* **1997**, *97*, 25-51.
- (32) Wheeler, M. D.; Newman, S. M.; Orr-Ewing, A. J.; Ashfold, M. N. R. *J. Am. Chem. Soc. Faraday Transactions* **1998**, *94*, 337-351.

- (33) Berden, G.; Peeters, R.; Meijer, G. *Int. Rev. Phys. Chem.* **2000**, *19*, 565-607.
- (34) *Cavity-Ringdown Spectroscopy: An Ultratrace-Absorption Measurement Technique*; Busch, K.; Busch, M. Eds.; ACS Symposium Series 720, American Chemical Society: Washington DC, 1999.
- (35) Berden, G.; Engeln, R. *Cavity Ring-Down Spectroscopy: Techniques and Applications*; Wiley & Sons: New York, 2009.
- (36) Kartouzian, A. Optical Properties of Size-Selected Supported Metal Clusters Measured by Cavity Ring-Down Spectroscopy. Ph.D. Dissertation, Technische Universität München, Munich, Germany, December 2010.
- (37) del Vitto, A.; Pacchioni, G.; Lim, K. H.; Rosch, N.; Antonietti, J. M.; Michalski, M.; Heiz, U.; Jones, H. *J. Phys. Chem. B* **2005**, *109*, 19876-19884.
- (38) Antonietti, J. M.; Michalski, M.; Heiz, U.; Jones, H.; Lim, K. H.; Rosch, N.; del Vitto, A.; Pacchioni, G. *Phys. Rev. Lett.* **2005**, *94*, 213402.
- (39) Kartouzian, A.; Thaemer, M.; Soini, T.; Peter, J.; Pitschi, P.; Gilb, S.; Heiz, U. *J. Appl. Phys.* **2008**, *104*, 124313.
- (40) Halmer, D.; von Basum, G.; Hering, P.; Murtz, M. *Rev. Sci. Instrum.* **2004**, *75*, 2187-2191.
- (41) Meijer, G.; Boogaarts, M. G. H.; Jongma, R. T.; Parker, D. H.; Wodtke, A. M. *Chem. Phys. Lett.* **1994**, *217*, 112-116.
- (42) Harbich, W. *Philos. Mag. B* **1999**, *79*, 1307-1320.
- (43) Fedrigo, S.; Harbich, W.; Buttet, J. *Phys. Rev. B* **1998**, *58*, 7428-7433.
- (44) Dinh, P. M.; Fehrer, F.; Bousquet, G.; Reinhard, P.-G.; Suraud, E. *Phys. Rev. A* **2007**, *76*, 043201.
- (45) Fedrigo, S.; Harbich, W.; Buttet, J. *Int. J. Mod. Phys. B* **1992**, *6*, 3767-3771.
- (46) Fedrigo, S.; Harbich, W.; Buttet, J. *Phys. Rev. B* **1993**, *47*, 10706-10715.
- (47) Conus, F.; Rodrigues, V.; Lecoultré, S.; Rydlo, A.; Félix, C. *J. Chem. Phys.* **2006**, *125*, 024511.
- (48) Fugol, I. Y. *Adv. Phys.* **1978**, *27*, 1-87.
- (49) Opalovskii, A. A.; Lobkov, E. U. *Usp. Khim.* **1975**, *44*, 193-213.
- (50) Brewer, L.; Chang, C. A.; King, B. *Inorg. Chem.* **1970**, *9*, 814-816.

- (51) Isakina, A. P.; Prokhvatilov, A. I.; Rodriguez-Carvajal, J. *Low Temp. Phys.* **2000**, *26*, 296-304.
- (52) Smets, A. H. M.; van Helden, J. H.; van de Sanden, M. C. M. *J. Non Cryst. Solids* **2002**, *299*, 610-614.
- (53) Aarts, I. M. P.; Hoex, B.; Smets, A. H. M.; Engeln, R.; Kessels, W. M. M.; van de Sanden, M. C. M. *Appl. Phys. Lett.* **2004**, *84*, 3079-3081.
- (54) Logunov, S. L. *Appl. Opt.* **2001**, *40*, 1570-1573.
- (55) Engeln, R.; von Helden, G.; van Roij, A. J. A.; Meijer, G. *J. Chem. Phys.* **1999**, *110*, 2732-2733.
- (56) Röttgen, M. A.; Judai, K.; Antonietti, J. M.; Heiz, U.; Rauschenbach, S.; Kern, K. *Rev. Sci. Instrum.* **2006**, *77*, 013302.
- (57) Fiedler, S. E.; Hese, A.; Ruth, A. A. *Rev. Sci. Instrum.* **2005**, *76*, 023107.
- (58) Terasaki, A.; Kondow, T. *J. Opt. Soc. Am. B* **2005**, *22*, 675-686.
- (59) Egashira, K.; Terasaki, A.; Kondow, T.; Terasaki, A.; Kondow, T. *J. Chem. Phys.* **2007**, *126*, 221102.
- (60) Kartouzian, A.; Thaemer, M.; Heiz, U. *Phys. Status Solidi B* **2010**, *247*, 1147-1151.
- (61) Kornath, A.; Zoermer, A.; Ludwig, R. *Inorg. Chem.* **2002**, *41*, 6206-6210.
- (62) Lewis, W. K.; Lindsay, C. M.; Bemish, R. J.; Miller, R. E. *J. Am. Chem. Soc.* **2005**, *127*, 7235-7242.
- (63) Schnöckel, H.; Kohnlein, H. *Polyhedron* **2002**, *21*, 489-501.

VITA
William Henry Hunter Woodward

*Nel mezzo del cammin di nostra vita
mi ritrovai per una selva oscura,
ché la diritta via era smarrita.*

William Henry Hunter Woodward was born in Lexington, Kentucky on June 22, 1984. Shortly afterward his family moved to Phoenixville, Pennsylvania where he attended Phoenixville Area High School, graduating in June of 2002. Afterwards he attended Dickinson College in Carlisle, Pennsylvania where he graduated with a Bachelor of Science in Chemistry in May of 2006. He began his graduate work in the lab of Professor A. Welford Castleman, Jr. at The Pennsylvania State University in June of 2006, where he worked directly alongside Dr. Patrick J. Roach, Dr. Zhi-Xun Luo, and Mr. Jordan C. Smith. During his time at Penn State he was privileged with the opportunity to represent his research at several conferences in the form of poster presentations, and gave two invited talks on behalf of Professor Castleman; one at the Energetic Materials Gordon Research Conference in Tilton, New Hampshire and another at the Cluster-Surface Interactions Workshop in Stratford-Upon-Avon, Warwickshire, United Kingdom. Both took place during the summer of 2010.